# CHARACTERISATION OF AMORPHOUS PHARMACEUTICAL MATERIALS

**Jeffery Neil Grazier**

A Doctoral Thesis

Submitted in partial fulfilment of the requirements for the award of

Ph.D of Loughborough University 2013

# Abstract

Small quantities of amorphous content can have a profound influence on the properties of a material, however their instability means that quantifying amorphous content over time is important for proving the stability of a drug. Quantifying amorphous content in α-lactose monohydrate by solid state $^{13}C$ CP MAS NMR, has been carried out by use of proton saturation recovery relaxation and differentiating between spectra by partial least squares (PLS), however these techniques have not proved sensitive on their own, this work investigates their sensitivity in combination. Crystalline α-lactose monohydrate and a rapidly quenched melt were combined to create a set of calibration mixes, whose spectra were recorded using proton saturation recovery relaxations ranging from 2 to 60 seconds. This technique showed a limit of detection of 0.17% (LOD = intercept + $3xS_{y/x}$), with a relaxation delay of 15 s and was able to recognise amorphous materials generated by spray and freeze drying. The atmospheric effects on the proton saturation recovery relaxation times of different amorphous lactose preparations were investigated. This found that an oxygen atmosphere reduced the relaxation times, of amorphous lactose that was prepared from a rapidly quenched melt. The loss of moisture from spray dried and freeze dried samples to less than 1% removed the significance of this effect.

Lactose is an important excipient in pharmaceuticals and a key ingredient of confectionary, very little research has been carried out in to the quantification of the isomers of different preparations of amorphous lactose. This work quantifies the isomer content by Gas Chromatography with Flame Ionisation Detection (GC-FID) using a DB-17 15m 0.53mm 1.00 µm column and derivatisation with N-(trimethylsilyl)imidazole. Two standard materials were first identified and characterised of α-lactose stable anhydrous and beta lactose, these were weighed in to calibration mixtures, derivatised and analysed by GC-FID. The calibration curve of β-lactose % peak area (y) against β-lactose content of mix (x) produced an equation of y = 0.9229x + 0.0374 with an $r^2$ value of 0.9977 The results of analysis for the different preparations of amorphous lactose were; spray dried 45.7±0.2% α : 54.3±0.2% β, freeze dried 49.8±0.1% α : 50.2±0.1% β, and a rapidly quenched melt 48.5±0.2% α : 51.5±0.2% β. This work has arrived at a substantially different result to Ramos who found that an isomer ratio of 66% α : 34% β for spray dried lactose was arrived at regardless of isomer content of the starting materials. This work may also assist crystallographic studies to select materials with low isomer impurity to further improve structure refinements.

Salbutamol sulfate used in the treatment of asthma, is micronised to between 0.5 and 5 microns for inhaler formulation to reach the respiratory regions of the lungs. The amorphous content of micronised samples of salbutamol sulfate were measured during a stability study and as part of a study into the adhesion of salbutamol sulfate to inhaler walls. Calibration standards of crystalline and spray dried salbutamol sulfate were characterised, weighed and mixed. Dynamic Vapour Sorption was used measure amorphous content via the Zografi and Mackin methods. The calibration of DVS change in mass (y) against amorphous content of mix (x) produced an equation of y = 0.110x + 0.003 with an $r^2$ value of 0.9991 and a limit of detection of 2%. Freshly micronised salbutamol sulfate was found to contain an amorphous content of 6 ± 2%. The adhesive properties were found to be greatest for freshly micronised material and lowest for the 3M development sample 3M PET 0 ± 2%. Storage of freshly micronised material at 20 °C in 65% humidity was found to reduce the amorphous content to an average of 1 ± 2% after one week. Storage after 1 week in a sealed jar in a desiccator saw an average amorphous content drop to 5 ± 2%. Measurement of salbutamol sulfate amorphous content will assist in the development of more stable salbutamol sulfate formulations.



Key Words: Amorphous; lactose; salbutamol sulfate; 13 C CP MAS NMR; dynamic vapour sorption; powder X-ray diffraction; FT-IR; differential scanning calorimetry

# Acknowledgements

I am eternally grateful to my supervisor Sandie Dann; who was brave enough to give me this opportunity as mature student and has successfully guided me through my research when “life got in the way of plans”. Without Sandie's patience and kind corrections to my crimes against the English language, I am sure I would have never submitted.

I want to give an enthusiastic thank you to Chris Blatchford my industrial supervisor at 3M, for his guidance and making available 3M equipment, without which I could not have completed my research. I have to admit to marvelling at Chris' expertise and knowledge of GC. I must finally thank Chris for his assistance and help in the writing up of my GLP notebooks.

Before starting my research at Loughborough I knew nothing about $^{13}C$ CP MAS NMR, all that I have learnt has been via Mark Edgars recommended reading and time spent teaching me. Mark deserves enormous credit for training me how to get spectra out of the instrument and for doing this a second time when I forgot everything.

Pauline King just deserves masses of praise; for keeping the instrumentation going on so little budget, for making lab clean ups actually happen, training me how to use equipment, ensuring we all worked safely and most importantly bringing in cake.

It would be impossible to write this without thanking Paul Kelly, whose imagination has brought about so many ideas centred on the capsaicin molecule. I must also thank Chris Raw, Glyn Derrick Joe Jackson, Lea Fan, Andy Butterworth, and Rob King for a number of noteworthy evenings as well as their comradery. I also wish to thank Nuria Lastra-Calvo and Toni Polainas for their friendship and for introducing me to so many of their friends. Daisy Ellis deserves a special mention for very kindly proof reading the thesis after viva corrections.

Away from University I have a huge thank you, to give to my father and step mother Jane for their support during my write up and looking after me while I was job hunting. The two people who I have to thank for urging me to take up the studentship at Loughborough are my brother Russell and daughter Frances. When I floated my options of a job testing air filters for CW agents or the studentship, they unreservedly recommended the studentship. Looking back I can't image how I could have got through the past few years without Russell's help and support, I also want to thank, Dawn, Harry, Chelsea and Charlie for the most wonderful times.

The most important person to me that I want to thank is my daughter, Frances who has given, so much towards my studies at Loughborough, giving up her weekends to visit me, suffering interrupted sleep in the halls of residence and facebook friend requests from Joe and Andy. The greatest complement I can give to Frances is to repeat her thoughts and her simple direct question when I first discussed the studentship with her; “You should do the PhD Dad, it's what you want to do, so what exactly will be your unique contribution to knowledge?”….

# CHAPTER 1

# Introduction

## 1.1 Structure of Amorphous Solids

### 1.1.1 Introduction

Every child is familiar with the amorphous material known as “candy floss” or “cotton candy”. Candy floss dissolves almost instantly in the mouth, delivering far greater sweetness than normal sugar from a supermarket packet. Unfortunately, every slow eater learns that this treat does not last; when exposed to atmospheric moisture and ambient temperature, the amorphous sucrose rapidly absorbs water. This is just one example of how the properties of amorphous materials are very different to those of bulk crystalline materials.

The connection between “candy floss” and pharmaceutical materials is the use of amorphous sugars in formulations, although lactose is the sugar commonly used rather than sucrose. Sugars are used for a variety of reasons, including as simple bulking agents to increase volume or as carrier particles in inhalers.[1] The properties of amorphous lactose can be highly desirable for formulators, because it dissolves more readily than crystalline lactose, so it can be used to aid the dissolution of the active pharmaceutical ingredient (API).[1] Amorphous lactose can also be used to modify a tablet property, which increase their tensile strength and reduces their friability.[1] Unfortunately, just like candy floss, amorphous lactose also has its disadvantages; it is unstable to atmospheric moisture and temperature, losing its useful properties as it crystallises. The instability of a material in a pharmaceutical formulation can pose a problem, since pharmaceuticals are expected to perform consistently and reproducibly compared to their clinical trials even after spending years on a pharmacy shelf anywhere in the world.[2] This makes quantifying the amorphous content of a material and predicting their long term behaviour under different conditions essential for assessing the shelf life of any formulation.

The “stickiness” or adhesive properties of amorphous lactose are critically important to dry powder inhalers. Lactose is used as a carrier particle to disperse small crystals of API into the inhaled breath by surface adhesion of the large carrier particle to the drug particle.[1] The ability of the carrier and the API to disaggregate at the right time is

crucial, generating the efficacy of the formulation. The process of creating the aggregated drug and lactose excipient particle requires reducing the particle size of lactose crystals. Particle size reduction can be deliberately achieved in a number of ways including micronisation and spray drying, however small quantities of amorphous lactose are created whenever crystalline lactose is ground. These areas of amorphous lactose which form on the surface of lactose particles can dramatically change the adhesive properties towards other materials. This can make the difference between delivering a drug to the respiratory regions of the lungs, or just impacting on the back of the throat, which has little therapeutic effect.[3]

Structure lies at the heart of all material properties, but the word amorphous is synonymous with a lack of structure, emerging in the early-18th century, from the Greek *amorphos* , meaning 'shapeless' ( a- 'without' + morphē 'form').[4] The historical perspective is necessary here because during this period, geologists following Steno's 1669 investigation into the angles between crystal faces, were classifying rocks for additional properties such as shape, colour, lustre, symmetry, and cleavage.[5] In 1774 using these measures, Werner recorded obsidian (amorphous volcanic glass) and opal (amorphous silicon dioxide) as "failing to crystallise".[6]

In the scientific literature, authors frequently refer to materials as being "amorphous to X-ray", when no clearly defined Bragg reflections are observed in an X-ray powder diffraction pattern. There seems to be significant confusion however, as to whether the absence of reflections are due to a disordered or glass-like arrangement or simply limited order due to the size of particles. Since the Bragg relation requires enough periodic repetition of unit cells to allow both constructive and destructive interference to occur to generate the reflection, it is possible to have particles which are simply too small to generate a diffraction pattern, yet are ordered on a short range scale

At the atomic scale a material can be said to be amorphous, if it "lacks the long range translational symmetry of crystalline materials".[7] It is not possible to prove a negative statement of what something lacks, however it is possible to describe "random

packing" and test for it. Modelling a random pack has to take account of the forces of attraction and repulsion between atoms, i.e. two atoms are unable to occupy the same space at the same time, (a truly random structure would be that of a group 0 element at high temperature and low pressure). [8]

## 1.2 The Frozen Liquid Model or Random Packing

In 1960 Bernal published the first experiment to provide an insight into amorphous structure. The experiment wrapped groups of quarter-inch ball bearings in thick elastic bands and dipped them into paint. The paint allowed the number of contacts on each ball to be counted. The results were expressed as a distribution for the number of contacts or co-ordination number, the results of over 1000 ball bearings can be seen in Figure 1.[9]

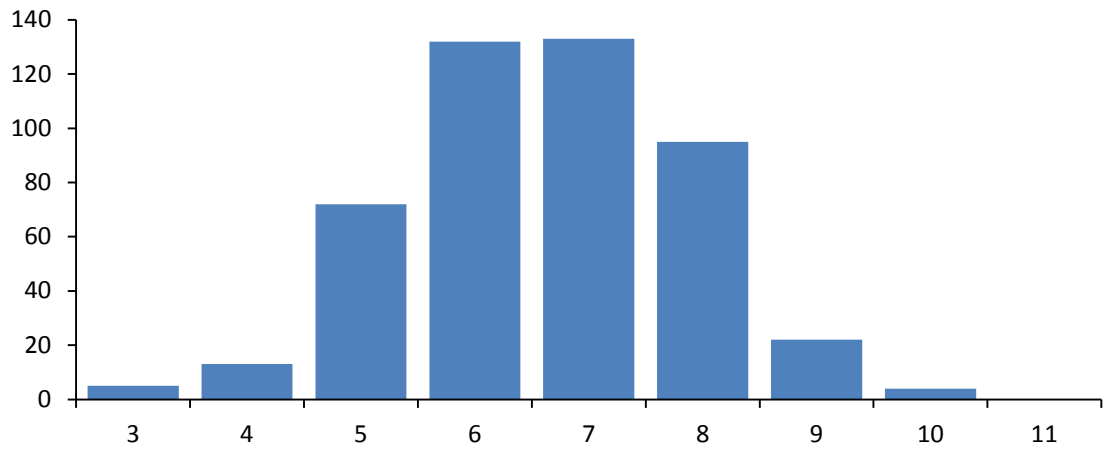


**Figure 1 Histogram of sphere contact numbers, found from sphere assembly.[9]**

The distribution can be seen to possess a median co-ordination number of about 6, half the maximum of 12 calculated by Newton from his "kissing spheres" problem.[10] In addition Bernal estimated volume occupancy of the ball bearings to be about 63%, in contrast to the "Kepler's conjecture" of 74% for uniform sphere packing in three-dimensions. The Kepler conjecture predicts cubic close-packed and hexagonal close - packed to be the most efficient and dense way to pack spheres. [11]

Underlying Bernal's experiment are rules that are seemingly obvious; that 2 ball bearings cannot occupy the same space, a force of compression is at work (the elastic bands) and that there is very little friction between ball bearings, (that's why ball bearings are made). These rules impose structure, since a truly random structure would allow the centre points of spheres to be super imposable or infinitely distant. The low friction and compaction prevented less dense arrangements of spheres being adopted.

### 1.2.1 Jammed Matter and Liquid Structure

In order to restrict the movement of a sphere or "jam" it, at least 4 other spheres are required to be in contact with the sphere. The phrase "jammed matter" now refers to computer simulations that vary the sphere properties of friction and packing density. Random, loose packing describes conditions where the packing density of spheres is dropped from the Bernal conditions and the average co-ordination number is allowed to drop to a minimum of 4.[12]

These loose packed structures have packing densities ranging from 53.6% to the Bernal figure of 63.4% and suggest a relationship between co-ordination number Z and random loose packed density ($\phi_{RLP}$), with a minimum average co-ordination number of 4 and a maximum of 6. This creates a phase diagram for Jamming Theory seen in Figure 2, and described in Equation 1.[13]

$$\phi_{RLP} = \frac{Z}{Z + 2\sqrt{3}} \qquad \textbf{Equation 1}$$

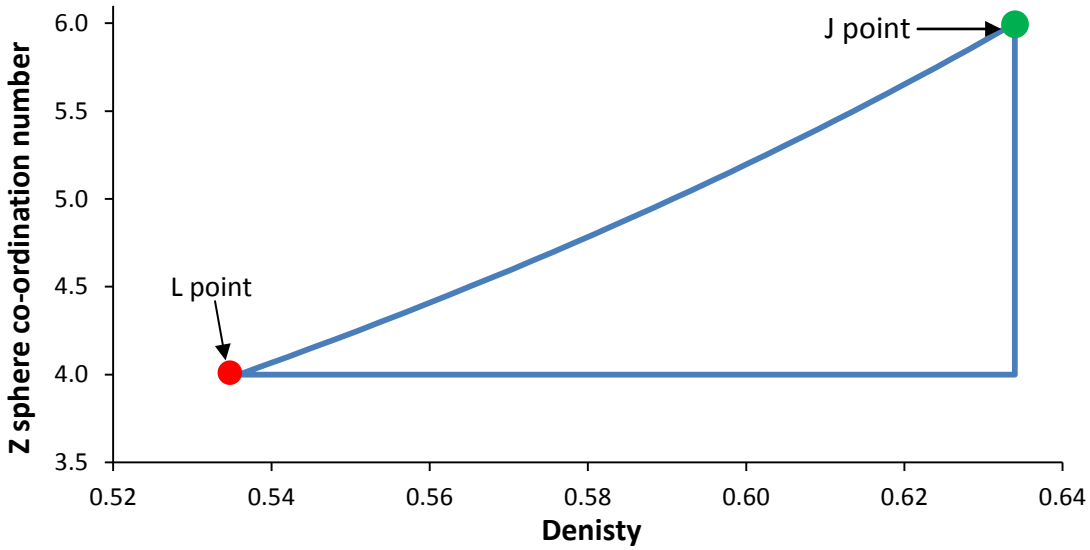


**Figure 2 A phase diagram of jamming[13]**

The idea of using spheres to represent atoms of a monoatomic gas is a valuable model. A gas has low density, with almost no spheres in contact with one another. The transition from a gas to liquid brings the spheres together in closer contact or compacts them. The idea of temperature and the degree of compaction are seen to be linked, the more compacted the spheres are, the lower the temperature. The spheres are loosely packed as a liquid, but with greater compaction become tightly packed, until ultimately the spheres form dense structures with translational symmetry (crystalline solids).[14]

The gas/liquid and liquid/solid phase transitions are represented in Figure 2 by the L point and the J point, respectively. Comparison between the sphere studies and argon properties can be made. Crystalline argon has a face centred cubic lattice, with a density of 1.616 g $cm^{-1}$,[15] which should have a space fill of 74%. Liquid argon at its boiling point has a density of 1.207 g $cm^{-1}$ [16] and should have a random loose packed structure with a space fill of 53.6%. The relationships shown in Equation 2 and Equation 3 suggest that this model is reasonable.

$$\frac{\mathbf{74.0\%}}{\mathbf{53.6\%}} = \mathbf{1.381} \qquad \textbf{Equation 2}$$

$$\frac{\mathbf{1.616}}{\mathbf{1.207}} = \mathbf{1.339} \qquad \textbf{Equation 3}$$

The density of argon at its melting point is 1.436 g $cm^{-1}$. [15] This should have a random packed structure with a space fill of 63.4%.[17] Comparison of these ratios is shown in Equation 4 and Equation 5.

$$\frac{74.0\%}{63.4\%} = 1.167 \qquad \textbf{Equation 4}$$

$$\frac{1.616}{1.410} = 1.146 \qquad \textbf{Equation 5}$$

The original Bernal Studies used 1/4" steel ball bearings, and found a space fill limit for the random close pack of 63.4%, By using soft latex spheres this limit is removed.[18] Atoms of argon are not scaled down ball bearings, the interactions between atoms of argon are described by the Lennard-Jones potential, and where London dispersion forces provide the force of attraction that is balanced against electro static repulsion.[19] Whilst the Bernal experiment provides a useful model of random structure, it comes as no surprise that it does not translate directly from 1/4" steel ball bearing to argon atoms exactly.

### 1.2.2 Jammed Matter and the Amorphous Solid

Y. Jin has undertaken experiments using computer simulations with compressible spheres that possess surface friction.[14] These simulations use algorithms such as Lubachevsky-Stillinger to produce random packing arrangements of hard spheres.[20] These models show continuity in properties of loose pack and tight packed random arrangements, but a discontinuity occurs, as further compaction produces ordered hexagonal close-packed and cubic close-packed arrangements. Initially these are small clusters of few spheres that form ordered hexagonal and cubic close packed arrangements, but with further compaction these clusters increase in size.[14] To understand this further, the description of the Voronoi cell needs to be introduced.

A Voronoi cell is constructed around a sphere by forming planes at the mid-point from lines drawn to the centre points of nearest spheres. These planes enclose a sphere with in a cell, to form a volume that can be measured, (see Figure 3).[8] Voronoi cells have a variable number of faces (dependant on the number of nearest neighbours)

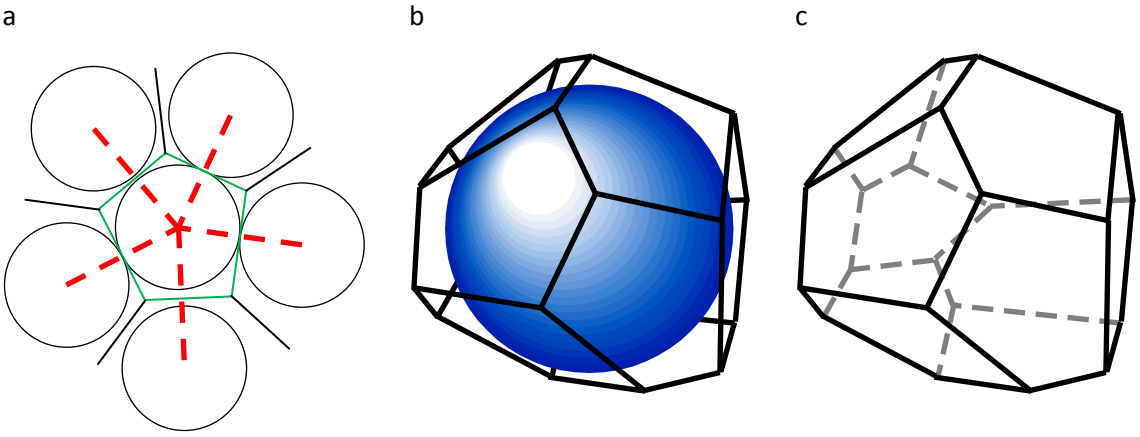


**Figure 3 Formation of a Voronoi cell surrounding a sphere**
**a) Two dimensional representation of a Voronoi cell in green**
**b) Voronoi cell surrounding a sphere**
**c) Empty Voronoi cell**

The Voronoi volume fraction $\varphi_{vor}$ is found by dividing the Voronoi volume by the sphere volume. The Voronoi volume fraction and packing density are different, packing density is a bulk property determined by counting the spheres contained within a volume, whereas Voronoi volume fraction is calculated for every individual sphere. A probability distribution best represents the range of values found within a single packing density. Figure 4 shows Voronoi volume fractions $\varphi_{vor}$ as different colours on the vertical axis and the packing density $\varphi$ on the horizontal axis.[14]

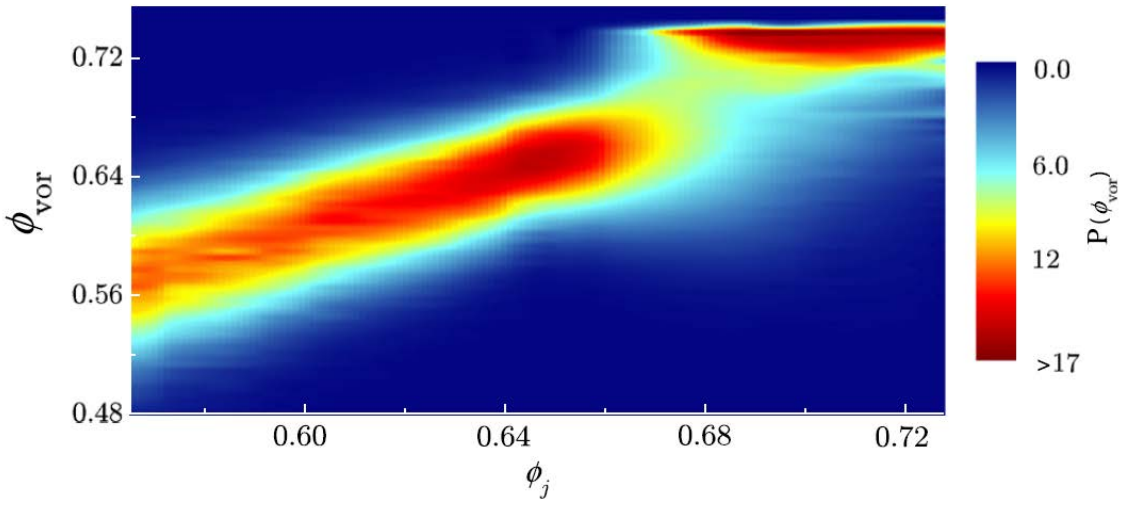


**Figure 4 Probability distribution of local volume fractions of the Voronoi volumes of each sphere, $P(\phi_{vor})$ (vertical axis) against packing density $\phi_j$ (horizontal axis)[14]**

The obvious feature of Figure 4 is the discontinuity between the two areas. The random loose packed line is also seen to range from 53.6% pack density to beyond the

Bernal random close pack limit of 63.4%. Jin suggests random close packing can extend to 68%, because the spheres are compressible. [14]

The second area ranges from 67% to 73% packing density, this area produces Voronoi volume fractions greater than 69%, where cubic close packing and hexagonal close packing are observed. This suggests that this region is highly ordered. The extended cubic close packing and hexagonal close packing arrangements can be examined in the data by converting each sphere's Cartesian co-ordinates relative to its neighbours into polar co-ordinates. This procedure is possible because these packing structures demand specific angles between touching spheres to achieve the close packed structures. This region was found to show bond angles identical to those seen in cubic and hexagonal close-packing. The region of ordered packing was found to extend over half the simulated space in some cases, although still containing regions of random close packing. [14]

## 1.3 Alternative Descriptions of the Amorphous State

So far only “random packing” also known as the "frozen liquid model"[7] has been explored in this thesis to explain the amorphous state, three alternative ideas are those of the nanocrystalline, defect model and the two state model, shown in Figure 5.

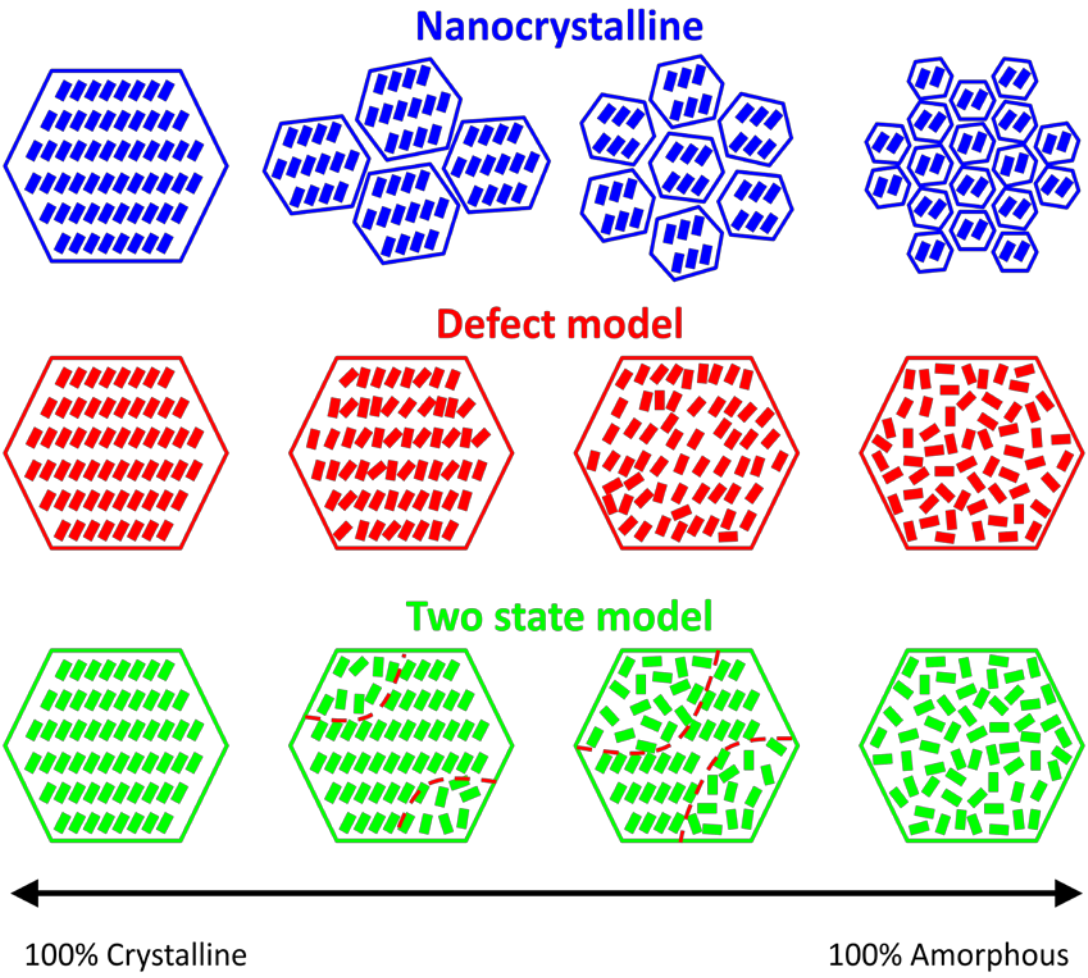


**Figure 5 Modelling routes between crystalline and amorphous states** [21]

X-ray diffraction does not aid characterisation of the nanocrystalline state. It may be composed of crystals too small to produce an X-ray pattern, although within the small crystals the packing motif is followed for translational, orientational or conformational symmetry required to generate an X-ray pattern. Only the defect model allows for a continuum to exist between crystalline and amorphous. The work hardening of metal presents an opportunity to explore this idea. The shaping of a metal by hammering, introduces defects, as the metal is worked it becomes more difficult to shape, and at the same time more brittle. Metals are shaped at an atomic scale by layers of atoms

sliding past one another, cold working of a metal introduces defects to the crystal structure that prevent the layers of atoms passing over one another. The two state model, is the complete opposite to this, allowing areas that are completely amorphous or totally crystalline.[21]

### 1.3.1 The Two State Model

The two state model originated in polymeric materials where very large numbers of monomeric units come together to produce huge polymeric structures. In such materials, the range in temperature over the whole structure and the viscosity of the mixture resulting from the interfering chains as the mixture crystallises results in ordered areas typically within the chain and disordering between them. This leads to a mixture of crystalline and amorphous properties in the same material.[21]

### 1.3.2 The Nanocrystalline Model

The size of a crystal sets a very clearly defined boundary to the extent of order. The nanocrystalline model can be explored using X-ray Powder Diffraction via the Scherrer equation that relates reflection (peak) width to crystal size. This is set out in Equation 6, where the integral peak width (β) is equal to the X-ray wavelength, multiplied by a constant and is inversely proportional to volume weighted crystallite size ($D_v$) measured perpendicular to the reflecting plane.[22]

$$\beta(2\theta) = \frac{K\lambda}{D_V \cos\theta} \qquad \textbf{Equation 6}$$

The value for constant K ranges from 0.62 to 2.08. [23] Integral peak width (β) is defined by peak area divided by the peak height and is related to the width at half maximum height (Γ) using Equation 7 and Equation 8 for Lorentzian and Gaussian peak shapes respectively.[24]

Lorentzian $$\beta(2\theta) = \frac{\pi\Gamma}{2} \qquad \textbf{Equation 7}$$

Gaussian $$\beta(2\theta) = \Gamma\sqrt{\left(\frac{\pi}{4\ln 2}\right)}$$ **Equation 8**

The upper size limit to measurement using the Scherrer equation is set by the noise associated with peak measurement.

### 1.3.3 The Defect Model

Referring back to Figure 5, the defect model shows a continuum between 100% crystalline and 100% amorphous. Defects occur in all crystals, and can be categorised as occurring at a distinct point, as a line or as a plane passing through the crystal. The defect model of the amorphous state imagines a perfect crystal with more and more defects added until eventually the solid loses its translational order (as shown in Figure 5) and becomes effectively amorphous. Crystalline materials have densities much greater than amorphous materials where the density falls as the number of defects increase.[21]

#### *1.3.3.1 Point Defects*

Intrinsic point defects are seen in the greatest quantity at high temperature, just prior to melting as the entropy contribution (TΔS) to the free energy reaches a maximum.[25] The Schottky point defect is stoichiometric defect mechanism, and generates pairs of vacant sites to maintain neutrality as shown in Figure 6. A Frenkel defect displaces an atom / ion from its usual site within the lattice, to an interstitial position, between occupied sites, (see Figure 6).[26] It is easy to see how Schottky defects reduce density as the total number of atoms within a unit cells falls as the entropy term increases and atoms are lost.

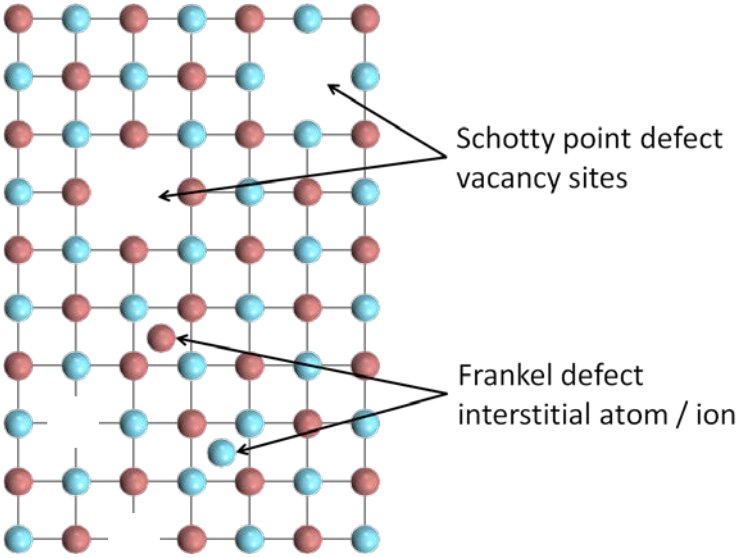


**Figure 6 Schottky and Frenkel defects[25]**

Extrinsic defects occur when a crystal is doped with an impurity with a different valency or coordination number. Deliberate doping is often carried out to alter properties such as ion conductivity or magnetic behaviour. Interchange of atoms can occur in alloys, which involve a distribution of atoms over a set of lattice sites (i.e. bronze). Solid solutions are specific type of extrinsic defect, where the replacement ions have the same charge and a size difference of less than 15%.[25]

### *1.3.3.2 Line Defects*

An edge dislocation can be described as an extra plane of atoms that is shorter than adjacent planes. All planes including the edge dislocation plane are parallel, except for those adjacent to the dislocation, (see Figure 7).[25, 26]

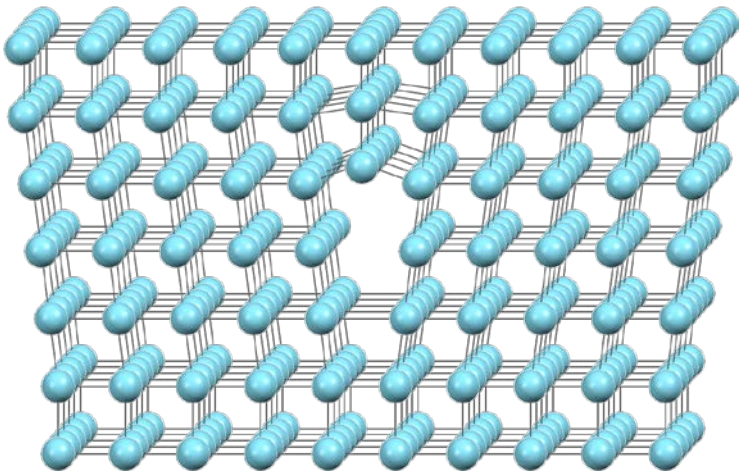

**Figure 7 line defect[26]**

A screw dislocation is formed, if a plane of atoms/ions fails to extend the whole length of the crystal, (see Figure 8). The screw dislocation can loop out of the crystal or extend across the crystal. A screw dislocation loop may eventually travel through the crystal forming at the opposite side. When this happens, the screw dislocation may travel across the entire crystal to form a step.[25] Both of these dislocation mechanisms leads to materials with lower densities, since they reduce packing density of the atoms.

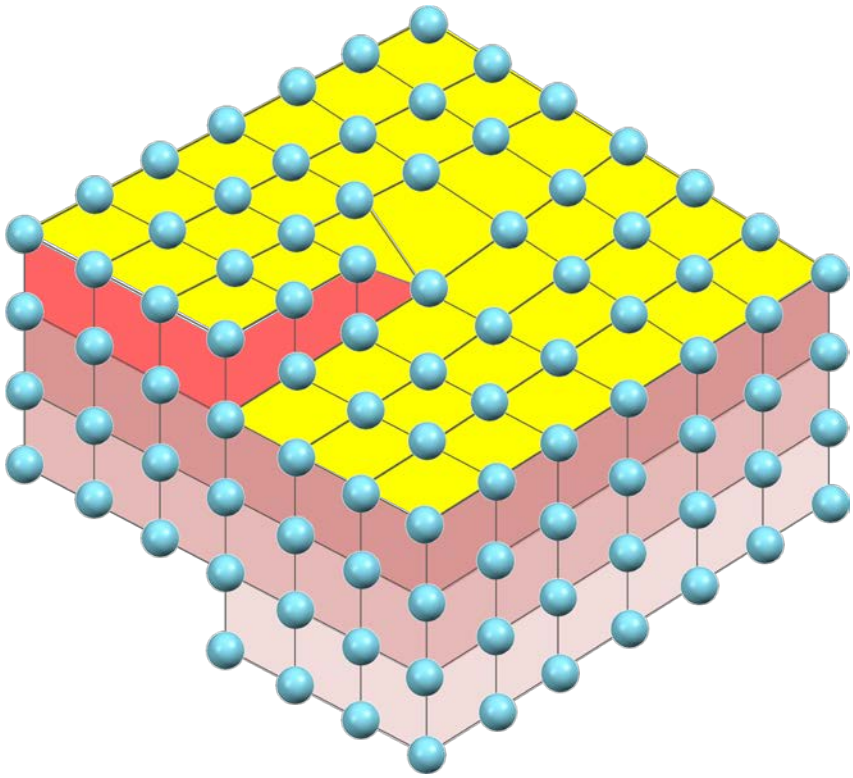

Figure 8 Screw Dislocation[25]

### *1.3.3.3 Defect Planes and Grain Boundary*

Stacking faults often occur in layer like structures resulting in the correct order within layers, but with differences in the layering.[26] Particle size reduction processes such as micronisation are known to create amorphous content.[21] Very little of the energy input into grinding processes is thought to produce fresh surface, since much of the energy is lost as heat in creating crystal dislocations and reducing "grain size".[27] Grain boundaries occur where two crystals are joined together, but have completely different orientations, (see Figure 9), meaning the structure is non-continuous and has more defects as the boundary between the grains.[26, 25] Transmission Electron Microscope (TEM) images of grain boundaries are shown in Figure 10.

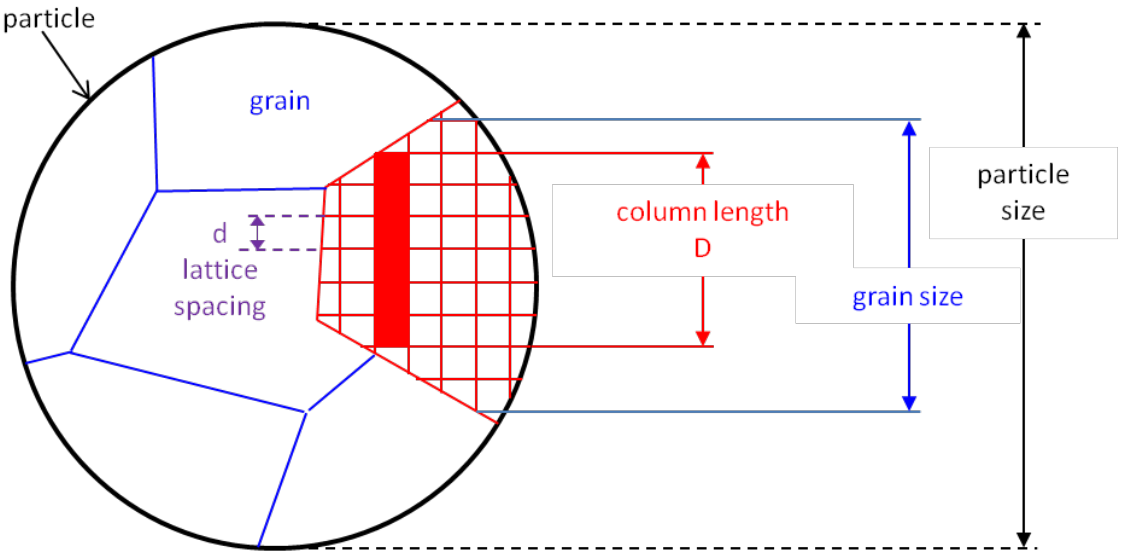


**Figure 9 Nanocrystalline Powder: Different Measurements**

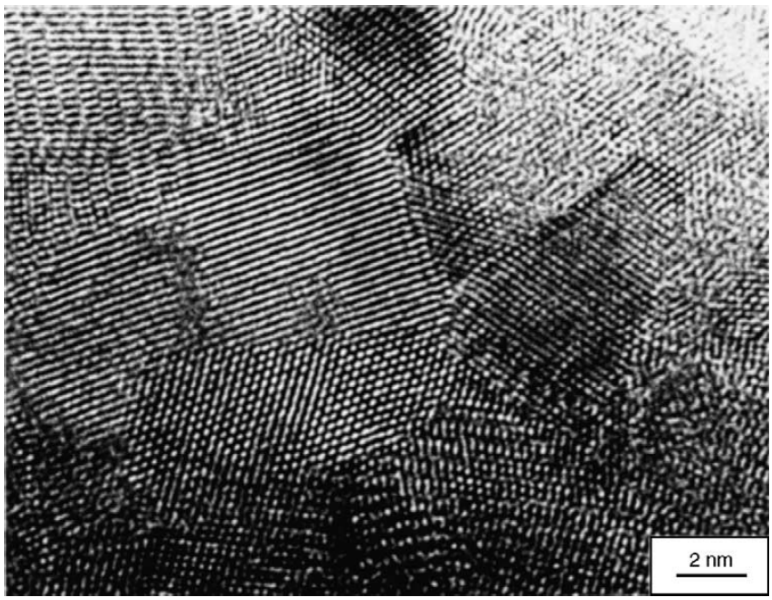


**Figure 10 Image of a region of nanocrystalline palladium containing a number of grains**[28]

The density measurements of nanocrystalline materials seen in Table 1 are between 98 to 100% of their coarse grained elemental measurements. The grain size in this case was measured by TEM. Table 1 shows that as grain size decreases for a number of different metals, the density also decreases, (where $\mathbf{d/d_0}$ is the nanocrystalline density divided by the bulk crystalline density). [29]

| Material | Grain size D (nm) | $d/d_0$ |
|---|---|---|
| Ag | 20 | 98.9% |
| Al | 37 | 99.9% |
| Cu | 27 | 99.4% |
| Ni | 11 | 99.4% |

**Table 1 Nanocrystalline grain size and density [29]**

When two crystals join at a grain boundary, the orientation of these grain boundaries determines the free volume of the interface between them, Figure 11 shows how this changes.[30]

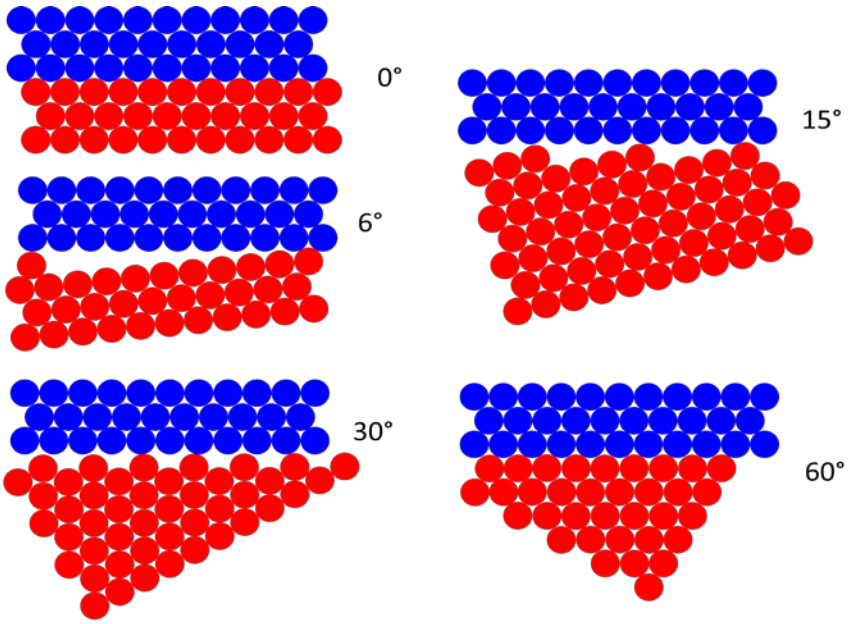


**Figure 11 Voids created at grain boundaries, assuming grain boundaries remain perfectly crystalline[30]**

As the volume of the grain (crystal) increases the fraction of atoms on grain boundaries decreases. Considering nickel with an atomic radius of 0.135 nm [16], and building up a cluster centred on a single atom in shells, the calculation is shown in Table 2. To add perspective to this a cluster with just 3 shells made up of 147 atoms would have a 92 atoms on the surface and possess a diameter of 0.945 nm.

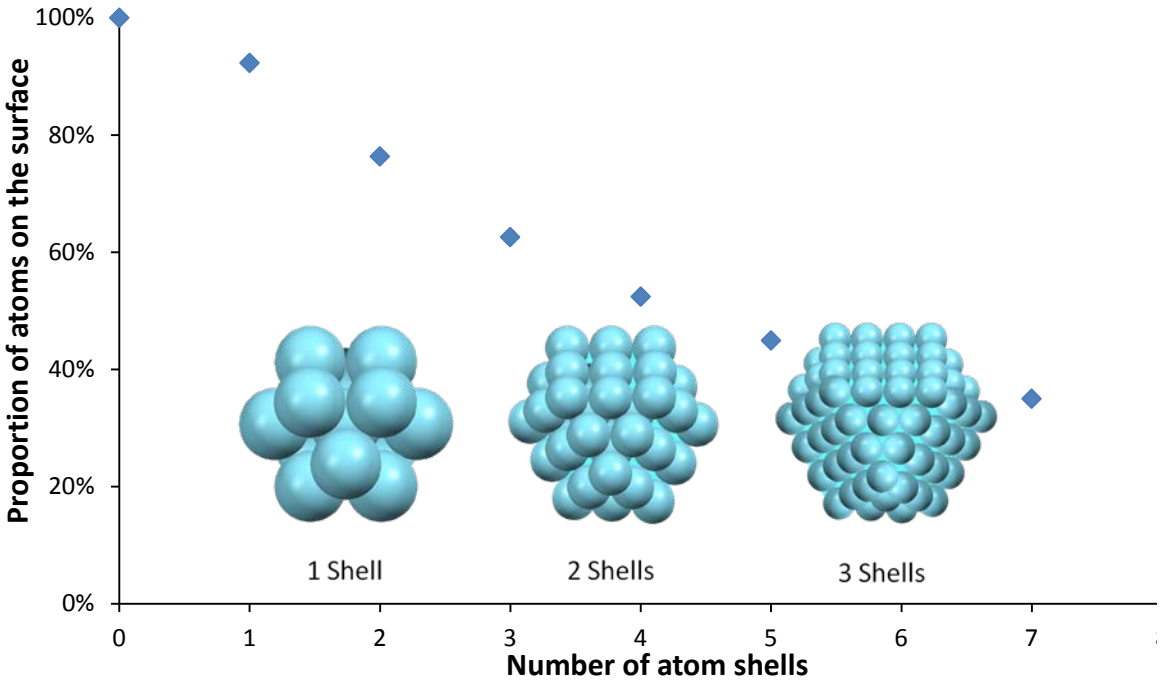


**Figure 12 Proportion of surface atoms on atom clusters made by surrounding a single atom with further shells of atoms[28]**

| Number of Shells | Total Number of atoms | Number of surface atoms | Proportion of atoms on the surface |
|---|---|---|---|
| 0 | 1 | 1 | 100% |
| 1 | 13 | 12 | 92% |
| 2 | 55 | 42 | 76% |
| 3 | 147 | 92 | 63% |
| 4 | 309 | 162 | 52% |
| 5 | 561 | 252 | 45% |

**Table 2 Proportion of surface atoms for atom clusters made from a number of shells of atoms surrounding a single atom[28]**

Zhao has predicted the combined effect of different defect types on nanocrystalline density using Equation 9, where $d_0$ is the density of large crystals after annealing to remove dislocations and $d_{nc}$ is the nanocrystalline density.[29]

$$\frac{d_0}{d_{nc}} = 1 + \frac{C_v(V + \Omega_0)}{\Omega_0} + \beta\rho_s + \frac{3\delta}{D} \qquad \textbf{Equation 9}$$

The three terms each account for the reduction in density due to vacancies, line defects and grain boundaries respectively. The grain size term $\frac{3\delta}{D}$ is derived from the surface area to volume fraction seen in Equation 10, where $D$ is the diameter of the nanocrystal and $\delta$ is a volume expansion coefficient for the crystal normal to the grain boundary, accounting for the voids shown in Figure 11.[29]

$$\frac{\left[4\pi.\left(\frac{D}{2}\right)^2\right]}{\left[\frac{4\pi}{3}.\left(\frac{D}{2}\right)^3\right]} = \frac{3}{D} \qquad \textbf{Equation 10}$$

The term $\beta\rho_s$ accounts for density increase due to dislocation, where $\beta$ is the excess volume per unit length of a dislocation and $\rho_s$ is the density of dislocations. The additional volume due to vacancies arising from point defects is described by $\frac{C_v(V+\Omega_0)}{\Omega_0}$, where $C_v$ is the vacancy concentration, $\Omega_0$ is the atomic volume and $V$ is the relaxation volume of the vacancy.[29]

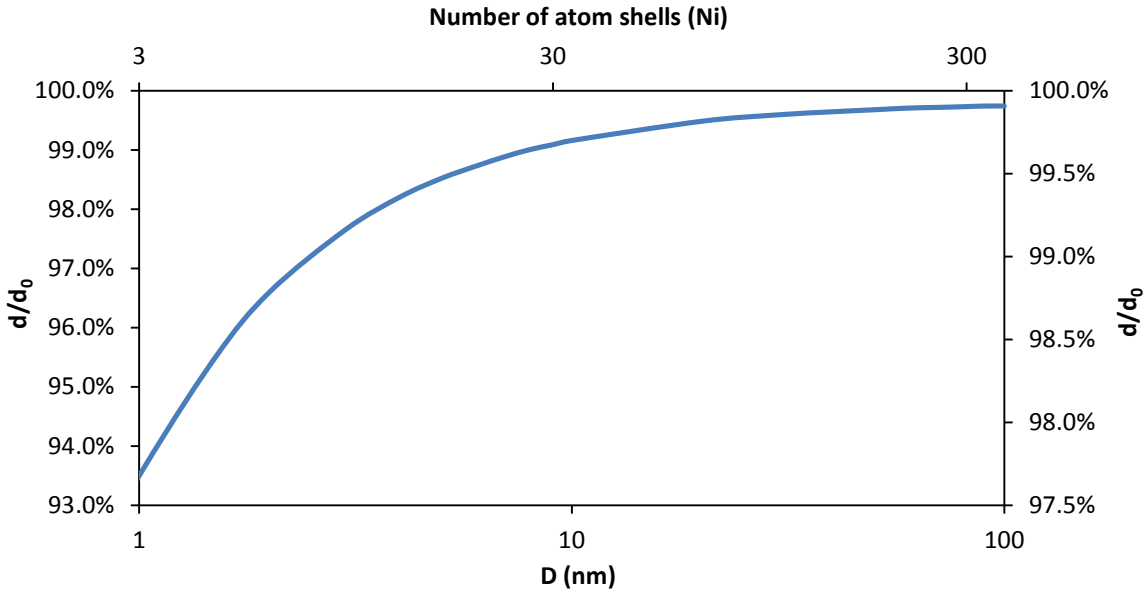


**Figure 13 Density ratio to bulk crystal density of nanocrystals of diameter D[29]**

Zhao was able to estimate the vacancies arising from cryo-grinding of nickel by measuring the heat flow from DSC after annealing above 260 °C. Figure 13 shows the dominance of grain boundary contribution to lowering density as nanocrystal size drops to 1 nm. Zhao estimated from neutron diffraction data that the density change with nanocrystal size $D$, using a value of 0.023 ± 0.004 nm for $\delta$ volume expansion in

nickel, that the random close pack density was achieved when $D = 0.41$ nm. This is approximately the same size as the cluster shown in Figure 12 for the smallest cluster with 1 shell of atoms surrounding a single atom.[29]

Although small grains (4 nm in diameter) can produce powder X-ray diffraction patterns with diffuse Bragg reflections. The effect of grain size on density is such that random close pack densities are not reached until the grain size drops to atom clusters less than a nanometre in size. This suggests that a nanocrystalline material can fail to produce Bragg reflections from X-ray powder diffraction, and yet may have a density greater than expected for a random close pack structure $\left(\frac{d_{nc}}{d_0} = \frac{63.4\%}{74.0\%} = 85.7\%\right)$. This means that a material which does not produce a power X-ray pattern can still possess order within grains which are too small to meet the Bragg condition.

## 1.4 Measuring the Extent of Order

Powder X-ray diffraction data can be used to determine the average particle size of grains within a sample. The data can be analysed using two approaches, measuring the peak widths of Bragg reflections for size and strain, or transforming the diffuse scattering data in to a paired density function.

### 1.4.1 Size and Strain Measurements

In the 1950's, Williamson & Stokes found the width of a reflection increased with 2θ angle proportionally to the cosine of θ. This was accounted for by the change in dimensions of the unit cell and referred to as lattice strain. This was drawn from the analogy of a length of wire loaded with weights; the change in dimension divided by the original length is the unit less measure of strain. Uniformly changing the lattice dimensions by +1% would result in a diffraction pattern with reflections shifted to a lower 2θ values, however lattice strain reflects the distribution of lattice dimensions, i.e. ±1%, so the reflection broadens. [31]

Figure 14 and Figure 15 show a ±1% change in unit cell dimensions, and how this represents the extremes of a normal distribution of strains. The individual changes in unit cell dimensions across 7 points shown in Figure 15 are plotted in Figure 16, their intensities multiplied by their relative quantities. The effects on the 2θ positions are shown by the coloured continuous lines, and the observed signal from the combined distribution is shown as a dashed black line in Figure 16.

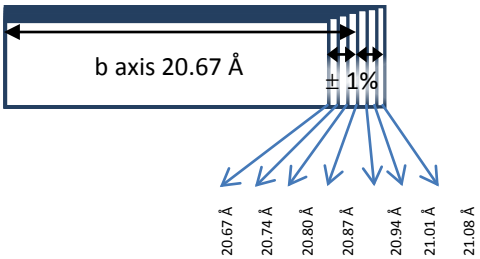


**Figure 14 Variation in unit cell size**

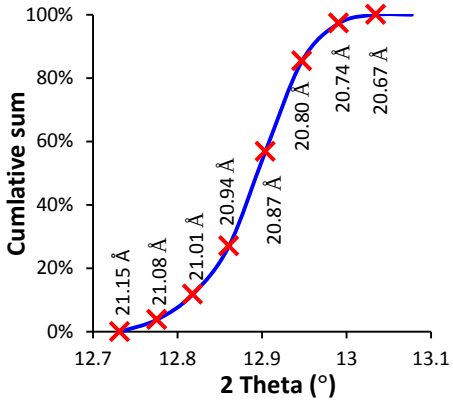


**Figure 15 Distribution of fraction of different unit cell sizes**

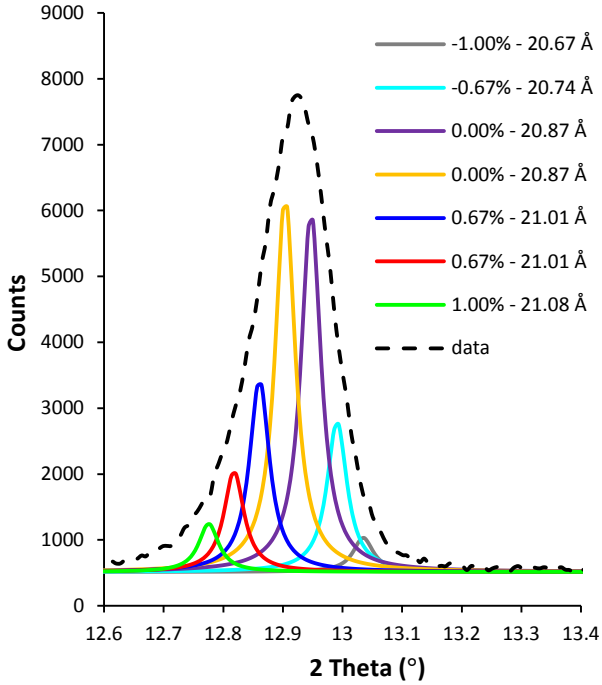


**Figure 16 Effect of combining different unit cell sizes on powder diffraction pattern**

The instrument on which measurements of peak width are made, also contributes to the peak width itself. Williamson and Hall were able to take account of instrument factors by measuring integral peak width of a crystalline standard against 2θ, and produce a best fit curve. Lattice strain $\varepsilon$ was found to be proportional to peak width $\beta(\theta)$ using Equation 11. The integral peak widths observed for the analyte material were measured and the peak width due to instrument factors subtracted, using Equation 12 (for Lorenz peak shape) and Equation 13 (for Gaussian peak shape) to give the calculated peak width due to size and strain factors.

$$\varepsilon = \frac{\beta(\theta)\cot\theta}{4} = \frac{\beta(\theta)}{4.\tan\theta} = \frac{\beta(\theta).\sin\theta}{4.\cos\theta} \qquad \textbf{Equation 11}$$

$$\beta_{obs} - \beta_{inst} = \beta_{strain} + \beta_{size} \qquad \textbf{Equation 12}$$

$$\beta_{obs}^2 - \beta_{inst}^2 = \beta_{strain}^2 + \beta_{size}^2$$ **Equation 13**

These instrument corrected peak widths were then multiplied by $\cos\theta$ and plotted against $4\sin\theta$. This produced a straight line plot, that allowed the lattice stain to be calculated from the slope and the crystal size from the intercept with the y axis (see Figure 17).[32,33]

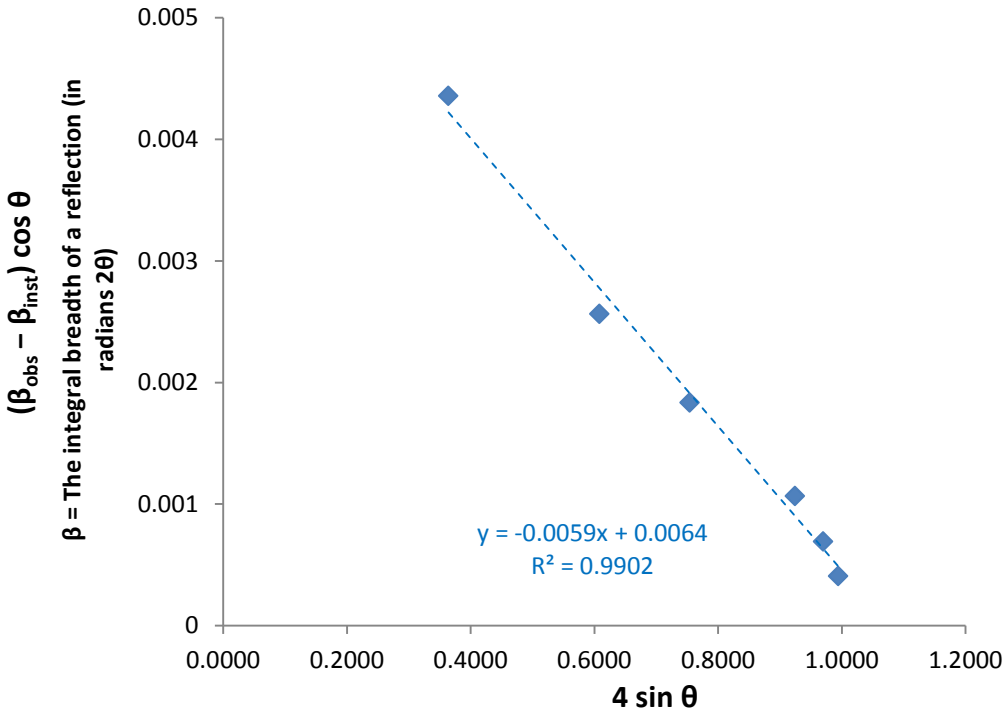


**Figure 17 Williamson Hall plot of $LaB_6$ peak width**

### 1.4.2 Paired Density Function (PDF)

When faced with powder diffraction patterns that show only broad diffuse reflections that merge into one another, total scattering methods which analyse the whole pattern including the background can be useful since both the Bragg and diffuse components contribute to produce a paired density function.

Following Bernal's work Scott wanted to show that random close packed spheres present short range order comparable to liquids. In order to make this possible, Scott needed to present his data in a manner that could be compared to the X-ray and neutron data collected on liquid argon. The first stage was to convert the "Cartesian co-ordinates" for each sphere in a random close pack into "polar co-ordinates". These describe position within and outside a sphere using two angles and a distance from the centre. By analysing each individual sphere's radius, co-ordinates to all other spheres and a histogram of average distance from spheres to their neighbours could be produced. This amounted to a probability distribution of finding pairs of spheres at a distance $r$ apart, and was equivalent to fluctuations in density. Scott processed this data from a similar ball bearing experiment to produce the Paired Density Function $g(r)$, which is a factor of the bulk density $\rho_0$ (this is shown pictorially in Figure 18). [34]

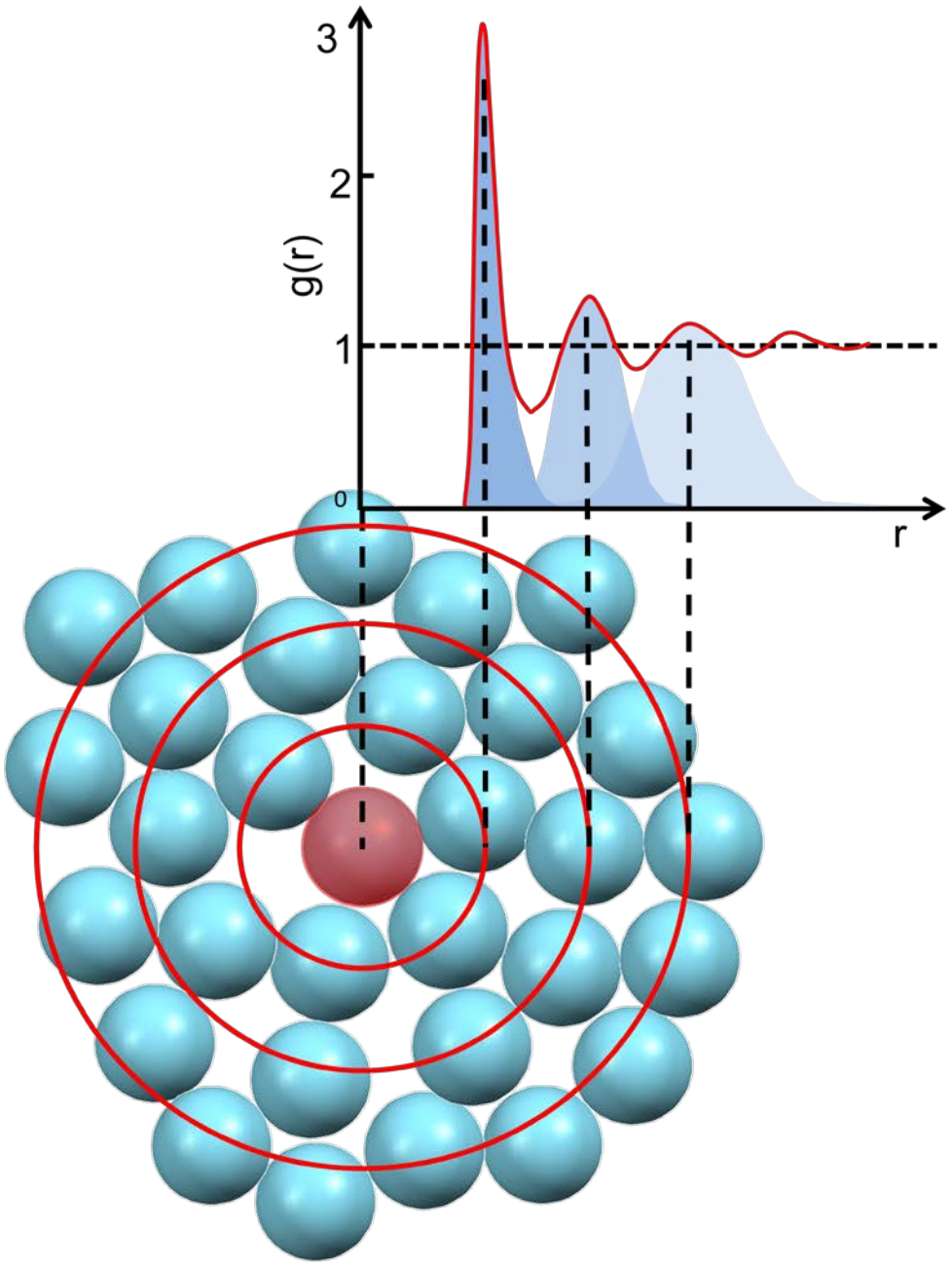


**Figure 18 2D – representation of pair distribution function for a random close pack**

The Paired Distribution Function (PDF) shown in Figure 19 demonstrates peaks and troughs that are proportional to the probability of finding a sphere at a given radius. For $g(r)>1$ there is an increased probability of finding a sphere at distance r. The PDF $g(r)$ has a convergent property, as $r$ increases eventually PDF $g(r)= 1$ (for random packing).

The PDF $g(r)$, is useful, since bond lengths can be determined by measuring from peak to peak and the co-ordination number can be found from the Gaussian integrated area

beneath the peak.[7] This procedure requires a short diversion by explaining an alternative means of calculating PDF $g(r)$. Imagine a sphere surrounded by shells of radius $r$ to $r+\delta r$, with a given shell contains $N$ spheres. The volume of this shell can be approximated from the volume equation for a sphere, see Equation 14. The density of the shell can be calculated using Equation 15, which predicts that the number of spheres $N(r)$ will be related to $1/4\pi r^2$.[7] The paired density function $g(r)$ provides a simplified means of looking at how the density of spheres changes with $r$, by removing the $1/4\pi r^2$ factor by simply dividing through by the overall density $\rho_0$. This means that as r gets larger $g(r)$ tends to unity, so PDF's of $g(r)$ should show $g(r)=1$ for large values of $r$, (provided the structure is a random pack).[35]

$$V(r) = \frac{4\pi(r+\delta r)^3}{3} - \frac{4\pi r^3}{3} \approx 4\pi r^2.\delta r \qquad \textbf{Equation 14}$$

$$\rho(r) = \frac{N(r)}{V(r)} = \frac{N(r)}{4\pi r^2.\delta r} \qquad \textbf{Equation 15}$$

$$g(r) = \frac{\rho(r)}{\rho_0} \qquad \textbf{Equation 16}$$

The PDF in Figure 19 shows oscillation with a negative exponential decay curve, about $g(r)$=1. The rate at which the PDF decays away against distance can be used as a means of determining the extent of order. By plotting the natural log of 1 plus the absolute value of 1-$g(r)$ against $r$ a straight line is obtained that intercepts the $r$ axis at about 5.7, this corresponds to were $g(r)$=1, and can be interpreted as the extent of order (see Figure 20). This negative exponential curve is effectively modelled in software such as PDFgui.

**Figure 19 Argon paired distribution function calculated using Lennard–Jones potential (– blue line).[36] Results from neutron diffraction from liquid argon at 85°K (– red line)[37]**

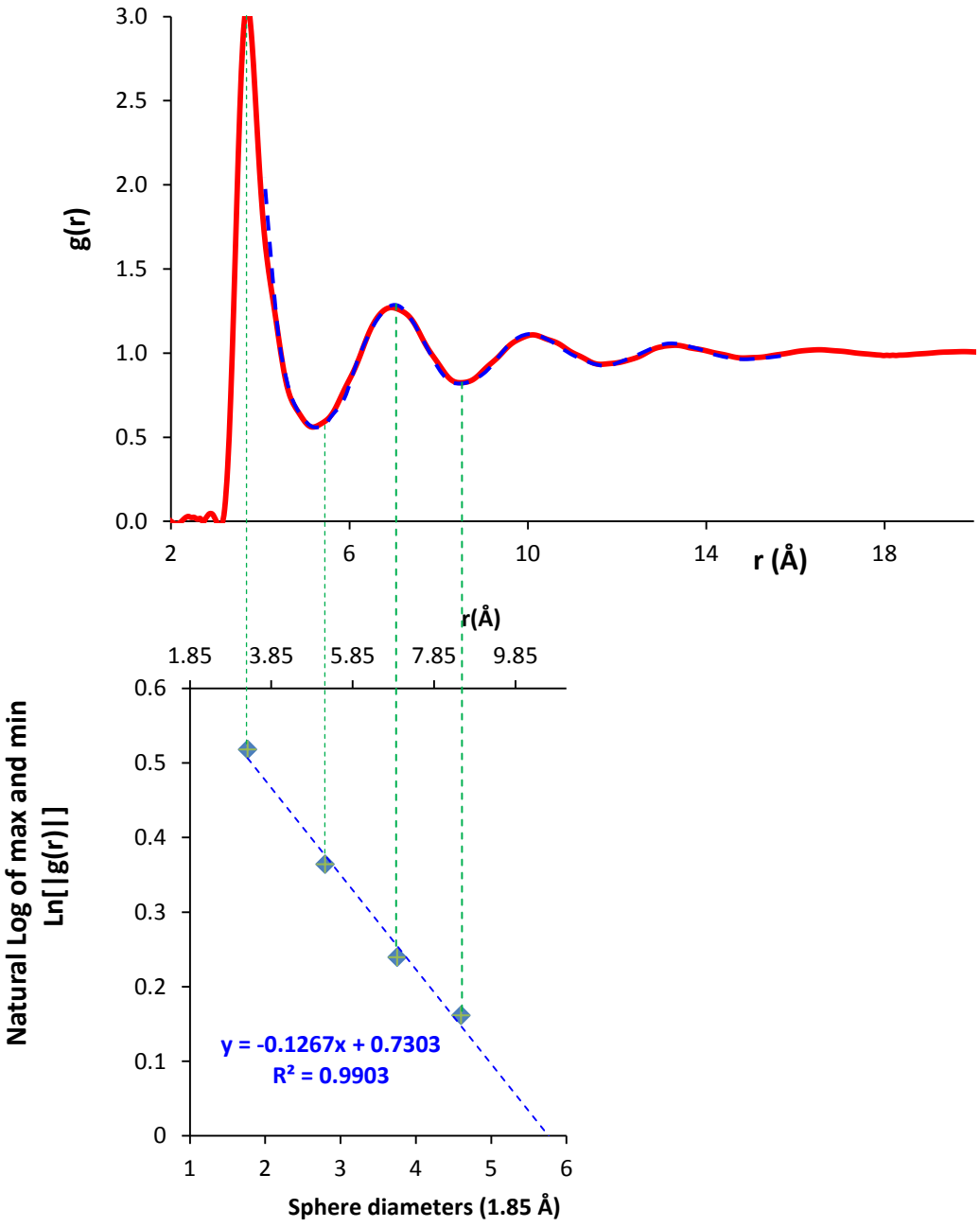


**Figure 20 plot of natural logarithm of unity minus the PDF peak maxima and minima, against radius**

The PDF can be obtained using software such as PDFfit2 or PDFgui. These programs output experimental pair distribution $G(r)$, which is related to $g(r)$ discussed earlier, via Equation 17.[35]

$$g(r) = 1 + \frac{G(r)}{4\pi r \rho_0}$$ **Equation 17**

Software such as PDFgui use crystallographic unit cell data from literature sources to refine parameters until they correspond to the local structure in a distorted crystal. In the absence of disorder the values determined from total scattering will be the same as that obtained from the Bragg peaks. Figure 19 and Figure 20 show how the PDF can be used to determine the extent of order, where $g(r) = 1$, which is a measure of crystal or grain size.[35]

## 1.5 Lactose

### 1.5.1 Chemical Structure of Lactose

Chemically, lactose is composed of two saccharide sub units galactose and glucose shown in Figure 21. It exists in four well characterised crystalline polymorphs, three anhydrous forms (α stable, α hygroscopic and β) as well as the hydrated form, α monohydrate.

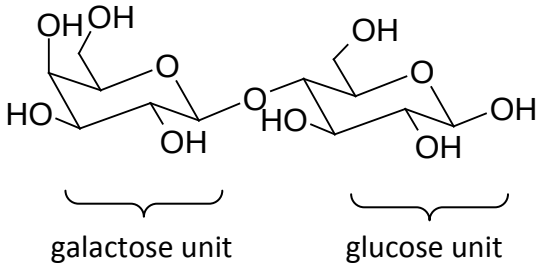


4-O-β-D-galacopyranose -β-D-glucopyranose

**Figure 21 Structure of β-lactose**

The existence of a substance in more than one solid form is known as polymorphism and is referred to as allotropy when observed in elements.[21] The properties of different polymorphs of the same substance can be profound, for instance graphite and diamond are both allotropes of carbon.[38] Individual polymorphs of a substance are formed under specific conditions and information about stability and likelihood of formation under different conditions can be determined using phase diagrams. However, in the area of compounds used in the pharmaceutical sector, the term polymorphism follows the McCrone definition which encompasses hydrates and solvates that rapidly convert between the forms in aqueous solution.[39]

Lactose shows configurationally polymorphism of the two anhydrous forms, since lactose has two stereoisomers, which are defined as either α or β by the position of the OH group on the first carbon of the glucose saccharide unit, shown in Figure 22.

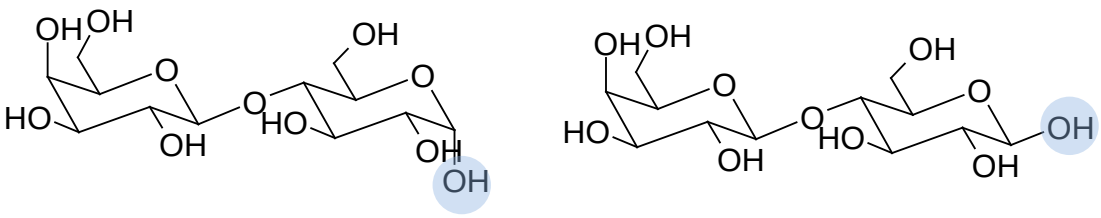


**Figure 22 The two stereo isomers of lactose**

The opportunity for hydrogen bonds to connect to different parts of a molecule directs the packing towards different crystal structures and different polymorphs. Even a very simple molecule such as water with only four points for contact points (two hydrogen's and two lone pairs) produces a number of polymorphs. The driving force behind the formation of these different structures is the increasing pressure used to form them. Pressure increases the density of the polymorphs by reducing the openness of the hydrogen bonding networks.[21,19] The hydrogen bonding networks in lactose polymorphs show different bond lengths, as seen in Table 3.

| | **Bond length (Å)** | |
|---|---|---|
| **Hydrogen bond** | **α-lactose monohydrate** | **α-lactose anhydrous hygroscopic** |
| O(2)-H(2) ... O(6) | 2.666 | 2.851 |
| O(6)-H(6) ... O(2) | 2.706 | 2.935 |
| O(11)-H(11) ... O(9) | 2.755 | 3.190 |

No data are available for the α-lactose anhydrous stable polymorph

**Table 3 Hydrogen bond lengths in the crystalline polymorphs of α-lactose monohydrate and α-lactose anhydrous hygroscopic.**

Polymorphs also occur through conformational changes (rotation and twisting of chemical bonds). Lactose polymorphs show twisting of the saccharide units relative to one another, see Figure 23.[40]

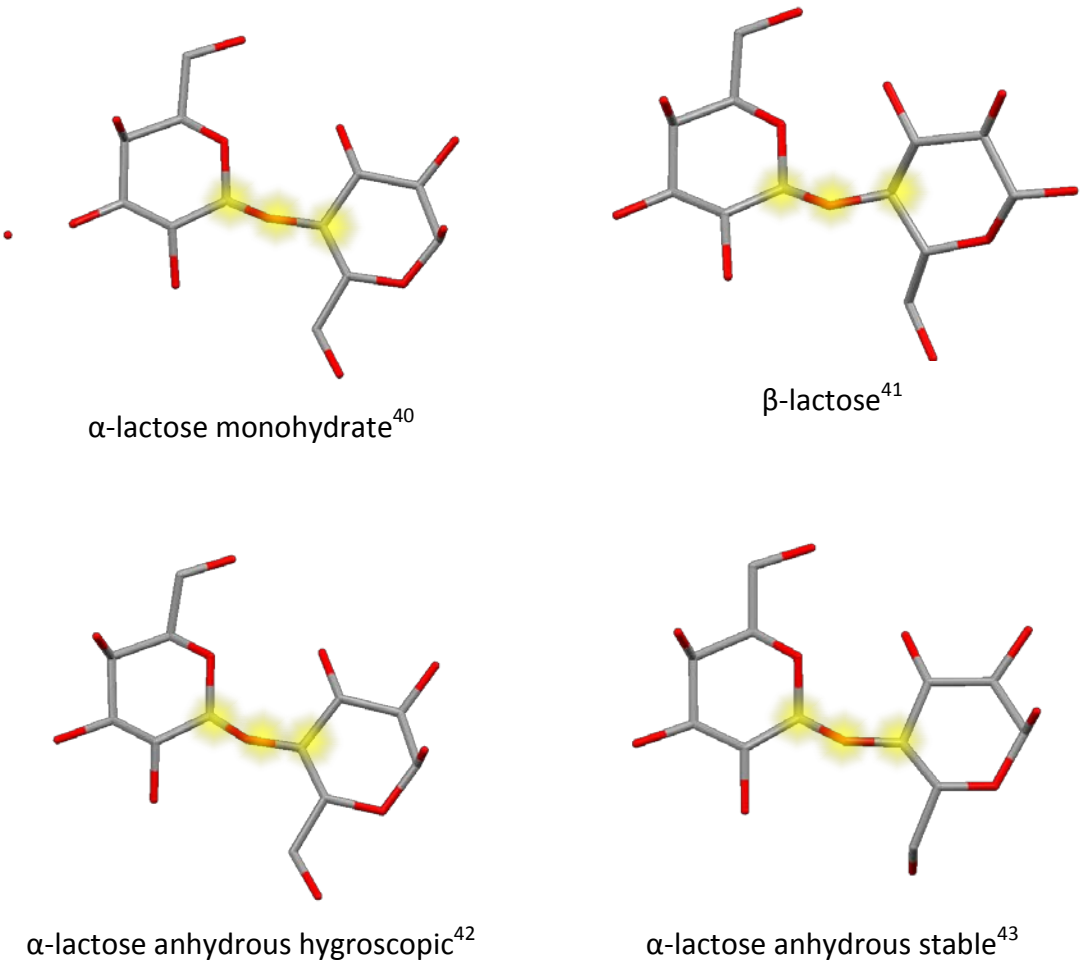

α-lactose monohydrate[40] β-lactose[41]

α-lactose anhydrous hygroscopic[42] α-lactose anhydrous stable[43]

**Figure 23 Conformational polymorphism in polymorphs of lactose**

Small organic molecules such as sugars and pharmaceuticals do not possess rotational symmetry, and so orientation becomes significant. In addition, many small organic molecules may also possess a torsion angle that defines their configuration. In crystals, small organic molecules align in arrays possessing translational symmetry along with identical orientation and configuration. Zografi argues that an ideal or truly amorphous material would have no order; translational, orientational or conformational.[44]

### 1.5.2 Polymorphs of Lactose

Crystals of α-lactose monohydrate and β-lactose can be prepared from a saturated aqueous solution held either above or below 93°C.[45]

β-lactose can also be prepared by refluxing alpha monohydrate for several hours in methanol in the presence of a strong base such as potassium methoxide. Two other crystalline polymorphs can be produced by removal of the water of crystallisation from α-lactose monohydrate.[46] The polymorph α-lactose anhydrous hygroscopic is prepared by heating α-lactose monohydrate under vacuum at 120°C for 16 hours. This crystalline polymorph is unstable and will readily absorb water from the atmosphere, to produce α-lactose monohydrate.[46] The polymorph α-lactose anhydrous stable is prepared by refluxing a 10% (w/v) slurry of α-lactose monohydrate in dry ethanol for 4 hours.[46] The diagrams of the molecular units of each crystalline polymorph (see Figure 22) demonstrate the presence of conformational polymorphism by the presence of different dihedral angles between the two saccharide units set out in Table 4.

| **Torsion Angles** | **H1'-C1'-O1-C (Φ) – galactose unit(°)** | **C1'-O1-C4-H4 (Ψ) – glucose unit(°)** |
|---|---|---|
| α-lactose monohydrate[47] | 27 | -25 |
| β-lactose[41] | 53 | -13 |
| α-lactose anhydrous hygroscopic[42] | 32 | -32 |
| α-lactose anhydrous stable[43] | 35 | -47 |

**Table 4 Dihedral angles for the glycoside link**

The crystalline polymorphs of lactose demonstrate packing polymorphism in their hydrogen bonding arrangements. All the polymorphs have the intra-molecular hydrogen bonds between the OH group on O(9) and the O(5) in common. The alpha forms have a number of intermolecular hydrogen bonds in common, which are shown in Table 3.[40] The longer hydrogen bond lengths of α-lactose anhydrous hygroscopic suggest that the structure is more open. The β-lactose polymorph does not have any intermolecular hydrogen bonds in common with any of the α-lactose polymorphs.

| Polymorph | Density (g cm$^{-3}$) |
|---|---|
| α-lactose monohydrate | 1.556[47] |
| β-lactose | 1.612[41] |
| α-lactose anhydrous stable | 1.579[43] |
| α-lactose anhydrous hygroscopic | 1.557[42] |

**Table 5 Density of crystalline lactose polymorphs**

## 1.6 Properties of Amorphous Lactose

### 1.6.1 Thermodynamic Properties

Crystalline materials undergo a phase change from solid to liquid with increasing temperature whereas amorphous materials possess a glass transition temperature. Below the glass transition point, amorphous materials behave as brittle solids, shattering when stressed. At temperatures above the glass transition point amorphous materials possess "rubbery" properties, since the molecular motion of the liquid state has not been entirely frozen in this region.[21] To understand the link between the physical properties of amorphous materials and their thermodynamic properties, a brief reminder of thermodynamics is useful.

Crystalline materials expand as they melt. The volume change of expansion requires work to be done against internal pressure which is calculated as $p\,\Delta V$. The internal energy U is the sum of the kinetic energy due to the motion such as translations, rotations, vibrations and potential energy of the bonding, so the change in $\Delta U$, associate with a phase change is calculated using Equation 18

$$\Delta U = q + p\,\Delta V \qquad \textbf{Equation 18}$$

Phase changes from solid to liquid are reversible; the energy associated with the transition is the same regardless of how the material is arrived at, the state functions of enthalpy, entropy and the Gibbs reflect this property. The heat needed to change the internal energy and to work against atmospheric pressure as expansion occurs when a solid is heated (or as crystalline solid melts), is the enthalpy state function, This is described in Equation 19, where this time p ΔV term refers to work against the external force of atmospheric pressure. Enthalpy change can also be calculated using

heat capacity with Equation 20, where $C_p$ is the heat capacity at constant pressure, which is integrated between temperature limits $T_1$ and $T_2$. [19, 48]

$$\Delta H = \Delta U + p\,\Delta V \qquad \textbf{Equation 19}$$

$$H = \int_{T_1}^{T_2} C_p\, dT \qquad \textbf{Equation 20}$$

Calculating the enthalpy from absolute zero to the melting point of the solid using Equation 20, instead of integrating from a temperature($T_1 = 0$), the total energy input to the solid is calculated. The enthalpy function is useful because it gives the total amount of energy transformed during a chemical or physical change. Unfortunately heat does not operate like a simple bank account, where the total energy input can be redeemed, not all this energy is available, some becomes dissipated, and this is described by the entropy function.[19, 48]

Returning to the changes occurring as a crystalline solid melts and expands, the entropy change ΔS, that occurs as volume changes from $V_1$ (solid) to $V_2$ (liquid) can be calculated for n moles using Equation 21, where R is the real gas constant. As temperature is increased from $T_1$ to $T_2$ entropy can be calculated using Equation 22, where $C_v$ is the heat capacity at constant volume.[19, 48]

$$\Delta S = n\,R\,Ln\left(\frac{V_2}{V_1}\right) \qquad \textbf{Equation 21}$$

$$\Delta S = n\,C_v\,Ln\left(\frac{T_2}{T_1}\right) \qquad \textbf{Equation 22}$$

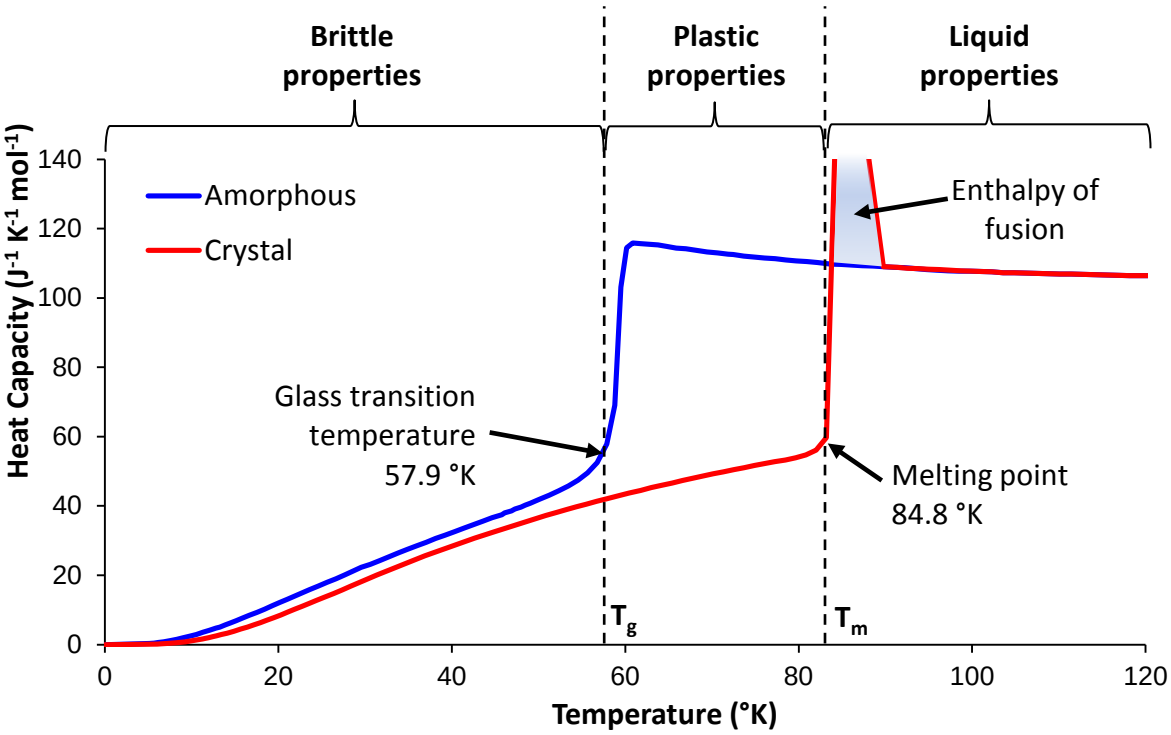


**Figure 24 Heat capacity of amorphous and crystalline 1-butene against temperature [49]**

As shown in Figure 24, the heat capacities of crystalline and amorphous versions of the same material are assumed to be identical when they are both liquids above the crystalline melting point and at absolute zero. Working along the heat capacity line for the amorphous material, from high to low temperature, the heat capacity does not change until the temperature drops below the glass transition temperature. At the glass transition temperature, the physical characteristics change from rubbery to brittle.[7]

Returning to the ideas expressed by Jin in his jammed matter studies, the continuation of the amorphous states heat capacity below the crystalline melting point can be explained. For a crystalline material, the change in co-ordination number from 12 (for close packed arrangements) to 6, requires an addition of heat energy q, to overcome the forces of attraction between atoms or molecules, this is the enthalpy of fusion.[14] By contrast, the average coordination number of an amorphous material, with brittle properties undergoing heat at the glass transition point will be 6, so no bond braking occurs at the glass transition point. Once the temperature of an amorphous material exceeds that of the glass transition point, the molecules have translational motion, so possess a similar heat capacity to the liquid.

Both enthalpy and entropy are dependent on the heat capacity of a material at constant pressure, this property can be measured and comparisons made between crystalline and amorphous materials.[7] Differential Scanning Calorimetry (DSC) is capable of measuring heat capacity from which thermodynamic properties such as enthalpy and entropy can be calculated.[50] The thermodynamic property of entropy can be plotted against temperature for the crystalline material and the amorphous in Figure 25. For the amorphous state, the properties of the liquid phase are seen to be extrapolated down below the melting point, a change in slope occurs at the glass transition point. After the glass transition point the amorphous entropy line follows a similar profile to that of the crystalline, but the entropy of the amorphous phase is always greater than the crystalline, (see Figure 25).[7]

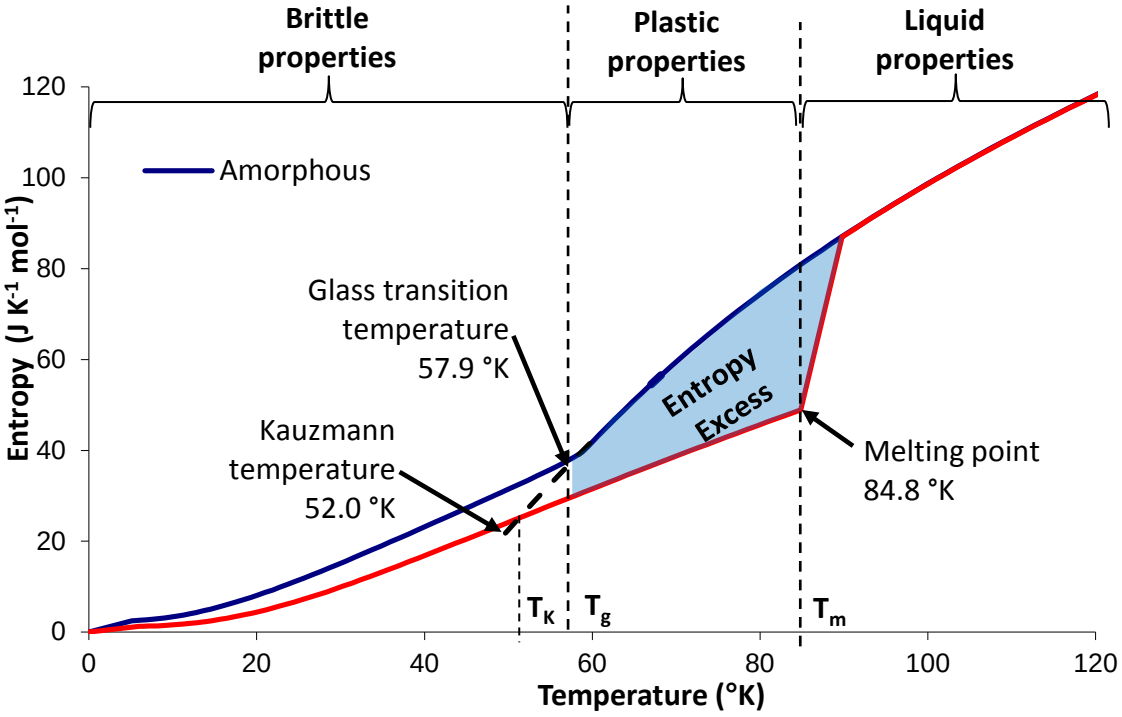


**Figure 25 Entropy of amorphous and crystalline 1-butene against temperature [49]**

Returning to Figure 25 the intercept between the crystalline and the extrapolated liquid properties represents a lower limit for the glass transition point, known as the Kauzmann temperature.[7] This represents the point at which relaxation processes occurring via conformational changes in the molecules of the amorphous material cease. Relaxation processes allow an amorphous material to lose some of its stored energy to the environment, this is due to molecules within the material undergoing conformational changes until they reach potential energy minima.[51] For saccharides

rings such as galactose and glucose their lowest energy confirmation is the chair form. The Kauzmann temperature represents an upper temperature limit for stable safe storage of an amorphous material.[7] Unfortunately the Kauzmann temperature has yet to be identified for any form of lactose.

The enthalpy function against temperature is shown in Figure 26. To show the enthalpy as identical when derived from either the amorphous or crystalline states, an offset value of 2013 J $mol^{-1}$ was added to all the amorphous values. This can be thought of as the enthalpy of fusion (the energy needed to break bonds in the crystal reducing the co-ordination number to 6).

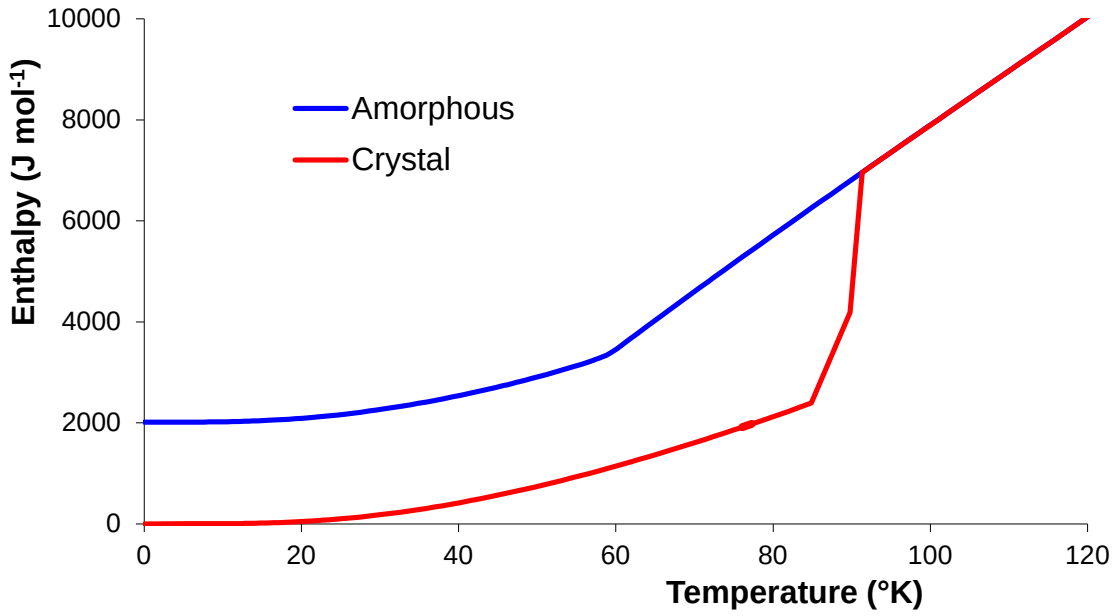


**Figure 26 Enthalpy of amorphous and crystalline 1-butene against temperature [49]**

After calculating both the enthalpy and the entropy the Gibbs function can be calculated. This shows the energy returned by changing the amorphous form to crystalline, (see Figure 27). The amorphous state possesses a more positive Gibbs function than the crystalline. It can be said that the amorphous state is thermodynamically unstable, and should spontaneously change to the crystalline form. This statement fails to take account of kinetic factors, i.e. the energy barrier to breaking bonds may be high, conferring stability on the amorphous state.

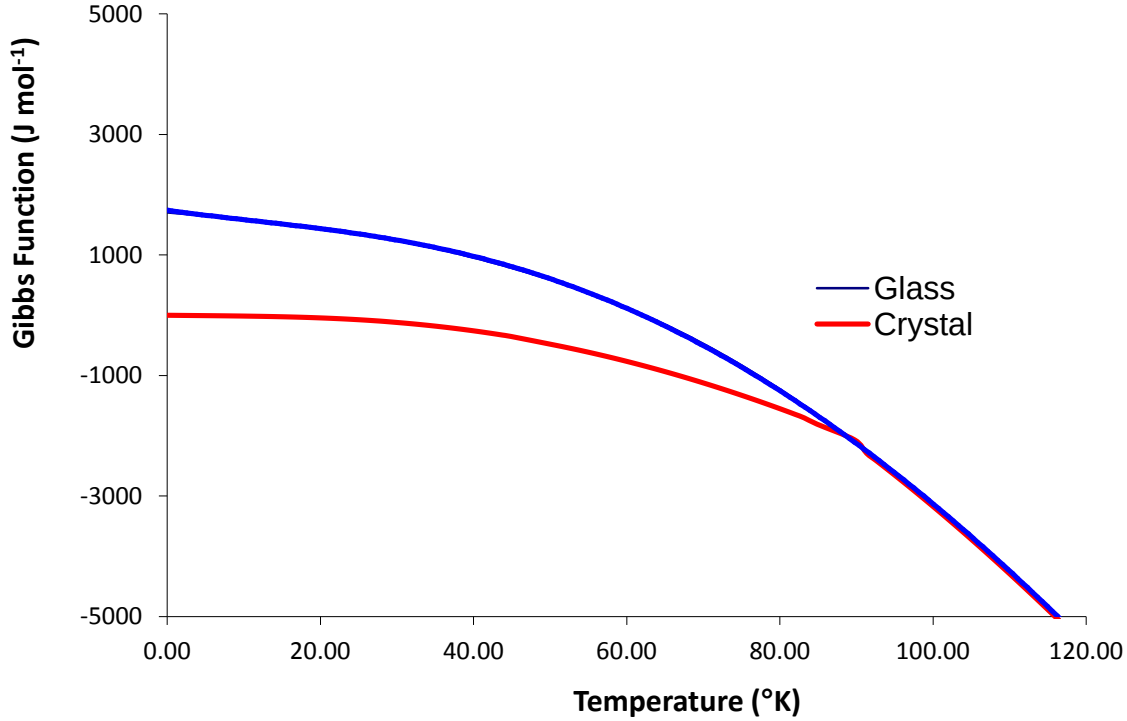


**Figure 27 Gibbs function for amorphous and crystalline 1-butene against temperature** [49]

The discussion so far has used a single example of an amorphous material. The rate of cooling of liquid that creates an amorphous material determines the properties of the amorphous material. Rapid cooling produces a high glass transition temperature with greater heat capacity, where as a slow cooling rate produces a low glass transition point with lower heat capacity (see Table 6). [7] This demonstrates that the properties of amorphous materials are heavily dependent on the conditions of their formation. Table 6 shows how the glass transition temperature and heat capacity of the brittle phase are dependent on conditions of glass formation (in this case the cooling rate of the DSC cell from melting crystalline fructose). This demonstrates that amorphous materials formed under different condition may possess different properties.

| Cooling ramp rate (°C per minute) | Glass transition point (°C) | $C_p$ amorphous - brittle (J $mol^{-1}$ $K^{-1}$) |
|---|---|---|
| 10 | 15.15 | 351 |
| 15 | 14.73 | 346 |
| 20 | 14.54 | 337 |
| 25 | 13.08 | 333 |
| 30 | 12.34 | 320 |

**Table 6 Cooling rates, glass transition points obtained and heat capacities of amorphous fructose formed from melts**

Reviews by Craig[52] and Yu[53] have both identified that glass transition points of sugars are typically two thirds of the melting point expressed in Kelvin. This ratio is a little greater than the observed value of a half for polymers. Craig suggests that the behaviour of sugars is typical of fragile glasses, showing viscosity profiles that deviate from Arrhenius behaviour, in contrast to polymers that show "strong" viscosity behaviour (following the Arrhenius equation).

### 1.6.2 Spectroscopic Properties

The distribution of co-ordination numbers seen by Bernal could be expected to impose a distribution of physical environments (seen in Figure 1) for the atoms in an amorphous material. While the individual covalent bonds remain largely unchanged, the environment is not as well defined due to the amorphous character. Certain techniques probe local order to a large extent and can be used to investigate amorphous material character. For example, when spectroscopic techniques such as solid state magic angle nuclear magnetic resonance and infra-red spectroscopy are applied to amorphous materials they produce features with broad distributions compared to their crystalline counterparts (see Figure 28 and Figure 29) although the features occur in similar places in the spectra.

In the case of small organic molecules such as lactose, magic angle cross polarised nuclear magnetic resonance produces broad spectral peaks for amorphous materials, which suggest each of the $^{13}C$ atoms found in the molecule are subject to a distribution of magnetic environments. Comparison of these peaks to spectra of their crystalline

polymorphs, shows that despite their distribution, the central peak positions are very similar. This suggests that the chemical bonding of the $^{13}C$ atoms within the molecule remains very similar to that of crystalline polymorphs, however they are still subject to a distribution of magnetic environments. The distributions occur not only as a result of random packing, but of surrounding molecules possessing a distribution of conformations and orientations.

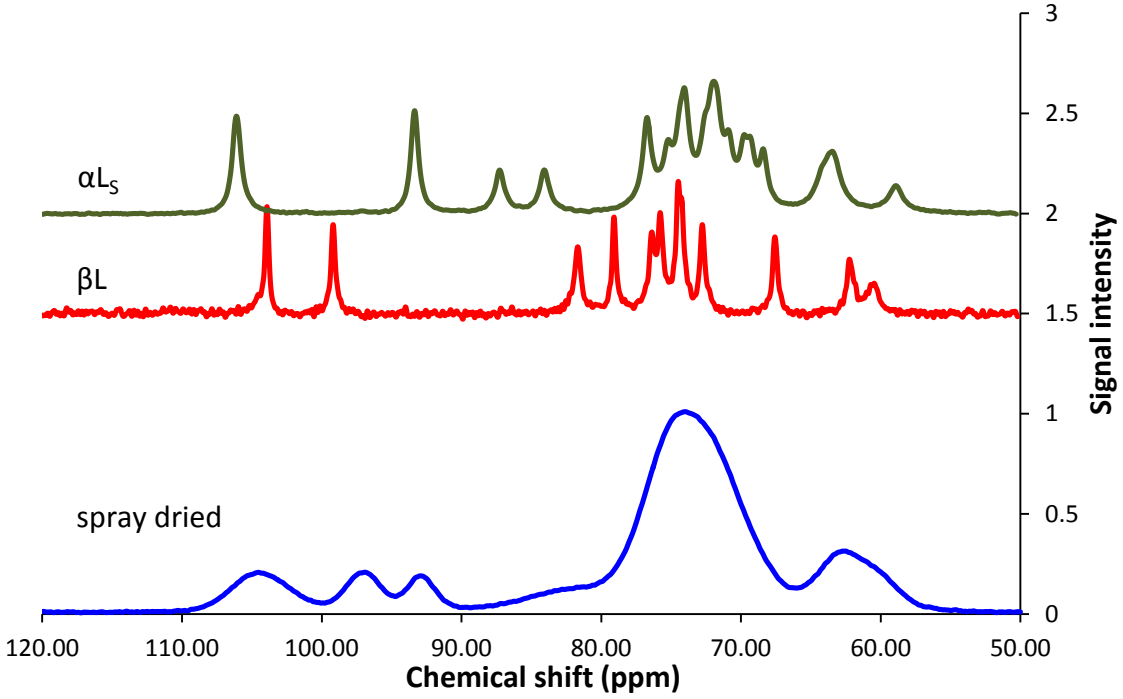


**Figure 28 Magic angle spinning cross polarised nuclear magnetic spectra of lactose polymorphs alpha lactose stable anhydrous (green), beta lactose (red) and spray dried lactose (blue).**

Likewise, the infra-red spectrum of amorphous lactose shows that a great degree of local order remains within the molecule; the central positions of peaks remain similar to the crystalline polymorphs, where as individual peaks show a great deal of broadening. This suggests once again that the chemical bonding of atoms within the molecule remain the same, however the individual atoms within the molecule are subject to a distribution of electromagnetic environments.[19]

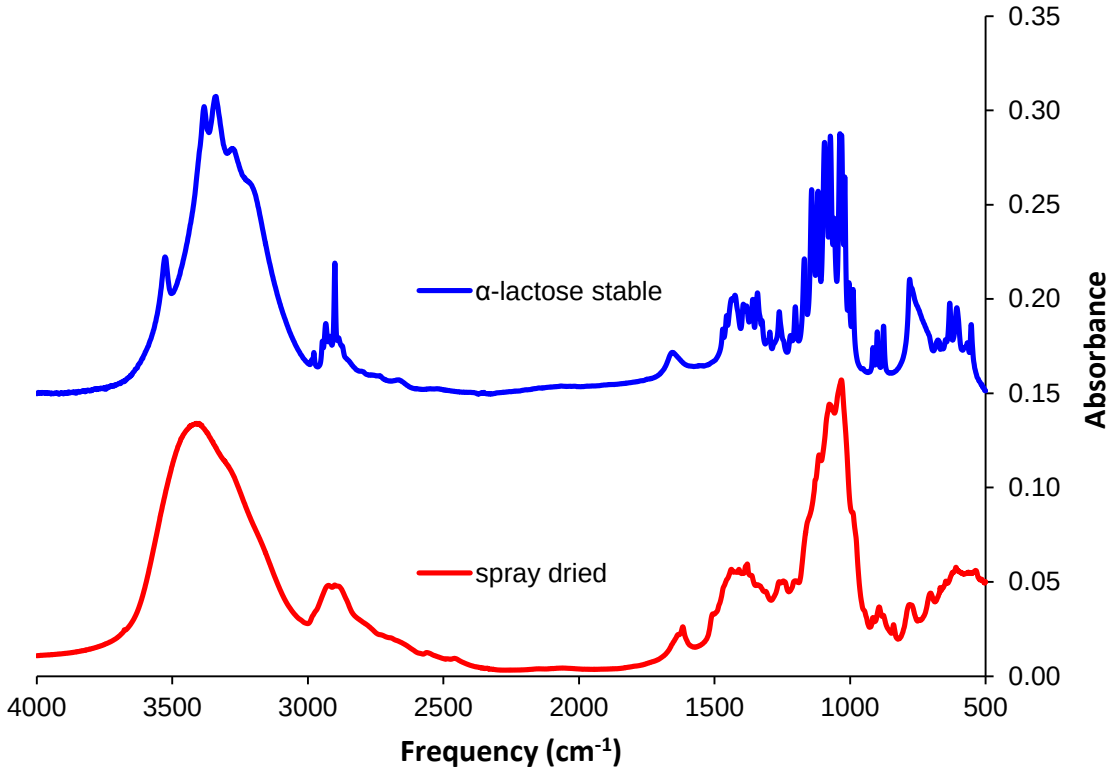


**Figure 29 Infra-red spectra of alpha lactose stable anhydrous and spray dried lactose taken by attenuated total internal reflection**

The -OH stretch region of 3500 - 3050 $cm^{-1}$ is particularly interesting, crystalline polymorphs produce a series of distinct peaks which reflects the different hydrogen bonds lengths that form the network holding the lattice together. By contrast amorphous lactose shows a single broad peak in the -OH stretch region.

The peak maximum described in wave numbers was shown by Wolkers to reflect the glass transition point of amorphous sugars. The shift to greater wave numbers in the amorphous sugars suggests the average hydrogen bond is longer.[54] This distribution of values for hydrogen bond length follows the idea of distribution obtained by Bernal for the co-ordination number. The continuous random network model shown in Figure 29 produces a distribution of bond lengths, co-ordination numbers and area per cell. This would seem like a reasonable analogy to the hydrogen bonding network found in amorphous lactose.[8]

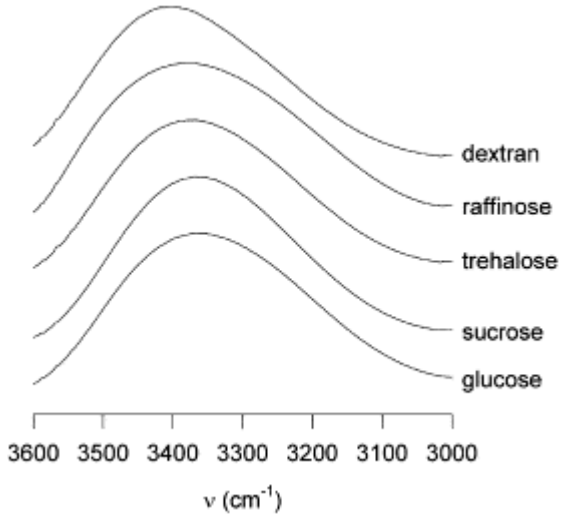


All spectra were recorded at 24 C

**Figure 30 the OH stretch in region 3600-3000 $cm^{-1}$ for a number of different sugars.[54]**

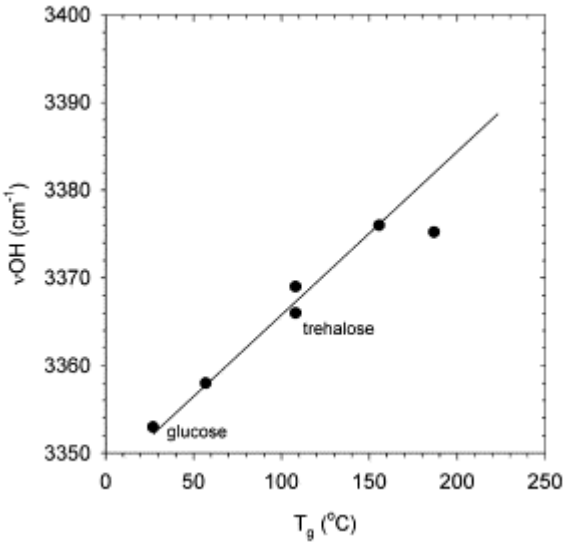


**Figure 31 Correlation between position of the OH stretching mode of amorphous carbohydrates and Tg.[54]**

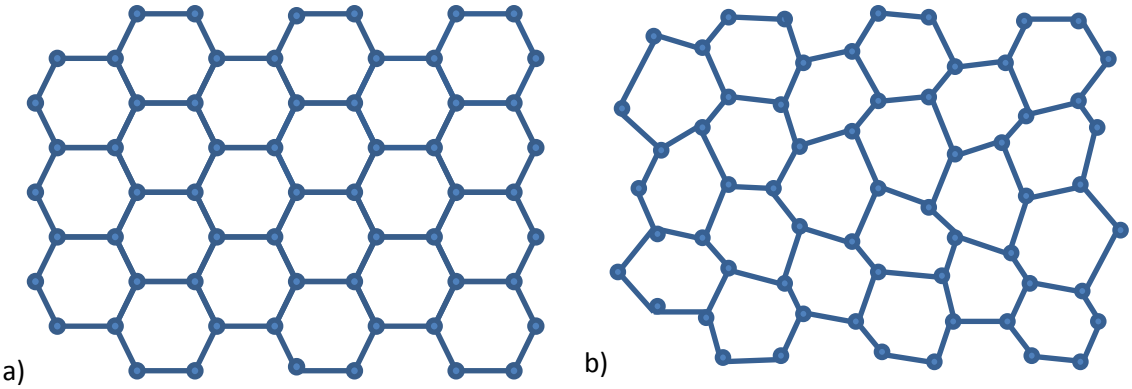


**Figure 32 a)The continuous network of a crystal and b) the continuous random network of an amorphous material[8]**

## 1.7 Amorphous Lactose and Pharmaceutical Inhalation Devices

Asthma inhalers are medical devices that are stored in pharmacies, sometimes for years. At the point of use the inhaler is expected to show the same level of efficacy as shown in its clinical trials. Pharmaceutical manufactures undertake extensive stability testing of their devices, storing them for variable lengths of time at different temperatures and humidity's to prove their devices will still be fit for purpose after storage.[55] A formulation containing an unstable amorphous sugar presents a stability problem that needs to be measured and monitored.

The design of a dry powder inhaler is exemplified in Figure 34. This was one the first ever dry powder inhalers to be marketed and exemplifies some of their problems. To operate the patient had to place a gelatine capsule (a single dose) in the rotor, pierce

the capsule and then inhale. The energy of the patient's breath was used to disperse the powder into the inhaled air. The design had a problem, when the capsules became damp the powder particles would clump together and fail to enter the patients lungs. To overcome this problem, the amount of drug formulated was much greater than that needed for a therapeutic effect. Modern dry powder inhalers have overcome this issue by using pre-prepared sealed blisters that are impermeable to moisture. Ensuring effective storage has allowed inhaler development to reduce the level of dose needed per inhalation.[1] An example of an active pharmaceutical ingredient (API) is salbutamol sulphate shown in Figure 33 which is a common API used in dry powder inhalers. Modern dry powder inhalers use extremely small levels of salbutamol sulphate just 200 µg per dose.[56]

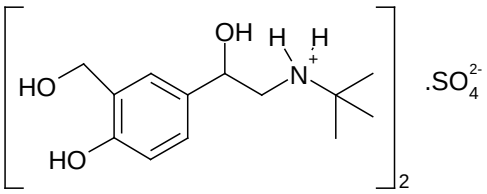


**Figure 33 structure of salbutamol sulphate**

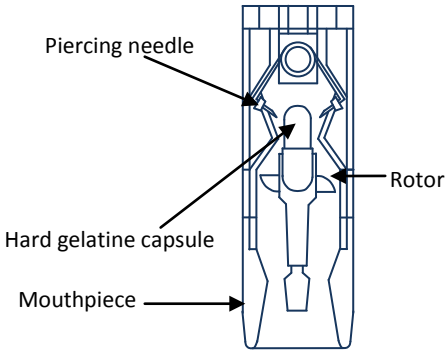


**Figure 34 Spinhaler (Rhone-Poulenc) Reproduced from Aulton[1]**

For the 200 µg of API in a dry powder inhaler such as "ventodisk" to achieve a therapeutic effect it must be deposited in the respiratory region of the lungs, the bronchioles and alveoli ducts, (in Figure 35 this is the red line described as pulmonary). To achieve this the API particles need to be sized 0.5 to 5 µm (see Figure 35 for the "total" blue line). Particles that are too small are exhaled and fail to deposit in the lung, where as particles which are too large impact on the back of the throat.

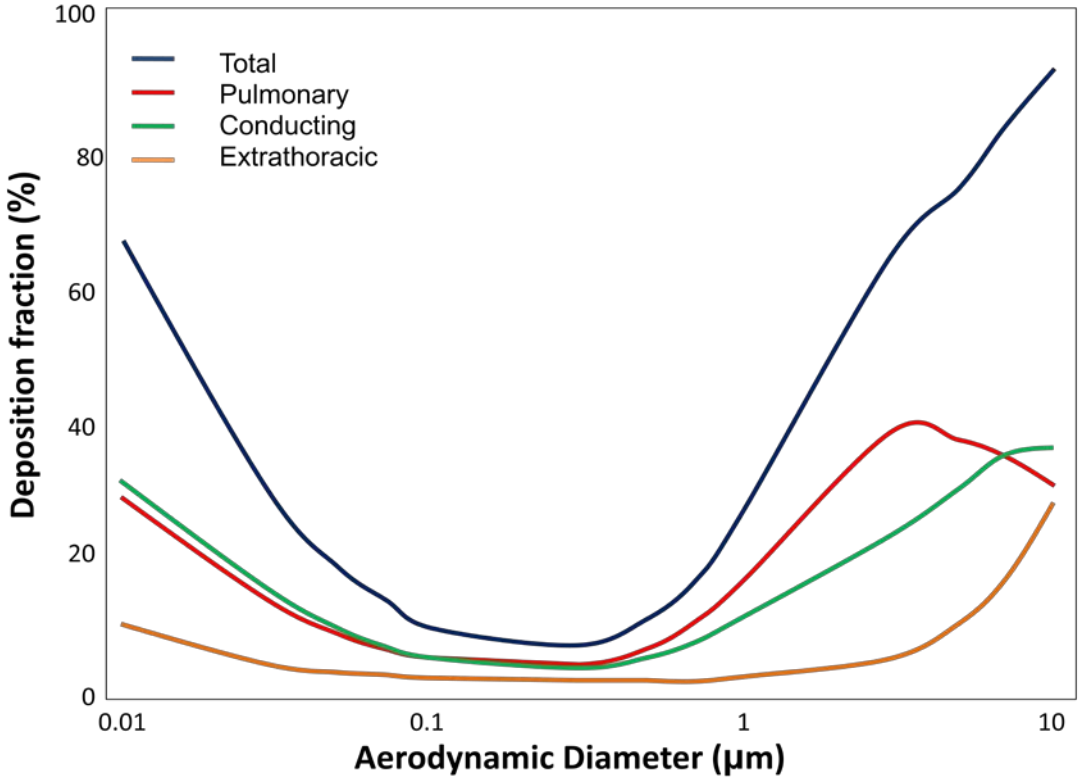


**Figure 35 Lung region and percent deposition of particles against aerodynamic diameter for a single breath.[57]**

The role of lactose is as a carrier excipient to ensure dose uniformity and dispersion of the API particles. An excipient is a medicine ingredient that helps deliver the API to the necessary tissues, but is not pharmaceutically active itself. [57, 58] Crystalline α-lactose monohydrate is extensively used as an excipient in the pharmaceutical industry for tabletting, since it is inexpensively produced as a bi-product of cheese manufacture; it is not particularly sweet, non toxic and stable.[59]

Modern dry powder inhalers often use α-lactose monohydrate crystals sized between 45 to 200 µm to carry the API crystals and aid their dispersion during inhalation. The API particles form a mono-layer on the α-lactose monohydrate crystals, the surface energies of both particles is such that the energy of the inhalation breath is sufficient to remove the API from the lactose crystals. On inhalation the α-lactose monohydrate crystals impact at the back of the throat, where as the API particles are dispersed in the air stream and conducted to the respiratory region of the lungs.[60]

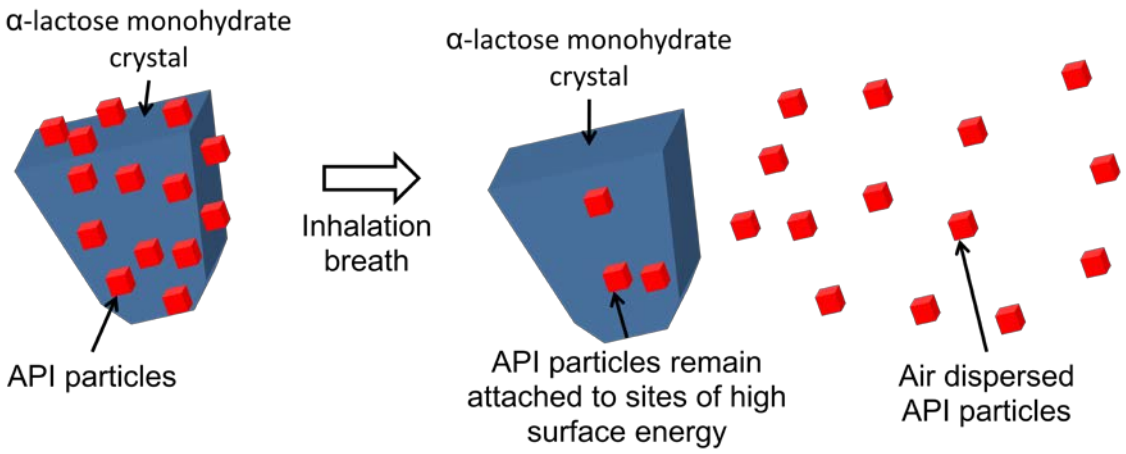


**Figure 36 Adhesive mixtures of coarse lactose with API particles**

The production of crystals of a specific size range is typically carried out by milling and sieving. Very little of the energy input to milling processes goes into the creation of breaking crystals apart, some of this energy introduces defects and fresh grain boundaries into the crystals.[1] The loss of crystal order introduced by the milling processes generates a small amount of amorphous lactose. [61]

Amorphous lactose generated by milling has a much higher surface energy than crystalline lactose, so the small amount of amorphous lactose has a profound effect on the function of the material.

| **Lactose sample** | **Dispersive surface energy mean ±sd (mJ $m^{-2}$)** |
|---|---|
| Crystalline (alpha monohydrate) | 31.2 ±1.1 |
| Spray dried (completely amorphous) | 37.1 ±2.3 |
| Milled (0.7% amorphous) | 41.6 ±1.4 |
| Physical mixture (99% crystalline 1% spray dried) | 31.5 ±0.4 |

**Table 7 The dispersive surface energy of lactose determined using IGC[61]**

The small areas of amorphous lactose on the crystal surface possess stronger adhesive properties, which means that API's are more strongly attracted to these areas and require more energy to remove them from the carrier crystal. The danger for the

formulators is that the API is not dispersed during inhalation, remaining attached to the crystal as it impacts on the back of the throat rather than delivering the API to the respiratory regions of the lungs. To avoid the problem, adhesive mixtures with coarse and fine lactose particles are used. These consist of α-lactose monohydrate crystals of size between 5 and 160 µm. The idea being that smaller crystals of α-lactose monohydrate crystals bind to the amorphous sites prior to the addition the API and maximise the amount of API delivered to the lungs.[60]

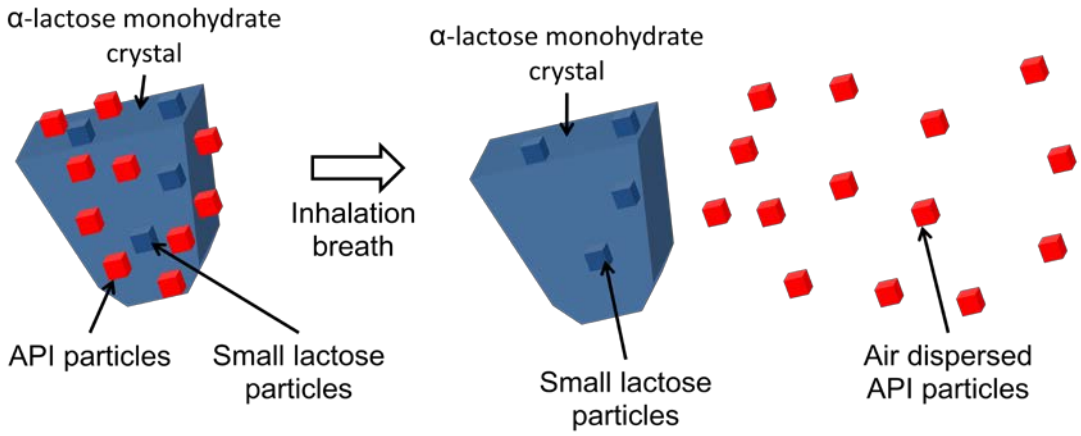


**Figure 37 Adhesive mixtures with coarse and fine lactose particles**

After storage an inhaler should behave identically to its clinical trials. The storage of a medicine should not compromise its efficacy, the ability to bring about therapeutic benefit to the patient. Storage should ideally be possible on the pharmacy shelf for at least a two year period assuming seasonal variations in temperature and humidity.[1] This poses a problem for amorphous lactose which is unstable and will become crystalline when exposed to moisture (under conditions of relative humidity greater than 58% and temperature greater than 25°C).[62] The instability of amorphous lactose poses a problem for the formulation of dry powder inhalers. The possibility exists that moisture could alter the performance of the devices to the extent that they may no longer function in the manner predicted by the clinical trials.[1]

## 1.8 Conclusions

Non crystalline solids have been recognised since the first systematic studies of solids, however the definition of amorphous materials has remained elusive. Attempts made using phrases such as an "absence of long range order" have not helped progress, since they are negative statements of what an amorphous material is not. Despite the lack of definition, the distinctive nature of amorphous materials has not been in doubt. The change in heat capacity measured by DSC is a distinct property that has been used for many years to prove the presence of an amorphous material. The variation in heat capacity of amorphous materials below their glass transition point means that it is not possible to use the glass transition point to quantify amorphous against crystalline content.

A positive statement or definition of the unique properties possessed by amorphous materials is required. The evidence from the jammed sphere packing studies suggests that the idea of "random order" answers this, since randomness can be tested for. Switching to this definition allows powder X-ray diffraction measurement to take place, since analysis by paired distribution functions provide evidence of long range random structure that can determine the extent of short range order.

## References

1 M. E. Aulton, *Pharmaceutics the Science of Dosage form Design, Second Edition. Churchill Livingstone 2002.*, Livingstone, Churchill, 2002.

2 U.S. Department of Health and Human Services, Food and Drug, *Guidance for Industry, Metered Dose Inhaler (MDI) andDry Powder Inhaler (DPI) Drug Products. Chemistry, Manufacturing, and Controls Documentation (DRAFT GUIDANCE)*, CDERGUID\2180DFT.WPD, CDER, Rockville, 1998.

3 H. E. Newell, G. Buckton, D. A. Butler, F. Thielmann and D. R. Williams, *International Journal of Pharmaceutics,* 2001, **217**, 45-56.

4 N. Bailey, *An universal etymological English dictionary · 1st edition, 1721 (1 vol.).*, Darby, London, 1721.

5 N. Steno, *De solido intra solidum naturaliter contento dissertationis prodromus (Of Solids Naturally Contained Within Solids)*, Moukee, Florence, 1679.

6 A. G. Werner, *Von den äusserlichen Kennzeichen der Fossilien (On the External Characters of Fossils, or of Minerals)*, Crusius, Leipzig, 1774.

7 S. R. Elliott, *Physics of amorphous materials (Second Edition)*, Longman Scientific & Technical, Harlow, 1990.

8 R. Zallen, *Richard Zallen. The physics of amorphous solids. New York ; Chichester : Wiley, 1998.*, Wiley, Chichester, 1998.

9 J. D. Bernal and J. Mason, *Nature,* 1960, **188**, 910 (DOI:10.1038/188908a0).

10 I. Stewart, *Professor Stewart's Hoard of Mathematical Treasures*, Profile Books Ltd, London, 2010.

11 J. Kepler, *Strena Seu De Nive Sexangula*, Francofurti, Prague, 1611.

12 Torquato S., *Rev. Mod. Phys. ,* 2010, **82**, 2633 (DOI:10.1103/RevModPhys.82.2633).

13 C. Song, P. Wang and H. A. Maske, *Nature,* 2008, **453**, 629 (DOI:10.1038/nature06981).

14 Y. Jin and H. A. Makse, *Physica A: Statistical Mechanics and its Applications,* 2010, **389**, 5362-5379 (DOI:10.1016/j.physa.2010.08.010).

15 W. Van Witzenburg, *Phys. Lett.,* 1967, **25A**, 293 (DOI:10.1016/0375-9601(67)90656-1).

16 D. R. Lide, *CRC handbook of chemistry and physics : a ready-reference book of chemical and physical data*, Boca Raton, London, 2009.

17 P. Wang, C. Song, Y. Jin and H. A. Makse, *Physica A: Statistical Mechanics and its Applications,* 2011, **390**, 427-455 (DOI:10.1016/j.physa.2010.10.017).

18 L. Mohan and R. T. Bonnecaze, *Softmatter,* 2011, **8**, 4216 (DOI:10.1039/C2SM06940G).

19 P. W. Atkins and J. De Paula, *Atkins' Physical chemistry.*, Oxford University Press, Oxford, 2002.

20 M. Skoge, A. Donev, F. H. Stillinger and S. Torquato, *Phys. Rev.,* 2006, **E. 74**, 041127 (DOI:10.1103/PhysRevE.74.041127).

21 R. Hilfiker, *Polymorphism : in the pharmaceutical industry / Weinheim : Wiley-VCH, 2006*, Wiley-VCH, Weinheim, 2006.

22 P. Scherrer, *Nachr. Ges. Wiss. Göttingen,* 1918, **26**, 98.

23 J. I. Langford and A. J. C. Wilson, *J. Appl. Cryst.,* 1978, **11**, 102.

24 C. Suryanarayana and G. M. Norton, *X-Ray Diffraction: A Practical Approach*, Plenum, New York, 1998.

25 A. R. West, *Basic solid state chemistry*, John Wiley & Sons, Chichester, 1999.

26 D. Palmer and G. Easterbook, *Block 2 Earth Materials S260 Geology*, Open University, Milton Keynes, 1999.

27 C. Knieke, M. Sommer and W. Peukert, *Powder Technol,* 2009, **195**, 25-30 (DOI:10.1016/j.powtec.2009.05.007).

28 S. C. Tjong and H. Chen, *j. mser,* 2004, **R 45**, 1 (DOI:10.1016/j.mser2004.07.001).

29 T. D. Shen, J. Zhang and Y. Zhao, *Acta Materialia,* 2008, **56**, 3663 (DOI:10.1016/j.actamat.2008.04.003).

30 H. B. Aaron and G. F. Bolling, *Surf. Sci.,* 1972, **31**, 27.

31 A. R. Stokes and A. J. C. Wilson, *Proceedings of the Physical Society,* 1944, , 174-181 (DOI:10.1088/0959-5309/56/3/303).

32 G. K. Williamson and W. H. Hall, *Acta Metallurgica,* 1953, **1**, 22-31.

33 E. Mittemeijer and U. Welzel, *Z. Kristallogr.,* 2008, **223**, 552 (DOI:10.1524/zkri.2008.1213).

34 G. D. Scott, *Nature,* 1962, **194**, 956 (DOI:10.1038/194957a0).

35 T. Egami, S. J. L. Billinge, T. Egami and B, *Underneath the Bragg Peaks: Structural Analysis of Complex Materials*, Pergamon, Amsterdam, 2003.

36 J. A. Barker, D. Henderson and R. O. Watts, *Physics Letters A,* 1970, **31**, 48-49 (DOI:10.1016/0375-9601(70)91019-4).

37 J. L. Yarnell, M. J. Katz, R. G. Wenzel and S. H. Koenig, *Phys. Rev. A.,* 1973, **7**, 2130.

38 N. N. Greenwood and A. Earnshaw, *Chemistry of the elements*, Pergamon Press Ltd, Oxford, 1984.

39 W. C. McCrone, *Polymorphism. In physics and chemistry of the organic solid state*, Wiley Interscience, New York, USA., 1965.

40 J. Kirk, *Fundamental Structural Aspects of Crystalline Lactose Polymorphs*, Loughborough Univerity, Loughborough, 2007.

41 S. Garnier, S. Petit and G. Coquerel, *Journal of Thermal Analysis and Calorimetry,* 2002, **68**, 489 (DOI:10.1023/A:1016087702409).

42 C. Platteau, J. Lefebvre, F. Affouard and P. Derollez, *Acta Crystallogr B.,* 2004, **Section B 60(4)**, 453.

43 C. Platteau, J. Lefebvre, F. Affouard, J. Willart, P. Derollez and F. Mallet, *Acta Crystallographica,* 2005, **Section B 61**, 185-191.

44 S. Bates, G. Zografi, D. Engers, K. Morris, K. Crowley and A. Newman, *Pharmaceut. Res,* 2006, **23**, 2333 (DOI:10.1007/s11095-006-9086-2).

45 G. Vuataz, *Lait,* 2002, **82**, 485-500 (DOI:DOI: 10.1051/lait:2004007).

46 J. H. Kirk, S. E. Dann and C. G. Blatchford, *International Journal of Pharmaceutics,* 2007, **334**, 103-114.

47 J. H. Smith, S. E. Dann, M. R. J. Elsegood, S. H. Dale and C. G. Blatchford, *Acta Cryst.,* 2005, **E61**, 2499 (DOI:10.1107/S1600536805021367).

48 H. D. B. Jenkins, *Chemical thermodynamics at a glance*, Blackwell, Oxford, 2007.

49 K. Takeda, O. Yamamuro and H. Suga, *Journal of Physics and Chemistry of Solids,* 1991, **52**, 607-615.

50 D. Q. M. Craig and M. Reading, *Thermal analysis of pharmaceuticals*, CRC distributor; Taylor & Francis, New York; London, 2006.

51 Craig,D,Q,M., M. Barnes, P. G. Royall and V. L. Kett, *Pharm. Res.,* 2000, **17**, 696-700.

52 D. Q. M. Craig, P. G. Royall, V. L. Kett and M. L. Hopton, *Int. J. Pharm.,* 1999, **179**, 179-207 (DOI:10.1016/S0378-5173(98)00338-X).

53 L. Yu, *Adv. Drug Deliv. Rev.,* 2001, **48**, 27-42 (DOI:10.1016/S0169-409X(01)00098-9).

54 W. F. Wolkers, A. E. Oliver, F. Tablin and J. H. Crowe, *Carbohydrate Research,* 2004, **339**, 1077-1085.

55 U.S. Department of Health and Human Services, Food and Drug Administration, Center for Drug Evaluation and Research (CDER)., *Guidance for Industry, Metered Dose Inhaler (MDI) and Dry Powder Inhaler (DPI) Drug Products. Chemistry, Manufacturing, and Controls Documentation (DRAFT GUIDANCE)*, CDERGUID\2180DFT.WPD, Center for Drug Evaluation and Research (CDER), Food and Drug Administration, 5630 Fishers Lane, rm. 1061, Rockville, MD 20852, 1998.

56 British Medical Association, *Nurse prescribers formula*, British Medical Association/Royal Pharmaceutical Society of Great Britain, London, 2002.

57 S. S. Park and A. S. Wexler, *Journal of Aerosol Science,* 2008, **39**, 266-276.

58 M. J. Telko and A. J. Hickey, *Respiratory Care,* 2005, **50**, 1113-1272.

59 T. K. Lindhorst, *Essentials of carbohydrate chemistry and biochemistry*, Wiley, Chichester, 2000.

60 H. Wierik, P. Diepenmaat and R. Damhuis, *Formulation of Lactose for Inhaled Delivery Systems*, Advanstar, Chester, 2002.

61 H. E. Newell, G. Buckton, D. A. Butler, F. Thielmann and D. R. Williams, *International Journal of Pharmaceutics,* 2001, **217**, 45-56.

62 D. J. Burnett, F. Thielmann and J. Booth, *International Journal of Pharmaceutics,* 2004, **287**, 123-133.

# CHAPTER 2

# Instrumentation and Equipment

## 2.1 Preparation of amorphous pharmaceutical materials

### 2.1.1 Rapid melt quench

The simplest method of preparing an amorphous material is by rapidly cooling a liquid.[1] For sugars this can be achieved by heating the sugar until it becomes molten and then cooling rapidly. In this thesis the methodology used was heating 2 g of sugar until it became molten, and then plunging the material into liquid nitrogen. This simple technique is not without its problems; heating a sugar can cause decomposition by caramelisation[2] and water condensation can occur on the cold sugar. To minimise the effect of water condensation on the sample during the quenching process, the material was rapidly transferred to a glove box via a vacuum chamber.

### 2.1.2 Spray drying

Amorphous materials can be generated from spray drying by rapid evaporation of a solvent from dilute solutions (approximately 10% w/v). An atomiser device is used to produce small droplets of the solution via a rapidly spinning disc (20,000 rpm), which then feeds on to a larger inverted bowl. The solution coating on the bowl becomes thinner until leaving the bowl as an atomised liquid (see Figure 1). [3]

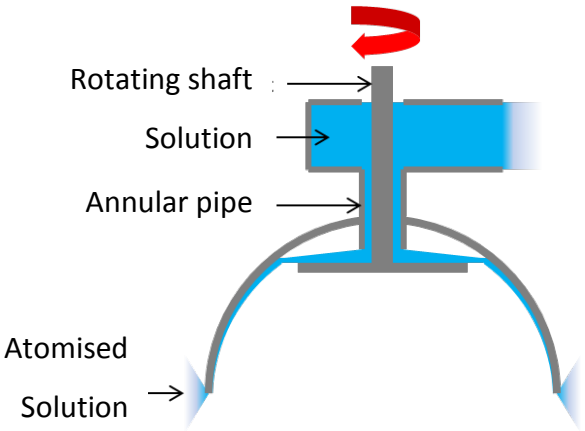


**Figure 1 Rotary bowl atomiser**[3]

The hot air is tangentially fed into the spray drier, so the air circulates around the drier suspending drying droplets. Large particles that are too heavy to be suspended by the air flow, fall in to a collecting bottle at the base of the cone. The dried particles are separated from the hot air by a cyclone and collected at the base of the cone (see Figure 2).[3]

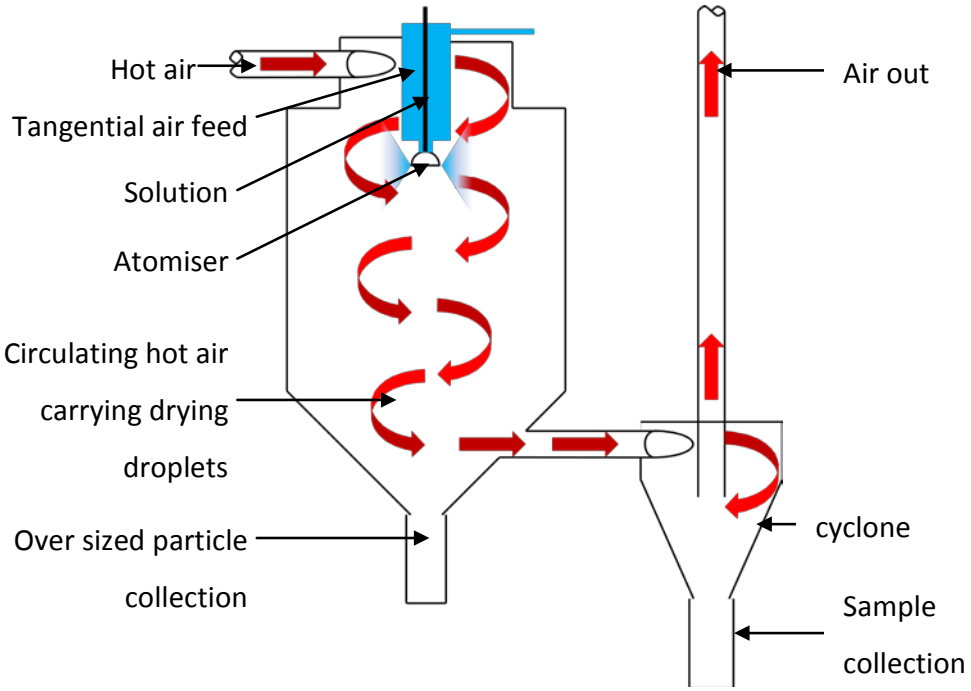


**Figure 2 Spray drier operation**

The actual drying time of a droplet is only a matter of a fraction of a second, with a total time spent in the drier of just a few seconds. The characteristic particle form gives a product with a low tap density, which is free flowing with almost spherical particles only a few microns in size (see Figure 3).[4]

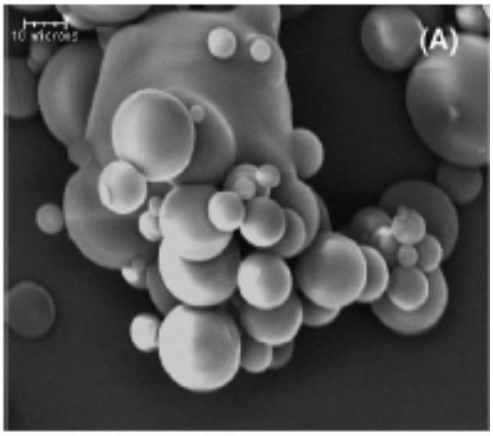


**Figure 3 Scanning electron micrographs of amorphous spray-dried lactose showing the characteristic spherical particle shape[4]**

### 2.1.3 Freeze drying

Amorphous materials generated by freeze drying are prepared in small vials with a relatively small capacity of a few millimetres. Freezing must always be fast to avoid fractionation of the sample solution. This can be achieved in a number of ways including immersion in low boiling point liquids e.g. liquid nitrogen. The phase diagram of water shows that below the triple point of water (at 610 Pa and 0.0075 °C)

the liquid state is not present. This means that solid water ice can sublime straight in to the gas state.[3]

The next step in the freeze drying process is to place the frozen samples in a freeze drier. The freeze drier typically operates in the temperature range -10 to -30ºC and critically below a pressure of 610 Pa. Heat has to be supplied to sublime the water in the samples (typically 5 W $m^{-3}$). The process is slow typically 1 mm thickness of ice per hour. Removal of the water vapour by a powerful vacuum pump is necessary to keep the pressure below 610 Pa.[3]

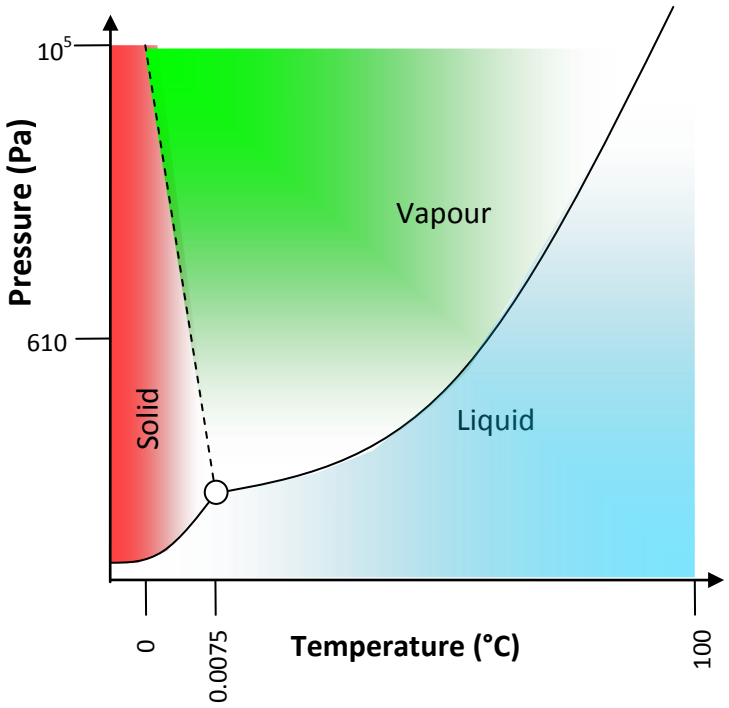


**Figure 4 Phase diagram of water[3]**

The last 5 to 10% moisture is usually removed by heating at 50 °C. The product is best sealed under vacuum to prevent it ever coming in to contact with the atmosphere until use, since freeze dried products are highly hydroscopic. The final amorphous product is highly porous with no definite morphology and is shown in Figure 5.[4]

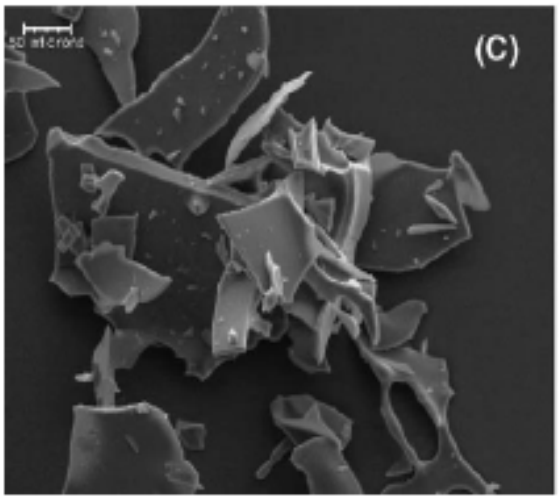


Figure 5 Scanning electron micrographs of amorphous freeze-dried lactose[4]

### 2.1.4 Micronisation

This micronisation process involves the reduction in average particle size using a milling process. The feed apparatus consists of a hollow, donut-shaped pipe arranged in a loop. The diameter of the pipe varies between 20-200 mm depending on the size of the loop which can extend up to 2 m. Air is injected as a high pressure jet through nozzles at the bottom of the loop to generate turbulence into which the solid particles are fed. The high kinetic energy of the air causes the particles to impact with other particles with sufficient momentum for fracture to occur.[3, 3, 5]

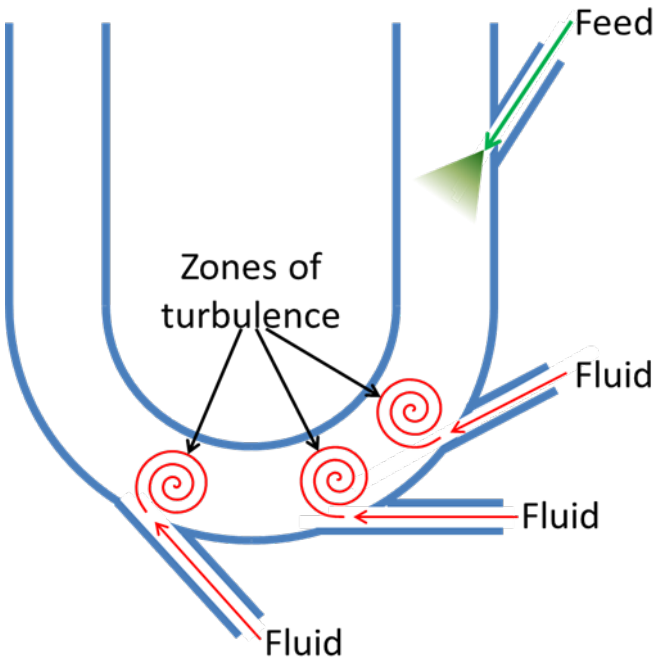


Figure 6 fluid energy mill[5]

A series of hydro cyclones is usually attached to the output of the fluid mill to classify and separate particles that have been reduced in size and those that still need to be milled down further. Particles that still need to be milled are fed back into the milling loop.

## 2.2 Instrumentation

### 2.2.1 Gas Chromatography

Gas chromatography separates and quantifies components in a mixture. The instrument can be divided in to three components an injector (or inlet), column and detector seen in Figure 7.[6] The gas chromatograph inlet vaporises the sample mixture and a carrier gas is used to transport the vaporised sample mixture on to a separating column. The time that each component in a mixture spends in the column is characteristic of that particular component and column pairing, provided a number of other parameters are held constant such as oven temperature profile, gas flow rate and pressure.[7] In this way, the mixture is separated into components that emerge from the column at different times. When components emerge from the column, a detector provides an electronic signal that is proportional to the component's concentration in the mixture which is recorded against time on the chromatograph.[7]

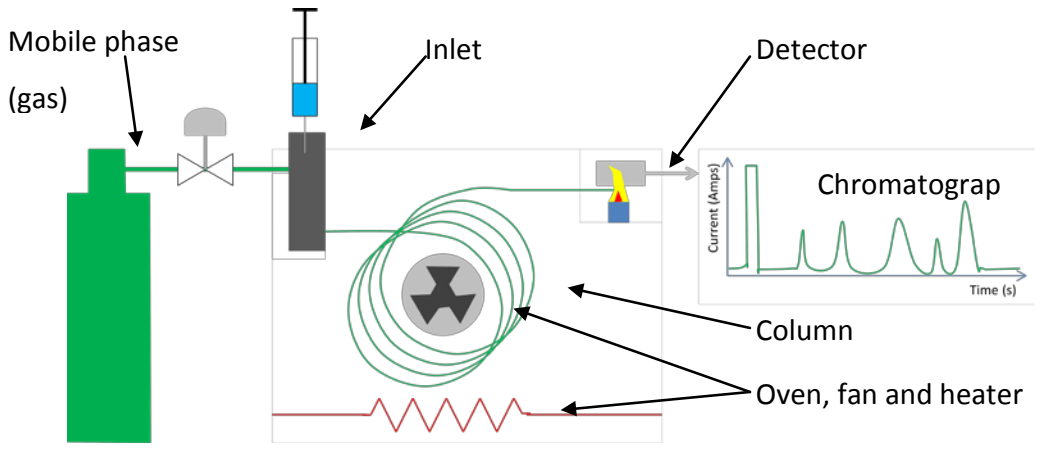


**Figure 7 Simplified diagram of a GC and chromatograph[6]**

The injector in its simplest 'splitless' mode, transfers the entire injected sample on to the column. The injector operates at a high temperature (typically 250 °C), to instantly vaporise the entire sample as it is injected.[6] A controlled flow of pressurised carrier gas is fed into the injector. In this particular mode, all the carrier gas entering the injector exits via the column.[7] In contrast in the "split" mode a mass flow controller

balances the carrier mobile phase leaving via the column and that going directly to an exhaust port. This at first appears wasteful of sample and carrier gas, but the detection limit of the instrument often lies in the pictogram ($10^{-12}$ g $s^{-1}$) range.[6] A sample solution at one part per million (w/v), with an injection volume of one micro litre would place one nanogram ($10^{-9}$ g) into the injector. This would be 1000 times more than necessary, so a "split" injection offers a useful means of reducing the sample load entering the column.[6]

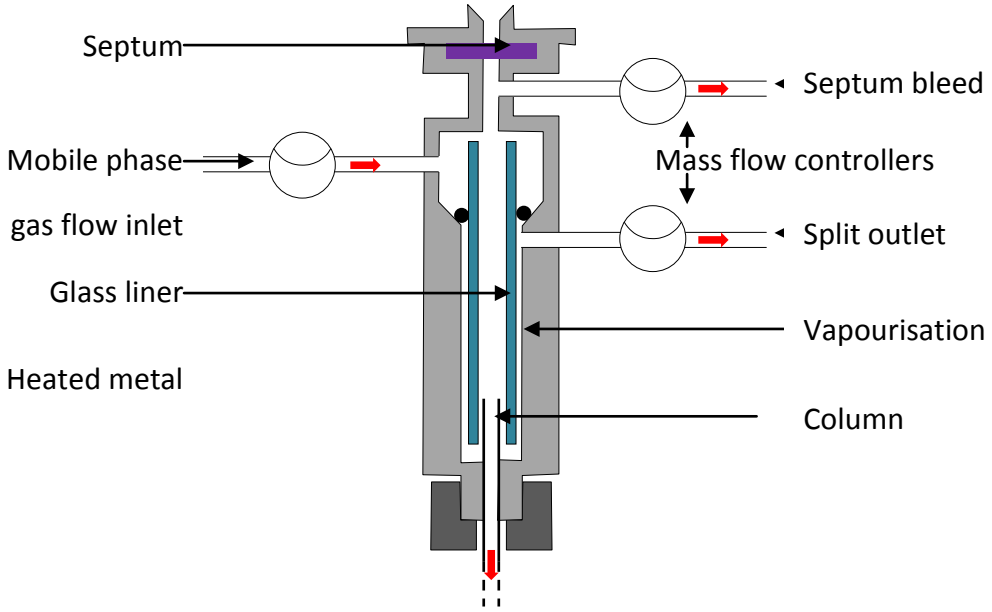


**Figure 8 GC inlet operated in split mode**

Capillary columns are typically used to separate organic molecules containing 6 or more carbon atoms. These comprise of 10 m or more of a small bore glass pipe made from fused silica, which is coated externally with a polyimide, (see Figure 9) to prevent the column snapping.[7]

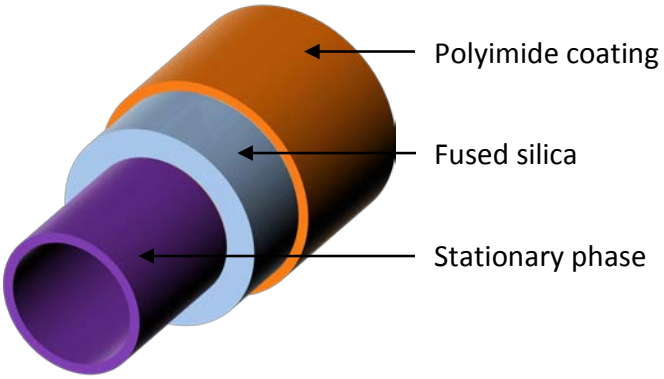


**Figure 9 Cross section of a capillary GC column**

The column achieves separation of the mixture by partitioning components between the carrier gas (also known as the mobile phase) and a liquid coating of the internal

walls of the column (the stationary phase).[7] Each component in the mixture is in equilibrium between the mobile and stationary phase. All the mixture components spend the same time travelling in the mobile phase of the column, however the amount of time each component spends in the stationary phase depends on how attracted it is to the stationary phase. Components that are not attracted to the stationary phase will spend very little time in the stationary phase and pass through the column quickly, whereas components that interact strongly with the stationary phase spend a great deal of time there and take a long time to pass through the column.

Columns are chosen specific to the component of interest in a mixture (known as the analyte). Columns are often described by their "polarity". To achieve a good separation, a column stationary phase is chosen that has a polarity related to the analyte.[7] Non polar analytes are aliphatic hydrocarbons. A typical mobile phase with low polarity would be composed from polysiloxanes, (see Figure 10) and interact via dispersion forces. Polar molecules would be for example alcohols or molecules containing a carbonyl carbon atom. Greater polarity is achieved my adding in polydiphenylsiloxane to the stationary phase (see Figure 10). The π electrons of the phenyl group interact with analyte molecule dipoles.[7]

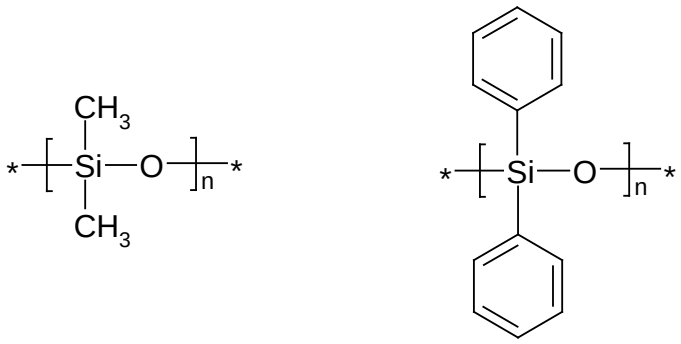


**Figure 10 Structure of polysiloxane and polydiphenylsiloxane stationary phases**

The stronger the interaction with the stationary phase, the more time the sample takes to pass through the column. Those components that do not interact with the stationary phase travel at the flow rate of the mobile phase through the column.[7] Increasing the column length can improve separations. Increasing the stationary phase depth provides more stationary phase for mixture components to interact with, improving separation and transporting more analyte to the detector. The down side of increasing the time an analyte spends in the stationary phase is increased time taken

to produce a chromatograph and get a result.[7] One way of improving this is by the use of a heating ramp. Increasing the temperature of a column increases the rate of interchange between mobile and stationary phases. The continuous flow of mobile phase sweeps the analyte along the column thus reducing the time spent in the stationary phase.[7]

The Flame Ionisation Detector (FID) ionises the analyte using a hydrogen/air flame (see Figure 11). The ions produced increase the current flow between the electrodes of the FID which is measured by a picoammeter.[7] The detection limits (typically 3 x $10^{-12}$ g/s for diphenyl) of the FID vary depending on the number of ions produced per molecule. This means that the FID produces a response that is specific to each analyte. The FID works well with hydrocarbons but the detection limit is poor for molecules such as formaldeyde.[7] This means that each analyte must have its own calibration. The linearity of response over a range as broad as $10^7$ has made the FID the default detector for GC.[7]

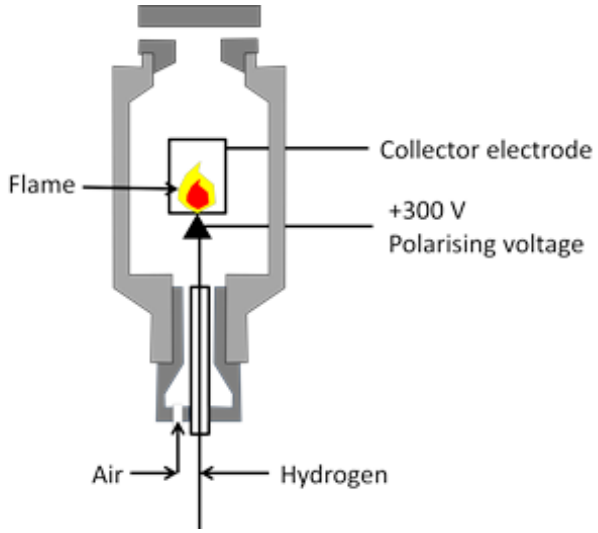


**Figure 11 Flame ionisation detector**

### 2.2.2 Dynamic Vapour Sorption (DVS)

The Dynamic Vapour Sorption technique records mass as a function of temperature and humidity. DVS has been used by Zografi, Mackin and Buckton to quantify amorphous content in a number of materials, as amorphous materials behave differently to crystalline materials in their interaction with water. Amorphous lactose is capable of absorbing up to 13% water, before crystallising as alpha lactose monohydrate with a mass gain of 5%.[8] The change in mass allows an inferred measurement to be made of the amorphous content as crystalline alpha lactose

monohydrate would not be expected to show a permanent weight gain during a similar cycle. Amorphous salbutamol sulphate content has also been quantified by monitoring the mass gain when a sample is subjected to a humid atmosphere[9].

DVS is a thermogravimetric (TG) technique that specialises in controlling the sample environment. Traditional TG utilises a continuous fixed flow of pure dry nitrogen gas to the sample environment. TG instruments have been used in two significantly different ways, ramps that change temperature at a fixed rate per unit of time and isothermally that is used to monitor reaction kinetics at a single temperature. Traditional TG typically monitors the occurrence and extent of decomposition reactions that produce volatiles.

The key component to any TG is a highly accurate microbalance. This utilises a balance beam; hung from one end is the sample and from the other, a counter weight. The beam is controlled using a torque motor to maintain a permanent horizontal position using light sensors to detect movement. The electrical current supplied to the torque motor is proportional to the mass placed on the balance[10].

DVS has been developed by the pharmaceutical industry to investigate stability at ambient temperatures and humidities. This means that the instrument is housed in a temperature controlled environment that typically ranges from 5 to 65°C and controls the relative humidity of the sample environment. DVS runs are typically isothermal rather than ramped, as humidity is changed and temperature kept constant.[11]

DVS instruments exercise a high degree of control over the sample environment. Two mass controllers are used to supply gas and vapour to the sample cell. The gas supplied to a DVS instrument is usually pure, dry nitrogen and is split between two mass controllers. The output from one mass flow controller goes directly to the sample environment, the other is bubbled through a solvent generating a saturated vapour. The gas flows are then combined and fed into the sample environment. The most common solvent used is water, others include octane, acetone, methanol, acetonitrile and dichloromethane.[12]

The gas leaving the sample chamber is monitored for vapour composition to ensure the outlet gas contents match the desired level. The most universal of detectors is electron ionisation quadrapolar mass spectroscopy, however a less expensive option is

a cooled optical mirror that determines the dew point temperature of the vapour leaving the sample cell.[12]

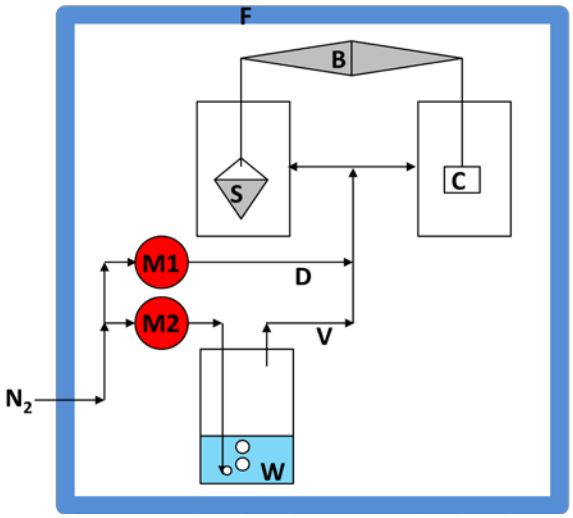


| | |
|---|---|
| F | Incubator |
| B | Balance beam |
| S | Sample pan |
| C | Counter weight |
| M1 | Mass flow controller (dry) |
| M2 | Mass flow controller (vapour) |
| $N_2$ | Nitrogen gas supply |
| W | Solvent (usually water) |
| D | Dry nitrogen supply |
| V | Nitrogen supply containing solvent vapour (usually water) |

**Figure 12 Schematic of gas flows in a DVS instrument**

DVS is typically operated in a series of stepped humidity changes that allow the sample mass to attain equilibrium, before continuing to the next humidity change. The surface moisture is first removed in the DVS by subjecting the sample to dry nitrogen until an equilibrium mass is attained. This dry mass represents the starting mass of the sample.

The amorphous content of lactose can be predicted by subjecting the dried sample to humidity of 65.5% or greater (at 25 °C), allowing the mass to equilibrate as crystalline α-lactose monohydrate is formed.[8] Buckton has proposed that the difference between starting and end mass can be used to calculate amorphous content (in the case of lactose), since lactose monohydrate weighs 5.27% more than anhydrous or amorphous lactose. The assumption in the Buckton's method is that any β-lactose isomer present in amorphous lactose is ultimately converted to α-lactose monohydrate. This assumption is challenged in Chapter 5, lactose isomer analysis.

By contrast salbutamol sulphate has no known crystalline hydrates or solvates, however amorphous salbutamol sulphate absorbs more much water vapour per unit mass than its crystalline polymorph. Amorphous content can be estimated by subjecting the sample to a humidity of less than 50%, and measuring the percentage increase in mass. This percentage mass gain corresponds linearly to amorphous content.[9]

DVS is also capable of providing surface area measurement, since the DVS controls the partial pressure of a sorbate, (water vapour or solvent) any vapour adsorbed on to the surface is continuously monitored using the sample mass. Measurements of surface area can be made prior to crystallisation events and after.[12]

### 2.2.3 Differential Scanning Calorimetry (DSC)

The heat capacity of different polymorphs varies significantly due to their different packing arrangements. For amorphous phases, this is due to their non-specific composition and poor packing density. The heat capacity tends to be both variable and higher than crystalline pure polymorphs (above the glass transition point). DSC measures the heat energy flowing into and out of a sample and allows heat capacities to be calculated. Measurements are made relative to a known reference standard allowing calculation of heat capacity. For heat flux instruments that measure the temperature difference between the sample and reference, the reference typically used is an empty crucible. The heat flows are measured under two conditions; isothermal maintaining a constant temperature and ramped where the temperature is changed at a fixed rate per unit of time. To control temperature within the cell a heater surrounds the cell, which is in turn surrounded by a cooling jacket to provide accurate temperature control.

Heat flux instruments utilise three separate thermocouples. The first thermocouple measures the temperature of the cell while the two other thermocouples are placed in contact with the sample and reference crucibles (see Figure 13). The sample and reference thermocouples are placed electrically in series and the voltage difference between these entities is measured. This difference is ultimately converted into an energy flow per second reading as described in Equation 1. To ensure a consistent environment in the cell, a consistent supply of high purity dry nitrogen is used.[10]

$$T_S - T_R = \Delta T \propto \frac{d\Delta q}{dt} \qquad \text{Equation 1}$$

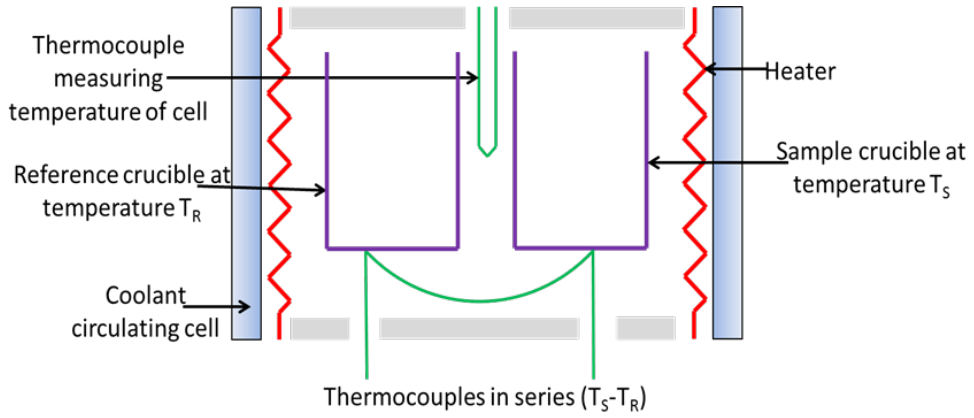


Figure 13 Heat Flux DSC[13]

### 2.2.4 Powder X-ray Diffraction

Crystalline polymorphs can be identified and in some cases quantified by powder diffraction.[14] Crystalline materials produce characteristic patterns where reflections of X-rays occur at particular angles and with distinctive relative intensities. X-rays used in powder diffraction are electromagnetic waves of specifically selected wavelengths that interact with the electrons found in the crystal structure. The technique uses Bragg's law (see Equation 2 and Figure 14).[15]

$$n\lambda = 2d\ sin\theta \qquad \text{Equation 2}$$

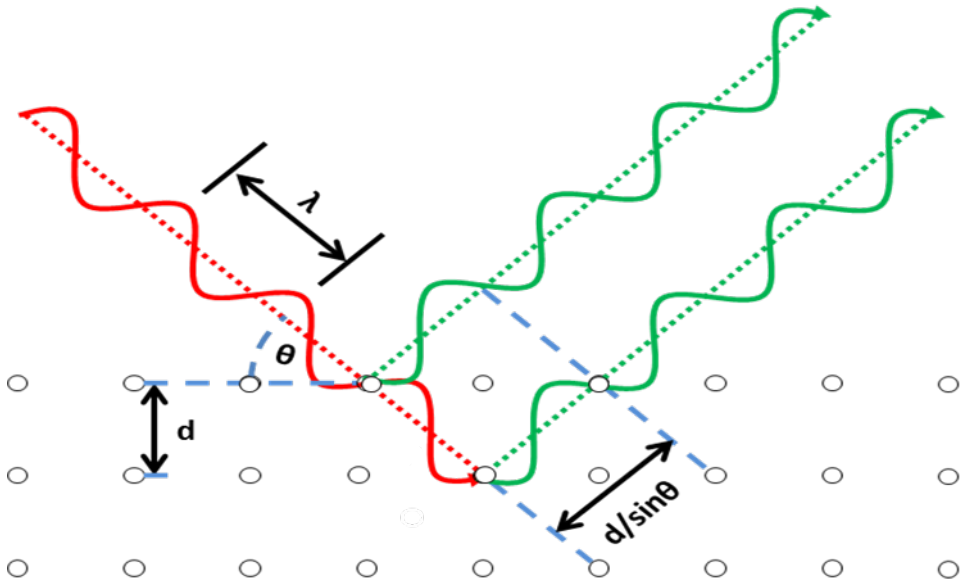


Figure 14 Bragg reflection

Crystals are composed of repeating symmetrical units that contain all the atomic structural components known as the "unit cell" and contain the smallest possible number of atoms given the unit cell's symmetry operations. The most symmetric crystal system is the cube, where the cell lengths are all the same and the angles are all right angles.[16]

The instrumentation for powder X-ray diffraction consists of an X-ray source, a sample holder and a detector. The schematic for a diffractometer is shown in Figure 15. X-rays are produced electrons that are accelerated towards a metal target in a vacuum. The impact removes electrons from their lower energy orbitals in the target atoms creating a vacancy. A photon of X-ray radiation is emitted by an electron in a high energy orbital descending into the vacant low energy orbital. The X-rays produced are specific to the target element.[16] The sample holder is spun to increase the sample area used for measurement. Spinning reduces the effect of large crystals producing reflections with unrepresentative intensities patterns. The movement of the sample plate and detector are co-ordinated so the angular rotation rate of the sample holder is exactly half that of the detector. The scattered X-rays are then detected and processed electronically. In these experiments a Position Sensitive Detector (PSD) was used to analyse the scattered data. When the gas inside the detector is ionised by an incident X-ray an electron-avalanche occurs producing an amplified signal.[17]

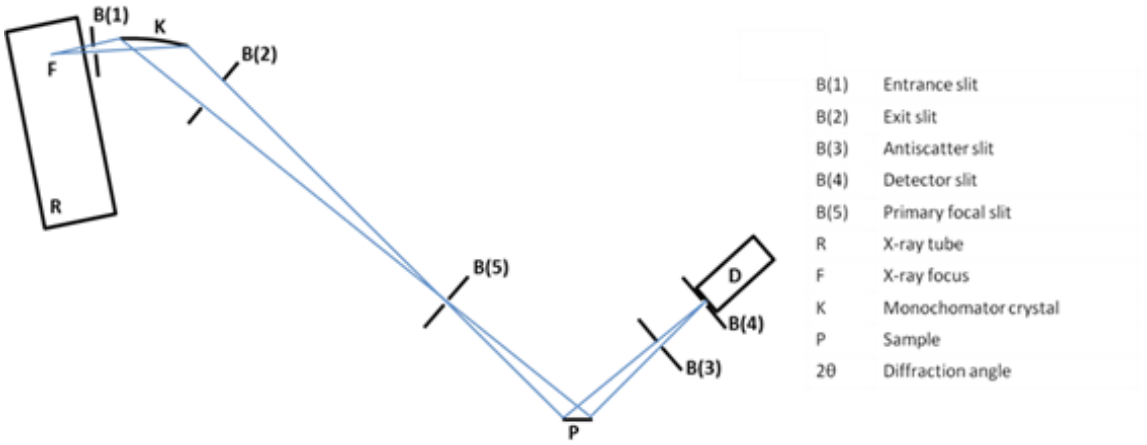


**Figure 15 The Bragg–Brentano instrument geometry for a diffractometer.**

### 2.2.5 Infra-red Spectroscopy

Crystalline polymorphs contain the same molecules, but are packed differently to one another. Infra red spectroscopy measures the absorbance of electromagnetic radiation at frequencies that cause chemical bonds to vibrate. Molecular vibrations in one molecule can be transferred to a neighbouring molecule by hydrogen bonding. The crystalline packing, orientation, and intermolecular distances define which frequencies of infra red radiation are able to absorb and transfer this energy. Differentiating one polymorph from another by comparison of infra red spectra is possible provided a number of these characteristic vibrations occur.[18]

Infra red absorbance occurs only at specific frequencies which are determined by the chemical bond length and atomic masses.[19] An infra red spectrum can be split roughly into two distinct parts, frequencies greater than 1500 $cm^{-1}$ attributed to the stretching of functional groups and those below 1500 $cm^{-1}$ that are caused by the rocking, wagging and twisting. In the region below 1500 $cm^{-1}$, vibrational modes operate via hydrogen bonds or weak London dispersion forces between neighbouring molecules giving rise to distinct absorbencies, thus allowing differentiation of solid forms.[19]

In order to produce an active absorption, conditions for harmonic motion must be satisfied and are determined by a combination of chemical bond length and atomic mass of the atoms in the bond. In infra-red spectroscopy, a further selection rule exits for energy to be transferred from an electromagnetic wave to a molecular vibration. This demands that the oscillating electrical field of the absorbed radiation must interact with the electrical dipole of the bond, such that the resulting vibration changes the electrical dipole moment of the bond.[20]

Modern infra-red instruments use Fourier transform technology in place of traditional gratings. Fourier transform is a mathematical procedure which converts a curve into a series of cosine terms known as a Fourier series. The key component of an FT-IR instrument is the interferometer. This is a mirror that moves back and forth whose position is known very accurately. The beam from the infra red light source is split at the interferometer mirror. Fourier analysis processes the interferogram mathematically by deconvoluting it into a series of component cosine waves, each with their own amplitude and frequency that ultimately correspond to spectral frequencies and absorbencies. [6]

Attenuated Total Internal Reflectance (ATR) is currently the most convenient sample presentation method, dramatically reducing the time taken per measurement. ATR allows the spectrum to be measured by simply placing a solid sample on a diamond, and applying pressure to bring the sample in close contact. The ATR technique does not pass infra red radiation through the sample. The electromagnetic field of the infra red beam is reflected internally from the surface of the diamond at which point it interacts with the electrical field of the sample absorbing specific frequencies of radiation, giving rise to a characteristic spectrum[6].

## 2.2.6 Solid State Nuclear Magnetic Resonance Spectroscopy

### *2.2.6.1 Introduction*

All atomic nuclei spin, even at temperatures close to 0 °K, the axis of spin also precesses. This property of precession is used by Nuclear Magnetic Resonance techniques to provide information about the magnetic environment of spin active nuclei. A schematic of an instrument is shown in Figure 16.

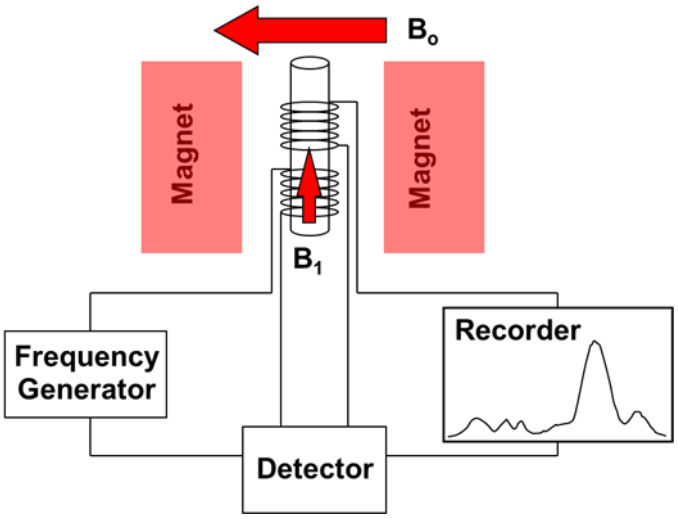


Figure 16 Schematic of an NMR instrument

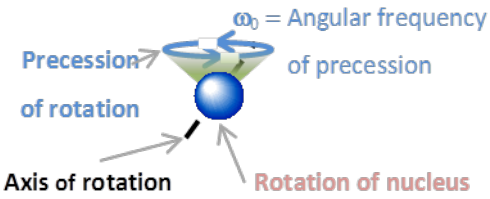


Figure 17 Nuclear spin and precession

The rate of nuclear precession $\upsilon$ (frequency in radians per second) is known as the Larmor frequency. It is related to the static instrument magnetic field $B_0$, the nuclear gyromagnetic ratio $\gamma$ see Equation 3. Differences in the Larmor frequency for a nucleus indicates differences in the magnetic environment or electron density (chemical bonding) surrounding the nucleus.[21]

$$2\pi\upsilon = \gamma B_0 \qquad \text{Equation 3}$$

For field strengths of between 2-14 Tesla, the excitation frequency lies in the radio part of the electromagnetic spectrum. Different spin active nuclei have different values of $\gamma$, so in a static magnetic field of 4.7 Tesla the proton signal would occur at 200 MHz and the $^{13}$C signal would appear at 50.5MHz.[22]

NMR is a relatively insensitive technique, one reason for this is because the signal is generated by only a small proportion of spin active nuclei. This is not helped by the fact that only certain isotope nuclei are spin active, common nuclei with spin quantum number of ½, are $^{1}$H, $^{13}$C and $^{19}$F. These nuclei have their precession axis randomly aligned in the absence of a magnetic field, however in a strong magnetic field they

align either with or against the magnetic field. These two alignments have slightly different energies. The lower energy state, where the nucleus magnetic moment aligns with the external magnetic field $B_0$ is labelled α, and the upper energy state labelled β.[23]

For a signal to be generated a nucleus must switch precession alignment, the energy required for this is known as the energy difference $\Delta E$. The energy difference $\Delta E$ is calculated using Equation 4, $w$here h is Plancks constant.[21]

$$\Delta E = \frac{\gamma h B_0}{2\pi} \qquad \textbf{Equation 4}$$

Another reason for the small number of nuclei generating a signal is due to the extremely small difference in populations of the α and β spin states, typically only one part in 10000, given by the Boltzmann distribution (see Equation 5). This also explains the desire for a strong instrument magnetic field, since the greater the magnetic field the greater the energy difference between spin states and the greater the population difference between the α and β spin states, ultimately generating a greater signal intensity.[21]

$$\frac{N_\beta}{N_\alpha} = exp\left(\frac{-\Delta E}{kT}\right) \qquad \textbf{Equation 5}$$

#### *2.2.6.2 The vector model*

The vector spin model assists in the understanding of how techniques such as cross polarisation operate along with how the radio frequency pulse changes the nuclear precession. The small difference in population favouring the α state with nuclei aligned parallel to the static magnetic field is assigned a vector $M$, which is the sum of the magnetizations of each individual nuclei precession.

The vector model is constructed in Cartesian coordinates with the magnetic field $B_0$ running parallel to the z-axis. The vector sum of magnetization $M_0$ is also aligned along the z-axis when the sample is at equilibrium. Applying a second radio frequency pulse via a magnetic coil placed parallel to the x-axis creates a second magnetic field $B_1$. This changes the alignment of the net magnetization vector $M$, moving it nearer to the x-y plane and at the same time causing it to precess about the z-axis. The precession occurs at the Larmor frequency.[22]

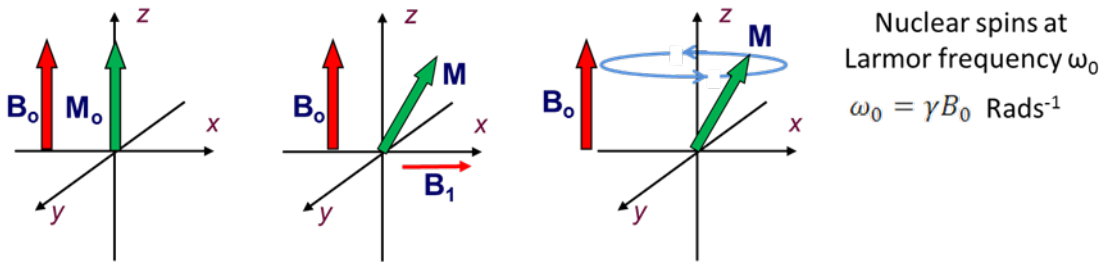


**Figure 18 Vector model showing the application of a second magnetic field $B_1$**

### *2.2.6.3 Free Induction Decay*

An inductance coil similar to the one used to deliver the radio frequency pulse can also be used to measure the varying magnetic field along the z-axis. After a radio frequency excitation pulse, the net magnetization vector $M$ eventually returns to an equilibrium position parallel to the z-axis. The signal from the inductance coil shows the varying magnetic field oscillating as $M$ precesses about the z- axis and returns to the equilibrium position. This signal is described as the free induction decay curve (FID) which is processed into a spectrum using Fourier transform mathematics.[20]

### *2.2.6.4 Excitation pulses and rotating frames*

When an excitation radio frequency of $\omega_1 = \omega_0 = \gamma B_0$ is applied, the magnetic field $B_1$ interacts with $M$ moving it towards the x-y plane. While the excitation radio frequency pulse is still being applied, precession occurs about the z-axis and the x-axis at the same time, this is known as nutation.

Since considering two simultaneous rotations is complex, a rotating frame reference can be used for simplification. In the rotating frame the z'axis remains parallel to the static magnetic field, however the x'-y' plane rotates about the z'axis at a rate equal to the frequency $\gamma B_0$. This concept produces a simplification by removing the magnetic field precession from consideration. In the rotating frame the effect of the excitation frequency $B_1$is to cause the net magnetization vector $M$ to precess about the x'-axis. A timed pulse ($t_p$) can be applied that effectively flips the net magnetization vector $M$ by a fixed angle (in radians) using the Equation 6. The duration of the pulse produces a particular flip angle, those typically used are $\frac{\pi}{2}$ and $\pi$ radians.[22]

$$\theta = \gamma B_1 t_p \qquad \textbf{Equation 6}$$

### 2.2.6.5 Cross Polarisation

To obtain a $^{13}C$ spectrum of a solid, two techniques are generally applied - cross polarisation and magic angle spinning, since the abundance of NMR active carbon is small and the solid state results in incomplete averaging of the applied field. Cross polarisation involves transferring the spin from an abundant nucleus, normally hydrogen, to the carbon to increase the sensitivity. For cross polarisation, the excitation pulse combination has to satisfy particular conditions and is known as the contact pulse. For the proton magnetisation, a $\frac{\pi}{2}$ pulse is applied along the x'axis to cause the proton net magnetization vector $M$ to precess about the y'axis, where angular frequency is given by Equation 7. An identical set of conditions are applied to the $^{13}C$ where angular frequency is given by Equation 8. When the two frequencies are equal, matching frame precession occurs (see Equation 9).

$$(\omega_1)_H = (\gamma B_1)_H \quad \textbf{Equation 7}$$

$$(\omega_1)_C = (\gamma B_1)_C \quad \textbf{Equation 8}$$

$$(\gamma B_1)_H = (\gamma B_1)_C \quad \textbf{Equation 9}$$

During signal acquisition the proton transmitter is left on, decoupling the $^{13}C$ spectrum from the hydrogen and further improving sensitivity.[22]

### 2.2.6.6 Dipolar broadening

Although cross polarisation improves the $^{13}C$ signal, solid state NMR spectra are subject to two major affects that cause line broadening, chemical shift anisotropy and dipolar broadening. Dipolar broadening is understood by considering the magnetic environment on individual nuclei (excluding the chemical shift arising from molecular structure), in a liquid this is constantly changing due to molecular motion, but averages out to produce a narrow peak. In a solid crystal the magnetic environment is fixed, every nucleus relative to another exerts its own local magnetic field $B_{loc}$ (see Equation 10) where $r$ is the distance from nuclei to nuclei, $\theta$ the angle of a line from nuclei to nuclei relative to the static magnetic field and $\mu$ magnetic moment for each nuclei. For a powder, each crystal will have its own alignment, so the exact magnetic field each nucleus is subject to variation and hence produces a broad peak.[22]

$$B_{loc} = \pm\mu r(3cos^2\theta - 1) \quad \textbf{Equation 10}$$

### 2.2.6.7 Chemical Shift Anisotropy

The magnetic field shielding produced by electron density is characteristic for particular chemical bonds and is used in liquid samples as a means of characterisation. The electron density distribution is not generally spherical and has directional properties. In a liquid the molecular tumbling reduces this as an inter-molecular effect while retaining its useful intra-molecular properties. For a solid single crystal, changing the orientation relative to the magnetic field produces different chemical shifts, which vary as a function of $(3cos^2\theta - 1)$. Powder crystalline samples produce broad dispersed peaks as crystals take up different alignments.[22]

### 2.2.6.8 Magic Angle Spinning

Chemical shift anisotropy and dipolar coupling both vary for single crystals in relation to the function $(3cos^2\theta - 1)$. At the "magic angle" of 54°44' $(3cos^2\theta - 1) = 0$ , so both chemical shift anisotropy and dipolar coupling are both eliminated from the spectrum. For crystalline powders each crystal will have a different orientation. By spinning on an axis orientated at the magic angle the orientation of the crystallites averages out to equal the magic angle.[22]

### 2.2.6.9 Chemical Shifts

Referring back to Boltzmann distribution as defined in Equation 11, the small amount of signal generated by spin active nuclei in MAS NMR has meant that the technique has tended to be used for qualitative characterisation rather than quantitative rather like infra red. NMR provides information on magnetic environment of the nucleus, since electrons surrounding a nucleus exert a magnetic field and are said to shield the nucleus from the external magnetic field. The extent of the shielding is expressed as a constant ($\sigma$) and the effective magnetic field ($B_{eff}$) that the nucleus is exposed is calculated in Equation 11. The magnetic environment nuclei can be influenced by a number of factors, the proximity of other spin active nuclei and the electron density in neighbouring atoms and bonds.[20]

$$B_{eff} = B_0(1 - \sigma) \qquad \textbf{Equation 11}$$

Nuclei of atoms, in particular chemical bonds produce characteristic values of $\sigma$, to compare readings for chemical shift from one NMR instrument to another a dimension

less parts per million scale $\delta$ is used, rather than frequencies or magnetic field strengths. This is because instruments are manufactured with static magnetic fields that vary from instrument to instrument. In order to compare readings from one instrument to another all signal frequencies ($\upsilon_s$) are compared to the signal from a reference material $\upsilon_{ref}$ seen in Equation 12. The standard often used to set a zero value for proton and $^{13}$C NMR is tetramethylsilane, although adamantane is often used as a secondary standard in solid state CP MAS NMR. Given that particular chemical bonds produce characteristic values of $\sigma$, the values of $\delta$ will also be characteristic and transferable from instrument to instrument. This allows a pattern of peaks produced with different values of $\delta$ for a particular solid to be reproducible by any instrument.[20]

$$\delta = \frac{\upsilon_s - \upsilon_{ref}}{\upsilon_{ref}} \times 10^6 \qquad \textbf{Equation 12}$$

***References***

1 R. Zallen, *Richard Zallen. The physics of amorphous solids. New York ; Chichester : Wiley, 1998.*, Wiley, Chichester, 1998.

2 D. E. Levy, *The Organic Chemistry of Sugars Hoboken*, CRC Press, 2005.

3 M. E. Aulton, *Pharmaceutics the Science of Dosage form Design, Second Edition. Churchill Livingstone 2002.*, Livingstone, Churchill, 2002.

4 M. K. Haque and Y. H. Roos, *Innovative Food Science & Emerging Technologies,* 2006, 7, 62-73.

5 M. J. Rhodes, *Introduction to particle technology*, John Wiley, Chichester, 1998.

6 D. C. Harris, *Quantitative chemical analysis*, W. H. Freeman, New York, 2002.

7 I. A. Fowlis, *Gas chromatography : analytical chemistry by open learning / author: Ian A. Fowlis. Published on behalf of ACOL (University of Greenwich)*, Wiley, Chichester, 1995.

8 D. J. Burnett, F. Thielmann and J. Booth, *International Journal of Pharmaceutics,* 2004, 287, 123-133.

9 M. Gorny, M. Jakobs, V. Mykhaylova and N. A. Urbanetz, *Drug Developement and Industrial Pharmacy,* 2007, 33, 235-243 (DOI:10.1080/03639040601128647).

10 D. Q. M. Craig and M. Reading, *Thermal analysis of pharmaceuticals*, CRC distributor; Taylor & Francis, New York; London, 2006.

11 D. Williams and M. Briggs, *Method and apparatus for investigating the properties of a solid material. British Patent: GB2408800 - 2005-06-08*, British, 2005.

12 Surface Measurment Systems, *DVS Advantage - Operation Manual*.

13 M. E. Brown, *Introduction to thermal analysis : techniques and applications*, Kluwer Academic Publishers, Boston, 2001.

14 D. Q. M. Craig, P. G. Royall, V. L. Kett and M. L. Hopton, *Int. J. Pharm.,* 1999, 179, 179-207 (DOI:10.1016/S0378-5173(98)00338-X).

15 A. R. West, *Basic solid state chemistry*, John Wiley & Sons, Chichester, 1999.

16 S. E. Dann, *Reactions and characterization of solids*, Royal Society of Chemistry, Cambridge, 2000.

17 C. Whiston, *X-ray methods, analytical chemistry by open learning*, Wiley, Chichester, 1987.

18 R. Hilfiker, *Polymorphism : in the pharmaceutical industry / Weinheim : Wiley-VCH, 2006*, Wiley-VCH, Weinheim, 2006.

19 J. H. vander Maas, *Basic infra red spectroscopy*, Heyden, London, 1975.

20 P. W. Atkins and J. De Paula, *Atkins' Physical chemistry.*, Oxford University Press, Oxford, 2002.

21 P. J. Hore, *Nuclear Magnetic Resonance*, Oxford University Press, Oxford, 1995.

22 J. K. M. Sanders and B. K. Hunter, *Modern NMR spectroscopy, a guide for chemists*, Oxford University Press, Oxford, 1993.

23 D. A. R. Williams, *Nuclear magnetic resonance spectroscopy*, Wiley, Chichester, 1986.

# CHAPTER 3

# Instrument Conditions

## 3.1 Introduction

Amorphous materials possess a glass transition point where their properties change from those characteristic of a brittle material to those akin to a plastic at a particular temperature. This is a distinctly different property to those shown by crystalline materials that possess a point of fusion. The heat capacity step change at the glass transition point therefore provides positive evidence of the presence of an amorphous material in a mixture. Differential Scanning Calorimetry (DSC), which examines phase changes as a function of temperature, is clearly a particularly useful technique for the characterisation of compounds which may have an amorphous content.

FT-IR is a short range technique which focuses on characteristic ranges expected for certain types of bond. While not as discriminating as many other analytical methods, it can be useful in that it can give information on the type of bonds present in small quantities of materials in any state. In terms of amorphous materials, the absorptions tend to be broad and less well-defined than those observed for crystalline species as a result of the disordered arrangement of molecules generating varying environments. In the case of lactose, the disordered packing of molecules found in amorphous lactose, as the result of random networks of hydrogen bonds, generate significantly broader absorption absorptions in their infra-red spectra.[1,2] The lack of sharp distinct features and the presence of broad indistinct peaks does not provide positive evidence that amorphous materials are present, instead these spectra show patterns that are consistent with the presence of amorphous material.[2] The instrument settings are important to ensure that broad spectral features are not merely poorly resolved sharp ones.

The solid state MAS-NMR spectra of amorphous materials demonstrate similar broadening effects to those observed in FT-IR, i.e. amorphous materials show broad features as opposed to the sharp features of crystalline materials. However, the NMR technique is much more complex then FT-IR spectroscopy, with many parameters that can be tuned to collect the best quality data. This can then be used to extract much more information about the material under study. For example, solid state $^{13}C$ CP-MAS-NMR can be used to identify amorphous materials by measuring proton relaxation times by exploiting the differences in relaxation behaviour between crystalline and amorphous materials.

One of the most prevalent techniques used for the analysis of amorphous materials is Dynamic Vapour Sorption (DVS). DVS uses moisture to force crystallisation of amorphous materials by exploiting the increased instability of amorphous materials relative to their crystalline counterparts to moisture. The mass change during the experimental cycle as a function of humidity allows the amorphous content to be calculated. This process can be achieved in a number of ways depending on the information required.

## 3.2 Differential Scanning Calorimetry with Thermogravimetric analysis

Differential Scanning Calorimetry (DSC) is particularly useful for the identification of amorphous materials as DSC can characterise a number of thermal properties; the glass transition point, melting point, heat capacity and enthalpy of fusion.[3] It has been used by Garnier to the characterise lactose polymorphs, since they possess significantly different melting points and heat capacities.[4]

At the glass transition point a distinct change in physical properties occurs from brittle to plastic. DSC measures heat flow which is proportional to sample heat capacity, this is useful, since a change in heat capacity occurs at the glass transition point. At temperatures below the glass transition point the heat capacity of an amorphous polymorph is slightly greater than that of the crystalline solid. Above the glass transition point the heat capacity is similar to that of the liquid.[1] Variation in the glass transition temperature of amorphous materials is possible, because the molecular volume is able to change, hence amorphous materials have a range of observed densities due to the differences in packing.[5]

### 3.2.1 Experimental method

A TA instruments STD Q-600 was used for thermal analysis of the samples. The temperature profile consisted of an isotherm of 15 minutes at 30°C, followed by a ramp to 260C at 10°C per minute and finally an isotherm of 10 minutes at 260°C. A sampling rate of 0.5 seconds was used along with a flow rate of 100 ml per minute of dry nitrogen. Open alumina 110 µL sample pans were used for both calibration and sample runs.

### 3.2.2 Mass calibration

The empty alumina pans were used as the zero mass standard and the 100 mg TA instruments standard weights. Both empty pans and 100 mg standards were run along the same experimental temperature profile.

### 3.2.3 Temperature calibration

Calibration of the sample cell temperature was carried out by determining the onset of melting for a series of standards, naphthalene, indium, zinc and tin. The onset of melting was used as this determines a single point at which melting starts see Figure 1.[6]

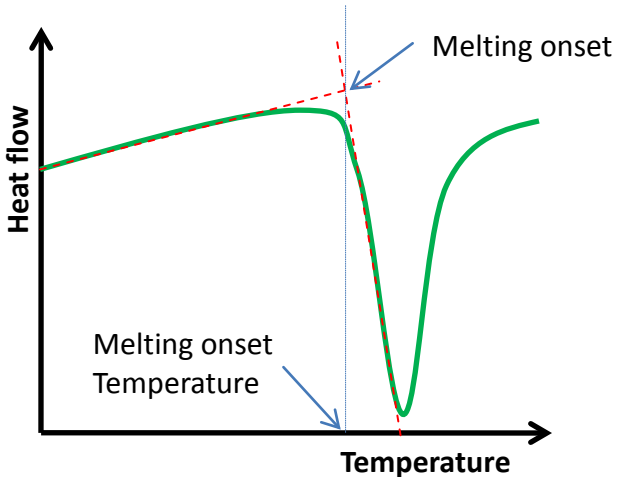


Figure 1 Melting point onset from brown [6]

### 3.2.4 Heat Capacity Calibration

A series of DSC runs need to be carried out using identical conditions of start and stop temperatures and heat up rate. A known mass of a material with a well-defined heat capacity (e.g. copper and α-aluminium oxide are two commonly used standards) are used in each of the calibration experiments. The DSC readings at any temperature within the calibration should produce a linear response to heat flow and the mass of the standard used. Unfortunately the intercept and slope values for this calibration measurement are not universal across the entire temperature range. Calculating the intercept and slope values at regular intervals across the entire temperature range used in the calibration allows polynomial functions to be fitted, allowing the calculation of the slope and intercept values for any temperature used in the calibration.[7]

The values of slope and intercept at a particular temperature allow the conversion of the instrument readings into an equivalent mass of standard material. These data can then, in turn, be converted into an equivalent heat capacity from tables for the standard.

## 3.3 Infra-red Spectroscopy

### 3.3.1 Introduction

Infra red spectroscopy has been shown to be a useful technique to differentiate between the crystalline polymorphs of lactose. The diagnostic region lies between 860 and 960 $cm^{-1}$[1,8] where a characteristic number of bands are observed for the anhydrous α and β forms as well as α lactose monohydrate

### 3.3.2 Experimental

The FT-IR spectra were collected using a Shimadzu FT-IR 8400. Measurements were made at a resolution of 1 $cm^{-1}$ with 32 scans, and a wavelength range of 4000 $cm^{-1}$ to 450 $cm^{-1}$ using a Specac Golden Gate Attenuated Total Reflectance (ATR) accessory.

A second spectrometer was also used, the Perkin Elmer Spectrum 100, again using Attenuated Total Reflectance (ATR) over a wavelength range of 4000 $cm^{-1}$ to 500 $cm^{-1}$, via 16 scans to produce a resolution of 1 $cm^{-1}$.

### 3.3.3 Dynamic vapour Sorption

Dynamic vapour sorption has been reported to be capable of determining amorphous lactose contents in samples containing both amorphous and crystalline lactose down to the minor component levels of 0.125%w/w.[9] The technique measures weight change for the reaction between amorphous lactose and water to form α-lactose monohydrate (a weight increase of 5.32%). The water for the reaction is provided by a dynamic humidifcation system ranging from 0 to 95% relative humidity which operates over a temperature range of 5 to 80 °C. [9]

DVS has also previously been used to examine a number of different active pharmaceutical ingredients. While the process is more complex for those materials which form hydrates and solvates, simple anhydrous compounds can be studied to give direct information about amorphous content. For example, amorphous salbutamol sulfate adsorbs water on to its surface until a crystallisation reaction occurs after which point all the moisture absorbed to facilitate the crystallisation process is immediately lost. This process occurs when salbutamol sulphate is exposed to relative humidities above 50% at 25 °C. The weight gain observed is then linearly proportional to the amorphous content.[10]

### 3.3.4 Calibration

The key components of this instrument are the balance and the humidity control system. The balance is simply calibrated using an empty pan and 100 mg F2 calibration weight (annually checked). The relative humidity system is calibrated using a saturated salt solution of a salt from Table 1. The relative humidity is set above the point listed in Table 1 and ramped down past the salts relative humidity and then back up.

| Salt solution | Relative humidity at 25 °C |
|---|---|
| LiCl | 11.3 % |
| $MgCl_2$ | 32.8 % |
| $Mg(NO_3)_2$ | 52.8 % |
| NaCl | 75.3 % |
| KCl | 84.3 % |

**Table 1 Relative humidities of saturated salt solutions**

Once these cycles have been completed, a plot of change in mass divided by change in relative humidity is plotted against time. This produces curves with turning points at the calibration point. The turning points are then mapped against the instruments vapour flow mass controller.[11]

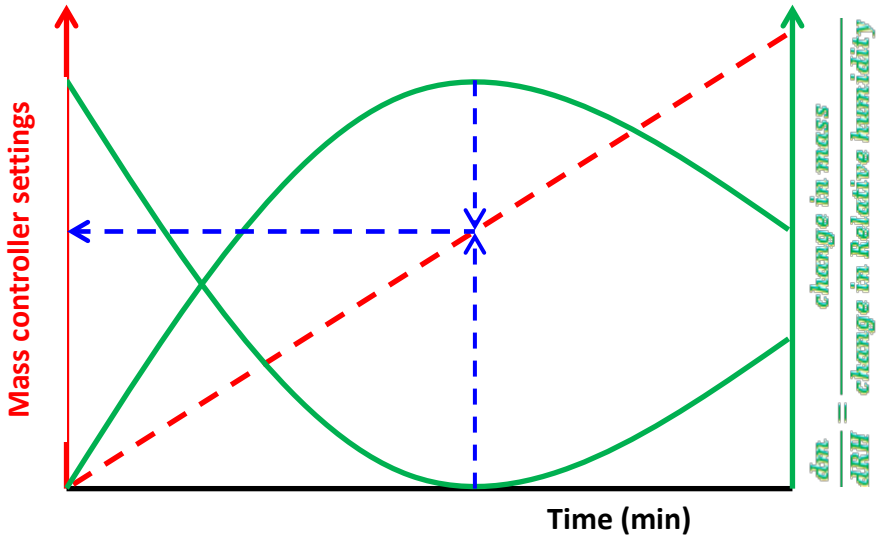


Figure 2 Relative humidity calibration[11]

### 3.3.5 Experimental method

The instrument used was a scientific and measurement systems DVS advantage 1. The temperature of the instrument was maintained at 25 °C and between 40 and 50 mg of sample was loaded onto a steel mesh pan. The humidity program was defined as a series of 10% steps increasing from 0 to 90% relative humidity and then returning back to 0%, followed by a repeat of the entire sequence see Figure 3. The sequence was only moved forward after a minimum of 15 minutes, and once the change in mass% per minute dropped to be below 0.002.

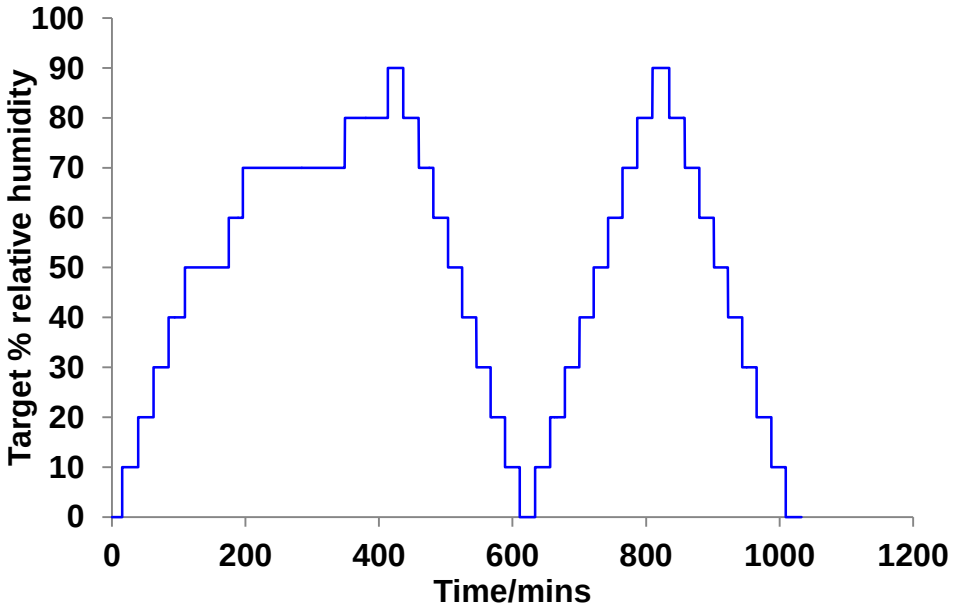


Figure 3 A typical DVS relative humidity ramp at 25 °C

## 3.4 Karl Fischer Coulometer

### 3.4.1 Introduction

Water acts as a plasticiser towards amorphous lactose, changing its properties by lowering the glass transition point.[3] Determination of moisture content in a sample of amorphous lactose provides a context for explaining its observed properties.

### 3.4.2 Calibration

Water content was measured using a Metrohm 684 Karl Fischer Coulometer using generator electrode without diaphragm and Hydranal-Coulomat AK reagent. A calibration curve was produced by titrating standards made from septum sealed, dimethylsulphoxide anhydrous (276855 Sigma-Aldrich) and de-ionised water.

The 5 ml serum vials were dried in an oven at 70 °C for 24 hours and then transferred hot into an argon glove box. Approximately 1ml of anhydrous dimethylsulphoxide was transferred in to the serum bottles by syringe and the vials weighed. Between zero and 0.11 ml of water were injected in to the serum vials, which were weighed once again. The instrument was prepared for titration and between 0.1 and 0.6 ml of calibration dimethylsulphoxide solution injected into the instrument titration cell.

### 3.4.3 Experimental method

Samples were prepared using serum vials and sealed in a similar manner to the calibration samples, placing lactose samples in to tarred vials and sealing them in the argon glove box. The sealed vials containing samples were taken out of the glove box and weighed. Approximately 1 ml of dimethylsulphoxide was then injected in to the vial and the lactose dissolved. Between 0.3 and 1 ml of sample were injected into the instrument cell for titration. Larger injection sizes were used for samples with low water content (less than 0.5%).

## 3.5 Powder X-ray Diffraction

### 3.5.1 Introduction

Powder X-ray diffraction (PXRD) was largely used for phase identification within this work. Crystalline materials reflect X-rays at particular angles that can show different relative intensities to one another, producing a pattern that is characteristic. This makes PXRD an excellent tool for identifying crystalline polymorphs of molecular crystals, (crystals whose molecules are arranged in ordered arrays and held together by week hydrogen bonds). By contrast the lack of long range order in amorphous lactose is observed in the X-ray powder diffraction pattern by the absence of any distinct peaks, and the presence of a diffuse halo seen Figure 4.[12]

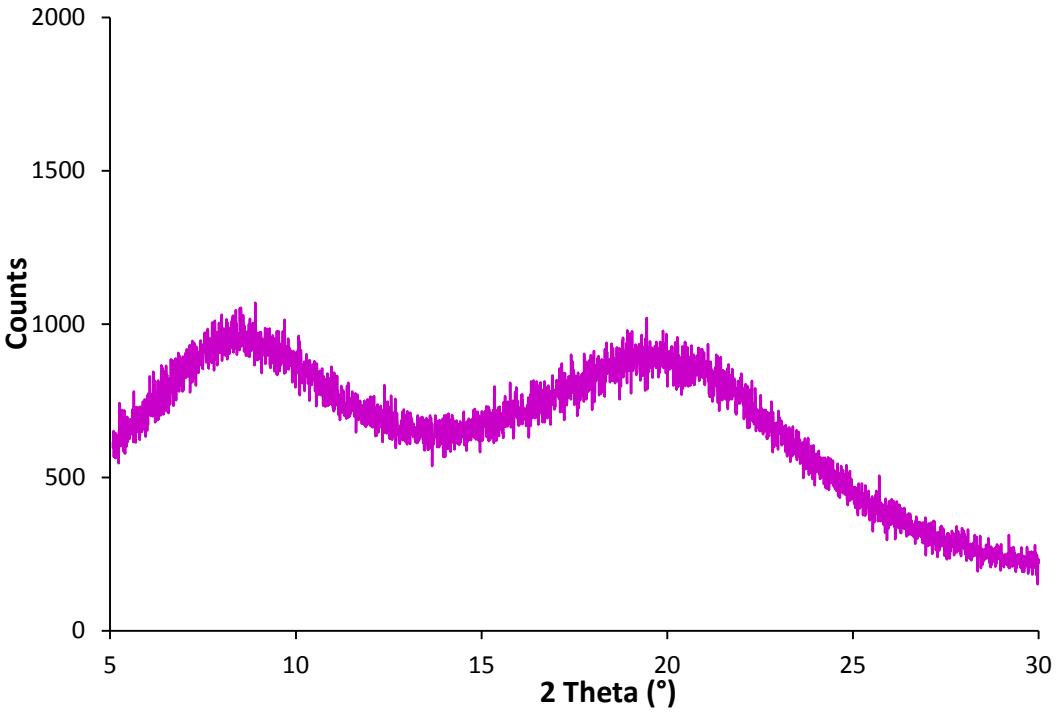


**Figure 4 Powder X-ray diffraction patterns for an amorphous lactose sample derived from rapidly quenching from a melt**

### 3.5.2 Experimental method

Powder diffraction patterns were recorded using a Bruker D8 Advance diffractometer, operating in Bragg-Brentano geometry, with an X-ray source of monochromated Cu $K\alpha_1$ at $\lambda = 1.5406$ Å and a position sensitive detector. The diffractometer $2\theta$ alignment was carried out using a glass slit and checked using a quartz standard. Typical patterns were collected over the $2\theta$ range 5–45°, using 0.014767° steps over a period of 45 minutes. Moisture sensitive samples were prepared in a glove box using perspex

holders (25 mm diameter with 1 mm depth), excess sample was removed using a microscope slide, and covered with a mylar film.

## 3.6 $^{13}C$–$^{1}H$ CP-MAS NMR

### 3.6.1 Introduction

Quantification of an amorphous and crystalline mixture of sugars can also be achieved by measurement of spin lattice relaxation times ($T_1$). This is the time taken for the nuclear spins to return to the equilibrium orientation after saturation. The $T_1$ times for a crystalline material are dramatically longer than for an amorphous material, since they have fewer relaxation pathways, due to their ordered crystalline arrangement. In terms of this thesis, reference materials were needed to define relaxation times for the crystalline lactose polymorphs and amorphous lactose.[13]

The Bruker Biospin 500 MHz spectrometer was used in two distinct ways, spectral characterisation and proton saturation recovery measurements of relaxation time. For both types of measurement samples were placed in 4 mm MAS BB $^{1}H$ probes and were spun at 10 kHz. All measurements were referenced to tetramethylsilane at 0 ppm and recorded over the range 318.63 to -30.11 ppm.

### 3.6.2 Spectral Characterisation

256 scans were taken to produce Free Induction Decay (FID) with 2 K data points over an acquisition time of 34 ms, a recycle delay of 240 s was employed before re-starting the pulse program. Fourier transform produced 32 K data points for each spectrum.

### 3.6.3 Proton Saturation Recovery Measurement of Relaxation Time

The pulse program for proton saturation recovery created a series of $^{1}H$ 180° radio frequency pulses a second apart as seen in Figure 5, the effect was to destroy the net magnetisation vector, hence its representation as a sphere in Figure 6b.

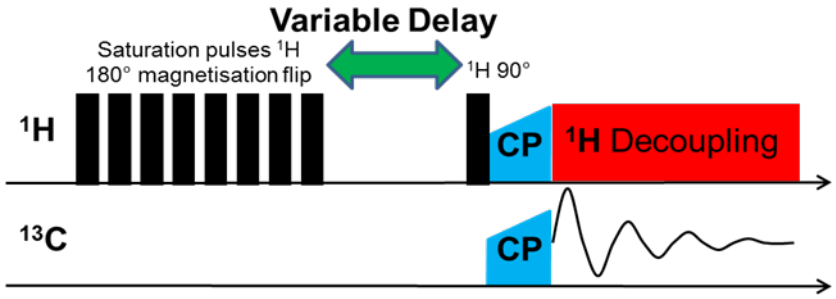


**Figure 5 Pulse sequence used in proton saturation recovery**

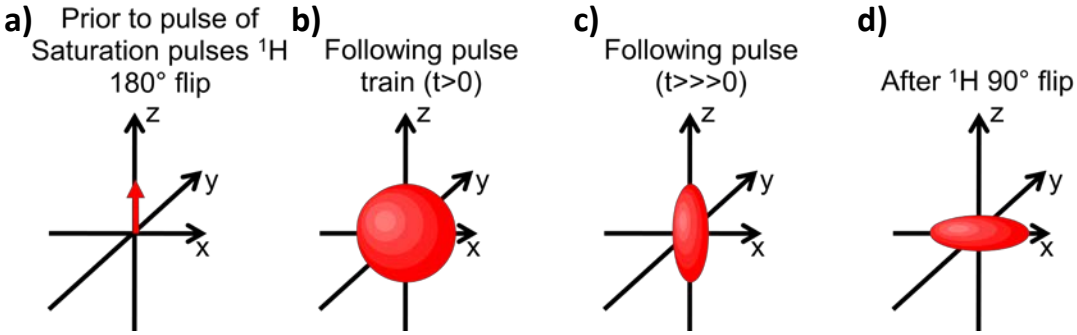


**Figure 6 Behaviour of the net magnetisation vector during radio frequency pulse sequence for proton saturation recovery**

Once the radio frequency pulse train ceased, the $^{1}H$ nuclei began to equilibrate and align with the magnetic field as seen in Figure 6. The time for this relaxation process to take place was then measured. A $^{1}H$ 90° radio frequency pulse moved the net magnetisation vector into the x'-y' plane, as seen in Figure 6c, immediately following the implementation of cross polarisation to transfer spin from the $^{1}H$ to the $^{13}C$ nuclei. After these processes, the FID signal acquisition took place. The advantage of proton saturation recovery was that there was no need to wait between FID and the next train of $^{1}H$ 180° pulses, making proton saturation recovery a relatively rapid technique by solid state NMR standards. For each sample relaxation delays of 2, 4, 10, 15, 20, 25, 30 and 60 seconds were applied. In a similar way to the standard spectral acquisition program, 256 scans were collect to produce FIDs with 2000 data points and the Fourier transform taken to produce 32 K data points for each spectrum.

***References***

1 R. Zallen, *Richard Zallen. The physics of amorphous solids. New York ; Chichester : Wiley, 1998.*, Wiley, Chichester, 1998.

2 C. Gustafsson, H. Lennholm, T. Iversen and C. Nyström, *International Journal of Pharmaceutics,* 1998, **174**, 243-252 (DOI:DOI: 10.1016/S0378-5173(98)00272-5).

3 D. Q. M. Craig and M. Reading, *Thermal analysis of pharmaceuticals*, CRC distributor; Taylor & Francis, New York; London, 2006.

4 S. Garnier, S. Petit, F. Mallet, M. -. Petit, D. Lemarchand, S. Coste, J. Lefebvre and G. Coquerel, *International Journal of Pharmaceutics,* 2008, **361**, 131-140.

5 S. R. Elliott, *Physics of amorphous materials (Second Edition)*, Longman Scientific & Technical, Harlow, 1990.

6 M. E. Brown, *Introduction to thermal analysis : techniques and applications*, Kluwer Academic Publishers, Boston, 2001.

7 P. J. Haines, *Principles of thermal analysis and calorimetry*, The Royal Society of Chemistry, Cambridge, 2002.

8 J. H. Kirk, S. E. Dann and C. G. Blatchford, *International Journal of Pharmaceutics,* 2007, **334**, 103-114.

9 G. Buckton and P. Darcy, *International Journal of Pharmaceutics,* 1995, **123**, 265-271.

10 M. Gorny, M. Jakobs, V. Mykhaylova and N. A. Urbanetz, *Drug Developement and Industrial Pharmacy,* 2007, **33**, 235-243 (DOI:10.1080/03639040601128647).

11 H. Nyqvist, *Calibration of relative humidity via gravimetric analysis of saturated salt solutions*, *Int. J. Pharm. Tech. & Prod. Mfr.,* 1983, **4**, 47.

12 S. E. Dann, *Reactions and characterization of solids*, Royal Society of Chemistry, Cambridge, 2000.

13 D. Le Botlan, F. Casseron and F. Lantier, *Analusis,* 1998, **26**, 198-204 (DOI:10.1051/analusis:1998135).

# CHAPTER 4

# Quantifying amorphous lactose using $^{13}$C CP MAS NMR

## 4.1 Introduction

The $^{13}$C CP MAS NMR spectra of α-lactose monohydrate and amorphous lactose show significant differences, despite showing resonances at similar chemical shifts. Since the identification and quantification of amorphous material is important for long term stability of drugs using lactose as an excipient, it seemed advantageous to investigate whether NMR could be used as a medium to discern between crystalline and amorphous materials. This chapter is an exploratory study into using key NMR parameters in a discerning way to actively discriminate between crystalline and amorphous lactose.

Figure 1 shows the spectra of amorphous lactose generated by rapidly quenching a melt and the four crystalline polymorphs of lactose characterised by Kirk.[1] The spectrum of amorphous lactose shows some similarities e.g. the broad resonance at 75 ppm seen in all the crystalline spectra and some differences e.g. the resonance at 94 ppm does not match exactly to any of the peaks in the polymorphs, but all the α forms show resonance between 91 and 93 ppm.

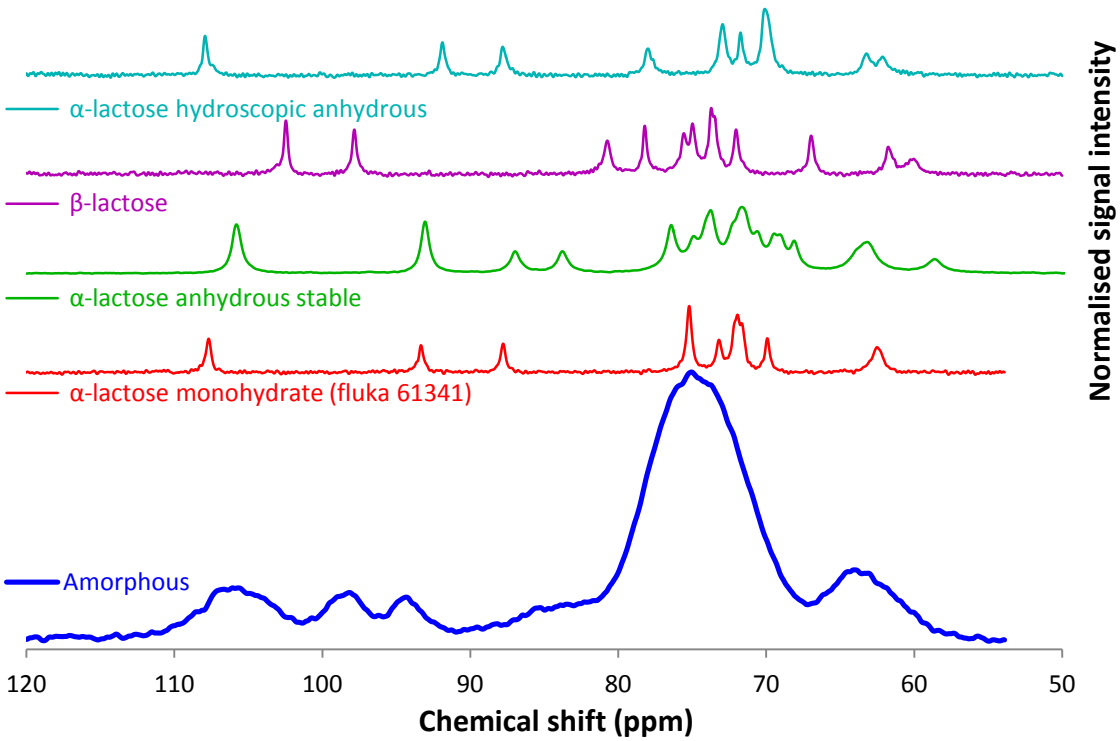


**Figure 1 solid state $^{13}$C CP MAS NMR of amorphous lactose and crystalline polymorphs**

To quantify components in a mixture, differentiating between the spectra is necessary. The similarities of the chemical shifts in spectra seen in Figure 1 rule out measuring relative peak intensities as a method of quantifying components in a mixture of lactose

phases. However, relaxation times can be used to distinguish between the crystalline and amorphous phases, since amorphous materials possess much shorter relaxation times than their crystalline equivalents. Therefore an opportunity therefore exists to select a suitable relaxation delay time which favours the detection of the signal from an amorphous material and at the same time reduces the signal from any crystalline material.

### 4.1.1 Relaxation in solids

Amorphous materials lack long range order and can be thought of as frozen liquids although vibrations still occur.[2] This means that nuclei are exposed to a variety of different magnetic environments from neighbouring atoms. Individual nuclei in crystalline solids have ordered regular structures so individual nuclei are situated near to specific atoms at set distances. This means that there is a much more limited set of magnetic environments. In contrast a greater variety of magnetic environments exist in amorphous materials, creating more opportunities for the transfer of spin energy, so spin lattice relaxation times are much smaller than for ordered crystalline materials.[3]

Spin lattice relaxation times are measured by recording the peak heights or intensities $I$, which follow Equation 1, where $\tau$ is the relaxation delay after the excitation radio frequency pulse. The critical values to this relationship are $I_0$, the maximum peak height intensity immediately following the pulse, and $T_1$, the spin lattice relaxation time. The value of $I_0$ can be determined from the peak height for long relaxation delays of approximately 6 times the value of $T_1$. The value of $T_1$ is found by fitting experimental data to Equation 1.[4]

$$I = I_0\left[1 - exp\left(-\frac{\tau}{T_1}\right)\right] \qquad \text{Equation 1}$$

## 4.2 Experimental

### 4.2.1 Preparation of standards

α-lactose monohydrate (Fluka 61341) was used as the 100% crystalline standard and the starting material for the preparation of the amorphous lactose. The amorphous standard was prepared by melting 5.00 g of α-lactose monohydrate in a nickel crucible in the open atmosphere. As the solid become liquid it was stirred using a spatula for 1 minute to ensure the entire mass became molten. The crucible was then plunged into

liquid nitrogen and transferred to an argon filled glove box, where it was crushed in a mortar and pestle to a powder. The rapidly quenched melt was used as the amorphous standard for further work, and the characteristics of the two materials were then carried using a variety of methods.

### 4.2.2 Characterisation of standards

Kirk[5] produced reference tables to identify α-lactose monohydrate using infra red spectroscopy and powder X-ray diffraction. The infra-red spectrum of amorphous lactose and α-lactose monohydrate are shown in Figure 2 along with the other crystalline polymorphs. The peak at 1595 cm$^{-1}$ for water appears in the α-lactose monohydrate spectrum, but is absent in the amorphous spectrum suggesting water is not present in the amorphous sample.

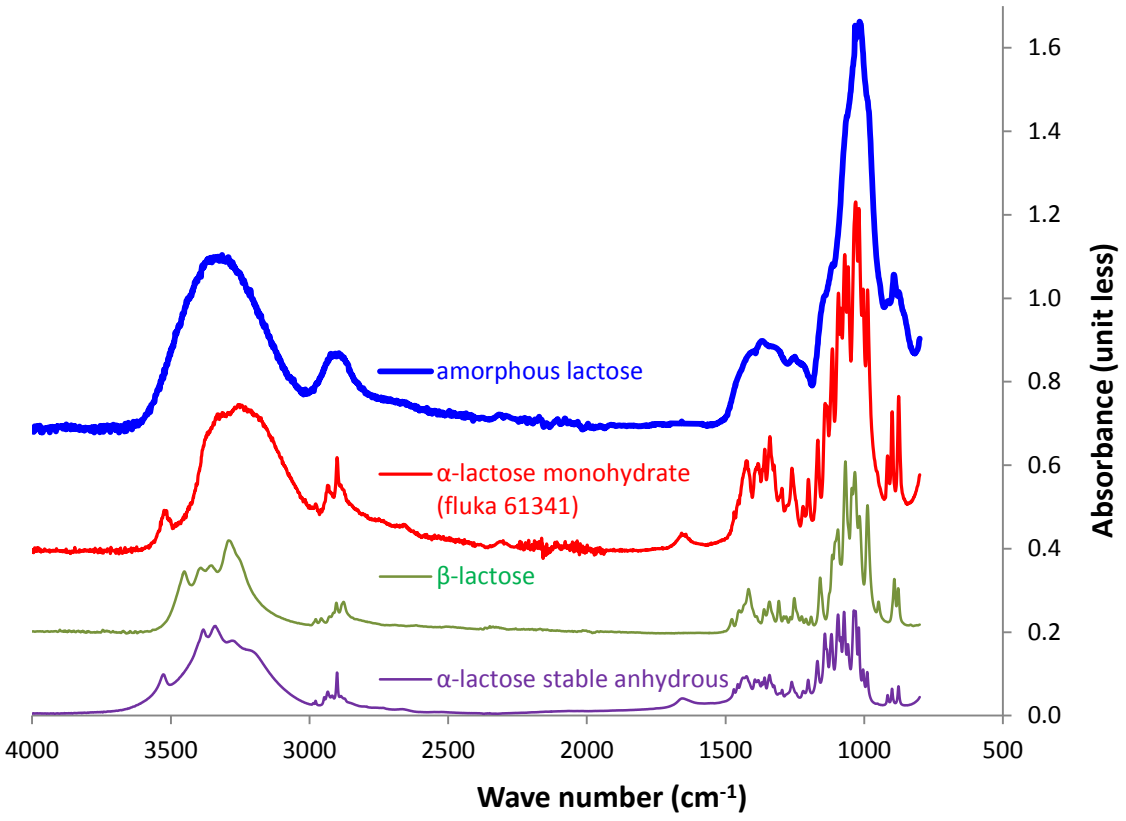


**Figure 2 FT-IR of Amorphous lactose sample along with the crystalline polymorphs (frequency range 4000-750 cm$^{-1}$)**

Figure 2 shows the spectrum of the amorphous sugar to consist of broad peaks, whereas the crystalline α-lactose monohydrate shows characteristic sharp peaks at 916, 899 and 876 cm$^{-1}$ as reported by Kirk et al[1]. An expansion of this diagnostic region is marked out in Figure 3 with dotted red lines. The absorbances in the region

between 860 and 960 cm$^{-1}$ of the amorphous lactose do not appear to correspond to the spectrum of any single phase crystalline polymorph.

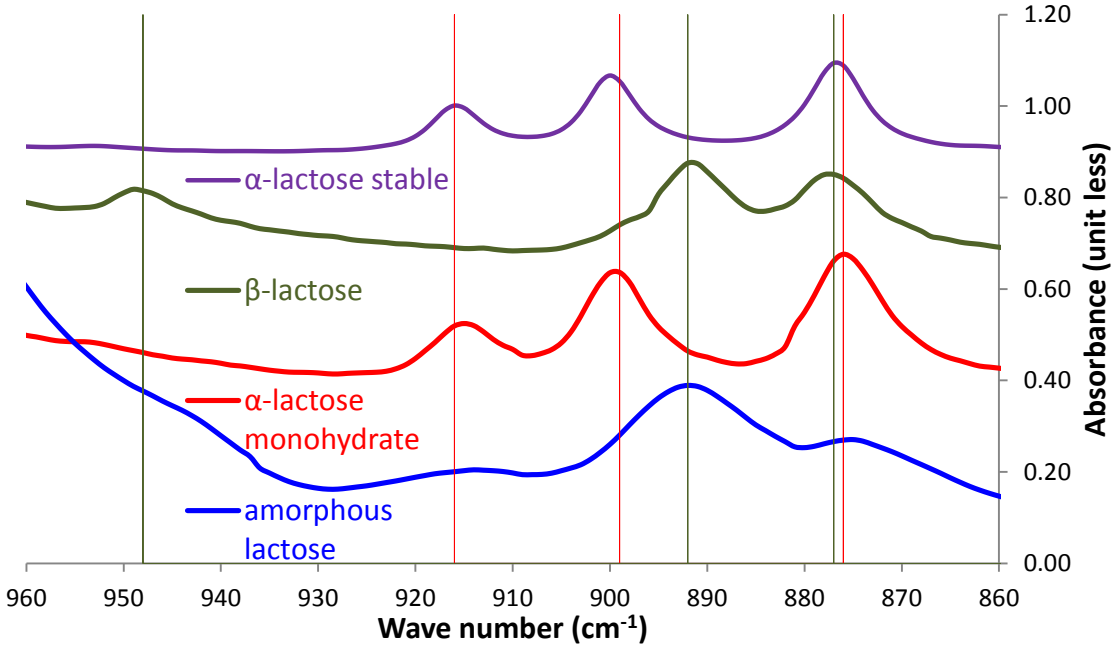


**Figure 3 FT-IR of Amorphous lactose sample and crystalline polymorphs (frequency range 940-860 cm$^{-1}$)**

The characteristic 2θ positions of reflections for the powder X-ray diffraction pattern of α-lactose monohydrate as defined by Kirk[1] are marked in red dotted lines on Figure 4. The match between the pattern of the starting material and the values proposed by Kirk is consistent with the identification of the starting material as α-lactose monohydrate. In Figure 4 the amorphous lactose can be seen to produce a broad halo, with no distinctive reflections as expected for an amorphous material.[6]

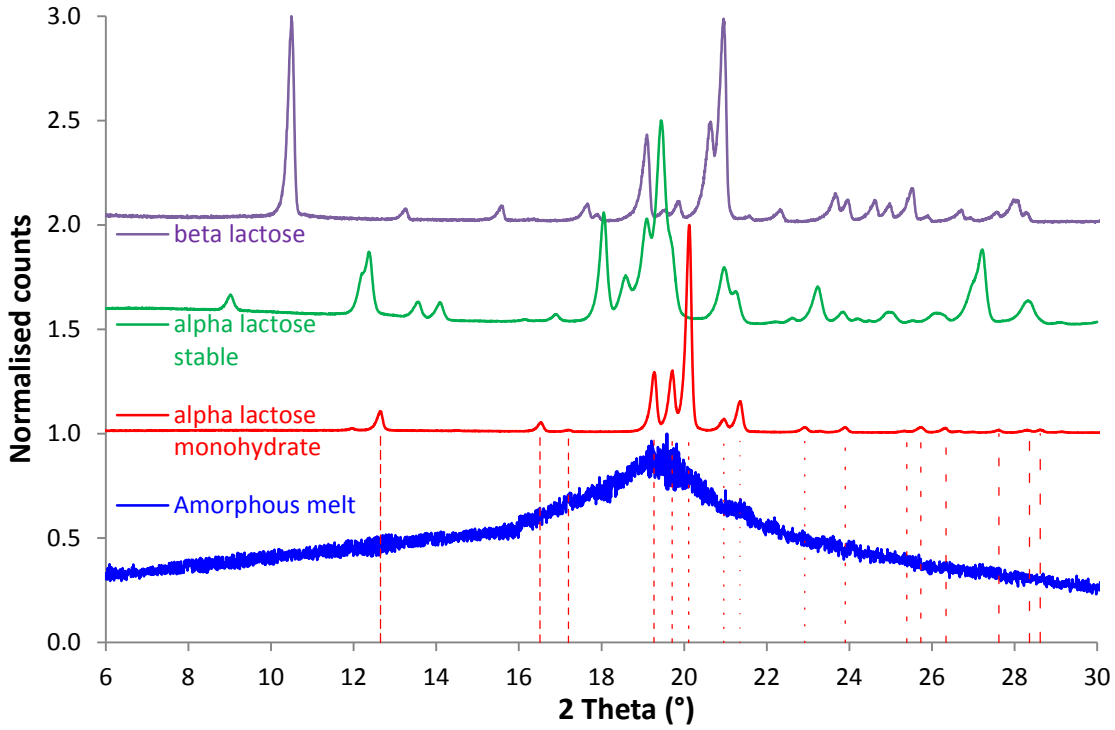


**Figure 4 Comparison of powder X-ray diffraction patterns of amorphous lactose and crystalline polymorphs with red reference lines for α-lactose monohydrate**

Figure 5 displays the DSC traces for crystalline α-lactose monohydrate and amorphous lactose. The crystalline α-lactose monohydrate shows a decomposition event 120 to 150 °C with a weight loss consistent with the loss of water and fusion onset occurring at 209.2°C. The amorphous lactose shows a glass transition onset at 106.9 °C which would normally be expected at about 100 to 120 °C[7]. The presence of a glass transition point is a positive indication that the melt prepared material is amorphous, the powder X-ray diffraction, FT-IR and $^{13}$C solid state NMR are consistent with this observation.

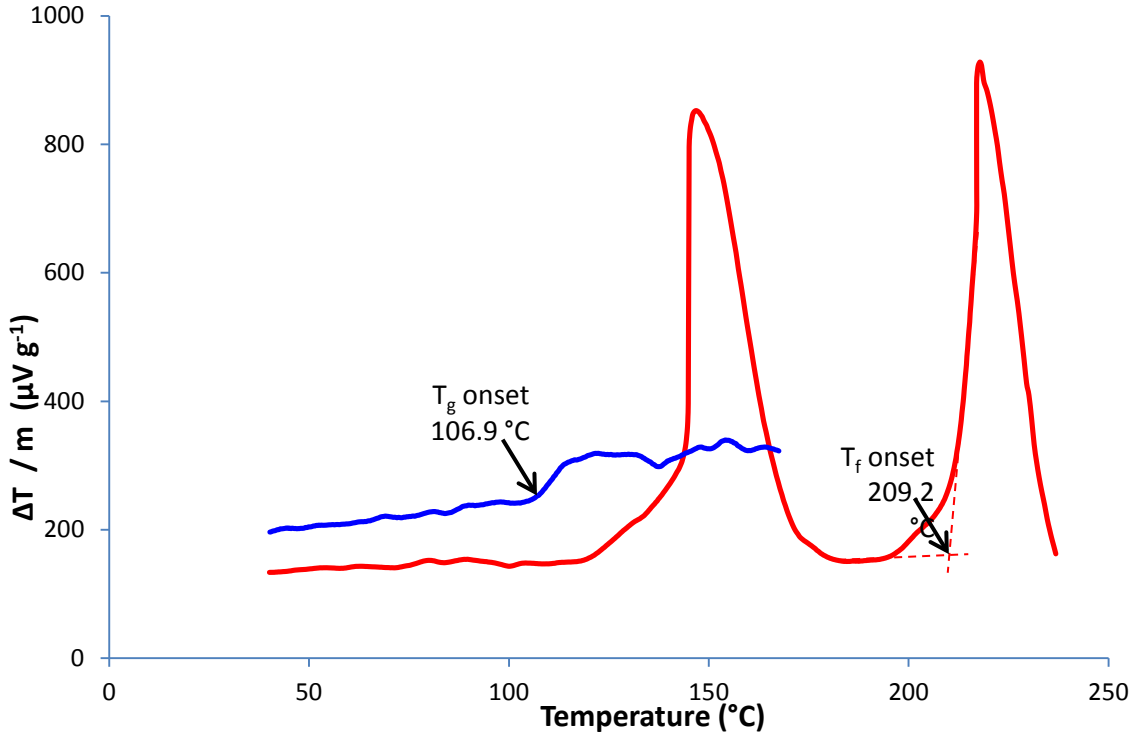


**Figure 5 DSC of amorphous lactose (blue) and α-lactose monohydrate (red).**

The $^{13}$C CP MAS NMR spectra of α-lactose monohydrate and amorphous lactose are displayed in Figure 1. The peak table and integrations for the CP MAS NMR of α-lactose monohydrate was proposed by Earl et al[8] and can be seen in Table 1. The measured values from Figure 1 are shown in Table 2.

| Carbon atom | Chemical (shift ppm) | Approximate Integral |
|---|---|---|
| C-1' (Gal) | 107.6 | 1 |
| C-1 (Glc) | 93.4 | 1 |
| C-4 (Glc) | 87.5 | 1 |
| C-2'-C-5' (Gal) and C-2, C-3, C-5 (Glc) | 68 - 78 | 7 |
| C-6 and C-6' | 62.8 | 2 |

**Table 1 Assignment of carbon atoms in α-lactose monohydrate by Earl[8]**

| Measured chemical shift | Approximate Integral |
|---|---|
| 107.7 | 1 |
| 93.3 | 1 |
| 87.8 | 1 |
| 75.2 | 2 |
| 73.2 | 1 |
| 71.9 | 3 |
| 69.9 | 1 |
| 62.5 | 2 |

**Table 2 Measured peak integrations of α-lactose monohydrate with 60 seconds relaxation delay[8]**

Chemical shifts are normally quoted relative to tetramethylsilane at 0 ppm, although solid state $^{13}$C CP MAS NMR typically uses a solid adamantane standard rather than the liquid tetramethylsilane to determine this point.

### 4.2.3 Preparation of mixtures

A set of six mixtures were prepared from amorphous lactose and crystalline α-lactose monohydrate. The mixtures were measured by weight and mixed in sample vials by stirring with a spatula and repeatedly inverting the sealed sample vial for 10 minutes.

| | | | | | | |
|---|---|---|---|---|---|---|
| Amorphous content | 100.00% | 52.06 % | 15.04 % | 5.66 % | 1.16 % | 0.00 % |
| Crystalline content | 0.00% | 47.94% | 84.96% | 94.34% | 98.84% | 100.00% |

Table 3 Mixture ratio of crystalline α-lactose monohydrate and amorphous lactose

## 4.3 Results

### 4.3.1 Estimating Relaxation Time

The six mixtures were examined using the proton saturation recovery method set out in chapter 3 section 5. A total of forty two spectra were recorded, 8 spectra for each mixture with a different relaxation delay. The spectra of the 100% crystalline α-lactose monohydrate are shown in Figure 6. The peak heights at 75 ppm show a progressive increase for the longer delays from 20 to 60 seconds.

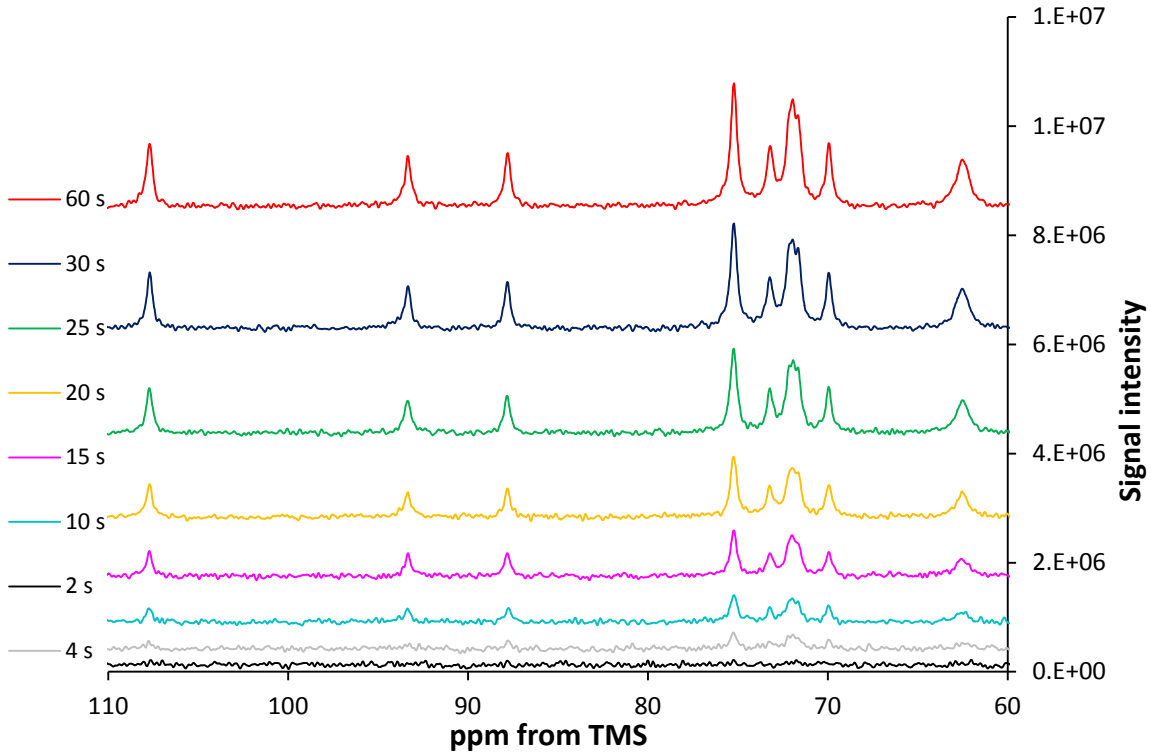


Figure 6 Spectra of α-lactose monohydrate fluka 61341 with relaxation delays up to 60 s

The natural log values of the α-lactose monohydrate peak heights were plotted against the inverse of relaxation delay time in Figure 7. The intercept on the y axis provides an

estimate of the log of the $I_0$ value in Equation 1 (of this chapter) and the slope provides an estimate of the relaxation time $T_1$ once multiplied by a factor of 2.

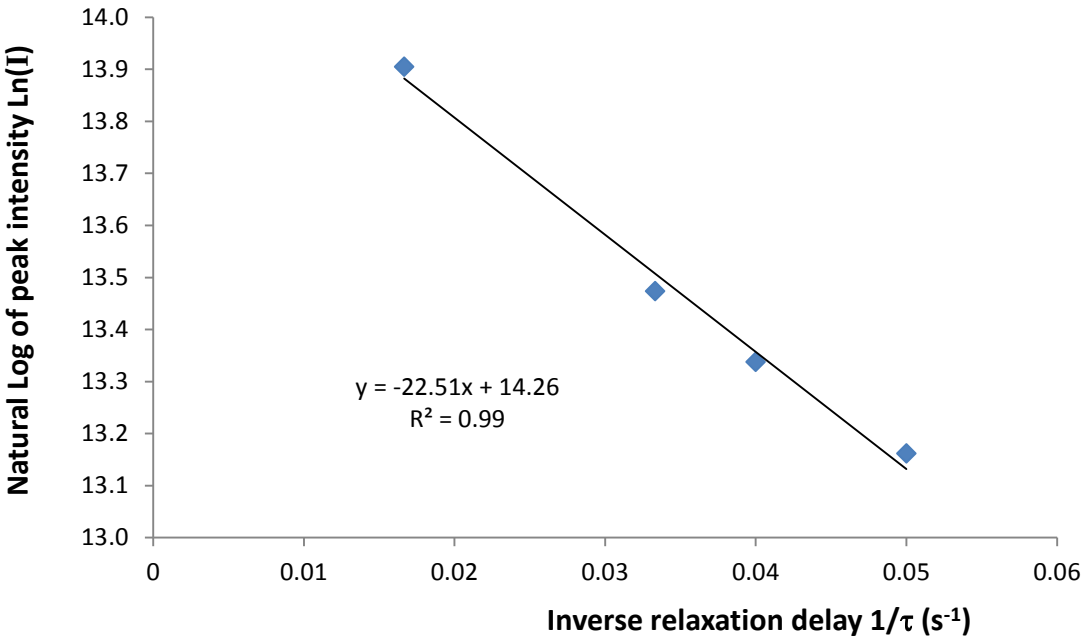


Figure 7 Plotting the natural log of peak intensity against the inverse of relaxation delay for 100% crystalline α-lactose monohydrate up to 60 s

The uncertainty in the relaxation time was calculated from the standard error for difference between each point and the straight line using Equation 2. The variable $\hat{y}_i$ seen in Equation 2 was the estimated y value calculated from the linear regression slope and intercept, the $y_i$ variable denotes the actual y value for a particular point. The standard error $s_b$ in the slope and ultimately the error in the relaxation time, was estimated using Equation 3, where $\hat{x}_i$ variable represented the average of the $x$ coordinates. The standard error $s_a$ in the intercept was calculated using Equation 4.

$$s_{y/x} = \sqrt{\frac{\sum_i (y_i - \hat{y}_i)^2}{n-2}} \qquad \textbf{Equation 2}$$

$$s_b = \frac{s_{y/x}}{\sqrt{\sum_i (x_i - \hat{x}_i)^2}} \qquad \textbf{Equation 3}$$

$$s_a = s_{y/x}\sqrt{\frac{\sum_i x_i^2}{n\sum_i (x_i - \hat{x}_i)^2}} \qquad \textbf{Equation 4}$$

The simplest check on the $T_1$ and $I_0$ values obtained from this process is simply to produce a curve Equation 1 using the estimated values. This was carried out for the α-lactose monohydrate crystalline results using values of $T_1 = 45.0$ and $I_0 = 1560000$ which is seen in Figure 8 as a red dotted line.

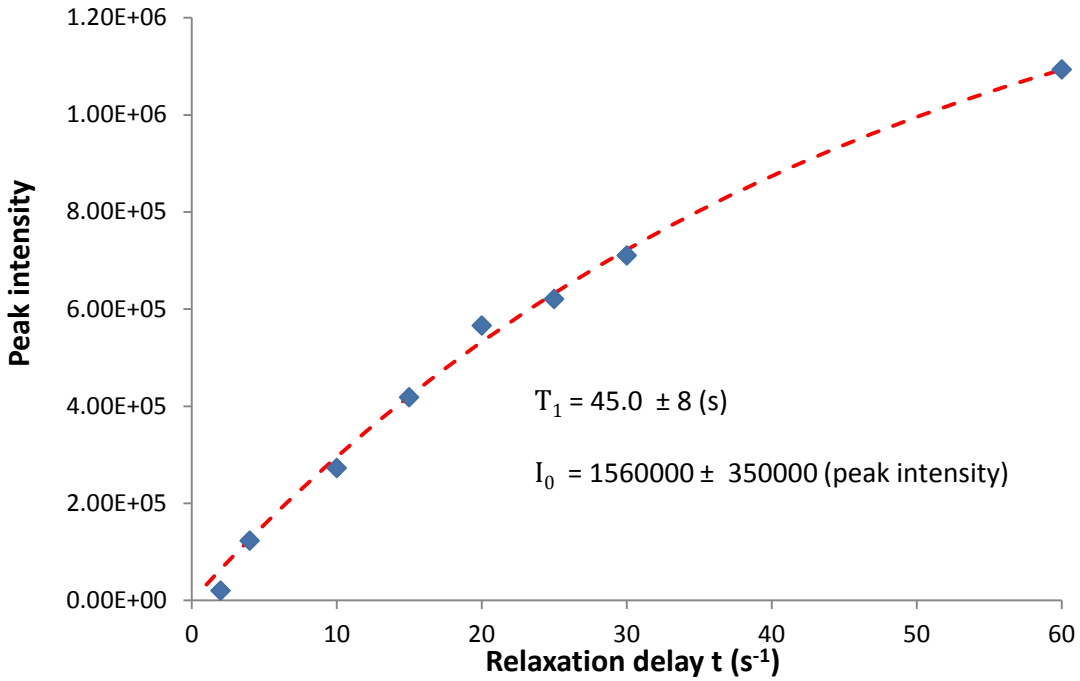


**Figure 8 Fitting maximum peak intensities to relaxation delay times using the values of $T_1$ = 45.9 and $I_0$ = 1560000 for 100% crystalline α-lactose monohydrate**

The spectra of the 100% amorphous lactose relaxation delays are shown in Figure 9. The peak heights at 75 ppm are very similar for delays of 25, 30 and 60 seconds suggesting the value of $T_1$ is much shorter for the amorphous sample compared with the crystalline α-lactose monohydrate.

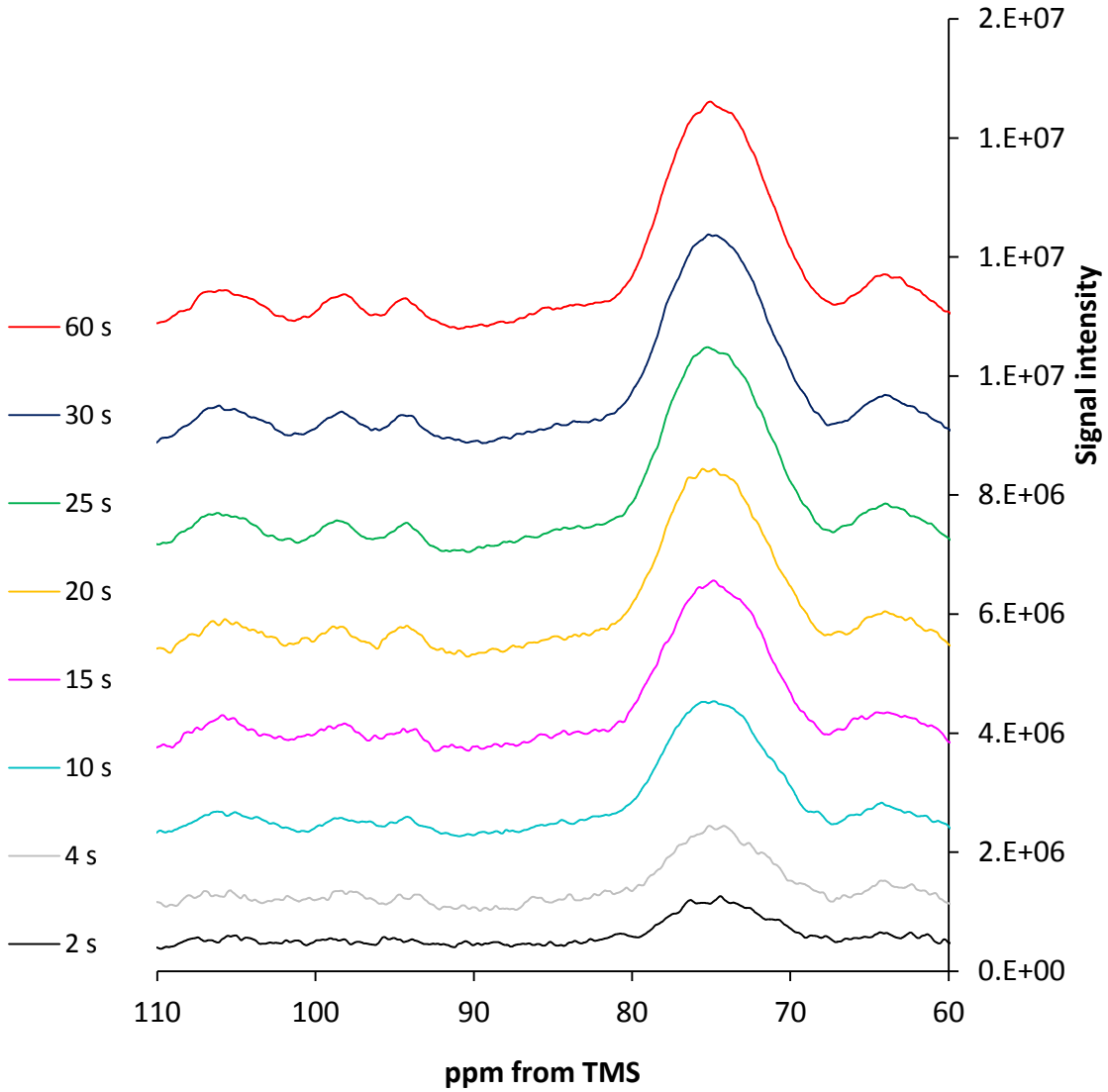


**Figure 9 Spectra of amorphous lactose for all relaxation delays**

The relaxation time of the amorphous sample can be calculated in an identical manner to the crystalline by identifying the line of best fit line to a plot of natural log of peak intensity against the inverse of relaxation delay, which can be seen in Figure 10. The values estimated for $T_1$ and $I_0$ w can again be tested by substituting their values into Equation 1 to calculate the red dotted line seen in Figure 11 along with the experimental values. This whole process was repeated for all the amorphous and crystalline mixtures set out in Table 3, the $T_1$ values obtained can be seen in Table 4.

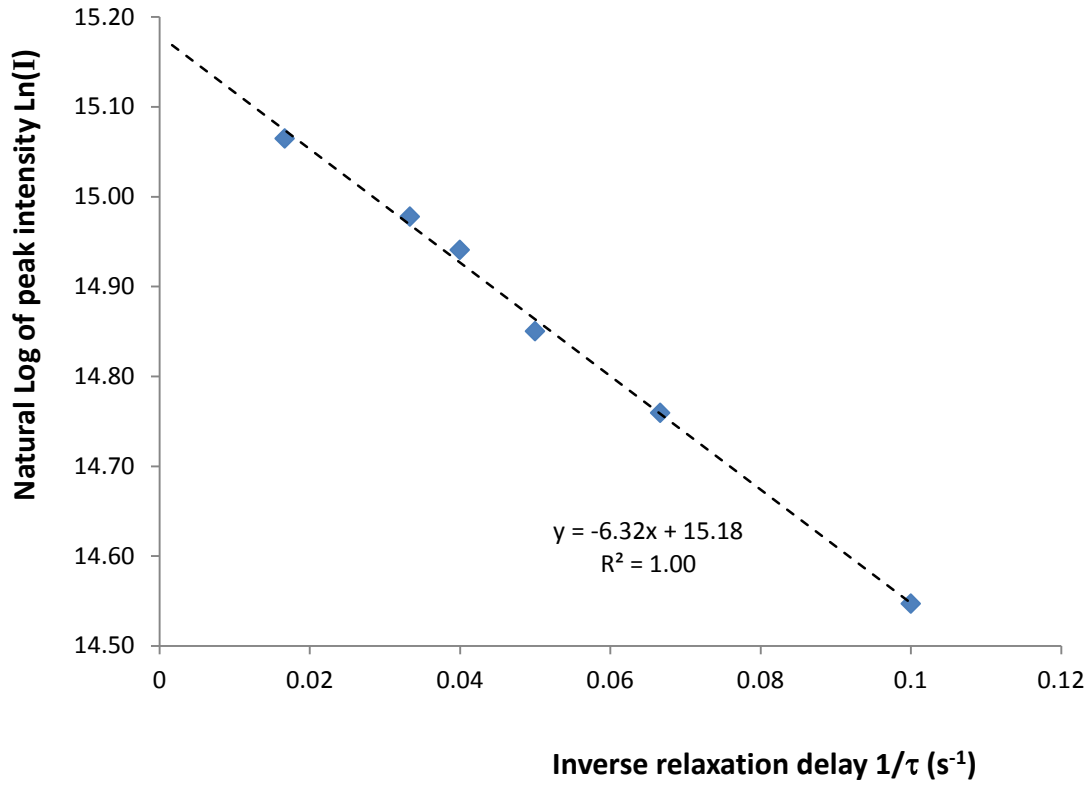


**Figure 10 Plotting the natural log of peak intensity against the inverse of relaxation delay for 100% amorphous lactose up to 60 s**

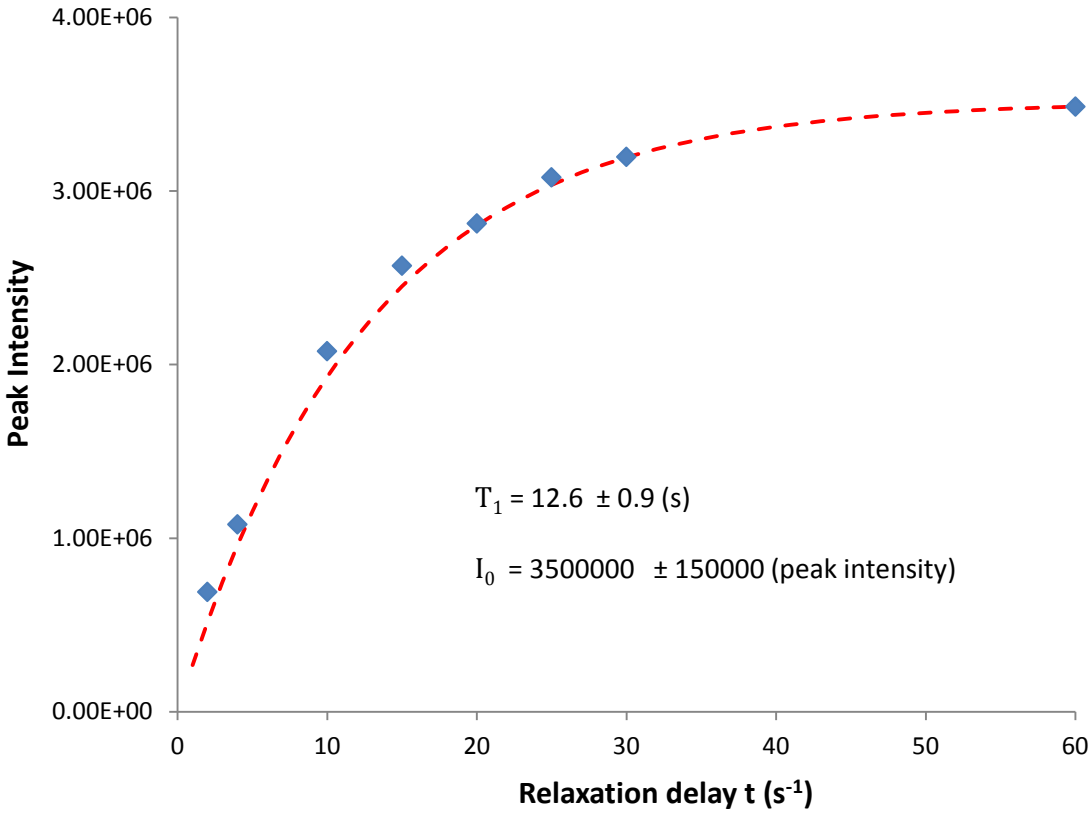


**Figure 11 Fitting maximum peak intensities to relaxation delay times using the values of $T_1$ = 12.6 and $I_0$ = 3500000 for 100% amorphous lactose**

## 4.4 Discussion

### 4.4.1 Using measured relaxation times to identify amorphous content

The resonance at 75 ppm appears in the spectra of amorphous lactose and crystalline polymorphs (refer back to Figure 1). This offers an opportunity to measure relaxation delays at the same resonance for amorphous crystalline mixtures. The $T_1$ value for the mixtures were estimated by fitting the peak heights at different relaxation delays identically to Figure 7 and Figure 10. This data can be used to estimate amorphous content by measuring $T_1$ of an unknown mixture and solving Equation 5.[3]

$$\frac{1}{T_{1m}} = \frac{(1-\mathrm{a})}{\mathrm{T_{1c}}} + \frac{\mathrm{a}}{\mathrm{T_{1a}}} \qquad \text{Equation 5}$$

Where $T_{1m}$ is the relaxation time for a mixture, $T_{1c}$ is relaxation time for the pure crystalline material, $T_{1a}$ is the relaxation time for the pure amorphous material and $a$ is the fractional amorphous content. Table 4 shows the $T_1$ estimates made using an identical process that were previously described in the experimental and results sections of this chapter. The uncertainty in these results is also estimated to the 95% confidence interval. The fourth column of Table 4 gives an estimate of Le Botlan's $T_{1m}$ using Equation 5, for amorphous content were $T_{1c} = 48.9$ and $T_{1a} = 12.4$.

| Amorphous content % (w/w) | Relaxation time $T_1$ (s) | 95% confidence limits - $T_1$ (s) | Le Botlan estimate $T_{1m}$ (s) |
|---|---|---|---|
| 0.00 | 49.2 | ± 13.1 | 48.9 |
| 1.20 | 45.9 | ± 18.3 | 47.2 |
| 5.70 | 43.3 | ± 12.7 | 41.9 |
| 15.00 | 35.7 | ± 7.5 | 33.9 |
| 52.10 | 18.2 | ± 3.3 | 19.3 |
| 100.00 | 12.6 | ± 0.9 | 12.4 |

Best fit crystalline $T_{1c}$ = 48.9 s

Best fit amorphous $T_{1a}$ = 12.4 s

**Table 4 Estimating amorphous content and relaxation time $T_1$ using Le Botlan equation**

The uncertainty in these results is much larger towards the lower amorphous contents, which is where most interest lies, since a small amount of amorphous content can have a profound effect on surface energies. The plot of $T_1$ relaxation times against amorphous content can be seen in Figure 12 along with the error bars and Le Botlan estimate for $T_{1m}$ as the red dotted line.

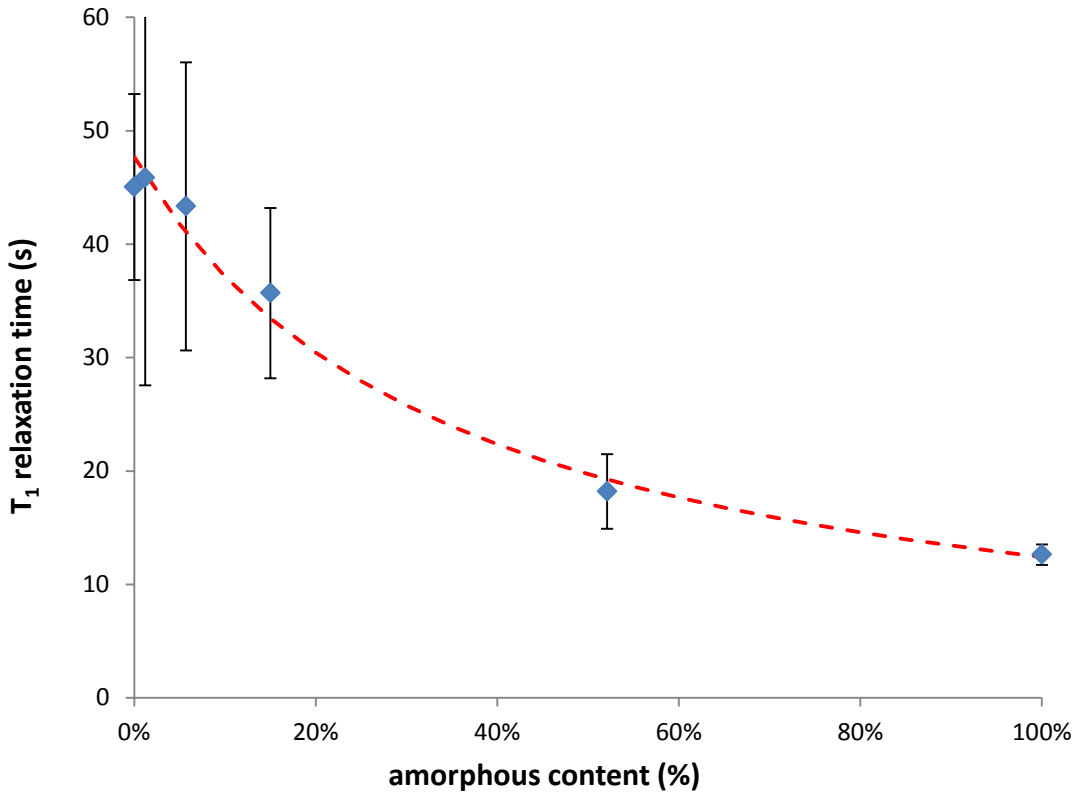


**Figure 12 Comparing mixtures of amorphous and crystalline α-lactose monohydrate relaxation times with error bars for the 95% confidence limits against amorphous content. A fit to the Le Botlan equation is attempted using the red dotted line.**

Figure 12 demonstrates the large errors in estimating amorphous content in an unknown mixture. Unfortunately this approach suggested that it was unlikely to produce useful results. To improve on this, more experimental work was required or a change in the way data was processed. $^{13}$C CP MAS NMR requires an expensive instrument, so the prospect of using longer relaxation delays and gathering improved data was not desirable, so an alternative data processing method was sought.

### 4.4.2 Partial Least Squares Regression

The short relaxation times of amorphous materials versus the long times of crystalline polymorphs offer an opportunity to differentiate the amorphous signal from a mixture. Figure 13 shows the normalised spectra for the amorphous and crystalline standards with a relaxation delay of only 2 seconds. The spectrum of the amorphous standard can be clearly seen whereas the crystalline standard has produced only noise. The ability to recognise the amorphous spectrum against noise and the crystalline component can be achieved by Partial Least Squares Regression (PLS).

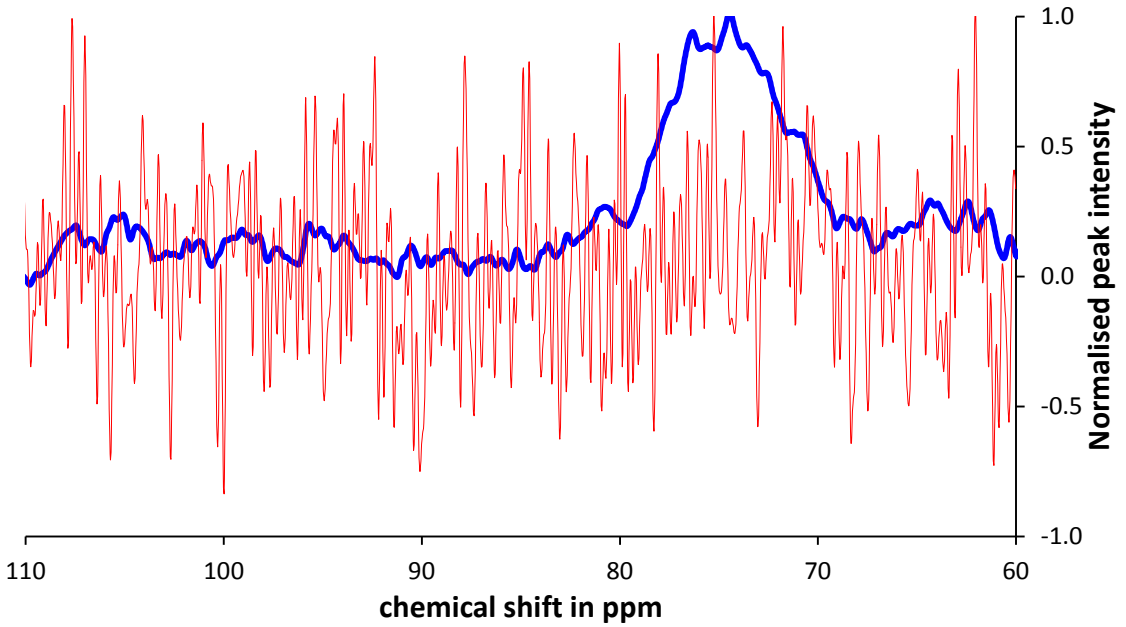


**Figure 13 $^{13}$C nmr spectra taken with 2 seconds relaxation delay using proton saturation recovery . 100% amorphous lactose sample (red), 100% crystalline α lactose monohydrate (blue)**

PLS has previously been applied to quantification of amorphous content in crystalline α lactose monohydrate by Gustafsson, however the selected relaxation delay time may enhance the accuracy and precision.[10] The determination of relaxation delay times for amorphous crystalline mixtures and pure standards also offers a means of confirmation using the Le Botlan equation as shown in Table 4.

The partial least squares method produces a single value for the amorphous content (response value) by matrix multiplication between a model and the normalised intensity of each spectral point. To prepare the partial least squares model; all spectra had to be baseline corrected for any slope, normalised to maximum peak height and manually phased so that peak maxima were coincident.[11]

The model was prepared using the XLSTAT macro within Microsoft Excel 2007.[9, 12] The inputs to each model were the percentage weight composition of the amorphous lactose and crystalline α lactose monohydrate for each mixture, along with the normalised intensity across the chemical shifts from 55 to 110 ppm (2817 spectral points).

The models were tested by comparing the percentage of amorphous lactose present in all six of the mixtures and the predicted values produced by processing the individual spectra. The linearity of predicted response against actual percentage weight

amorphous lactose can be seen in Table 5. In all cases the slope was equal to 1.000 and the $r^2$ to 1.000 indicating excellent linearity.

| Amorphous weight in mix (% w/w) | Relaxation delay | | | | | | | |
|---|---|---|---|---|---|---|---|---|
| | 2 | 4 | 10 | 15 | 20 | 25 | 30 | 60 |
| 100.00 | 100.00 | 100.00 | 100.00 | 100.00 | 99.99 | 100.02 | 100.04 | 99.93 |
| 52.06 | 52.10 | 52.05 | 52.06 | 52.07 | 52.06 | 52.08 | 52.04 | 52.18 |
| 15.04 | 14.92 | 15.11 | 15.09 | 15.02 | 15.07 | 14.83 | 14.83 | 15.18 |
| 5.66 | 5.70 | 5.49 | 5.60 | 5.63 | 5.75 | 5.67 | 5.66 | 5.49 |
| 1.16 | 1.22 | 1.27 | 1.17 | 1.20 | 1.04 | 1.34 | 1.40 | 1.13 |
| 0.00 | 0.00 | 0.00 | 0.00 | 0.00 | 0.01 | 0.00 | 0.00 | 0.00 |
| Slope | 1.0000 | 1.0000 | 1.0000 | 1.0000 | 1.0000 | 1.0000 | 1.0000 | 1.0000 |
| Intercept | 0.0008 | 0.0012 | 0.0004 | 0.0003 | 0.0009 | 0.0016 | 0.0022 | 0.0014 |
| Pearson's $r^2$ | 1.0000 | 1.0000 | 1.0000 | 1.0000 | 1.0000 | 1.0000 | 1.0000 | 1.0000 |

**Table 5 Linear regression statistics for model response output for each relaxation delay**

Techniques of particular interest to the pharmaceutical industry are those that can quantify low levels of amorphous content, since even low levels of amorphous material can profoundly influence physical properties (see section 1.3). Detection limits are of great importance as they quantify the lowest amorphous content a technique can be expected to quantify. Linear regression analysis was used to estimate the detection limits of the data processing of the proton saturation relaxation delay with partial least squares analysis. Detection limit was defined by Miller and Miller in Equation 6 which is interpreted as blank signal $y_B$ plus three standard deviation of the blank. To convert the linear regression statistics in to detection limit the standard deviation of the points from the line is estimated by $s_{y/x}$ using Equation 7.[13]

$$Limit\ of\ detection = y_B + 3s_B \qquad \textbf{Equation 6}$$

The standard deviation $s_{y/x}$ is used as alternative to $3_{SB}$, and the standard deviations for the coefficients of the line $y = a + bx$ are calculated using equations 5 and 6. These allow the 95% confidence limits to be calculated for any reading.

$$s_{y/x} = \sqrt{\frac{\sum_i (y_i - \hat{y}_i)^2}{n-2}} \qquad \textbf{Equation 7}$$

$$s_b = \frac{s_{y/x}}{\sqrt{\sum_i (x_i - \hat{x}_i)^2}} \qquad \textbf{Equation 8}$$

$$s_a = s_{y/x}\sqrt{\frac{\sum_i x_i^2}{n\sum_i (x_i - \hat{x}_i)^2}} \qquad \textbf{Equation 9}$$

The calculated values for the detection limits are shown in Table 5. The detection limits show very low values with relaxation times of 10 and 15 seconds (marked in yellow).[13]

| | Relaxation delays (s) | | | | | | | |
|---|---|---|---|---|---|---|---|---|
| | 2 | 4 | 10 | 15 | 20 | 25 | 30 | 60 |
| Slope standard deviation $s_b$ | 0.39% | 0.55% | 0.20% | 0.15% | 0.41% | 0.75% | 1.22% | 0.67% |
| Intercept standard deviation $s_a$ | 0.18% | 0.25% | 0.09% | 0.07% | 0.19% | 0.35% | 0.57% | 0.31% |
| Detection limit = $a + 3s_{y/x}$ | 0.46% | 0.64% | 0.24% | 0.17% | .49% | .89% | 1.25% | 0.79% |

**Table 6 Detection limits and confidence limit statistics for model response output for each relaxation delay**

The detection limit estimated for the proton saturation relaxation delay with partial least squares analysis used here compares very favourably with other techniques set out in Table 7 where the detection limit is calculated as $a + 3s_{y/x}$.

| Method | Measures | Detection limit | Reference |
|---|---|---|---|
| PXRD | X-ray powder diffraction, whole pattern fitting | 0.64% | Chen[14] |
| Isothermal Calorimetry | Heat flow associated with crystallisation of amorphous lactose | 1.0% | Dilworth[15] |
| Dynamic Vapour Sorption | Mass gain from amorphous lactose crystallising to α-lactose monohydrate | 0.12% | Buckton[16] |
| Differential Scanning Calorimetry | Heat flow after Tg during heat up | 0.57% | Saunders[17] |

**Table 7 Detection limits for amorphous lactose for a variety of methods**

Table 6 show the PLS technique to possess calculated detection limits in many cases better than other techniques, however the robustness of this technique needs to tested against other sources of amorphous lactose. Using a relaxation 60 s an amorphous content of spray dried and freeze dried lactose after vacuum drying was determined to be 100.7 % and 100.2 %. This demonstrates that the technique is able to effectively identify amorphous content regardless of preparative method.

One of the key problems with amorphous materials such as lactose is their ability to absorb water from the atmosphere. Handling techniques such as working in a glove box atmosphere of argon or nitrogen can be deployed to counter this, however an

understanding of how these atmospheres influence results is necessary to produce a robust method and will be investigated in a subsequent chapter.

### 4.4.3 Conclusions

The determination of amorphous lactose content in a crystalline / amorphous mixture has been shown to be possible using the proton saturation relaxation delay with partial least squares analysis.[18] The low detection limit suggests the technique has potential for measuring very low levels of amorphous content, which are of particular interest for inhalation formulation. The measurement of other preparations of amorphous lactose as 100% demonstrates the technique has the potential to quantify mixtures of amorphous and crystalline lactose that have been prepared by different routes.

The speed of measurement is much faster than DVS which can take about 8 hours to measure a single sample, whereas this technique is able to carry out 255 scans with a 10 second relaxation delay in less than 1 hour. The speed of assay may make the technique attractive despite the drying of samples and need to exclude moisture by working in a glove box.

***References***

1 J. H. Kirk, S. E. Dann and C. G. Blatchford, *International Journal of Pharmaceutics,* 2007, 334, 103-114.

2 S. R. Elliott, *Physics of amorphous materials (Second Edition)*, Longman Scientific & Technical, Harlow, 1990.

3 D. Le Botlan, F. Casseron and F. Lantier, *Analusis,* 1998, 26, 198-204 (DOI:10.1051/analusis:1998135).

4 R. J. Abraham, *Proton and carbon - 13 NMR spectroscopy*, Wiley, Chichester, 1985.

5 J. Kirk, *Fundamental Structural Aspects of Crystalline Lactose Polymorphs*, Loughborough Univerity, Loughborough, 2007.

6 S. E. Dann, *Reactions and characterization of solids*, Royal Society of Chemistry, Cambridge, 2000.

7 M. K. Haque, K. Kawai and T. Suzuki, *Carbohydrate Research,* 2006, 341, 1884-1889.

8 W. L. Earl and F. W. Parrish, *Carbohydr. Res.,* 1983, 115, 23-32 (DOI:DOI: 10.1016/0008-6215(83)88131-2).

9 Microsoft, *Excell*, Seattle, 2007.

10 C. Gustafsson, H. Lennholm, T. Iversen and C. Nyström, *Int. J. Pharm.,* 1998, 174, 243-252 (DOI:DOI: 10.1016/S0378-5173(98)00272-5).

11 G. Hanrahan, *Environmental Chemometrics Principles and Modern Applications*, CRC press, Boca Raton, 2009.

12 addinsoft, *Xlstat*, New York, 2007.

13 J. N. M. Miller J.C., *Statistics and Chemometrics for Analytical Chemistry*, Pearson Education, Edinburgh, 2000.

14 X. Chen, J. G. Stowell, K. R. Morris and S. R. Byrn, *J. Pharm. Biomed. Anal.,* In Press, Accepted Manuscript (DOI:DOI: 10.1016/j.jpba.2009.09.021).

15 S. E. Dilworth, G. Buckton, S. Gaisford and R. Ramos, *Int. J. Pharm.,* 2004, 284, 83-94 (DOI:DOI: 10.1016/j.ijpharm.2004.07.016).

16 G. Buckton and P. Darcy, *Int. J. Pharm.,* 1995, 123, 265-271 (DOI:DOI: 10.1016/0378-5173(95)00083-U).

17 M. Saunders, K. Podluii, S. Shergill, G. Buckton and P. Royall, *Int. J. Pharm.,* 2004, 274, 35-40 (DOI:DOI: 10.1016/j.ijpharm.2004.01.018).

18 C. Gustafsson, H. Lennholm, T. Iversen and C. Nyström, *International Journal of Pharmaceutics,* 1998, 174, 243-252 (DOI:DOI: 10.1016/S0378-5173(98)00272-5).

# CHAPTER 5

# Lactose isomer analysis

## 5.1 Introduction to GC analysis of lactose anomers

The difference between the two anomers of lactose is a result of the position of the OH group on the glucose subunit. The OH group lies in the horizontal plane for the alpha form while for the beta anomer the OH group lies in a vertical orientation, as seen in Figure 1.[1]

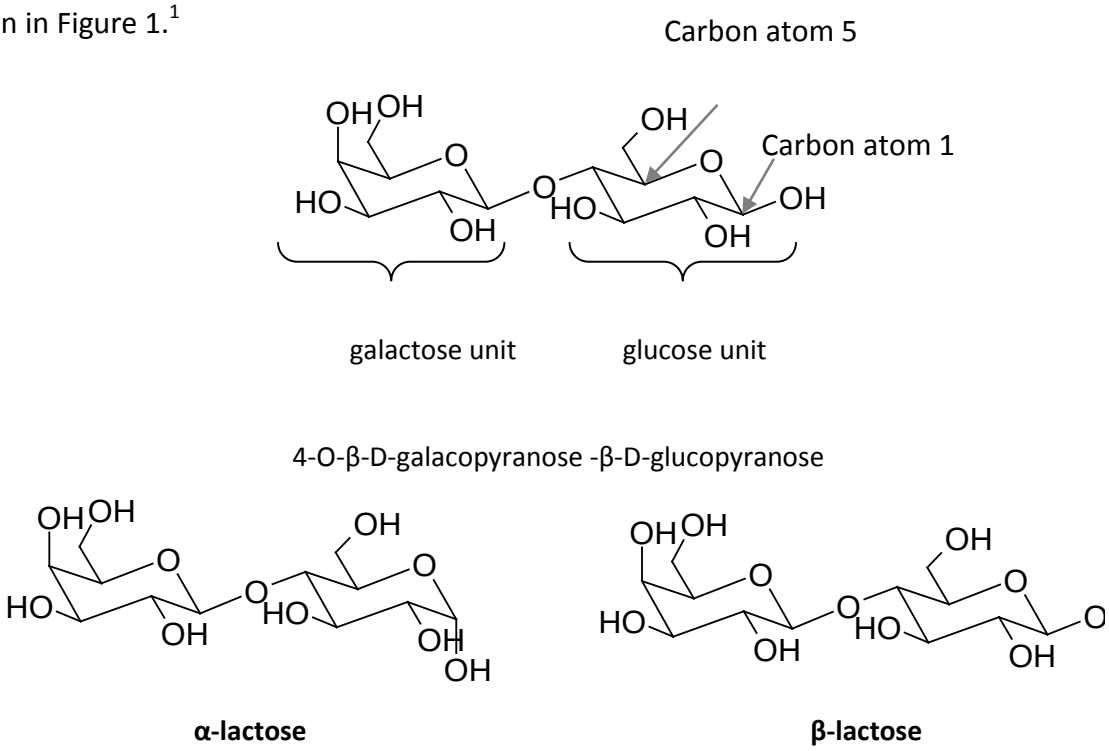


**Figure 1 Orientation of the OH group on carbon atom 1 of the glucose unit of lactose**[1]

If anhydrous α and β lactose polymorphs are placed in water they dissolve to form identical solutions .[2] The formation of an identical solution occurs because the lactose polymorphs undergo a process of mutarotation when in solution. The pyranose rings shown in Figure 1 are in equilibrium with the open chain aldehyde form of the glucose subunit. The mutoration process occurs via the carbonyl group on carbon atom 1 (in the open chain form) interacting with the alcohol group on carbon atom 5 to reform the pyranose ring, producing a chiral centre on carbon atom 1, with the OH group in either an α (axial) or β (equatorial) position. In solution at 20 °C, the isomer ratio has been reported to be 37.3% : 62.7% α to β by Fox.[3] More of the β isomer is expected, because the lowest energy form for the ring is the chair configuration, where the OH group on carbon atom 1 lies in an equatorial position, (with less steric interaction with other atoms). This process can become more facile using acid or base catalysis which are shown in Figure 2. [3]

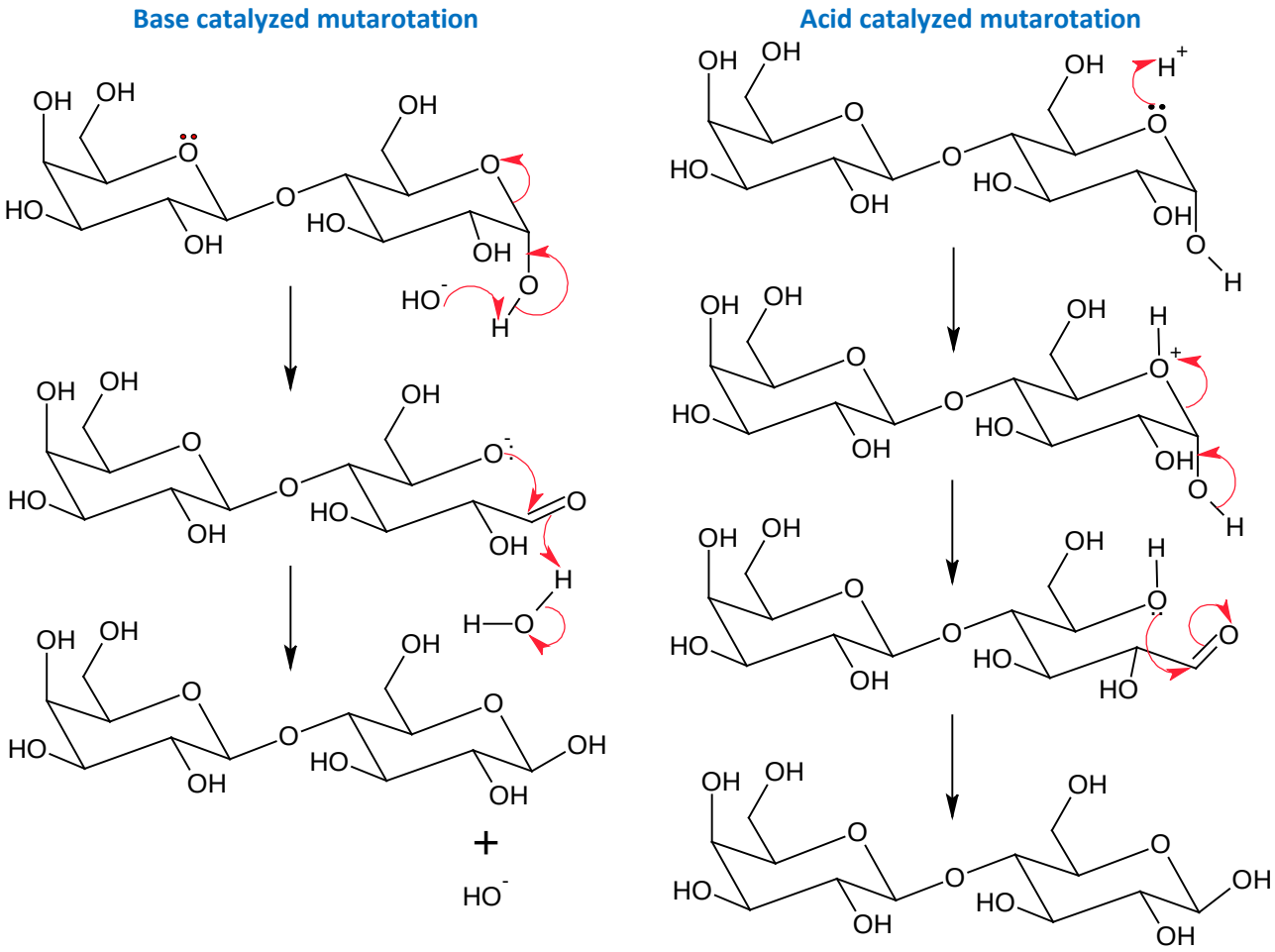


Figure 2 Mutarotation mechanism [4]

Previously Ramos carried out isomer analysis on amorphous lactose prepared via a spray dry method using GC-FID derivatisation. Ramos reported that an isomer composition of 66% α and 34% β was arrived at regardless of the starting material being α-lactose monohydrate or β lactose.[5] This finding is somewhat unexpected since spray dried mixtures are prepared from aqueous solutions which should reflect the equilibrium concentration with the beta anomer significantly in excess. These authors did not undertake isomer analysis of amorphous lactose prepared by other methods such as freeze drying and rapid quenching from the melt . The purpose of this work is to remedy this situation and investigate the final α:β lactose ratio on amorphous material prepared by different methods to establish whether the method of preparation effects the final anomer ratio.

The separation of anomers is difficult by chemical means, since both molecules possess identical chemical bonds, however separation can still be achieved by utilising the differences in their physical properties. Chromatography can achieve separation by continuous partitioning of the analytes between mobile and stationary phases, to bring about separations ordered by the time analytes spend in the stationary phase.[6] All

analytes spend the same amount of time in the mobile phase, but different lengths of time in the stationary phase; the time an analyte spends in the stationary phase is determined by its similarity to the polarity of the stationary phase.[7]

High performance liquid chromatography, might be thought of as an obvious choice for separating isomers of a highly soluble sugar. A typical HPLC analysis would be designed to take about 15 to 30 minutes, with the analyte peak emerging from start to finish in about one minute. By contrast gas chromatography (GC) may elute an analyte peak in less than 15 seconds from start to finish, despite taking a similar 15 to 30 minutes per analysis. This means that GC possesses a superior resolving power for separating the two structural isomers.

There is an immediate issue using GC to separate lactose isomers, since the analytes presented to a GC instrument have to be volatile (i.e. with boiling points below 300 °C) and for lactose this is not the case. A derivatisation method has to be applied to lower the boiling point. This approach was first carried out by Sweeley to identify different saccharides in a mixture.[8] To reduce the polarity of lactose, Sweeley used a derivatisation agent N-(trimethylsilyl)imidazole (TMSI) to methylate the alcohol groups, (see Figure 3 for the reaction scheme).[8]

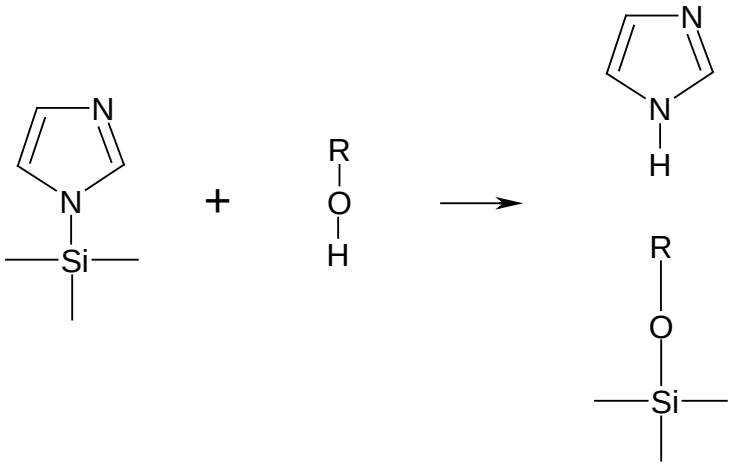


**Figure 3 Reaction between N-(trimethylsilyl)imidazole and an alcohol**

The separation of lactose isomers was developed by Dwivedi, who added dimethylsulphoxide anhydrous (DMSO) to dissolve the lactose sample followed by TMSI and finally pyridine to avoid phase separation of the DMSO and TMSI solvents.[9] Dwivedi investigated whether DMSO or TMSI should be added first, and concluded that, the addition of TMSI first slowed down the dissolution of the lactose and that the

DMSO should be added first to dissolve the lactose.[9] Dwivedi also allowed the derivatised samples to stand at room temperature for 24 hours before analysis by GC.[9]

## 5.2 GC-conditions

In 1988, Dwivedi used a packed column of length of 0.9 m and 4 mm internal diameter, with a stationary phase of 3% OV-225 on 80 to 100 mesh chromosorb W.[9] This particular stationary phase contained a 50/50 mixture of cyanopropylphenyl and phenylmethylpolysiloxane, which could be described as a polar column. A modern gas chromatograph with flame ionisation detector (GC-FID), an Agilent 5890 instrument with chemstation software was chosen to carry out the analysis for this thesis. Currently packed columns are rarely used in gas chromatography, since open tubular columns produce much greater resolution. A less polar open tubular column (than Dwivedi's) of 50% phenyl siloxane to 50% methyl siloxane was used, of 15.0 m length, with an internal diameter 530.00 µm and 1.00 µm film thickens (DB-17 15m 0.53mm 1.00 µm). The use of a more polar column would have produced an unnecessarily long elution time. The use of an open tubular column, also demanded a change to the mobile phase conditions and inlet (injector) split conditions, (these are shown in Table 1). The injection size was also reduced to 0.5 µL of the derivatised solution for injection to the GC inlet.

| | |
|---|---|
| Mode: | Split |
| Initial temp: | 300 °C (On) |
| Pressure: | 5.00 psi (On) |
| Split ratio: | 35.7:1 |
| Split flow: | 354.9 mL/min |
| Total flow: | 368.4 mL/min |
| Gas saver: | Off |
| Gas type: | Helium |

**Table 1 GC inlet (injector) conditions**

The oven conditions set out by Dwivedi were used (see Figure 4), but the Flame Ionisation Detector (FID) had to be altered following the change of column. The FID conditions used in this study were 30 ml/min of hydrogen and 350 ml/min of air, using nitrogen as the makeup gas at a flow rate of 10 ml/min. The data from the FID were recorded at a rate of 20 Hz.

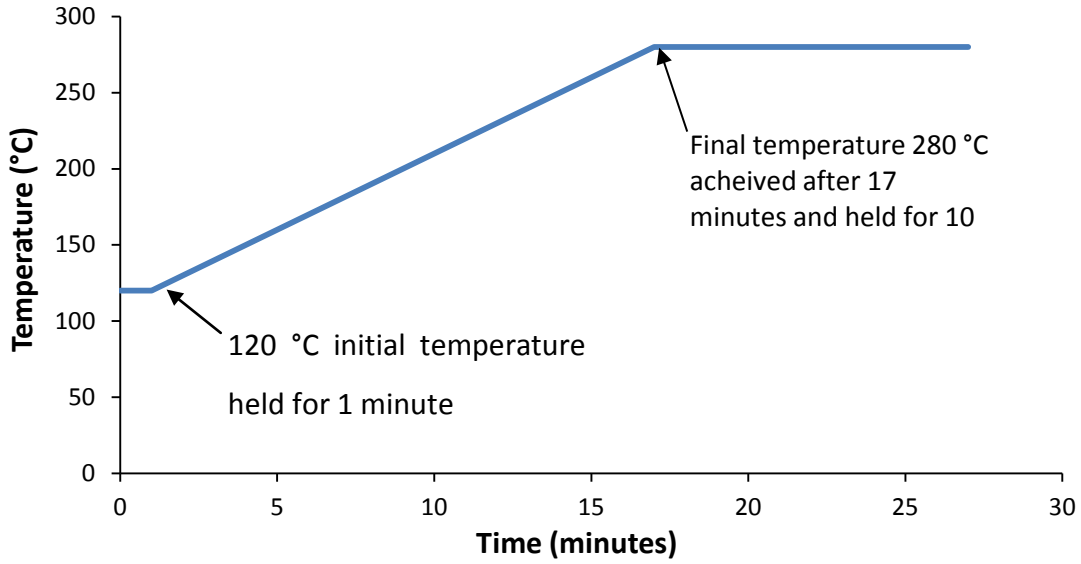


Figure 4 GC oven conditions

## 5.3 Investigating the GC response to the derivatisation of α-lactose stable and β-lactose

### 5.3.1 Introduction

Initially 10mg samples of α-lactose anhydrous stable and β-lactose were dissolved by adding anhydrous (Sigma-Aldrich 41647) contained in sealed dry 5 ml serum vial. Once every sample had been dissolved in DMSO (this took approximately 20 minutes), the TMSI (Sigma-Aldrich 153583) and anhydrous pyridine (Sigma-Aldrich 270970) were added. The derivatised peaks eluted at 13.4 minutes for α-lactose and 14.2 minutes for β-lactose. The α-lactose and β-lactose retention times were determined by picking out the larger of two peaks eluting. The normalised peak areas for α-lactose stable anhydrous (batch ID 10101901) and β-lactose (batch ID 08071402) isomer showed values of between 90 to 95%, which is a much broader range and lower content than expected. By comparison, the results obtained by Dwivedi for α-lactose monohydrate 96.5 ±0.2%, using the addition sequence of DMSO + TMSI + pyridine. While α-lactose monohydrate studied by Dwivedi and anhydrous α-lactose under investigation in this study are different (i.e. one contains water and one does not), the difference in repeatability between this study and that of Dwivedi perhaps suggest that mutarotation is occurs during the derivatisation process. By Changing the time period between DMSO and the TMSI addition, mutarotation can be tested for.

### 5.3.2 Experimental

This investigation was carried out using a beta lactose sample that had been prepared by refluxing 3.0g of α-lactose monohydrate (Fluka 61341) in 100 ml of methanol, with 0.11g of potassium methoxide and dried using 10 g of freshly heated molecular sieves. The time zero value was established by adding the TMSI first, directly to the dry powdered lactose in the sealed serum vial, which was then shaken for 30 seconds before the DMSO and pyridine were added. Further vials were prepared by adding the DMSO first to dissolve the lactose and then waiting between 1 and 32 minutes before injecting the TMSI. The derivatised samples were allowed to stand at room temperature for 24 hours before analysis by GC.

### 5.3.3 Results

The observation was made that all vials showed a clear solution after the pyridine addition and shaking, suggesting that the sample and its derivative dissolved. The normalised peak areas for the β-lactose peak eluted at 14.2 minutes are shown in Table 2 and Figure 5.

| Sample description | Repeat | Injection 1 | Injection 2 | Injection 3 | Average | 95% Confidence Limit |
|---|---|---|---|---|---|---|
| Addition of TMSI directly on lactose sample followed by DMSO and then pyridine. | 1 | | 95.9% | 96.1% | 96.0% | 1.24% |
| | 2 | | 96.2% | 96.1% | 96.1% | 0.97% |
| | 3 | 96.4% | 96.2% | 96.1% | 96.2% | 0.31% |
| | 4 | 96.3% | 96.1% | 95.8% | 96.1% | 0.59% |
| | | | Overall average | | 96.1% | 0.12% |

| Sample description | Time (min) | Injection 1 | Injection 2 | Injection 3 | Average | 95% Confidence Limit |
|---|---|---|---|---|---|---|
| Time in minutes between DMSO and TMSI additions | 1 | 96.0% | 96.0% | 96.0% | 96.0% | 0.12% |
| | 2 | 95.9% | 95.9% | 95.7% | 95.8% | 0.33% |
| | 4 | 94.8% | 94.9% | 94.9% | 94.8% | 0.10% |
| | 8 | 94.9% | 95.1% | 94.7% | 94.9% | 0.53% |
| | 16 | 94.5% | 94.6% | 94.6% | 94.6% | 0.16% |
| | 32 | 91.4% | 91.1% | 91.5% | 91.3% | 0.42% |

**Table 2 Fraction of beta lactose isomer found when the order of addition of DMSO and TMSI were changed**

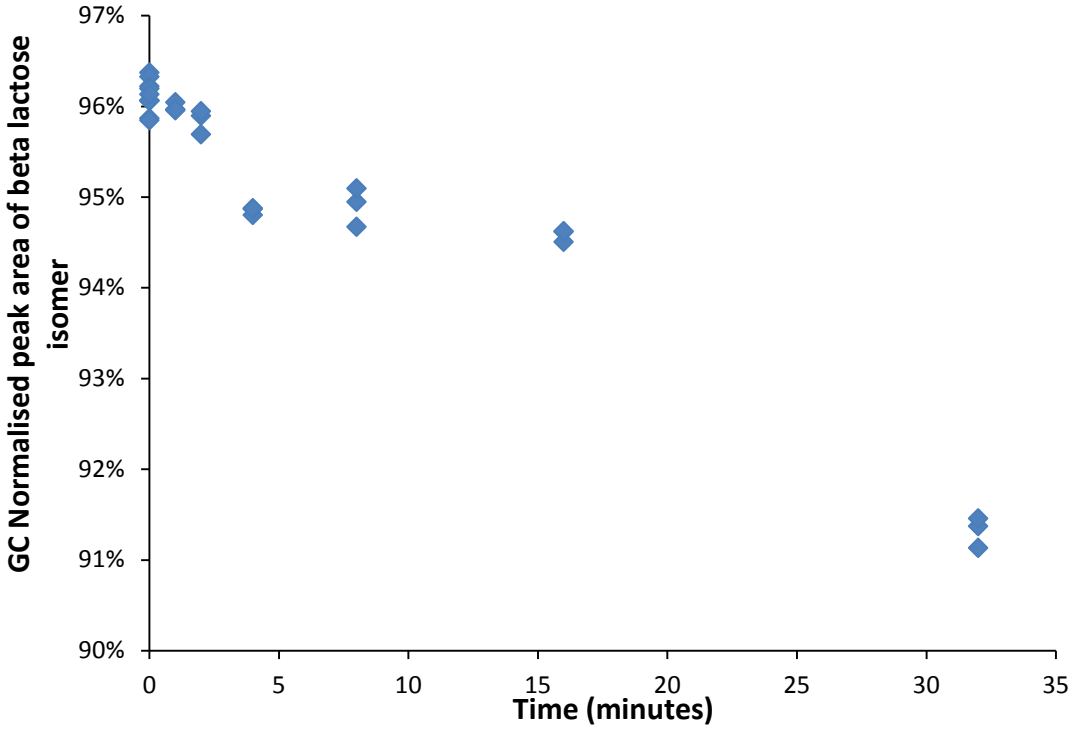


**Figure 5 Fraction of beta lactose isomer against time between DMSO and TMSI injection into serum / sample vial**

### 5.3.4 Discussion

The decrease in normalised β-lactose peak area with time, suggests that mutarotation occurred during the time between dissolving the lactose in DMSO and the reaction with TMSI. This could have been due to traces of water left in the DMSO, which was specified at less than 50 ppm. Since the objective of the analysis was to measure the optical isomer ratio, when further samples were prepared for analysis by GC, the order of addition was changed to; TMSI first, DMSO, and finally pyridine.

These findings were in contrast to Dwivedi's, who concluded that DMSO should be added first to any sample with a high β-lactose content.[9] The basis for Dwivedi's conclusion was an ANOVA study of variance, which investigated different addition sequences as significantly different in their precision. Dwivedi's work did not investigate the timing between dissolving the lactose in DMSO and the TMSI addition.[9]

## 5.4 Selection of standards for normalised peak area calibration

### 5.4.1 Introduction

The intention of this work was to produce a series of known mixtures of crystalline well characterised α-lactose and β-lactose standards that could be derivatised and injected into the GC to correlate to the α/β normalised peak areas. α-Lactose monohydrate was not selected as a standard, since the water of crystallisation could be released on dissolution in DMSO and facilitate mutarotation. A batch mixture (10101901), made up of 100 g of α-lactose anhydrous stable was used as standard, since no water of crystallisation was associated with this polymorph and it was also known to be stable to an 80% relative humidity at 25°C, (see Figure 13). This batch had been prepared from 10 repeat preparations by refluxing 10 g of α-lactose monohydrate in 100 ml of dry ethanol. This α-lactose anhydrous stable batch mix (10101901) had been well characterised by X-ray powder diffraction, elemental analysis (CHN), DVS, DSC, FT-IR and solid state CP-MAS-NMR.

Previous work had investigated variations in the synthesis of β-lactose, using different weights and different reflux times. All the β-lactose syntheses were carried out in 100 ml of dry ethanol with 0.1 g of potassium methoxide (Sigma Aldrich 60408). To ensure a response to α-lactose could be measured, the standard was added to the list of the materials analysed, (set out in Table 3). To ensure repeatability each sample was injected 3 times.

### 5.4.2 Results and discussion

The results for the different β-lactose syntheses are summarised in Table 3 along with the synthetic conditions that were varied.

| | GC normalised peak area | | | Synthesis conditions | |
|---|---|---|---|---|---|
| | α (%) | β (%) | | Weight (g) | Reflux time (hours) |
| 10101901 | 94.7 ± 0.1 | 5.3 ± 0.1 | | 10 | 16 |
| 08060201 | 4.6 ± 0.6 | 95.4 ± 0.6 | | 12.50 | 16 |
| 08060202 | 4.0 ± 0.9 | 96.0 ± 0.9 | | 6.25 | 16 |
| 08060203 | 4.2 ± 0.9 | 95.8 ± 0.9 | | 3.25 | 16 |
| 08060204 | 4.4 ± 0.9 | 95.6 ± 0.9 | | 1.57 | 16 |
| 08060301 | 6.0 ± 0.4 | 94.0 ± 0.4 | | 12.50 | 3 |
| 08060302 | 5.8 ± 0.6 | 94.2 ± 0.6 | | 6.25 | 3 |
| 08060304 | 5.9 ± 0.7 | 94.1 ± 0.7 | | 1.57 | 3 |
| 08071401 | 3.1 ± 0.1 | 96.9 ± 0.1 | | 6.25 | 70 |
| 08071402 | 3.2 ± 0.6 | 96.8 ± 0.6 | | 3.25 | 70 |

**Table 3 Normalised GC peak area responses to β-lactose synthesis reflux times and weight of α-lactose monohydrate**

The α-lactose content is plotted against the reflux time in Figure 6, this shows how increasing reflux time appears to reduce the α-lactose content in the β-lactose product.

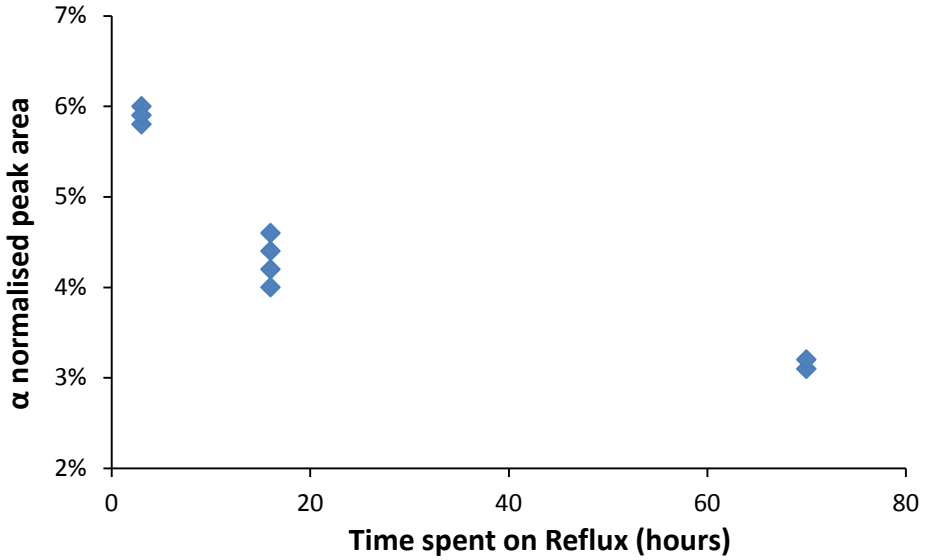


**Figure 6 Normalised GC peak area for α-lactose against reflux time for β-lactose synthesis**

The two syntheses that produced the lowest α-lactose content were prepared by refluxing for 70 hours. Only about 0.4 g of the original 6 g of sample 08071401 remained after studies on grinding had been carried out, however 2.7 g remaining of

sample 08071402, so this was selected to validate the normalised peak areas of the peaks eluted at 13.4 and 14.2 minutes against α and β isomer content.

## 5.5 Investigating the relationship between GC normalised peak area and α/β lactose isomer content of sample

### 5.5.1 Introduction

The link between isomer content and the normalised peak areas at 13.4 and 14.2 minutes, was investigated by creating a series of mixtures of the α-lactose stable (ID 10101901) and β-lactose (ID 08071402). Before investigating the GC response to the α/β mixes, the two standard samples were characterised to ensure they were consistent with the known properties of α-lactose stable and β-lactose. Previous work by Kirk,[10] had identified key features of the FT-IR, NMR spectra, DSC trace and power X-ray diffraction patterns. Once the integrity of the standards (α-lactose stable ID 10101901 and β-lactose ID 08071402) had been established, mixtures of these standards were prepared and samples derivatised and analysed on the GC-FID.

### 5.5.2 Experimental

The α-lactose stable and β-lactose standards were first characterised by FT-IR, X-ray powder diffraction, MAS-CP NMR, DSC and DVS using methods outlined in chapter 3. The standards were dried for one week in an argon glove box, stored over a phosphorus pentoxide desiccant. A series of mixtures was generated from the α and β lactose standards at approximately 10% w/w intervals in 75x25mm glass vials, (all weighings were carried out in the glove box under dry argon). The mixing was carried out on a Stuart roller mixer at 60 rpm for 24 hours.

Prior to derivatisation, the 5 ml serum vials were dried at 70°C for 24 hours and then transferred to a dry argon glove box and stored over phosphorus pentoxide in a desiccator for one week. Derivatisation was carried out by weighing 10 ±1 mg of lactose into a 5 ml serum vials and sealing with a butyl rubber cap, under argon in a glove box. To each sample 0.5 ml of 1-(trimethylsilyl)imidazole (394874 Fluka) was added, immediately followed by 1.0 ml dimethylsulphoxide anhydrous (276855 Sigma-Aldrich) and finally 1.0 ml of pyridine anhydrous (270970 Sigma-Aldrich). The

derivatised samples were shaken for 30 seconds and then allowed to stand at room temperature for 24 hours before analysis.

### *5.5.3* Results and discussion

#### *5.5.3.1 Powder X-ray diffraction*

The powder X-ray diffraction patterns of the α-lactose stable and β-lactose standards are shown in Figure 7. The alignments of the reflection 2θ values are in agreement with those reported by Kirk.[10] This suggests that the standards used to produce these mixtures were highly crystalline and consistent with high levels of single isomer content.

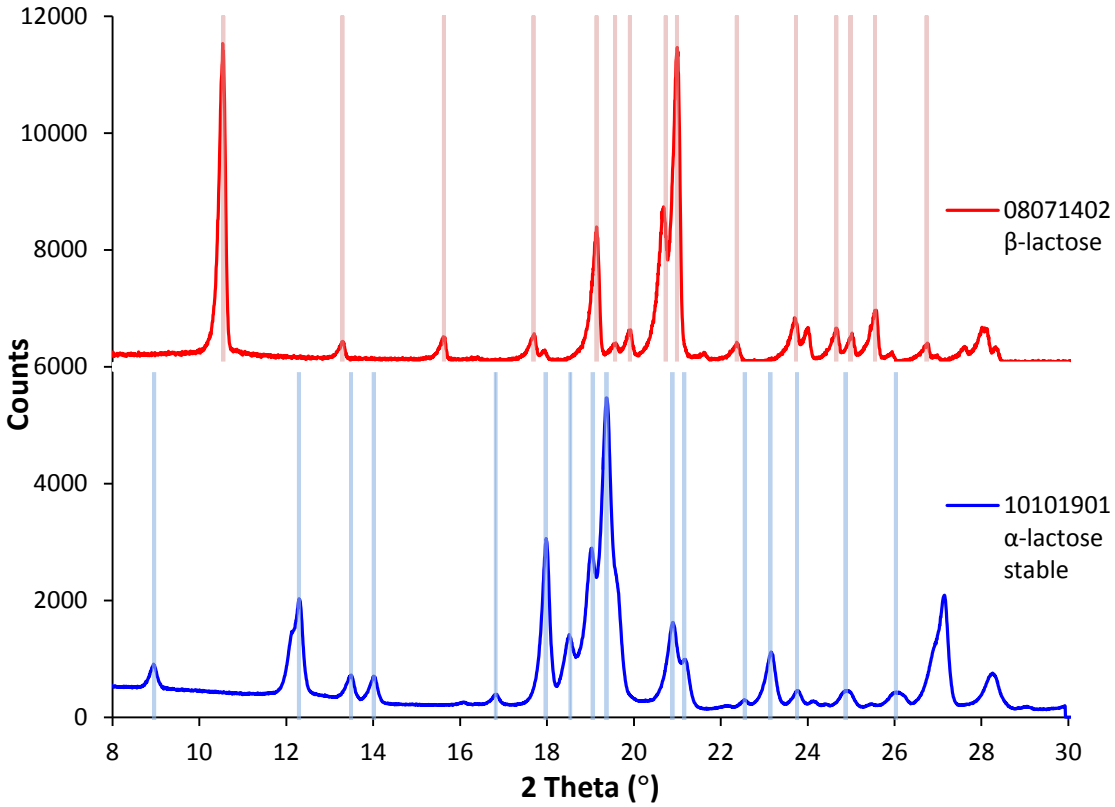


**Figure 7 Powder X-ray diffraction patterns of α-lactose stable 10101901 (blue) and β-lactose stable 08071402 (red), thin pale blue and red lines represent 2 theta reflections for α-lactose stable and β-lactose stable reported Kirk[10]**

### 5.5.3.2 $^{13}C$ CP-MAS NMR

The $^{13}C$ CP-MAS NMR spectra of the α-lactose stable and β-lactose standards are shown in Figure 8. The alignments of peaks are in agreement with the values reported by Kirk.[10] This suggests that standards used to produce the mixes are consistent with high levels of single isomer content.

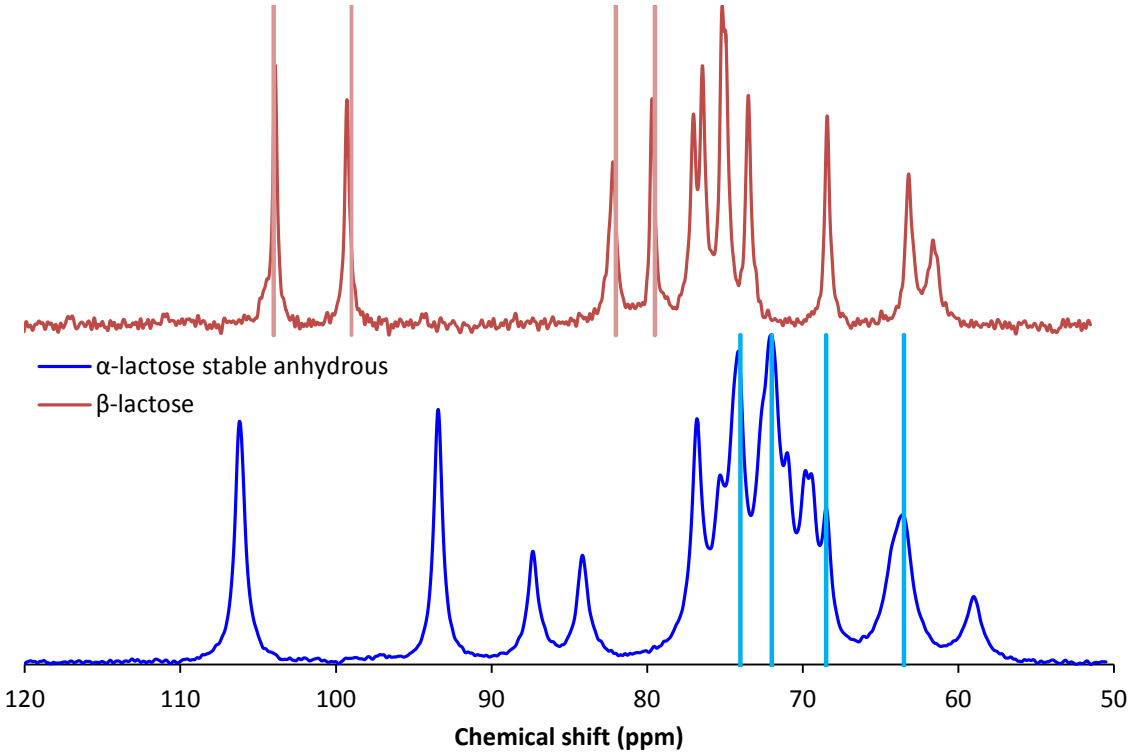


**Figure 8 solid state CP-MAS-NMR of α-lactose stable 10101901 (blue) and β-lactose stable 08071402 (red), thin pale blue and red lines represent chemical shifts for α-lactose stable and β-lactose stable reported by Kirk[10]**

### 5.5.3.3 FT-IR

The infrared spectra of the α-lactose stable and β-lactose standards are shown in Figure 9. The β-lactose sample is consistent with the values reported by Kirk, however the α-lactose stable sample shows no peak at 855 $cm^{-1}$ and a peak at 892 instead of 899 $cm^{-1}$.[10]

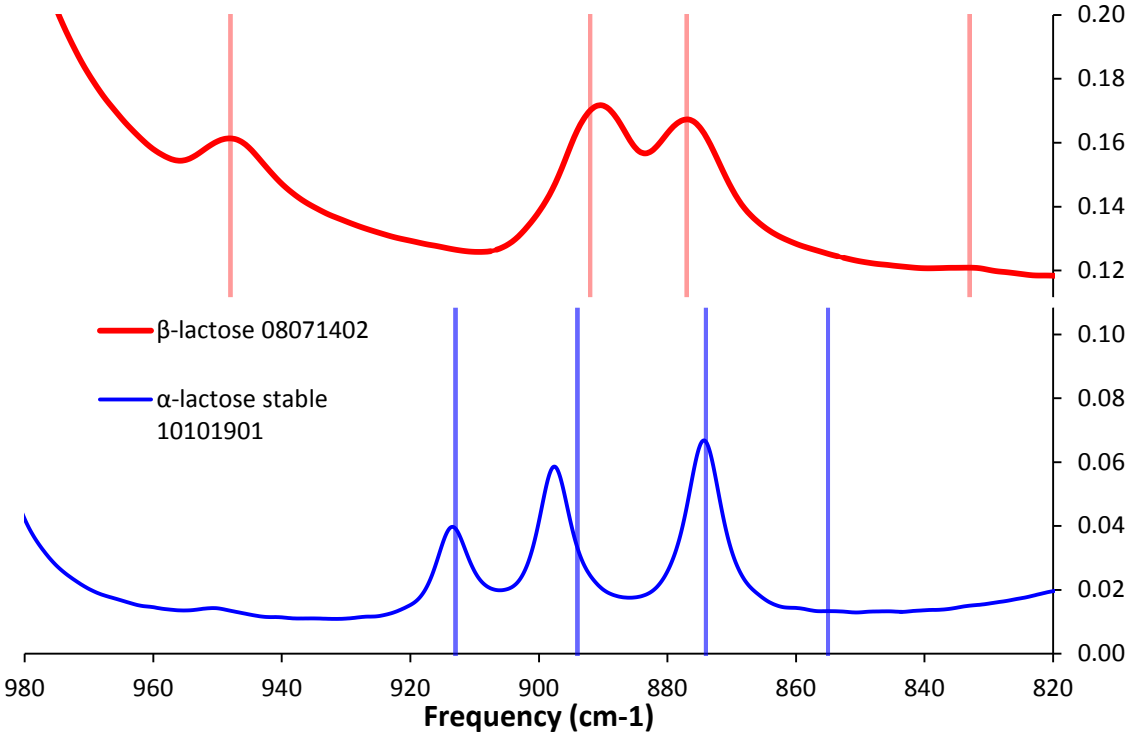


**Figure 9 Fourier transform infra red spectra of α-lactose stable 10101901 (blue) and β-lactose stable 08071402 (red), thin pale blue and red lines represent wave numbers for α-lactose stable and β-lactose stable reported by Kirk[10]**

### *5.5.3.4 Differential Scanning Calorimetry*

Differential Scanning Calorimetry analysis was carried out to determine the melting points. Temperatures corresponding to the endothermic maxima were also recorded, for comparison to values reported by Ross.[11] The onset of fusion temperatures were determined by extrapolating lines for the crystalline heat capacity and the fusion endotherm. The melting point determined by the endothermic maxima for both α-lactose stable 10101901 and β-lactose 08071402, shown in Figure 10 are in good agreement with the melting point data recorded by Ross listed in Table 4.[11]

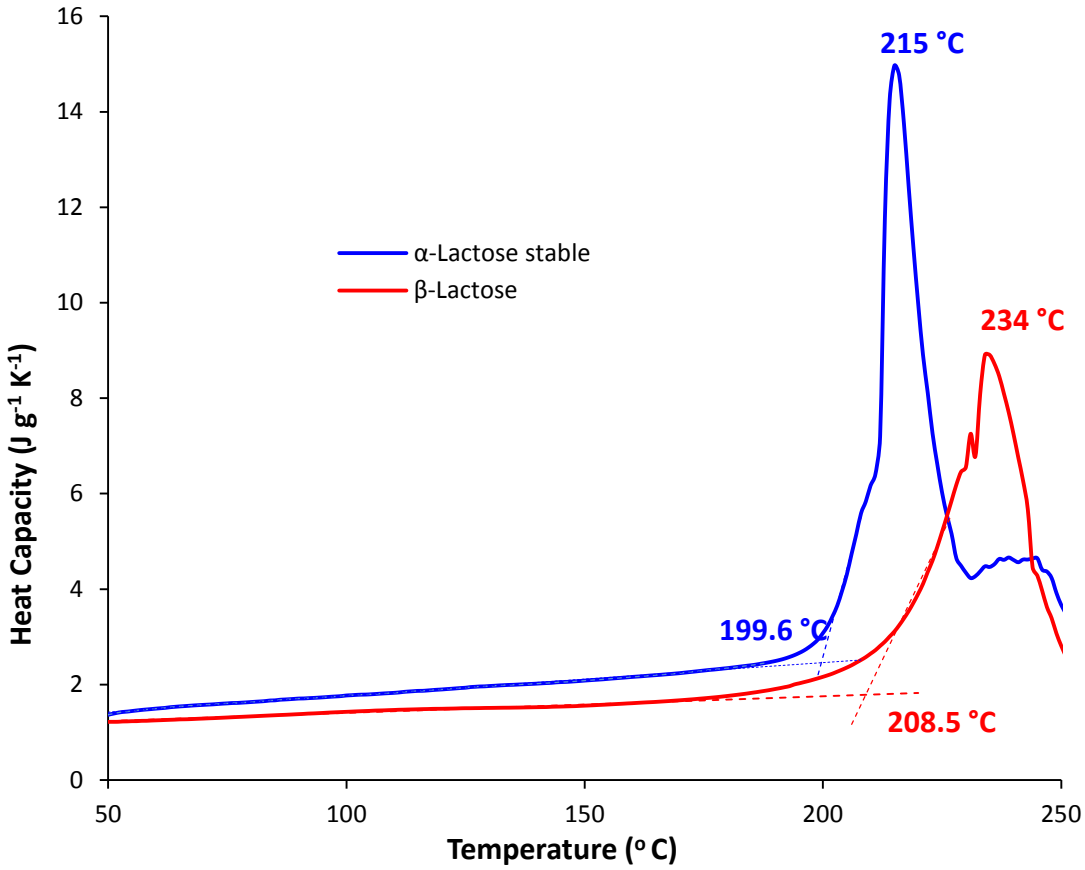


Figure 10 DSC trace for α-lactose stable 10101901 (blue) and β-lactose 08071402 (red)

| | Range determined by Ross | Maximum Values from Figure 10 |
|---|---|---|
| **α-lactose stable** | 210 – 220 °C | 215 °C |
| **β-lactose** | 230 – 238 °C | 234 °C |

Table 4 Literature data on melting points of α-lactose stable 10101901 and β-lactose 08071402.[11]

### *5.5.3.5 Dynamic Vapour Sorption*

DVS experiments were carried out on both standards and α lactose monohydrate. The thermograms for these lactose crystalline polymorphs and are shown in Figure 11, Figure 12 and Figure 13 for α monohydrate, β and anhydrous α respectively. The DVS runs on the α-lactose monohydrate and β-lactose show a small mass change of -0.01 and 0.09% respectively. The α-lactose monohydrate result represents experimental error. The change in mass expected from a complete conversion of anhydrous lactose to α-lactose monohydrate is calculated to be 5.32% using Equation 1. By dividing the final mass change % by 5.32, the extent of conversion to α-lactose monohydrate can be determined, in the case of β-lactose sample this represents about 1.7% of the original sample mass, which must correspond to an anhydrous α lactose impurity since

β lactose is moisture stable. In contrast the α-lactose stable shows a weight gain of 5.20%, (slightly less than the theoretical 5.32% maximum) corresponding to a conversion of 97.74% of the original sample to α-lactose monohydrate, suggesting a 2.26% impurity which is possibly unconverted α-lactose monohydrate or β-lactose.

$$100 \times \frac{(360.31 - 342.11)}{342.11} = 5.32\% \qquad \text{Equation 1}$$

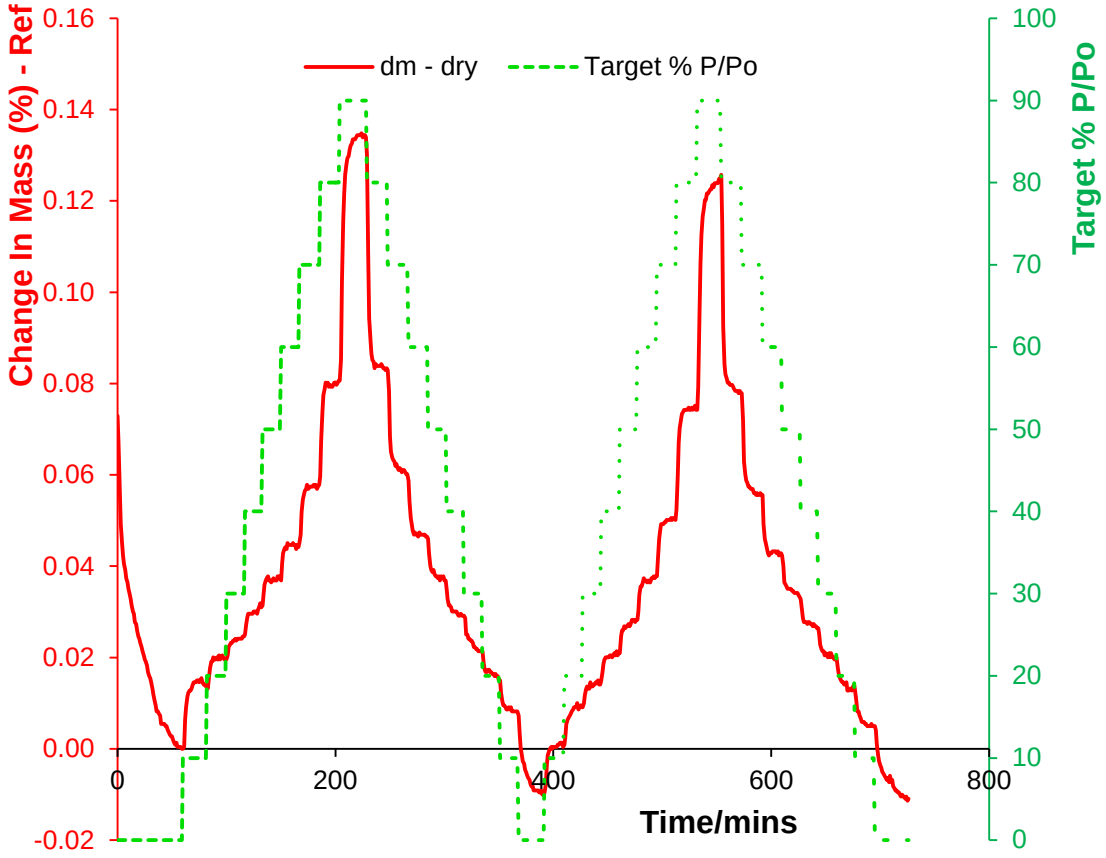


Figure 11 DVS run using α-lactose monohydrate (fluka 61341)

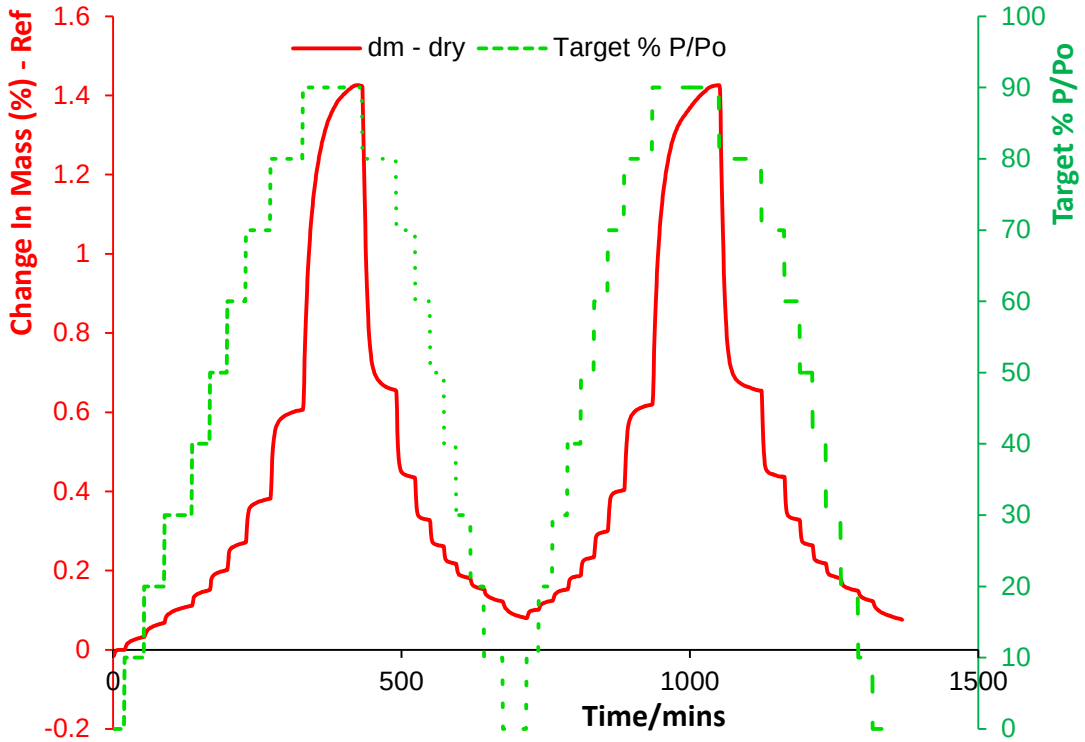


Figure 12 DVS run using β-lactose (08071402)

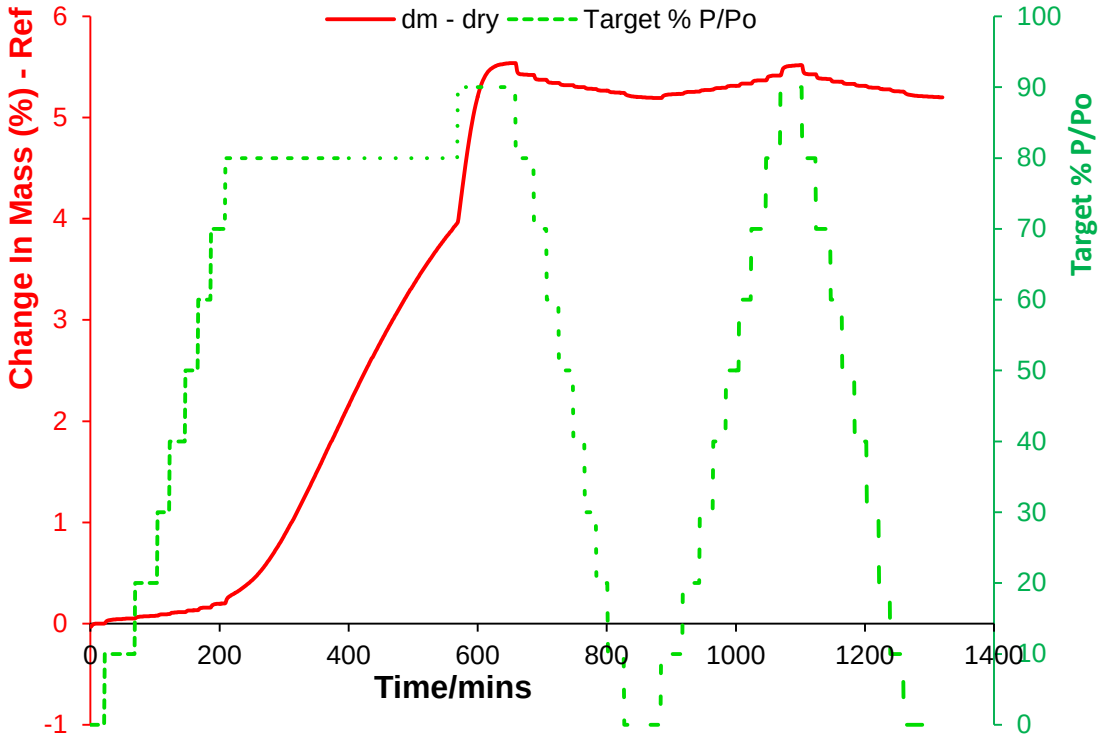


Figure 13 DVS run using α-lactose stable (10101901)

### *5.5.3.6 GC response to known mixtures of the α and β standards*

The results for GC-FID calibration set of mixtures generated from the anhydrous α and β lactose standards at approximately 10% w/w intervals are shown in Table 5 as normalised peak area results and plotted out in Figure 14. The calibration using the α

and β lactose standards produced a correlation coefficient ($r^2$) of greater than 0.99, but neither α or β standards gave the expected 100% values, both showing 3.7% isomer impurity by normalised peak area. Explanations for the 3.7% impurity are that mutarotation occurs to a small extent during the analysis, or that the synthesis of both of these standards attempt to produce equilibrium conditions that favour one isomer over another, and that the impurity simply represents the equilibrium position at the end of the experiment.

| Weight (g) | | | Weight % | | Normalised peak area | |
|---|---|---|---|---|---|---|
| α | β | toal | α | β | α | β |
| | | | 100% | 0% | 96.8 ± 0.1% | 3.2 ± 0.1% |
| 0.9004 | 0.1000 | 1.0004 | 90.00% | 10.00% | 87.4 ± 0.1% | 12.6 ± 0.1% |
| 0.4004 | 0.1003 | 0.5007 | 79.97% | 20.03% | 75.7 ± 0.2% | 24.3 ± 0.2% |
| 0.2331 | 0.0999 | 0.3330 | 70.00% | 30.00% | 67.3 ± 0.2% | 32.7 ± 0.2% |
| 0.1603 | 0.1007 | 0.2610 | 61.42 | 38.58% | 59.0 ± 0.2% | 41.0 ± 0.2% |
| 0.1505 | 0.1517 | 0.3022 | 49.80% | 50.20% | 50.4 ± 0.1% | 49.6 ± 0.1% |
| 0.1007 | 0.1603 | 0.2610 | 38.58% | 61.42% | 42.5 ± 0.4% | 57.5 ± 0.4% |
| 0.1002 | 0.2336 | 0.3338 | 30.02% | 69.98% | 31.8 ± 0.3% | 68.2 ± 0.3% |
| 0.4004 | 0.1001 | 0.5005 | 80.00% | 20.00% | 79.4 ± 0.1% | 20.6 ± 0.1% |
| 0.1004 | 0.9005 | 1.0009 | 10.03% | 89.97% | 12.8 ± 0.2% | 87.2 ± 0.2% |
| | | | 0% | 100% | 3.4 ± 0.2% | 96.6 ± 0.2% |

**Table 5 Weights of crystalline α-lactose stable 10101901 and β-lactose 08071402 used in producing a series of mixtures and the GC response expressed as % normalised peak area**

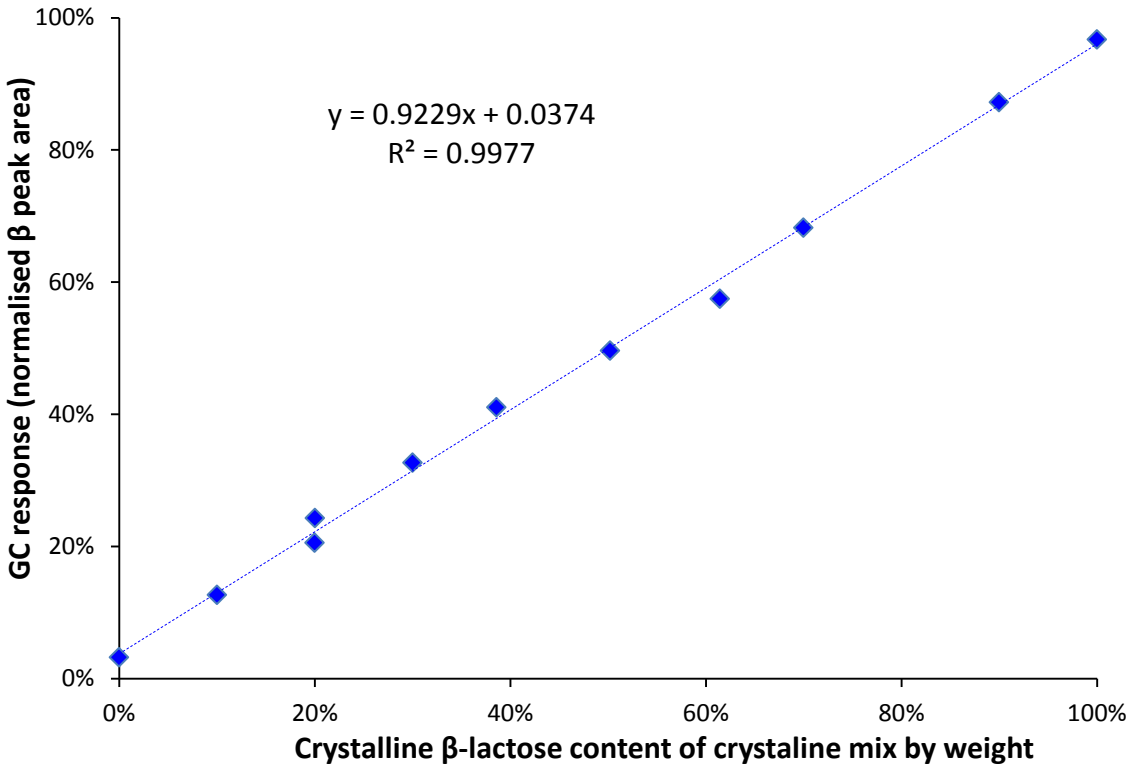


**Figure 14 Graph of crystalline β-lactose 08071402 content of mix against the GC response to derivatised β-lactose expressed as % normalised peak area**

### 5.5.4 Discussion

The correlation and linearity of the GC response to the changing crystalline mix of α/β lactose suggests that the technique is capable of detecting and comparing different anomeric mixtures of anhydrous α and β lactose. The DVS and GC responses suggest that the crystalline α/β standards were not 100% pure when they were presented to the instrument. This could either be to incomplete conversion of the original monohydrate to the alpha and beta anhydrous anomers or changes in the samples before they were analysed. For example, where the dissolution/derivatisation process allowed mutarorotation before analysis could be performed. Further work would be required to investigate the formation of the samples derived from TMSI treatment, perhaps by further controlling the water content in DMSO.

## 5.6 Investigating isomers in amorphous lactose preparations

### 5.6.1 Introduction

A number of different methods can be used to prepare amorphous lactose as described in chapter 2. The three common methods are spray drying, freeze drying and the rapid quench of a molten mass. For this work, the spray dried and freeze dried samples were supplied by DMV-Fonterra Excipients GmbH. The third melt sample was prepared by heating 2.0 g α-lactose stable until molten, which was then quenched in liquid nitrogen and immediately stored under dry argon in a glove box.

### 5.6.2 Experimental

Identical procedures to those set out in section 5.5.2 were used. All possible steps had been taken to reduce the samples exposure to moisture, since all the samples had all been stored for a minimum of 10 months over phosphorus pentoxide in desiccators held within an argon glove box. The X-ray powder diffraction patterns were obtained using a perspex sample holder covered with a mylar film. In all other respects the powder diffraction pattern, FT-IR spectra, $^{13}C$ CP-MAS NMR and DSC obtained were identical to those in section 5.5.2, and are seen in Figure 15, Figure 16, Figure 17, Figure 18 and Figure 19. The GC derivatisation with TMSI of lactose polymorph standards and amorphous preparations was repeated in three separate vials with each undergoing triplicate injections using the method set out in section 5.5.2.

### 5.6.3 Results and discussion for characterisation of standards

#### *5.6.3.1 XRD*

No crystalline reflections were observed in the powder X-ray diffraction patterns for the three preparations shown in Figure 15, which is consistent with amorphous and nanocrystalline properties.

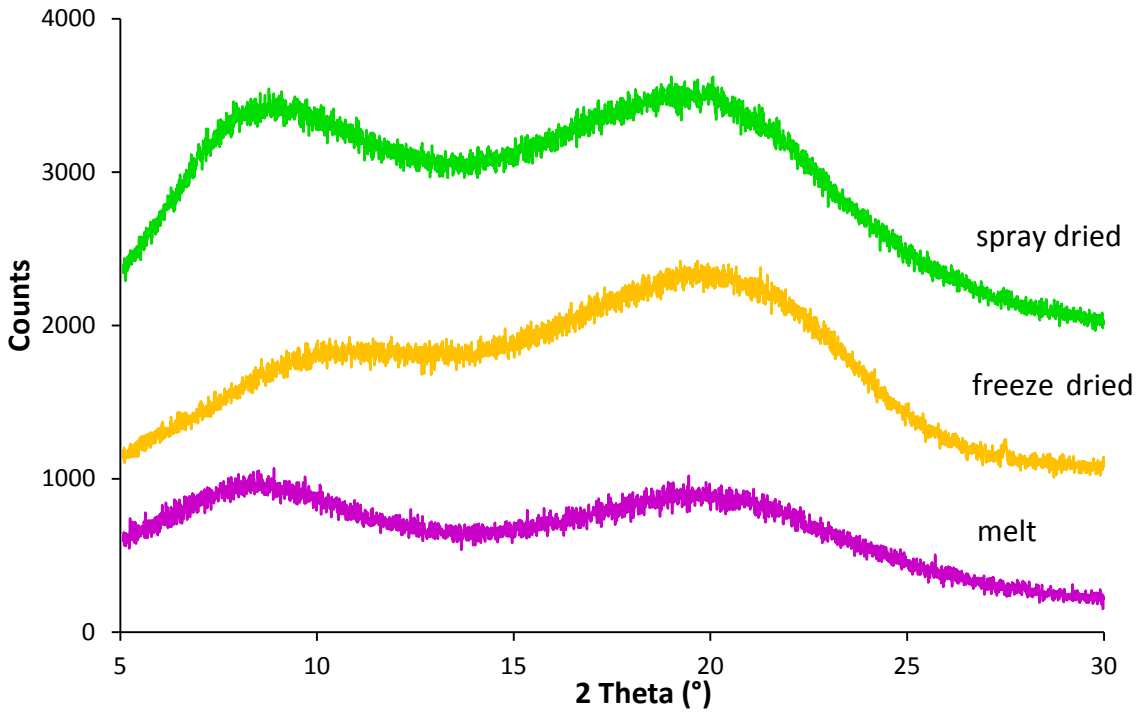


**Figure 15 Offset powder X-ray diffraction patterns for amorphous lactose samples derived from spray drying, freeze drying and rapid quenching from melt**

### *5.6.3.2 Differential Scanning Calorimetry*

Differential Scanning Calorimetry was carried out on the three samples (see Figure 16). The glass transition changes shown are consistent with amorphous properties.

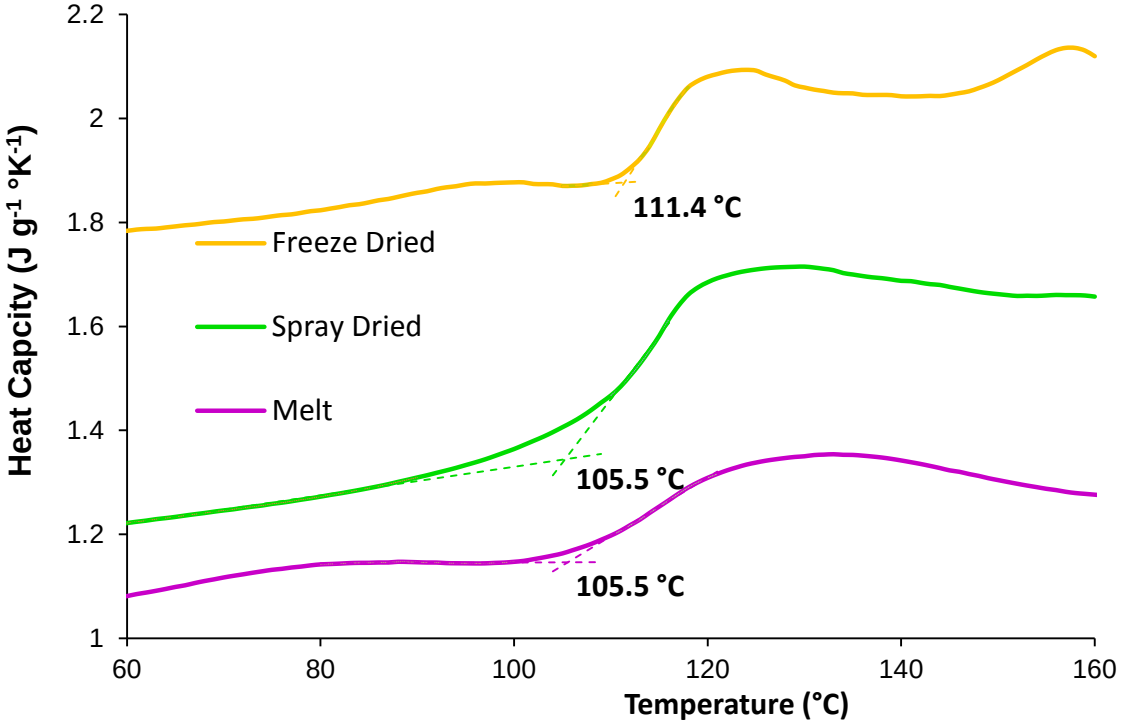


**Figure 16 Offset DSC trace for spray dried, freeze dried and melt samples (readings offset)**

### *5.6.3.3 FT-IR*

The infra red spectra in Figure 17 shows that the three amorphous preparations possess absorbencies consistent with a mixture of both α and β lactose isomers. The 50:50 combined spectrum of α-lactose stable and β-lactose shows some similarities to the amorphous preparations, although the peaks in the 50:50 spectrum are much sharper than the broad features of the spray dried freeze dried and melt samples.

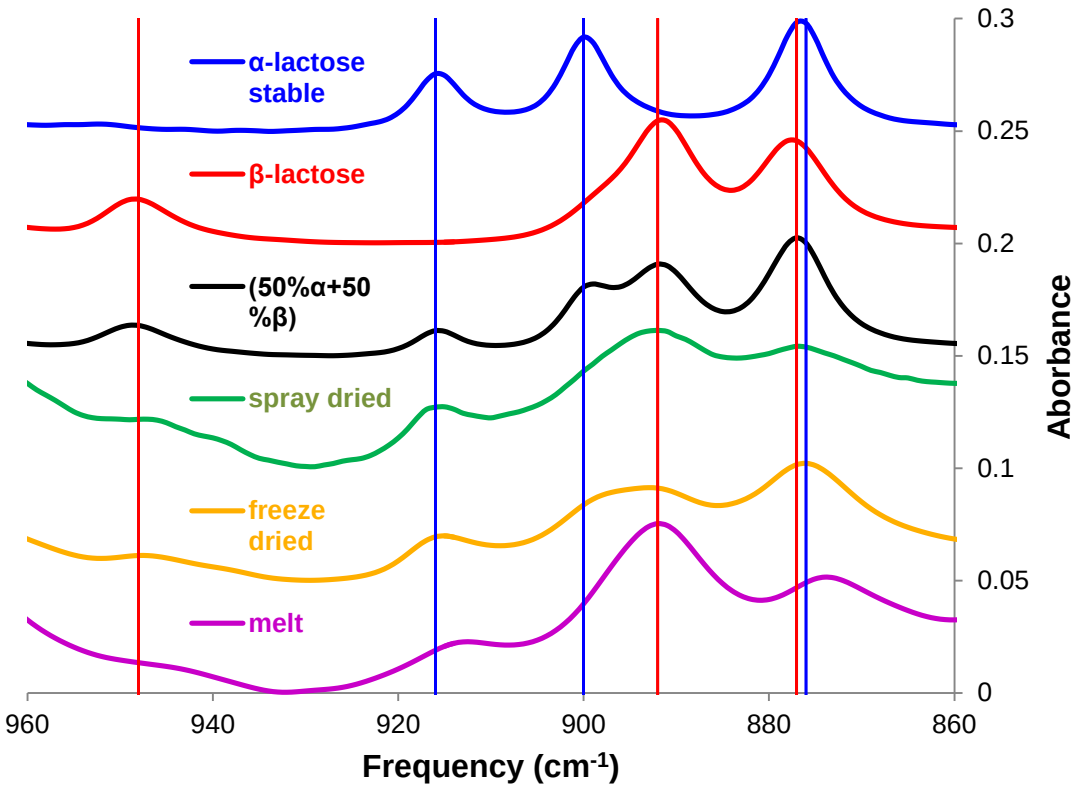


**Figure 17 FT-IR spectrum of 50:50 mixture of α-lactose stable and β-lactose compared to the spay dried lactose infra red spectrum, (between 960 and 860 $cm^{-1}$)**

Water absorbs in the infra-red at 1595 $cm^{-1}$ in the vapour state and 1644 $cm^{-1}$ in the liquid state; the shift between the two absorptions is due to hydrogen bonding. In Figure 18, absorbance is observed between 1600 and 1650 $cm^{-1}$ for all three amorphous forms. The largest peak arises in the freeze dried and the smallest in the melt, suggesting the freeze dried sample may contain the most water and the melt the least, though IR spectroscopy is not generally considered quantitative. The freeze dried, spray dried and melt samples show absorbance maxima at 1613 and 1632 $cm^{-1}$, at 1630 $cm^{-1}$ respectively. The major absorption peak of water at circa 3500 $cm^{-1}$ is obscured by the stretch of the OH group on the glucose sub-unit.

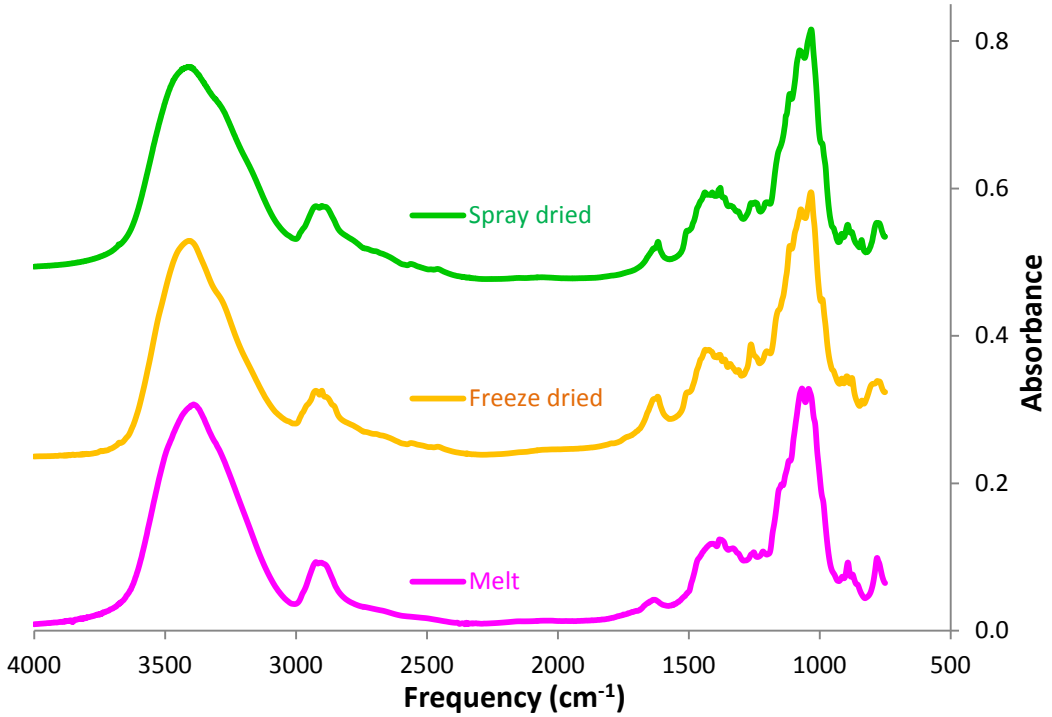


**Figure 18 FT-IR of spray dried, freeze dried and melt lactose samples (between 750 and 4000 $cm^{-1}$)**

### *5.6.3.4 $^{13}C$ CP-MAS NMR*

The $^{13}C$ CP-MAS NMR spectra in Figure 19 show the three amorphous preparations, these show much broader peaks than the crystalline samples. Figure 19 shows the peaks identified by Kirk as characteristic of crystalline lactose polymorphs by dashed / dotted black, red and blue lines.[10] The two peaks in the crystalline β-lactose spectrum at 79 and 82 ppm appear as deviation from the baseline in the amorphous preparations. The α-lactose monohydrate and α-lactose stable spectra show a sharp peak at 93 ppm, which is also seen as a broader peak in the spectra of the amorphous preparations. A peak at 97 ppm in the spectrum of all three amorphous preparations shows no direct equivalent in any of the crystalline polymorph spectra shown. The peak at 105 ppm appears at a lower chemical shift than would otherwise be expected for a direct combination of the α-lactose monohydrate and β-lactose polymorphs. The peak at 88 ppm in the α-lactose monohydrate spectra does not appear in the spectra of the amorphous preparations, this suggests that the α-lactose present is more similar to α-lactose stable than α-lactose monohydrate. The amorphous preparations also appear consistent with a mixture of both α and β lactose isomers in approximately equal quantities.

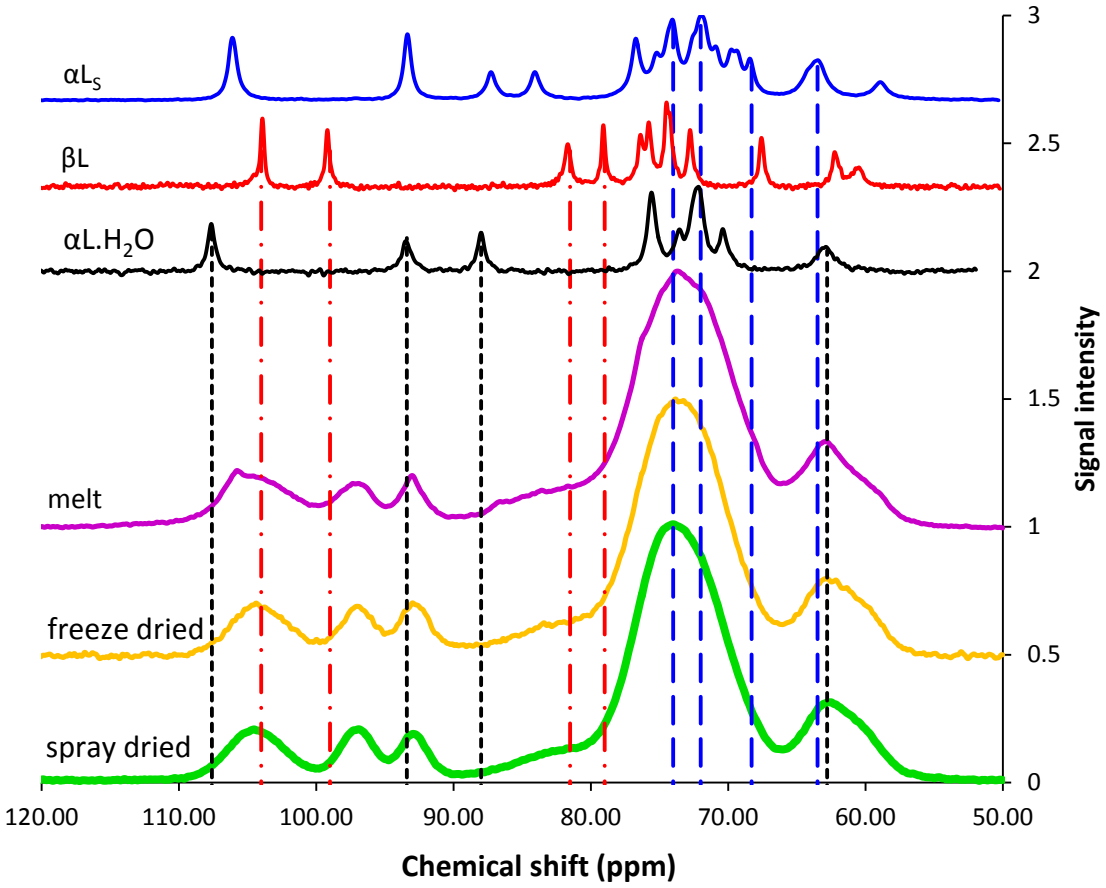


**Figure 19 $^{13}$C CP MAS NMR spectra of freeze dried, spray dried and melt. The vertical dashed / dotted black, red and blue lines mark the peaks that characterise lactose polymorphs reported by Kirk[10]**

### *5.6.3.5 Dynamic Vapour Sorption*

The DVS runs on the spray dried and freeze dried samples (Figure 20 and Figure 21) show very similar results, with an increase in the water adsorbed at the 40% relative humidity (RH) and re-crystallisation occurring at 60% RH. The weight difference between the initial and final readings was 2.72% and 2.90% for the freeze dried and spray dried samples.

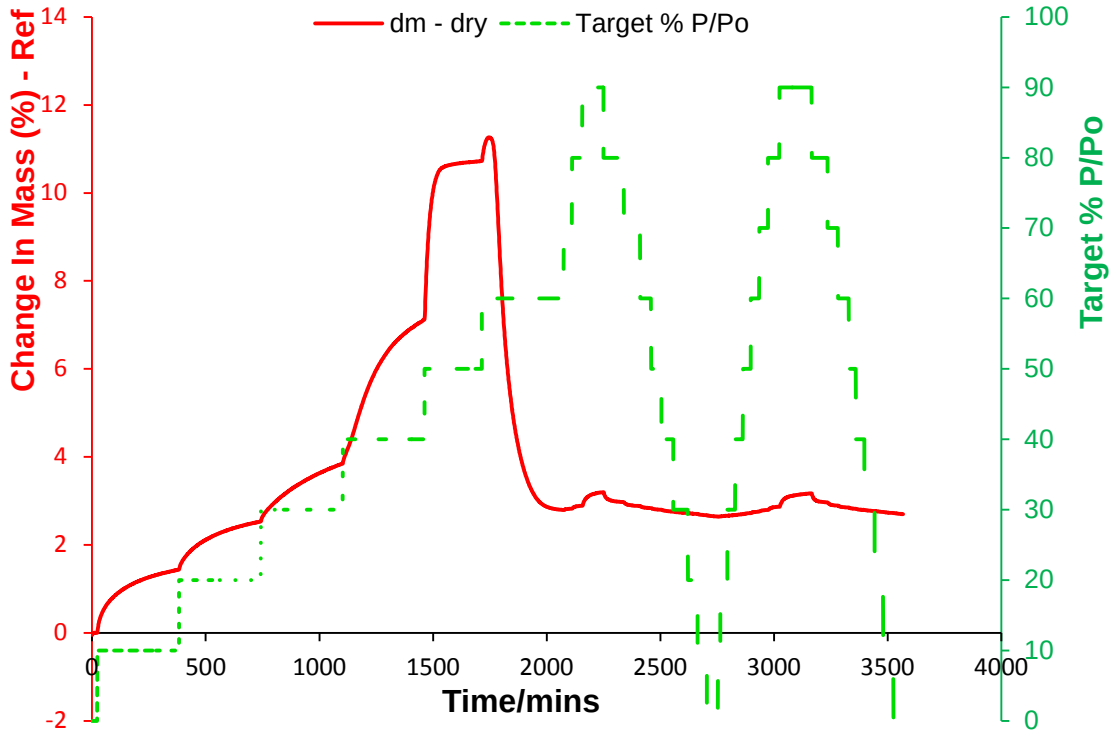


Figure 20 DVS using spray dried lactose

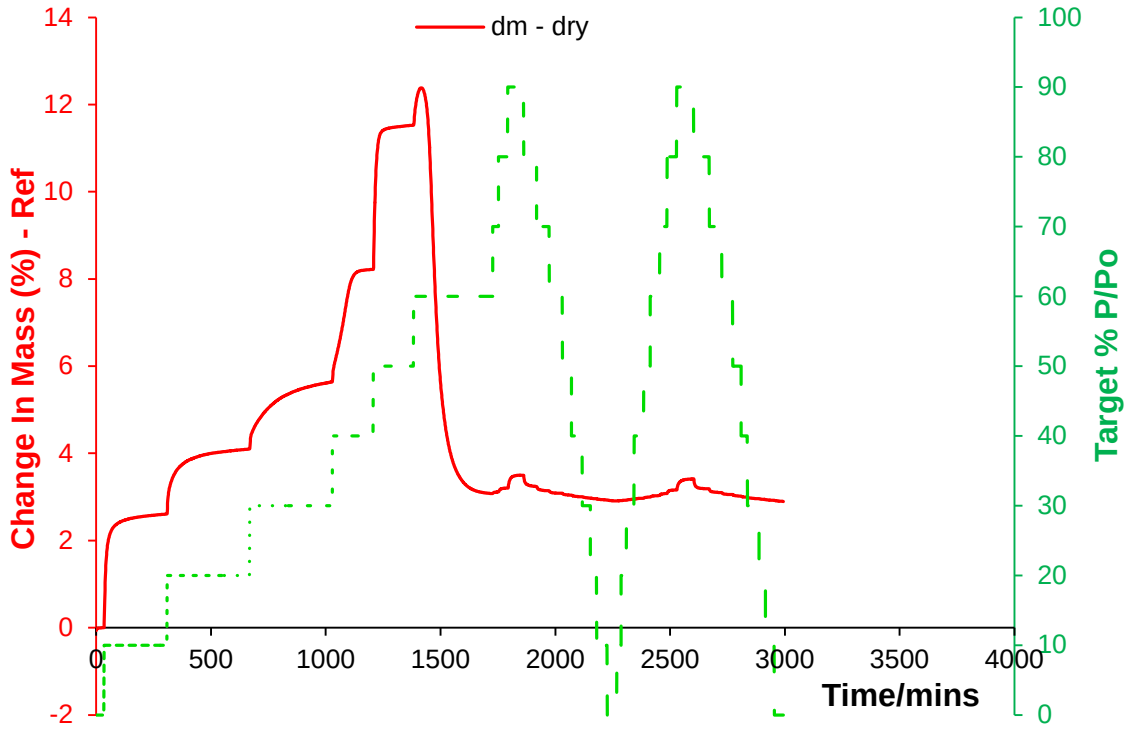


Figure 21 DVS using freeze dried lactose

The DVS trace for the sample made by the melt sample showed a completely different pattern to the freeze and spray dried samples. The amount of water absorbed by this sample was much greater than that the spray and freeze dried samples. The second cycle for the melt sample was little different to the first, which was in sharp contrast

those of the spray and freeze dried samples that showed much less absorbance of moisture. This behaviour is unusual, since the second cycle should show entirely crystalline behaviour. The issue here may be to do with the grain boundary of the melt produced sample being more difficult to penetrate than amorphous samples prepared by other methods. The melt sample also appeared to retain moisture even with exposure to dry nitrogen for several hours with a final weight gain of 7.49%.

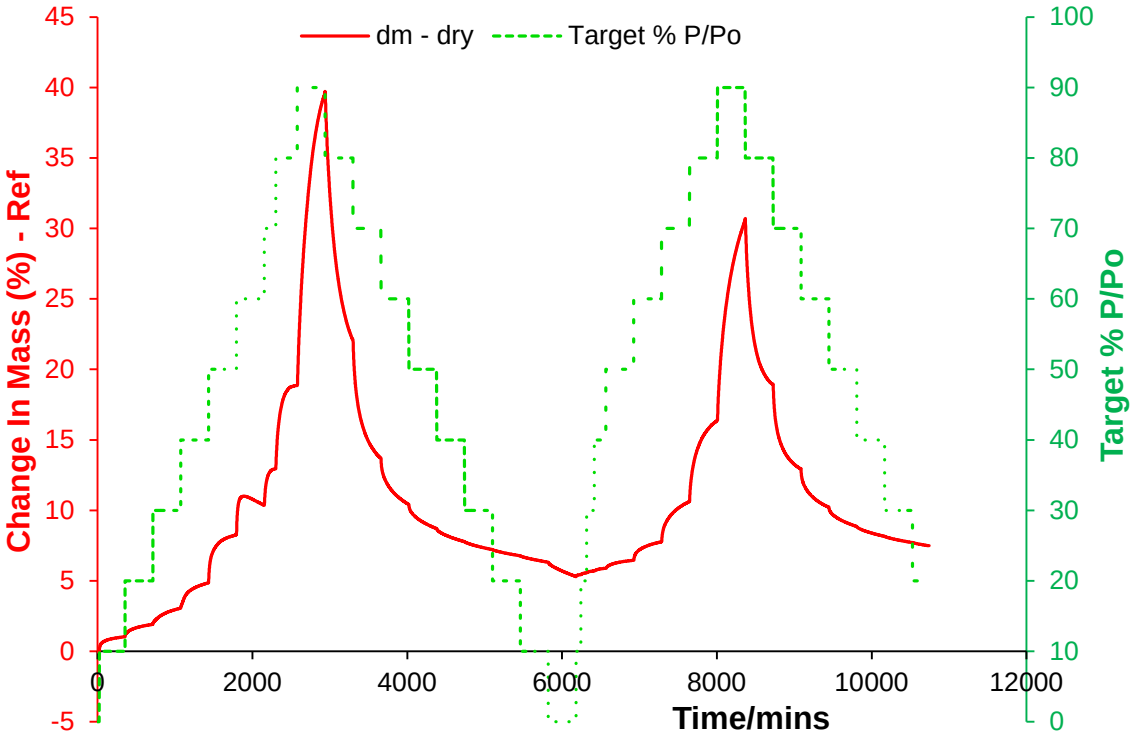


**Figure 22 DVS run for a melt made from a rapid quench melt of α-lactose stable**

| Sample | DVS mass change (%) |
|---|---|
| α-lactose stable (10101901) | 5.20% |
| β-lactose (08060202) | 0.09% |
| Spray dried | 2.72% |
| Freeze dried | 2.90% |
| melt | 14.14% |

**Table 6 DVS mass change for α-lactose stable standard, a sample of β-lactose and amorphous lactose prepared by different routes**

The melt sample produced a result that was difficult to reconcile, suggesting that it retained moisture even under 0% relative humidity conditions for up to 6 hours. The spray dried and freeze dried samples show an increase in weight, however this weight change was not the 5.32% expected if the entire sample was converted from anhydrous α lactose to α-lactose monohydrate as proposed by Buckton and Darcy.[12] If

all the anhydrous α-lactose in the spray dried and freeze dried samples detected by the GC derivatisation method were converted to α-lactose monohydrate, then a mass increase of 2.43 and 2.65% would have been expected for the spray and freeze dried samples respectively. The difference between these weight change values was 0.29% and 0.25% the equivalent of 5.5% and 4.7% of the original sample weight. The DVS and GC results are consistent with the idea of the amorphous spray dried and freeze dried lactose containing both α and β lactose in roughly similar proportions.

#### *5.6.3.6 GC-FID derivatisation of lactose isomers*

The three amorphous samples of lactose were subjected to isomer analysis by GC derivatisation, the results are summarised in tables 7, 8 and 9. The results show all three amorphous preparations to contain a mixture of isomers. The melt was also shown to be composed of a mixture of the isomers despite its preparation method from same α-lactose stable standard shown in Table 9.

| **Spray dried amorphous lactose** | **Vial** | **GC Injection repeat** | | |
|---|---|---|---|---|
| | | **a** | **b** | **c** |
| Serum vial number | 14 | 45.2% | 46.0% | 45.9% |
| | 17 | 45.4% | 45.6% | 46.0% |
| | 20 | 45.5% | 45.8% | 45.8% |
| | | **overall average =** | | **45.7%** |
| | | **95% confidence limits =** | | **±0.21%** |

**Table 7 Spray dried analysis results of GC normalised peak area responses to α-lactose**

| **Freeze dried amorphous lactose** | **Vial** | **GC Injection repeat** | | |
|---|---|---|---|---|
| | | **a** | **b** | **c** |
| Serum vial number | 15 | 49.7% | 49.7% | 49.7% |
| | 18 | 49.7% | 50.1% | 49.7% |
| | 21 | 49.8% | 50.0% | 50.0% |
| | | **overall average =** | | **49.8%** |
| | | **95% confidence limits =** | | **±0.12%** |

**Table 8 Freeze dried analysis results of GC normalised peak area responses to α-lactose**

| **Rapid quench melt amorphous lactose** | **Vial** | **GC Injection repeat** | | |
|---|---|---|---|---|
| | | **a** | **b** | **c** |
| Serum vial number | 16 | 48.2% | 48.6% | 48.8% |
| | 19 | 48.3% | 48.5% | 48.3% |
| | 22 | 48.0% | 48.2% | 48.6% |
| | | **overall average =** | | **48.5%** |
| | | **95% confidence limits =** | | **±0.22%** |

**Table 9 Melt analysis results of GC normalised peak area responses to α-lactose**

### 5.6.4 Discussion

The X-ray powder diffraction, FT-IR, $^{13}$C CP-MAS NMR and DSC results suggest that the spray dried, freeze dried and melt preparations are amorphous in nature. The $^{13}$C CP-MAS NMR and DVS results suggest that the α-lactose detected in the amorphous preparations possess similar properties to α-lactose stable. The $^{13}$C CP-MAS NMR, FT-IR and GC derivatisation analysis suggest that the amorphous samples contain approximately equal portions of both α and β anhydrous anomers. Given that the spray dried and freeze dried samples were prepared from solutions at room temperature, allowing mutarotation to occur should produce a 37 % α monohydrate: 63 % β isomer ratio. The results for the amorphous preparations suggest an isomer mix slightly favouring the β isomer which is consistent with anomeric mixtures of lactose generated in solution. This result is in direct opposition to the findings of Ramos, who found 66% α and 34% β isomer mix for spray dried lactose.[5] A particularly unexpected result from this work arises from the melt sample which was prepared from the α-lactose stable standard material and produced a 48 % : 52 % α to β isomer ratio, suggesting that mutarotation occurs while the sample is molten.

## 5.7 Characterising the DVS residues

### 5.7.1 Introduction

Buckton and Darcy suggest that amorphous lactose is wholly converted to α-lactose monohydrate by DVS using water as the sorbate.[12] This work seeks to demonstrate that DVS experiments on amorphous lactose composed of a mixture of α and β lactose isomers, produces a residue mixture of α-lactose monohydrate and β-lactose.

### 5.7.2 Experimental

The residues were taken from the DVS runs shown in section 5.6.3.5. The experimental methods are set out in chapter 3

## 5.7.3 Results and discussion

### *5.7.3.1 X-ray powder diffraction*

X-ray powder diffraction patterns of both the residues of the DVS runs on the spray and freeze dried samples show reflections that suggest the presence of crystalline α-lactose monohydrate and β-lactose, (see Figure 23).

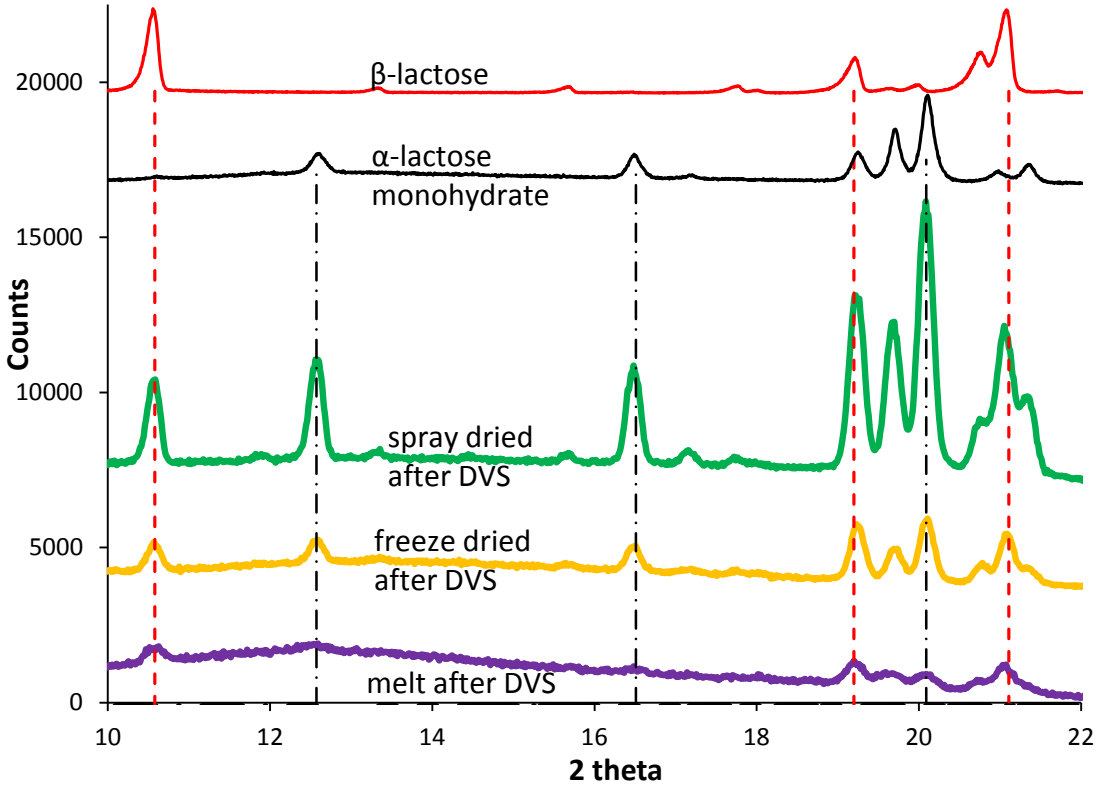


**Figure 23 X-ray powder diffraction of DVS residues of spray and freeze dried lactose**

### *5.7.3.2 Results - FT-IR*

The infra red spectrum of the DVS residues displayed in Figure 24 showed more structure in the OH stretch region between 3500 and 3000 $cm^{-1}$ than the original amorphous samples. The CH stretch is also much better defined between 3000 and 2800 $cm^{-1}$, suggesting these samples were crystalline rather than amorphous. Figure 25 shows the infrared spectrum between 960 and 860 $cm^{-1}$, the peak maxima for α-lactose monohydrate (blue) and β-lactose (red) identified by Kirk[10] are shown as vertical lines. The vertical lines are a good match to the peaks the DVS residues for all three amorphous forms tested.

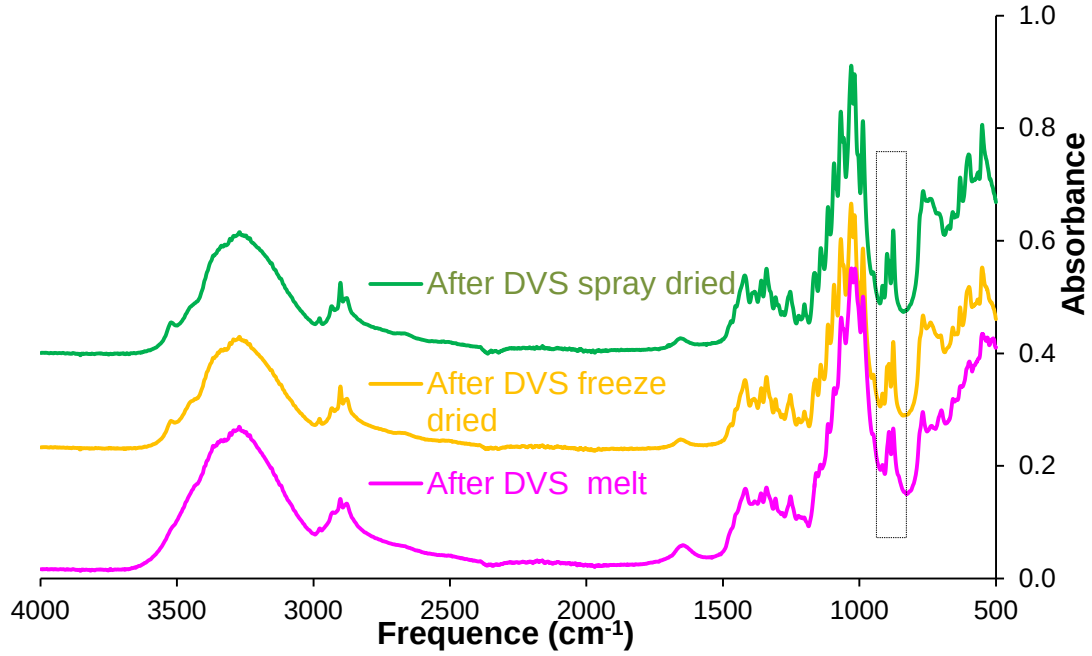


Figure 24 FT-IR spectra of DVS residues 4000 to 500 $cm^{-1}$

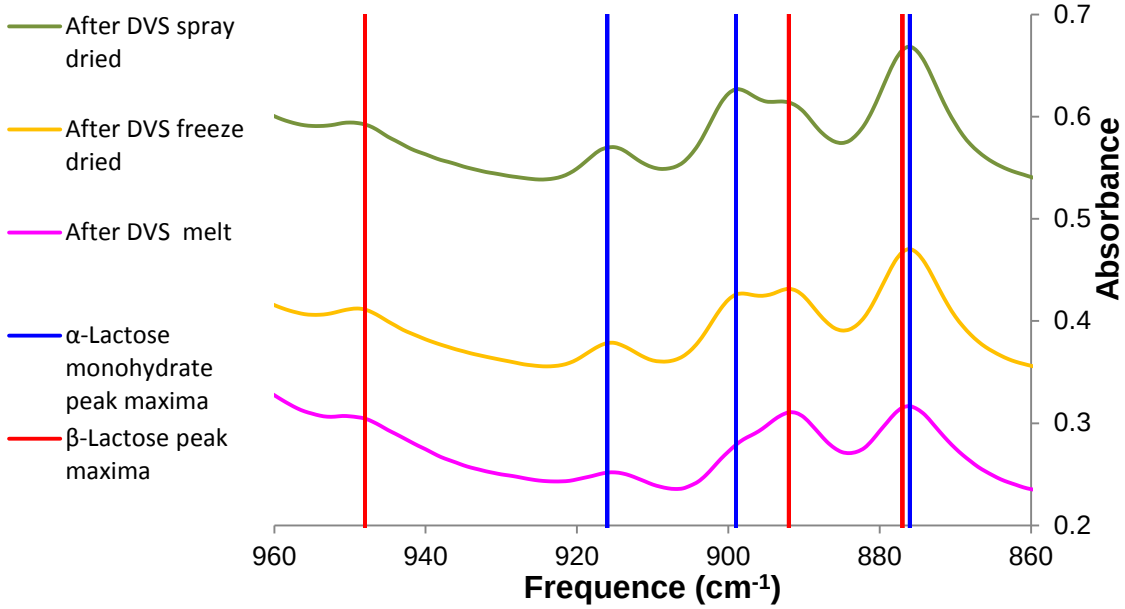


Figure 25 FT-IR spectra of DVS residues 960 to 860 $cm^{-1}$

| DVS residues | | |
|---|---|---|
| Spray dried ($cm^{-1}$) | Freeze dried ($cm^{-1}$) | Melt ($cm^{-1}$) |
| 949 | 949 | 950 |
| 916 | 916 | 916 |
| 899 | 899 | 892 |
| 892 | 892 | 876 |

| Crystalline polymorphs | | | |
|---|---|---|---|
| α-Lactose monohydrate ($cm^{-1}$) | β-Lactose ($cm^{-1}$) | α-Lactose stable anhydrous ($cm^{-1}$) | α-Lactose anhydrous hydroscopic ($cm^{-1}$) |
| | 948 | 930 | |
| 916 | | 913 | 913 |
| 899 | 892 | 894 | 897 |
| 876 | 877 | 874 | 874 |

Table 10 FT-IR peaks for DVS residues and crystalline polymorphs (960 - 860 $cm^{-1}$)

The absorbances for the DVS residues shown in Table 10, list values at 899 and 916 $cm^{-1}$ corresponding to crystalline α-lactose monohydrate, in addition the residue peak at 949 $cm^{-1}$ corresponds to that of β-lactose. This suggests the presence of crystalline α-lactose monohydrate and β-lactose in the DVS residues.

### *5.7.3.3 Solid state $^{13}C$ CP MAS NMR*

Figure 26 shows the solid state $^{13}C$ CP MAS NMR spectrum of the residue remaining after spray dried lactose had been run on the DVS instrument. The residue spectrum appears to be a combination of α-lactose monohydrate and β-lactose. Unfortunately insufficient residues were recovered from the freeze dried and melt DVS runs, to produce their spectra.

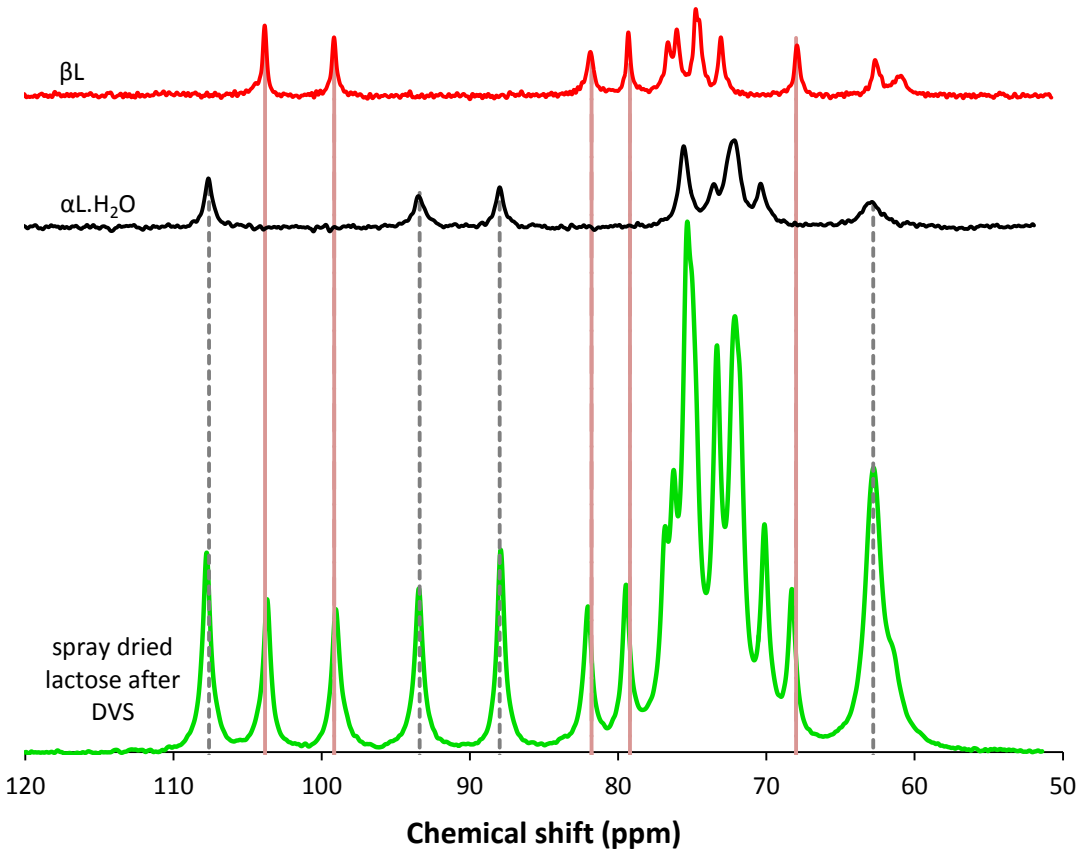


**Figure 26 $^{13}C$ solid state NMR spectrum of spray dried lactose after DVS characterisation**

#### *5.7.3.4 Discussion*

The X-ray powder diffraction patterns shows peaks coincident at the 2θ angles at which α-lactose monohydrate and β-lactose would be expected. The FT-IR spectra show peaks at the same wave numbers as a mixture of α-lactose monohydrate and β-lactose. Once again the solid state $^{13}C$ NMR suggests the residues are a combination of α-lactose monohydrate and β-lactose. The evidence from powder X-ray diffraction, FT-IR and solid state NMR, all suggests that the DVS residues from amorphous samples of spray dried, freeze dried lactose crystallise out in to a mixture of α-lactose monohydrate and β-lactose.

If all the amorphous lactose were to be converted to crystalline α-lactose monohydrate than a mass gain of 5.32% would be expected. The DVS runs on crystalline lactose polymorphs showed only the α-lactose anhydrous stable producing significant mass change of 5.2%. This suggests that the α-lactose present in the spray dried and freeze dried samples has some similarity to α-lactose anhydrous stable. The DVS experiments for spray dried and freeze dried samples show a mass gains at the end of their runs of 2.72% and 2.92% suggesting a final α-lactose monohydrate content of 51.4% and 55.2% respectively. These values are similar to the GC-FID isomer content of the original spray dried and freeze dried samples.

The evidence gathered from FT-IR, powder X-ray diffraction and CP MAS NMR all suggest that the (water sorbate) form a mixture of α-lactose monohydrate and β-lactose crystalline polymorphs.

## 5.8 Conclusions

Gas Chromatography is a useful technique for quantifying the proportion of lactose anomers in mixtures. This is achieved using a derivatisation technique which minimises mutarotation by addition of reactants to dry lactose in the specific order of N-(trimethylsilyl)imidazole , dimethylsulphoxide and finally pyridine.

All three amorphous lactose samples examined in this work were found to be composed of a mixture of α-lactose stable anhydrous and β-lactose, in approximately similar proportions. The formation of amorphous lactose by freeze drying and spray drying both occur via water solutions, in which mutarotation would be expected. In contrast the melt sample was prepared from 95% α-lactose in the form of the crystalline α-lactose anhydrous stable polymorph, this suggests that mutarotation occurs during this process.

The analysis of the residues from the DVS experiments on spray dried amorphous lactose preparations shows it to be composed of a mixture of crystalline α-lactose monohydrate and β-lactose, in similar proportions to their amorphous starting materials. These conclusions contradict Buckton and Darcy's suggestion that amorphous lactose converts entirely to α-lactose monohydrate during a DVS experiment.[12]

***References***

1 T. K. Lindhorst, *Essentials of carbohydrate chemistry and biochemistry*, Wiley, Chichester, 2000.

2 R. Liu, *Water-Insoluble Drug Formulation, Second Edition*, CRC Press, United States, 2008.

3 P. F. Fox and P. L. H. McSweeney, *Dairy Chemistry and Biochemistry*, Springer, Berlin, 1998.

4 J. F. Robyt, *Essentials Of Carbohydrate Chemistry<br />*, Springer, India, 2009.

5 R. Ramos, S. Gaisford and G. Buckton, *Int. J. Pharm.,* 2005, 300, 13-21 (DOI:DOI: 10.1016/j.ijpharm.2005.04.022).

6 I. A. Fowlis, *Gaschromatography: analytical chemistry by open learning / author: Ian A.Fowlis.Published on behalf of ACOL (University of Greenwich)*, Wiley, Chichester, 1995.

7 D. C. Harris, *Quantitative chemical analysis*, W. H. Freeman, New York, 2002.

8 C. C. Sweeley, R. Bentley, M. Makita and W. W. Wells, *J. Am. Chem. Soc.,* 1963, 85, 2497 (DOI:10.1021/ja00899a032).

9 S. K. Dwivedi, *Anomeric Composition and Solid State Properties of Lactose*, University of British Columbia, Canada, 1988.

10 J. H. Kirk, S. E. Dann and C. G. Blatchford, *International Journal of Pharmaceutics,* 2007, 334, 103-114.

11 K. D. Ross, *J. Dairy Sci.,* 1978, 61, 152-158.

12 G. Buckton and P. Darcy, *International Journal of Pharmaceutics,* 1995, 123, 265-271.

# CHAPTER 6

# The influence of moisture and oxygen on $^{13}C$ solid state CP-MAS NMR

## 6.1 Introduction

At low humidity levels, amorphous sugars absorb water to equilibrium levels that are dependent on the relative humidity and the amount of amorphous material present. The measured mass change minus the equivalent mass change for the crystalline sample has been used by Mackin to calculate the amorphous content of unknown samples.[1] This method assumes all amorphous materials absorb water in an identical manner regardless of their preparation method, which may not be the case. This is because different preparation methods could lead to different levels of disorder due to the different water contents e.g. spray dried and temperatures of preparation.

The role of plasticiser in polymer science is to reduce the glass transition point and modify the properties from brittle to plastic. Once dissolved in the polymer during manufacture the plasticiser works by sitting in between polymer chains allowing them move more freely relative to one another. Water absorbed by amorphous sugars acts as a plasticiser reducing the glass transition point.[2]

In simple techniques which involve a change in mass such as DVS, the sample is changed during the process and a response is evaluated without any structural information pertaining to the crystalline or amorphous state of that sample being available. However some information on local order can be obtained using techniques which are affected by short range interactions. For example, $^{13}C$ solid state CP-MAS NMR spectroscopy can be used to investigate the extent of short range order, giving details of the chemical environment of individual carbon atoms within a small molecule by careful choice of particular parameters such as relaxation time. Crystalline lactose polymorphs are used in pharmaceutical formulations but during the process of formulation, amorphous lactose can also be produced via different processes such as micronisation. This chapter will attempt to characterise amorphous lactose using solid state NMR and compare the spectra produced, including the spectral parameters. The four crystalline polymorphs of lactose have been previously characterised by $^{13}C$ solid state NMR and their spectra published[3] and hence differences between the spectra of crystalline and amorphous materials from different sources can easily be compared.

Liquid $^{13}C$ NMR spectral acquisition takes much less time than a comparable solid state $^{13}C$ NMR, since small molecules dissolved in a liquid are subjected to the ever

changing dipolar interactions from the random motion of the solvent molecules to bring about relaxation. Solid state $^{13}C$ NMR relaxation processes are slow and occur through the thermal vibration and internal molecular motions occurring within the solid. Previous studies by Lubach and co-workers have suggested that relaxation times in solids can be strongly affected by the presence of water, where physisorbed water facilitates faster relaxation. However the effect of different atmospheres has not been investigated. This study considers the effects of using different gases to alter the relaxation times of $^{13}C$ in amorphous lactose. Some previous work investigated the effect on the NMR parameters of dissolved oxygen in liquids which may provide useful information on the nature of a solid, since this includes diffusion terms and could show the extent to which oxygen may percolate into the solid structure.

## 6.2 Experimental

The samples used in this work are the same samples used in the lactose isomer analysis chapter. The spray dried and freeze dried samples were supplied by DMV-Fonterra Excipients GmbH. A third sample was prepared by heating 2.0 g of crystalline α-lactose stable until molten, which was then quenched in liquid nitrogen and immediately stored under argon in a glove box.

DVS, XRD FT-IR and DSC characterisation were carried out on the three amorphous samples from spray-drying, freeze-drying and melt phase preparation according to the experimental details set out chapter 3 with the results given in chapter 4. In addition, elemental analysis and Karl Fischer moisture analysis were carried out before investigating the effect of oxygen gas on $^{13}C$ CP MAS NMR proton saturation recovery relaxation. The relaxation times for the three amorphous samples prepared via different methods were initially measured by placing the samples in solid state rotors and sealing with a cap under an argon atmosphere in a glove box. After each set of NMR measurements, the rotor cap was removed and the sample placed in a Schlenk tube, evacuated 3 times and flooded with either $N_2$ or $O_2$ gas, after which the rotor cap was replaced and repeat analyses taken.

The effect of moisture on the glass transition point was investigated using the SDT Q600 by holding the freeze dried sample under dry nitrogen gas for 2 hours at temperatures ranging from 30 to 70 °C in 10 °C intervals, before carrying out the

calibrated experiment measuring heat flow between 30 and 260 °C at a rate of 10 °C per min.

## 6.3 Results for the spray dried, freeze dried and melt samples

### 6.3.1 Elemental Analysis

CHN Elemental analysis was performed on an Exeter Analytical CE 440 elemental analyzer. The results of the three amorphous samples are set out in Table 1 along with the calculated values for α-lactose monohydrate and anhydrous lactose. The values obtained for carbon and hydrogen were not commensurate with the expected values for anhydrous lactose for either spray dried or freeze dried lactose, whereas the melt prepared sample is similar.

| Sample | C% | H% | N% | Estimated % water |
|---|---|---|---|---|
| Lactose (monohydrate expected) | 40.00% | 6.71% | 0.00% | 5.00% |
| Lactose (anhydrous expected) | 42.11% | 6.48% | 0.00% | 0.00% |
| spray dried | 40.81% | 6.65% | 0.08% | 3.09% |
| freeze dried | 39.91% | 6.62% | 0.10% | 5.19% |
| lactose melt | 42.33% | 6.28% | 0.10% | 0.00% |

**Table 1 CHN analysis on arrival, prior to drying**

The results for carbon and hydrogen for the freeze dried are nearly identical to α-lactose monohydrate, suggesting that freeze dried lactose contains a similar level of water. The total amount of water present in samples can be estimated from the carbon and hydrogen results. The estimated water content is shown in the column "**Estimated % water**". The effect of water content $w$ was estimated for carbon and hydrogen $E_C$ and $E_H$ using equations 1 to 2.

$$E_C = (1 - w) * 0.4211 \quad \text{Equation 1}$$

$$E_H = [(1 - w) * 0.0648] + [w * 0.1119] \quad \text{Equation 2}$$

$$SUM = \sqrt{(M_C - E_C)^2 + (M_H - E_H)^2} \quad \text{Equation 3}$$

The values of $M_C$ and $M_H$ were set using the carbon and hydrogen contents in table 1 for each sample. The estimated water content ($w$) shown in column 5 of Table 1 was

calculated using the Microsoft Excel Solver algorithm, this was set to minimise $SUM$ (Equation 3) by changing the water content ($w$), which was initially set to 0.1 (10%).[4]

### 6.3.2 Karl Fischer water determination

The Karl Fischer titrations were carried out on the spray dried and melt samples (see Table 2).

| Description | Result % | 95% confidence limit |
|---|---|---|
| Spray Dried | 2.9 | ±0.4 |
| Melt | 0.2 | ±0.4 |

**Table 2 Karl Fischer results prior to vacuum drying at 40°C**

The melt sample showed a very low water content (0.2% w/w), in agreement with the CHN results implying that the sample was anhydrous. Measurements were not made on the freeze dried sample as it arrived, since very little sample was available. The entire freeze dried sample and some of the spray dried sample were vacuum dried at 40 °C for 48 hours to reduce the water content, and measurements repeated (see Table 3). The freeze dried sample shows large confidence limits relative to the result, since the amount of material used in the analysis was small due to its low bulk density.

| **Description** | **Result %** | **95% confidence limit** |
|---|---|---|
| spray dried | 1.1 | ±0.6 |
| freeze dried | 0.5 | ±1.2 |

**Table 3 Karl Fischer measurements after vacuum drying at 40°C**

### 6.3.3 Dynamic vapour sorption results

The DVS experiments on the amorphous preparations are seen in figures 20, 21 and 22 of Chapter 5. The DVS program was set to equilibrate for a maximum of 6 hours at each individual humidity point. This maximum time point was reached in the case of all the points shown in Figure 1, meaning that equilibrium had not been reached. Figure 1 shows how easily each of the amorphous preparation absorbs water, with the freeze dried preparation absorbing most easily and the melt preparation the most resistant. Another important point to Figure 1 is that a 5.32% mass change represents

a one to one relationship between the number of moles of lactose and moles of absorbed water.

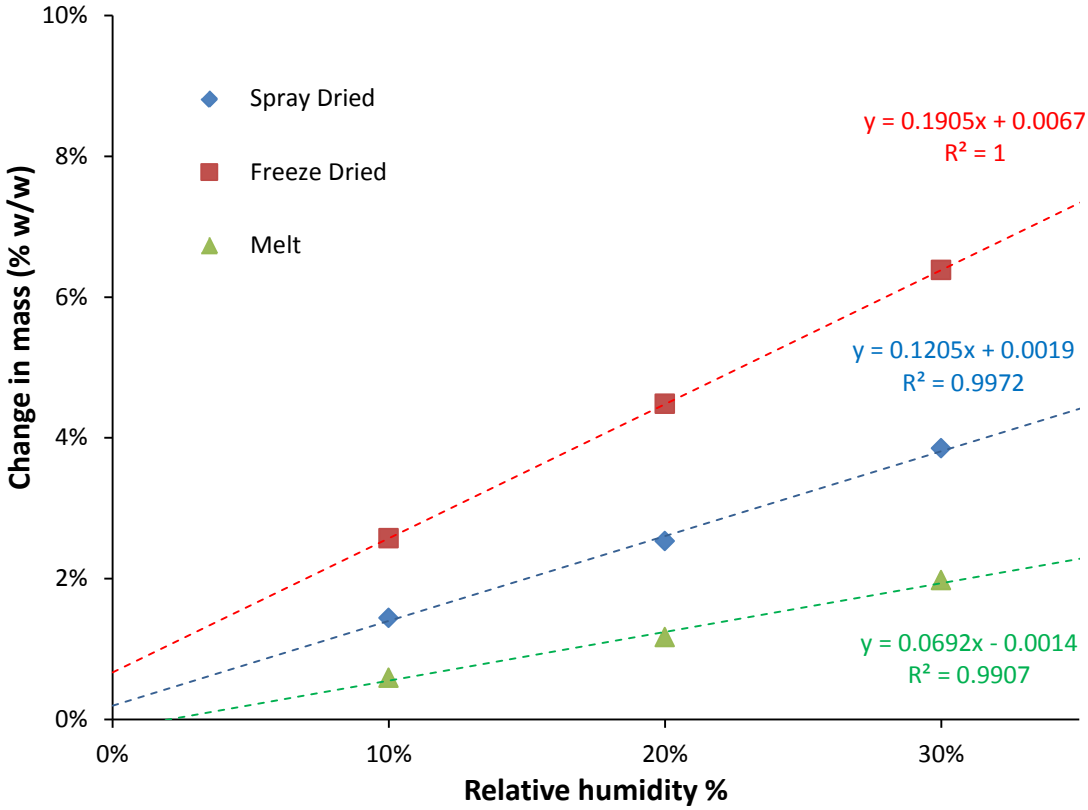


**Figure 1 DVS change in mass with relative humidity level for spray dried, freeze dried and melt samples**

The DVS trace for the sample made by the melt showed a completely different pattern to the freeze and spray dried samples (see figure 22 of Chapter 5). The amount of water absorbed by this sample was much greater than either the spray-dried and freeze-dried samples. The second cycle for the melt sample was little different to the first, which was in sharp contrast to those of the spray and freeze dried samples that showed much less absorbance of moisture. The melt sample appeared to retain moisture even with exposure to dry nitrogen for several hours, with a final weight gain of 14.1%.

### 6.3.4 Differential Scanning Calorimetry results

Glass transition temperatures are reduced by plasticisers, in the case of amorphous sugars, water acts as a plasticiser, reducing the glass transition point, predicted by Equation 4. [5]

$$Tg = \frac{w_a T_a + k w_b T_b}{w_a + k w_b}$$ **Equation 4**

Obtaining an amorphous sample of lactose completely free of water is very difficult, since solutions are used to produce the freeze dried and the spray dried samples. Water can also be released via the caramelisation reactions of lactose once melted which involves decomposition of the sugar. The spray dried sample was held at different temperatures for different lengths of time to find the conditions that minimised the impact of moisture on the glass transition temperature. The glass transition points of spray dried lactose, dried at different temperatures, are shown in Table 4.

| Hold temperature (°C) | time at temperature (hours) | Weight loss % | glass transition onset (°C) |
|---|---|---|---|
| 30 | 14 | 0.93 | 78.4 |
| 40 | 14 | 0.37 | 91.9 |
| 50 | 10 | 0.27 | 101.2 |
| 60 | 5 | 0.11 | 105.5 |
| 70 | 5 | 0.07 | 104.4 |

**Table 4 Glass transition onset temperatures measured weight loss measured using SDTQ600 combined DSC and TGA**

The dotted line in Figure 2 was fitted using the Gordon Taylor equation applying values of k=16.5, $T_{ga}$ = 382.2 °K (109.2 °C) and $T_{gb}$ = 136 °K.[5] This shows how the presence of even a small amount of moisture can have a profound influence on the properties of amorphous lactose.

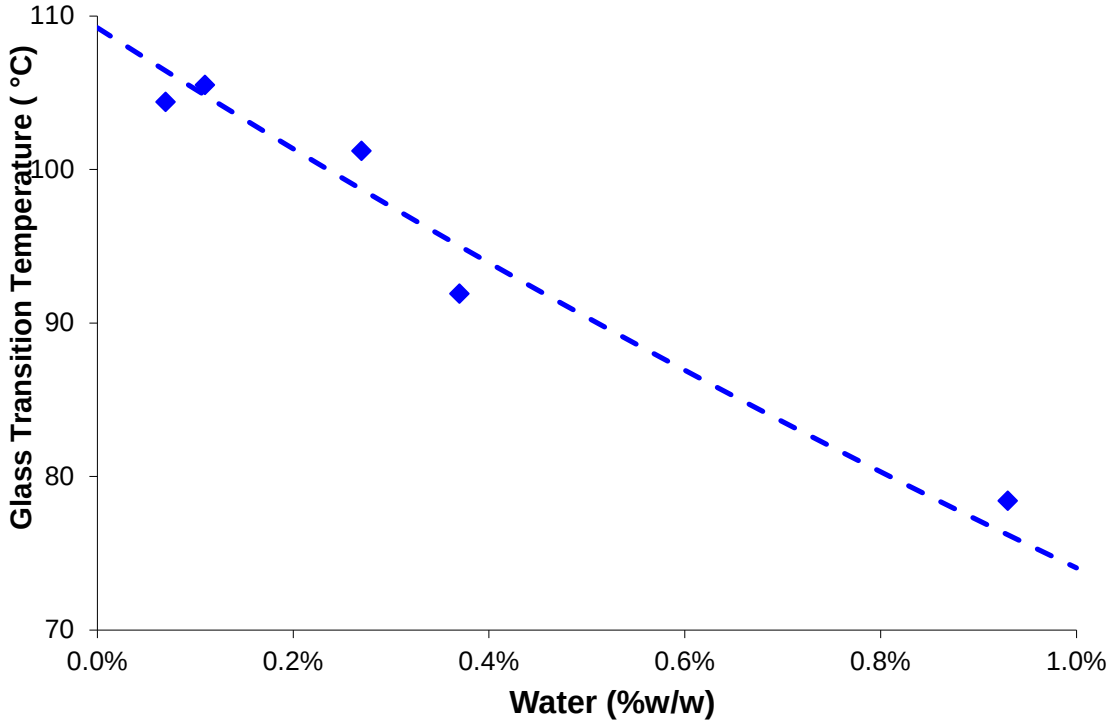


**Figure 2 Plot of Glass transition temperature onset against moisture content for spray dried lactose**

A glass transition is seen in all three samples at similar temperatures (see figure 16 in Chapter 5). The difference in heat capacity before and after the glass transition point was greatest for the spray dried sample and least for the melt sample (sees Table 5**)**.

| Sample | Glass transition point (°C) | Heat capacity difference before and after glass transition point (J / g) |
|---|---|---|
| Freeze dried | 111.4 | 0.18 |
| Spray Dried | 105.5 | 0.39 |
| Melt | 105.5 | 0.28 |

**Table 5 Glass transition onset temperatures and differences in heat capacity before and after the glass transition point for the 3 amorphous preparations**

### 6.3.5 Solid state $^{13}C$ NMR

The solid state $^{13}C$ NMR spectra of the spray dried, freeze dried and melt samples are shown in Figure 3. Amorphous materials tend to show broad peaks in solid state $^{13}C$ NMR spectra, in contrast to crystalline materials that produce very sharply defined peaks. Solid state $^{13}C$ NMR spectra of amorphous materials for different preparation routes tend to show very little changes in chemical shift.

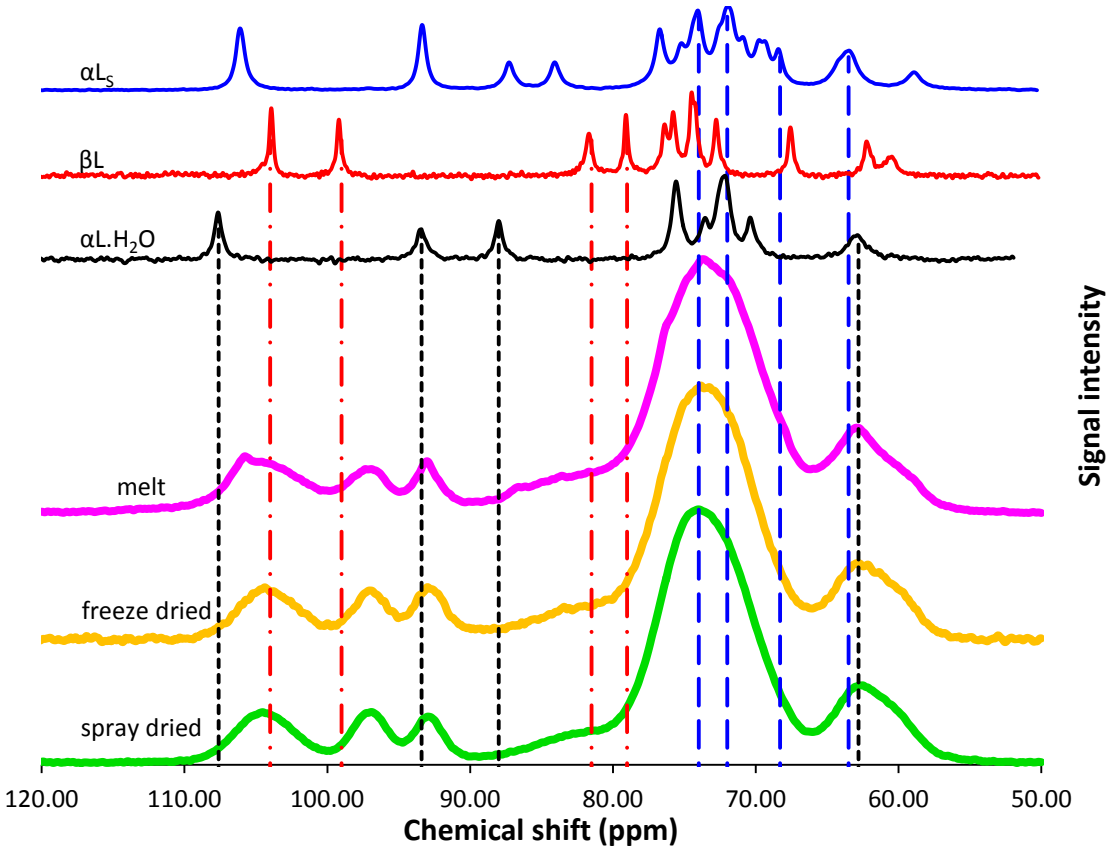


**Figure 3 $^{13}C$ solid state spectra of freeze dried, spray dried and melt**

Figure 3 is over laid by dashed lines at the chemical shifts for the polymorphs characterised by Kirk.[3] These lines suggest that the samples show chemical shifts consistent with a mixture of α-lactose monohydrate and β-lactose. The spectra obtained for the three samples appear identical. The proton relaxation times were also measured in an identical manner to that described in chapter 4, but with relaxation delays of 0.2, 0.5, 2, 4, 8, 15, 25 and 40 seconds.

The $T_1$ proton relaxation times were found using Equation 5, (which is described in chapter 4), given that $T_1$ was about 10 seconds for amorphous lactose, so when $\tau = 40$ an approximation can be made that $e^{-40/10} \cong 0$, so it follows that $I \cong I_0$.

$$I = I_0\left(1 - e^{-\tau/T_1}\right) \qquad \textbf{Equation 5}$$

With an approximate value of $I_0$ , the value of $T_1$ was found from the inverse of the slope plotting $ln\left(1 - \frac{I}{I_0}\right)$ against relaxation delay, this is shown in figures 4, 6 & 8 along with their fits in figures 5, 7 & 9. The measured $T_1$ proton relaxation times for the different samples and different atmospheres are shown in Table 6.

| | Peak | Chemical shift (ppm) | Relaxation times (s) | | |
|---|---|---|---|---|---|
| | | | Spray dried | Freeze dried | Melt |
| Atmosphere: **Argon** | 1 | 62.5 | 11.9 ( ± 0.8) | 9.0 ( ± 0.3) | 16.3 ( ± 0.4) |
| | 2 | 74.1 | 11.2 ( ± 0.9) | 7.2 ( ± 1.7) | 12.5 ( ± 0.3) |
| | 3 | 92.9 | 12.7 ( ± 1.0) | 9.0 ( ± 1.1) | 19.5 ( ± 1.6) |
| | 4 | 96.9 | 12.3 ( ± 0.9) | 4.0 ( ± 0.7) | 12.2 ( ± 1.7) |
| | 5 | 104.5 | 10.7 ( ± 0.6) | 7.2 ( ± 0.1) | 11.4 ( ± 1.4) |
| Atmosphere: **Oxygen** | 1 | 62.5 | 11.2 ( ± 0.4) | 4.1 ( ± 0.4) | 7.2 ( ± 0.2) |
| | 2 | 74.1 | 10.1 ( ± 0.7) | 6.6 ( ± 0.7) | 8.9 ( ± 0.2) |
| | 3 | 92.9 | 10.5 ( ± 1.0) | 3.9 ( ± 1.0) | 11.7 ( ± 0.4) |
| | 4 | 96.9 | 10.6 ( ± 1.2) | 4.1 ( ± 1.2) | 7.9 ( ± 0.2) |
| | 5 | 104.5 | 9.4 ( ± 1.3) | 5.8 ( ± 1.3) | 4.0 ( ± 0.3) |
| Atmosphere: **Nitrogen** | 1 | 62.5 | 10.8 ( ± 1.0) | 7.8 ( ± 1.0) | 11.0 ( ± 0.5) |
| | 2 | 74.1 | 9.5 ( ± 0.8) | 9.1 ( ± 0.8) | 12.1 ( ± 0.4) |
| | 3 | 92.9 | 13.8 ( ± 2.1) | 6.3 ( ± 2.1) | 12.9 ( ± 0.9) |
| | 4 | 96.9 | 8.5 ( ± 1.1) | 6.6 ( ± 1.1) | 11.0 ( ± 1.2) |
| | 5 | 104.5 | 9.5 ( ± 4.0) | 8.4 ( ± 4.0) | 12.9 ( ± 2.2) |

**Table 6 along with their 95% confidence limits.**

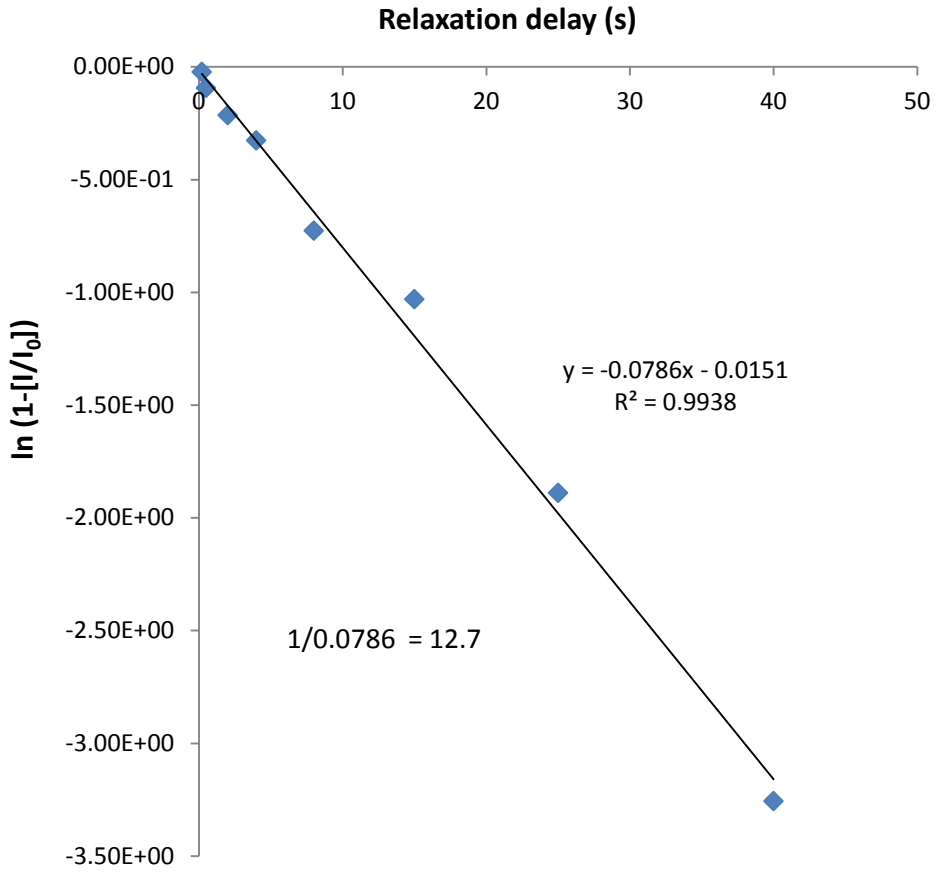


**Figure 4 Plotting $ln\left(1-\frac{I}{I_0}\right)$ against relaxation delay to calculate proton saturation relaxation time, for the spray dried sample at 74.1 ppm under an argon atmosphere**

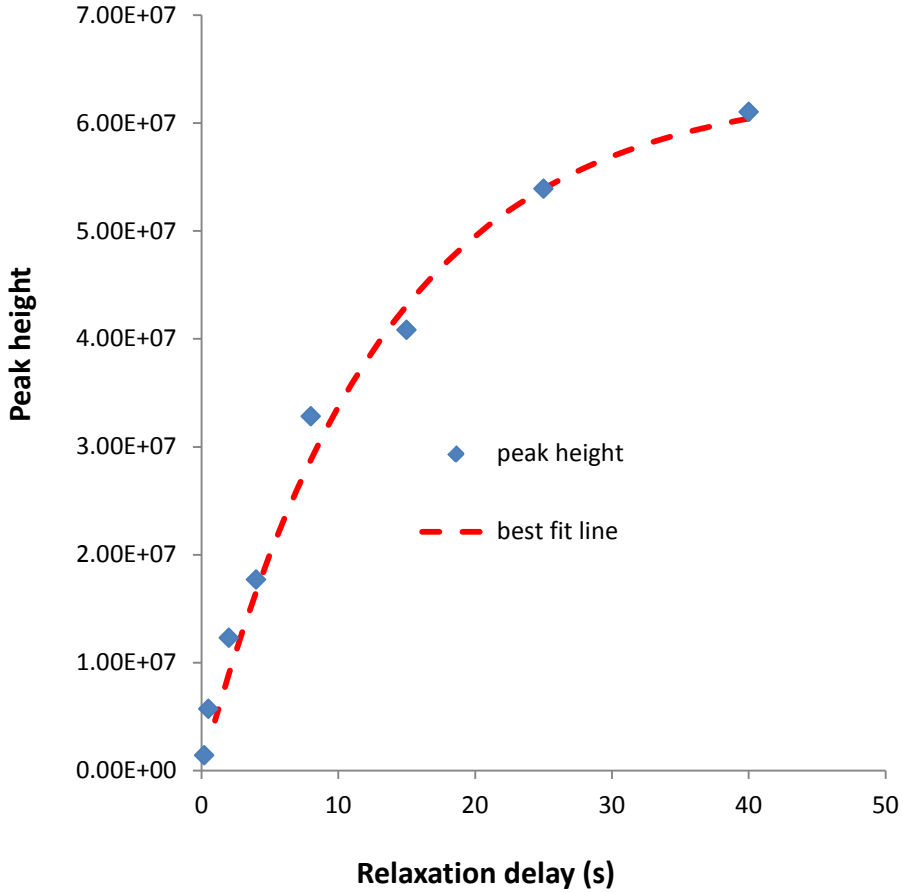


**Figure 5 Plotting peak height against relaxation delay and best fit line calculated for $I_0$ = 63500000 and $T_1$ = 12.7 s, for the spray dried sample at 74.1 ppm under an argon atmosphere**

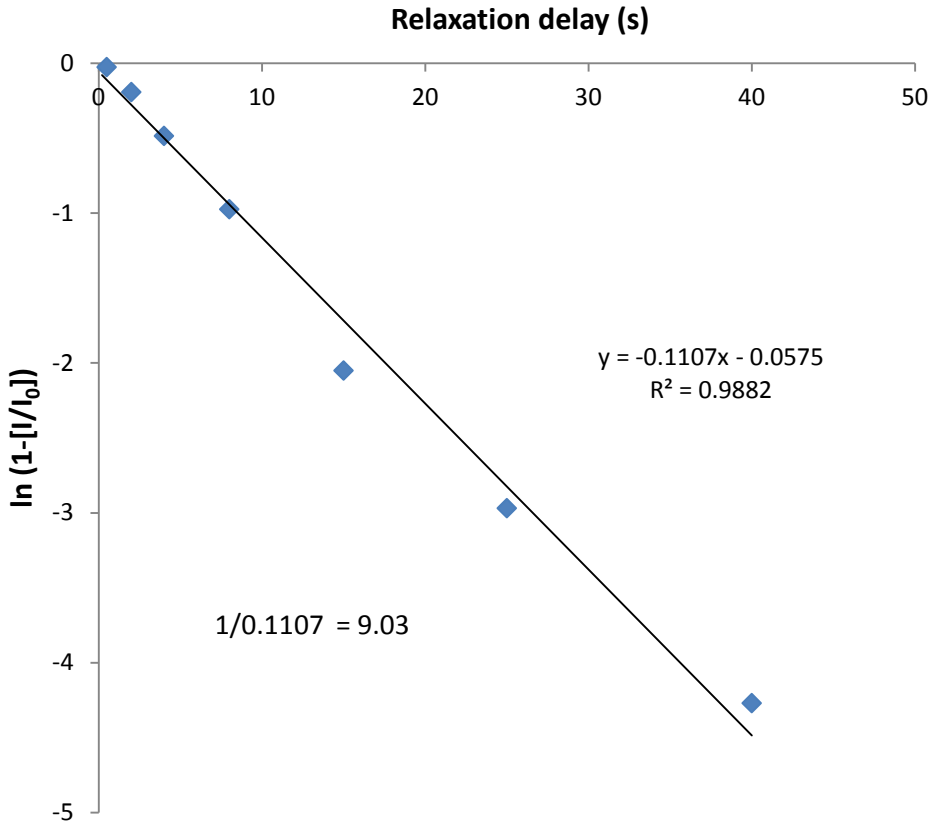


**Figure 6 Plotting $ln\left(1-\frac{I}{I_0}\right)$ against relaxation delay to calculate proton saturation relaxation time, for the freeze dried sample at 74.1 ppm under an argon atmosphere**

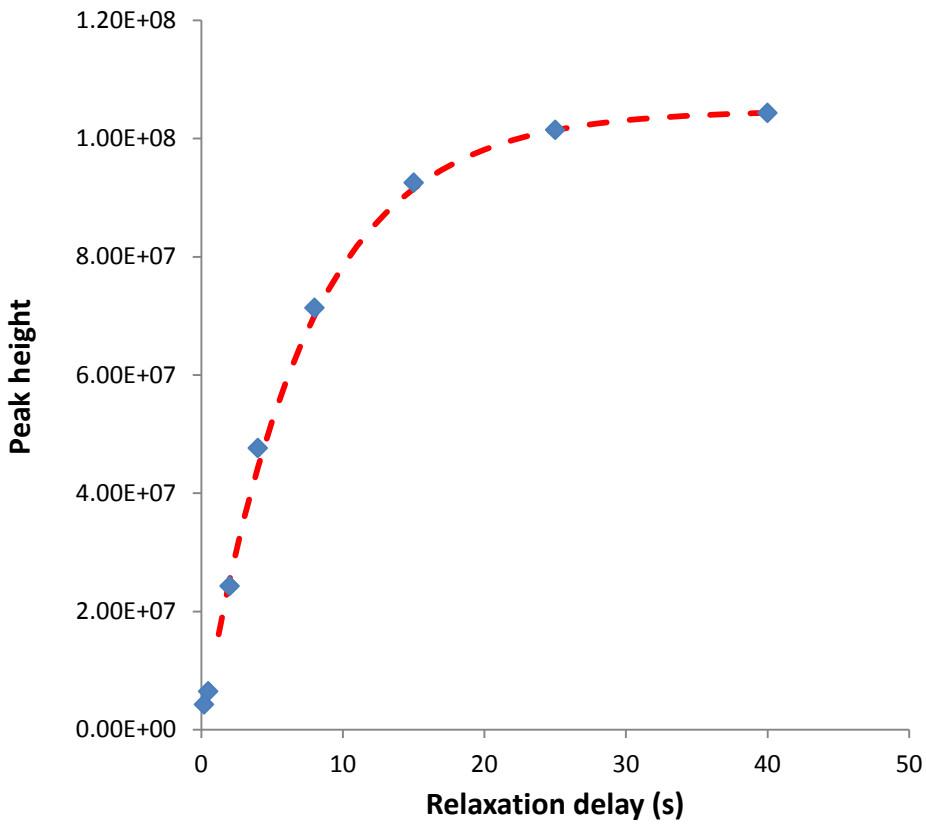


**Figure 7 Plotting peak height against relaxation delay and best fit line calculated for $I_0$ = 100000000 and $T_1$ = 9.03 s, for the freeze dried sample at 74.1 ppm under an argon atmosphere**

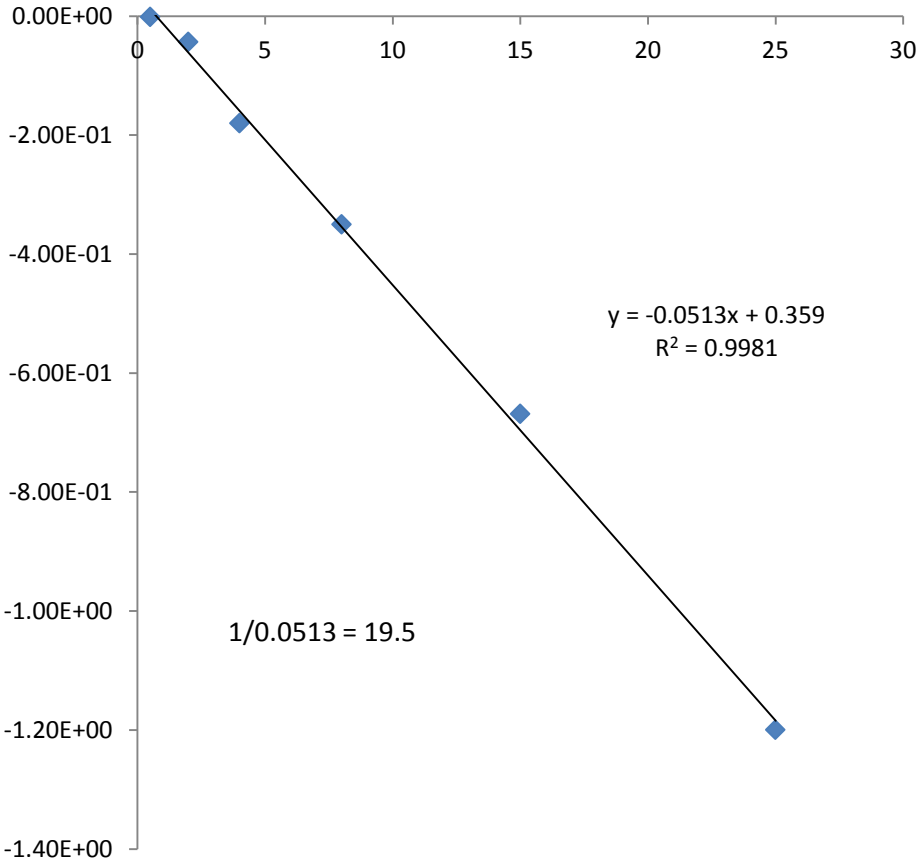


**Figure 8 Plotting $ln\left(1-\frac{I}{I_0}\right)$ against relaxation delay to calculate proton saturation relaxation time, for the melt sample at 74.1 ppm under an argon atmosphere**

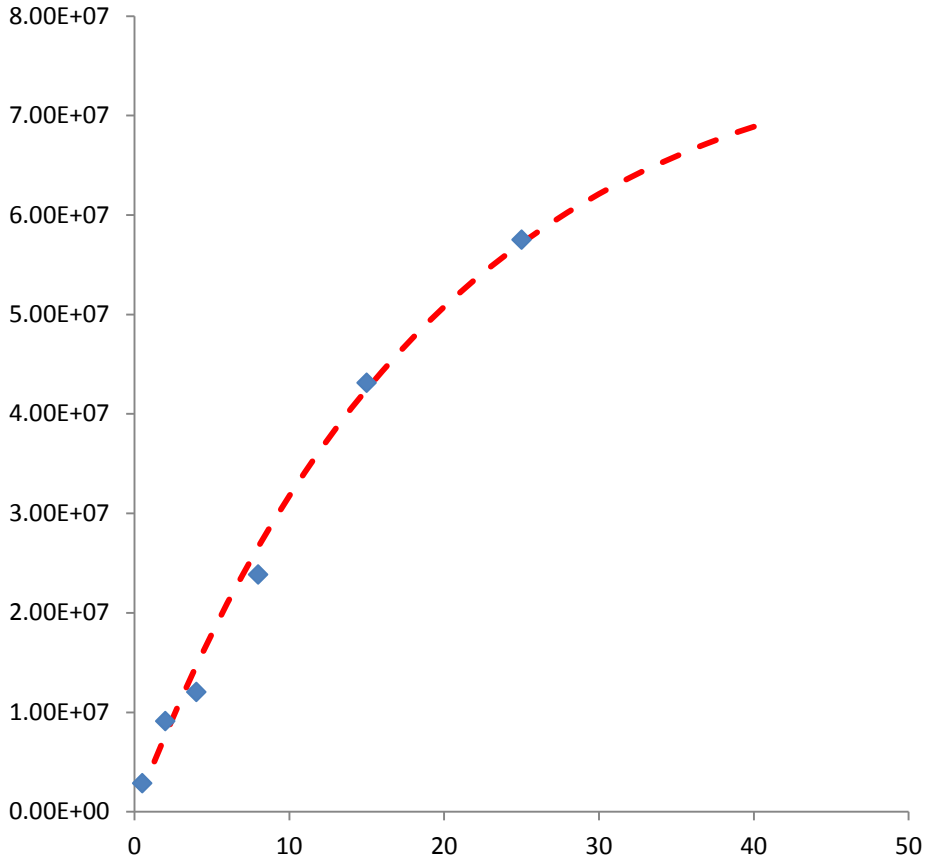


**Figure 9 Plotting peak height against relaxation delay and best fit line calculated for $I_0$ = 79000000 and $T_1$ = 19.5 s, for the melt sample at 74.1 ppm under an argon atmosphere**

| | Peak | Chemical shift (ppm) | Relaxation times (s) Spray dried | Freeze dried | Melt |
|---|---|---|---|---|---|
| Atmosphere: **Argon** | 1 | 62.5 | 11.9 ( ± 0.8) | 9.0 ( ± 0.3) | 16.3 ( ± 0.4) |
| | 2 | 74.1 | 11.2 ( ± 0.9) | 7.2 ( ± 1.7) | 12.5 ( ± 0.3) |
| | 3 | 92.9 | 12.7 ( ± 1.0) | 9.0 ( ± 1.1) | 19.5 ( ± 1.6) |
| | 4 | 96.9 | 12.3 ( ± 0.9) | 4.0 ( ± 0.7) | 12.2 ( ± 1.7) |
| | 5 | 104.5 | 10.7 ( ± 0.6) | 7.2 ( ± 0.1) | 11.4 ( ± 1.4) |
| Atmosphere: **Oxygen** | 1 | 62.5 | 11.2 ( ± 0.4) | 4.1 ( ± 0.4) | 7.2 ( ± 0.2) |
| | 2 | 74.1 | 10.1 ( ± 0.7) | 6.6 ( ± 0.7) | 8.9 ( ± 0.2) |
| | 3 | 92.9 | 10.5 ( ± 1.0) | 3.9 ( ± 1.0) | 11.7 ( ± 0.4) |
| | 4 | 96.9 | 10.6 ( ± 1.2) | 4.1 ( ± 1.2) | 7.9 ( ± 0.2) |
| | 5 | 104.5 | 9.4 ( ± 1.3) | 5.8 ( ± 1.3) | 4.0 ( ± 0.3) |
| Atmosphere: **Nitrogen** | 1 | 62.5 | 10.8 ( ± 1.0) | 7.8 ( ± 1.0) | 11.0 ( ± 0.5) |
| | 2 | 74.1 | 9.5 ( ± 0.8) | 9.1 ( ± 0.8) | 12.1 ( ± 0.4) |
| | 3 | 92.9 | 13.8 ( ± 2.1) | 6.3 ( ± 2.1) | 12.9 ( ± 0.9) |
| | 4 | 96.9 | 8.5 ( ± 1.1) | 6.6 ( ± 1.1) | 11.0 ( ± 1.2) |
| | 5 | 104.5 | 9.5 ( ± 4.0) | 8.4 ( ± 4.0) | 12.9 ( ± 2.2) |

**Table 7 Proton relaxation times $T_1$ for samples with no drying carried out, 95% confidence limits of error expressed in the brackets**

The Karl Fischer result for the spray dried lactose was 2.9%. The measurement of relaxation times has been shown to be dependent on the amount of water present in amorphous lactose by Lubach.[6] Vacuum drying at 40°C for 48 hours was carried out to remove the water with minimal alteration to the samples. The Karl Fischer results after vacuum drying were 1.1 % and 0.5 % for the spray and freeze dried samples. The solid state NMR relaxation times are shown in Table 7, these show a marked increase in the relaxation time for the freeze dried sample, whereas the spray dried sample shows only a small increase.

| | Peak | Chemical shift (ppm) | Relaxation times (s) Spray dried | Freeze dried |
|---|---|---|---|---|
| Atmosphere: **Argon** | 1 | 62.5 | 15.3 ( ± 2.3) | 9.0 ( ± 0.3) |
| | 2 | 74.1 | 13.6 ( ± 0.6) | 7.2 ( ± 1.7) |
| | 3 | 92.9 | 13.8 ( ± 6.9) | 9.0 ( ± 1.1) |
| | 4 | 96.9 | 17.4 ( ± 8.0) | 4.0 ( ± 0.7) |
| | 5 | 104.5 | 12.0 ( ± 2.6) | 7.2 ( ± 0.1) |
| Atmosphere: **Oxygen** | 1 | 62.5 | 11.8 ( ± 0.4) | 11.4 ( ± 0.4) |
| | 2 | 74.1 | 13.5 ( ± 0.7) | 7.3 ( ± 0.7) |
| | 3 | 92.9 | 14.7 ( ± 1.0) | 12.9 ( ± 1.0) |
| | 4 | 96.9 | 12.8 ( ± 1.2) | 4.3 ( ± 1.2) |
| | 5 | 104.5 | 9.3 ( ± 1.3) | 9.8 ( ± 1.3) |
| Atmosphere: **Nitrogen** | 1 | 62.5 | 11.1 ( ± 1.0) | 9.9 ( ± 1.0) |
| | 2 | 74.1 | 11.4 ( ± 0.8) | 9.2 ( ± 0.8) |
| | 3 | 92.9 | 14.6 ( ± 2.1) | 8.8 ( ± 2.1) |
| | 4 | 96.9 | 20.1 ( ± 1.1) | 12.2 ( ± 1.1) |
| | 5 | 104.5 | 12.9 ( ± 4.0) | 7.1 ( ± 4.0) |

**Table 8 Proton relaxation times of samples after vacuum drying at 40°C for 48 hours, with 95% confidence limits of error expressed in the brackets**

## 6.4 Discussion – lactose spray dried, freeze dried and melt samples

The elemental analysis suggested the presence of water in the spray dried and freeze dried samples as they arrived, and the Karl Fischer results prove the presence of water in amounts consistent with the elemental analysis. These results showed the freeze dried sample contained the most moisture on arrival and the melt the least. The DVS results for the sorption of relative humidity between 10 and 30% (see Figure 1) again show the freeze dried sample to absorb moisture most readily and the melt least. The effect of moisture on amorphous lactose is to reduce the glass transition point. This is seen in Figure 2 where 1% reduces the glass transition point by 30 °C.

The spectra of the three amorphous samples were shown in Figure 3 to be identical, however the $T_1$ proton relaxation times, shown in Table 6 appear different. This was examined further by applying t-tests to compare the relaxation times of the samples against one another. The null hypothesis implies that any difference that exists between the two sets of results can be attributed to random variation. In this case the null hypothesis tests; that no difference exists between $T_1$ proton relaxation times for the different samples. Table 8 shows the percentage probability results; were a value of 100% suggests that the values were drawn from the same population, and a value of

0% suggests that each set of results was drawn from two different populations with different means.

| | Peak | Chemical shift (ppm) | Spray dried v's Freeze dried | Freeze dried v's Melt | Spray dried v's Melt |
|---|---|---|---|---|---|
| Atmosphere: **Argon** | 1 | 62.5 | 0% | 0% | 2% |
| | 2 | 74.1 | 0% | 0% | 1% |
| | 3 | 92.9 | 0% | 0% | 2% |
| | 4 | 96.9 | 0% | 0% | 54% |
| | 5 | 104.5 | 0% | 0% | 4% |
| Atmosphere: **Oxygen** | 1 | 62.5 | 0% | 0% | 3% |
| | 2 | 74.1 | 0% | 0% | 0% |
| | 3 | 92.9 | 0% | 0% | 0% |
| | 4 | 96.9 | 0% | 0% | 0% |
| | 5 | 104.5 | 0% | 0% | 1% |
| Atmosphere: **Nitrogen** | 1 | 62.5 | 0% | 0% | 10% |
| | 2 | 74.1 | 0% | 0% | 0% |
| | 3 | 92.9 | 0% | 0% | 18% |
| | 4 | 96.9 | 0% | 0% | 0% |
| | 5 | 104.5 | 0% | 0% | 0% |

**Table 9 Comparison of proton relaxation times $T_1$ between the samples with no drying, showing the probability that the two data sets are drawn from the same population using two sided t-tests**

The null hypothesis in this case was rejected, for the comparison of the spray dried against freeze dried samples, along with the freeze dried against melt samples. The null hypothesis was accepted for the comparison of spray dried and melts samples suggesting that these did not possess significantly different $T_1$ proton relaxation times. To conclude the $T_1$ times for the spray dried v's freeze dried samples appear to be different to one another and the freeze dried v's melt samples also appear to be different, but the spray dried and melt samples show some similarity.

The idea that atmosphere could change $T_1$ proton relaxation times was tested again by using t-tests for the argon, oxygen and nitrogen atmospheres. Comparisons were made between pairs of results (Ar / $O_2$), (Ar / $N_2$) and finally ($O_2$ / $N_2$). This was carried out using two tailed t-tests, the results can be seen in Table 9. The $T_1$ relaxation time data for the different atmospheres were tested using a null hypothesis; that any difference between results was purely a product of random error and each atmosphere produced results that were drawn from the same population. The tabulated results set out in Table 8 represent the percentage probability that the two sets of results could have

been drawn from the same population, once again a 100% value suggests that any difference in results is purely a product of random error and a 0% that the results were drawn from different populations with different means.

| Comparison | Peak | Chemical shift (ppm) | Probability of similarity | | |
|---|---|---|---|---|---|
| | | | Spray dried | Freeze dried | Melt |
| **Ar / $O_2$** | 1 | 62.5 | 1% | 0% | 0% |
| | 2 | 74.1 | 0% | 6% | 0% |
| | 3 | 92.9 | 0% | 0% | 0% |
| | 4 | 96.9 | 0% | 38% | 0% |
| | 5 | 104.5 | 0% | 0% | 0% |
| **$O_2$ / $N_2$** | 1 | 62.5 | 4% | 0% | 0% |
| | 2 | 74.1 | 0% | 0% | 0% |
| | 3 | 92.9 | 0% | 0% | 0% |
| | 4 | 96.9 | 0% | 0% | 0% |
| | 5 | 104.5 | 56% | 0% | 0% |
| **Ar / $N_2$** | 1 | 62.5 | 0% | 0% | 0% |
| | 2 | 74.1 | 0% | 0% | 0% |
| | 3 | 92.9 | 5% | 0% | 0% |
| | 4 | 96.9 | 0% | 0% | 0% |
| | 5 | 104.5 | 0% | 0% | 0% |

**Table 10 Probability of similarity between $T_1$ relaxation times, using two tailed t-tests, for all samples before drying**

The results in Table 9 suggest that the null hypothesis can be rejected for the melt and those differences in the $T_1$ proton relaxation times observed under different atmospheres are unlikely to be a result of random variation. The freeze dried results similarly allow a rejection of the null hypothesis, with the exception of the 96.9 and 74.1 ppm peaks, when argon and oxygen are compared. The null hypothesis is also rejected for the spray dried results with the exception of the 104.5 peak comparing oxygen and nitrogen.

The observation of the lowest $T_1$ values for the freeze dried sample that also contained the most moisture, is consistent with the prediction by Lubach, that moisture reduces the $T_1$ relaxation times.[6] To minimise the effect of moisture on the experiment, the freeze dried and spray dried samples were vacuum dried for 48 hours at 40 °C. The melt sample was not dried any further because of its very low initial moisture content.

The moisture free samples were compared using two sided t-tests to detect differences in $T_1$ values beyond random variation in Table 10.

| | Peak | Chemical shift (ppm) | SD v's FD | FD v's Melt | SD v's Melt |
|---|---|---|---|---|---|
| Atmosphere: **Argon** | 1 | 62.5 | 0% | 0% | 21% |
| | 2 | 74.1 | 0% | 0% | 1% |
| | 3 | 92.9 | 1% | 9% | 12% |
| | 4 | 96.9 | 92% | 3% | 3% |
| | 5 | 104.5 | 0% | 0% | 26% |
| Atmosphere: **Oxygen** | 1 | 62.5 | 1% | 0% | 1% |
| | 2 | 74.1 | 0% | 0% | 0% |
| | 3 | 92.9 | 0% | 0% | 0% |
| | 4 | 96.9 | 0% | 0% | 0% |
| | 5 | 104.5 | 2% | 0% | 3% |
| Atmosphere: **Nitrogen** | 1 | 62.5 | 0% | 0% | 94% |
| | 2 | 74.1 | 0% | 0% | 0% |
| | 3 | 92.9 | 0% | 0% | 0% |
| | 4 | 96.9 | 0% | 0% | 0% |
| | 5 | 104.5 | 0% | 0% | 89% |

**Table 11 Comparison of proton relaxation times $T_1$ between the samples after drying, showing the probability that the two data sets are drawn from the same population using two sided t-tests (100% suggests results are drawn from the same population and 0 suggests they are drawn from populations with different means)**

The results shown in Table 10 suggest that differences between the $T_1$ proton relaxation times for freeze dried and spray dried lactose are unlikely to be due random variation, with the exception of peak 4 at 96.9 ppm under an argon atmosphere. Similarly the freeze dried and melt samples show different relaxation times that are unlikely to be due to random variation, with the exception of the peak at 92.9 ppm under an oxygen atmosphere. Finally the spray dried and melt samples show results at the 104.5 and 62.5 ppm peaks that may have been drawn from the same population under argon and nitrogen atmospheres.

The comparisons of the different atmospheres for the vacuum dried spray dried and freeze dried samples are shown in Table 11. Again this shows the probability of the two sets of data being drawn from the same population calculated from the two sided t-test.

| Comparison | Peak | Chemical shift (ppm) | Probability of similarity | |
|---|---|---|---|---|
| | | | Spray dried | Freeze dried |
| **Ar / $O_2$** | 1 | 62.5 | 0% | 0% |
| | 2 | 74.1 | 49% | 66% |
| | 3 | 92.9 | 35% | 0% |
| | 4 | 96.9 | 0% | 9% |
| | 5 | 104.5 | 0% | 0% |
| **$O_2$ / $N_2$** | 1 | 62.5 | 1% | 0% |
| | 2 | 74.1 | 0% | 0% |
| | 3 | 92.9 | 76% | 0% |
| | 4 | 96.9 | 0% | 0% |
| | 5 | 104.5 | 0% | 0% |
| **Ar / $N_2$** | 1 | 62.5 | 0% | 0% |
| | 2 | 74.1 | 0% | 0% |
| | 3 | 92.9 | 39% | 16% |
| | 4 | 96.9 | 1% | 0% |
| | 5 | 104.5 | 6% | 12% |

**Table 12 Probability of similarity between $T_1$ relaxation times, using two tailed t-tests, for all samples after drying**

With the exception of the freeze dried sample comparing the oxygen and nitrogen atmospheres at least one peak suggests that the difference in results may have been due to random variation. The outcome of this part of the experiment suggests that atmosphere does not make a difference to the $T_1$ proton relaxation times of vacuum dried amorphous materials prepared from solutions.

## 6.5 Conclusions

The three amorphous preparations behave differently toward moisture, as shown by the DVS results, the freeze dried material most readily absorbs moisture and the melt the least. This is significant, since it means that any attempt to calculate amorphous content is dependent on the preparation method of the amorphous material.

The effect of oxygen gas on the amorphous melt $T_1$ proton saturation relaxation time was significant. The effect of oxygen gas on the spray dried and freeze dried samples was much more pronounced when these samples contained moisture. When vacuum dried to contain less than 1% moisture the spray dried and freeze dried samples showed some similar $T_1$ proton saturation relaxation times for some peaks.

The previous work in chapter 4 of this thesis was based around all amorphous lactose forms showing similar $T_1$ proton saturation relaxation times. Only when vacuum dried did the different amorphous forms of lactose start to show similar $T_1$ values. This means that the removal of moisture from any amorphous material present in a mixture is critical to the performance of the technique outline in chapter 4.

***Reference***

1 L. Mackin, R. Zanon, J. M. Park, K. Foster, H. Opalenik and M. Demonte, *International Journal of Pharmaceutics,* 2002, 231, 227-236.

2 D. Q. M. Craig and M. Reading, *Thermal analysis of pharmaceuticals*, CRC distributor; Taylor & Francis, New York; London, 2006.

3 J. H. Kirk, S. E. Dann and C. G. Blatchford, *International Journal of Pharmaceutics,* 2007, 334, 103-114.

4 Microsoft, *Excell*, Seattle, 2007.

5 B. C. Z. Hancock G., *J. Pharm. Sci.,* 1997, 86, 1-12.

6 J. W. Lubach, D. Xu, B. E. Segmuller and E. J. Munson, *J. Pharm. Sci.,* 2007, 96, 777 (DOI:10.1002/jps.20684).

# CHAPTER 7

# Salbutamol amorphous content quantification by dynamic vapour sorption

## 7.1 Introduction

Chapter 1 describes salbutamol sulfates use as an Active Pharmaceutical Ingredient (API) in asthma inhalers and how it is delivered to the respiratory regions of the lungs as particles sized between 0.5 to 5 µm. To produce particles of these dimensions, a size reduction process of the bulk crystalline material is required, such as micronisation. These processes generate amorphous content that increases the surface energy of the particles, making them more likely to stick to other surfaces, (chapter 1 section 1.7). Only one polymorph of salbutamol sulfate with 50:50 R amd S optical isomers has been identified and characterised. Both isomers are present in the raw material, but since separation entails additional cost and both isomers show pharmaceutical activity, the mixture is used for drug applications. Unlike lactose, salbutamol sulfate does not possess known hydrates and dynamic vapour sorption measurements (DVS) can be used to identify its amorphous content.[1-4]

The instrumentation for DVS was described in chapter 2 section 2.2.2. Previously Gorny used DVS measurements to estimate amorphous salbutamol sulfate content. The experiments conducted by these authors used a SPS11 Projekt Messtechik instrument with a sample mass of 2.0 g, using water as the sorbent vapour.[5] The instrument used in this thesis is the SMS Advantage-1 with a sample size of between 40 to 50 mg. The major advantage offered by SMS Advantage-1 instrument is speed, taking 4 days to run a completely amorphous sample and 1 day to run a micronised sample, compared to the 12 and 6 days respectively using the SPS11. Despite these instrumentation differences, comparisons between this study and Gorny's have been possible, since DVS measures mass change at equilibrium, although the time taken to reach equilibrium may be different. This means that data processing for DVS methods should be directly transferable from one instrument to another.

To produce a calibration on the DVS instrument, mixtures of known crystalline and amorphous content were produced from two standard materials, one amorphous and the other crystalline. This work characterises the 100% amorphous and crystalline standards by a number of techniques and then investigates the response of a series of mixtures on the DVS for linearity of response and its sensitivity.

## 7.2 Characterising the crystalline and amorphous standards

Prior to producing a series of calibration mixtures and running these on the DVS instrument, confirmation of their amorphous and crystalline nature was confirmed using standard measurements. The task of demonstrating a material to be near 100% pure can only be achieved by showing that it behaves as the pure material would be expected to and contains no measurable impurities. Although the solubility of polymorphs can vary enormously, once dissolved they produce identical solutions. This meant there was no benefit in carrying out any kind of test that dissolved the solid, so all characterisation work was carried out on the solid powders.

### 7.2.1 Standard materials preparation and sourcing

The amorphous standard of spray dried salbutamol sulfate was prepared and supplied by 3M Heathcare Ltd. This sample was kept in a sealed desiccator containing fresh phosphorus pentoxide within an argon glove box for one year before this work was carried out. The crystalline salbutamol sulfate was prepared from a micronised 3M supplied sample by holding the sample at 98% relative humidity environment for 28 d to facilitate crystallisation. This process was carried out using 5.00g of the micronised material spread evenly across two Petri dishes and placed in a desiccator over a saturated salt solution of potassium sulfate and allowed to equilibrate with laboratory temperature over 28 d.

### 7.2.2 Differential Scanning Calorimetry and Thermal Gravimetric Analysis

Samples of between 15 to 25 mg were placed in the DSC instrument and dried for 3 hours at 70 °C to reduce the moisture content as much as possible before the experiment was carried out. The instrument was cooled back to 30 °C and the heat flow recorded during a heating ramp of 10 °C per minute to 260 °C.

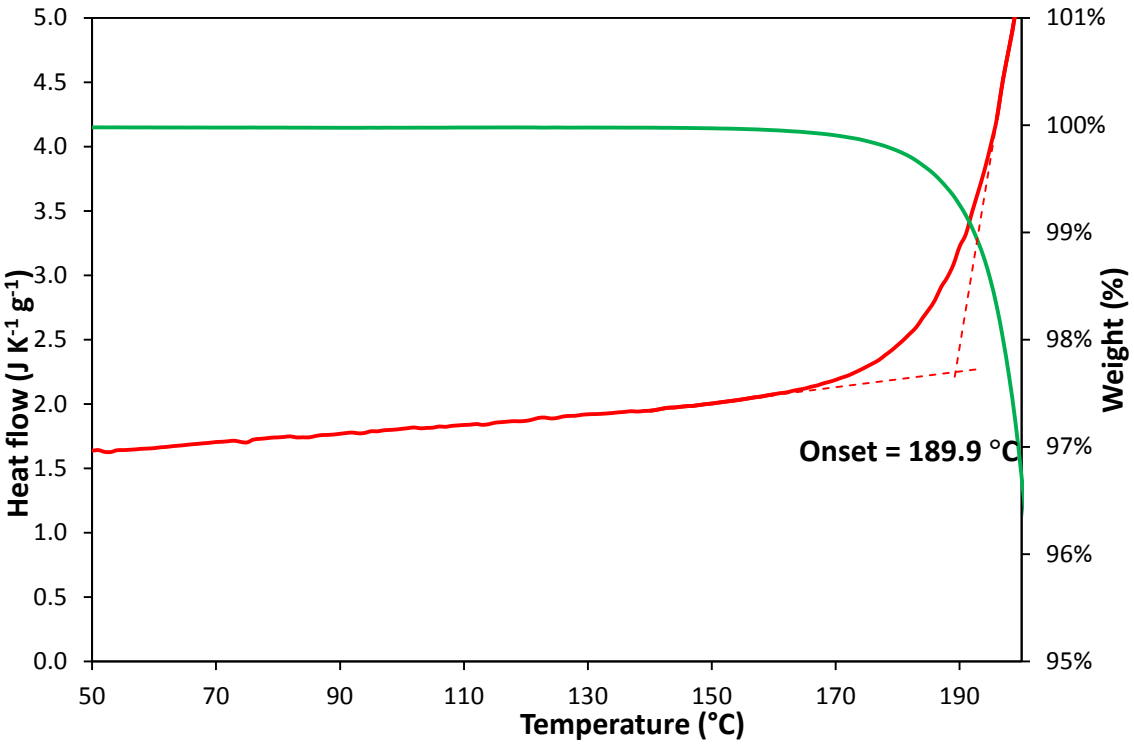


**Figure 1 DSC (- red) and TGA (- green) traces for crystalline salbutamol sulfate**

The onset of melting for the crystalline standard was recorded in Figure 1. This was found to be in close agreement with York's estimate of about 190.0 °C from co-solvent of crystallisation using water and isopropyl alcohol.[6]

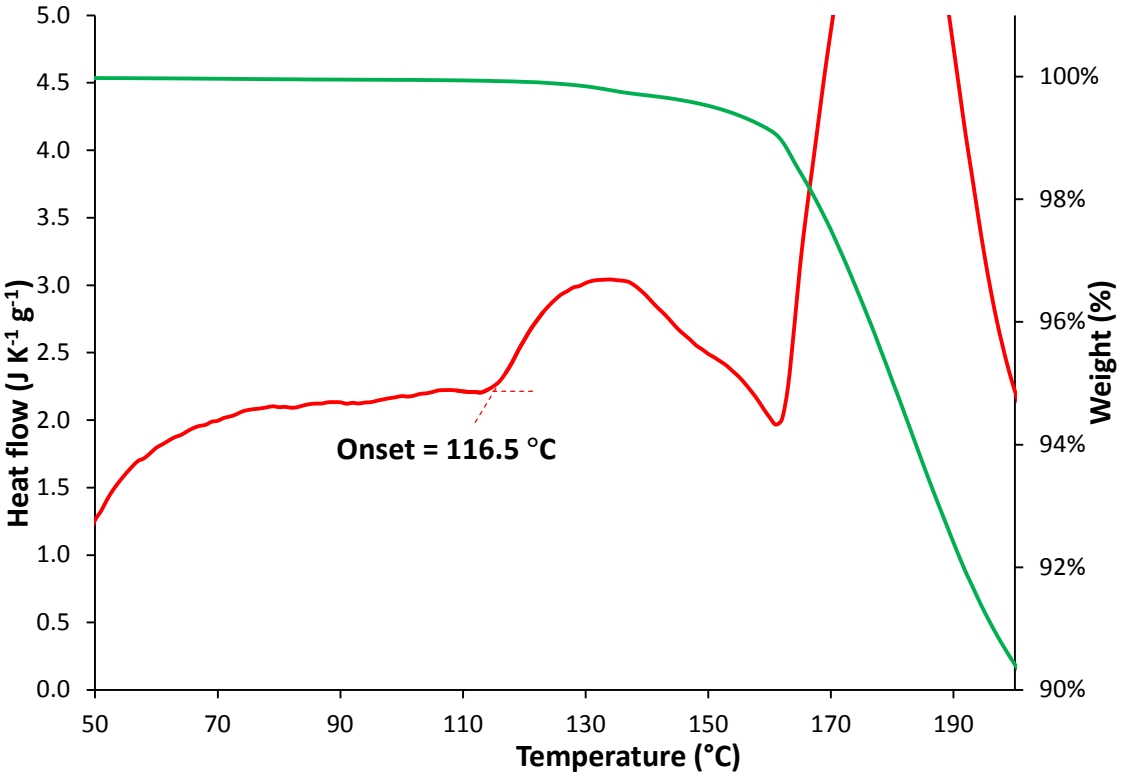


**Figure 2 DSC (- red) and TGA (- green) traces for spray dried salbutamol sulfate**

The Craig estimated glass transition point of spray dried salbutamol sulfate, with zero moisture content was 121.7±0.7 °C.[7] On face value, this is considerably different to the onset value seen in Figure 2, however water acts as a plasticiser in many amorphous pharmaceuticals. The effect of moisture on the glass transition point is calculated via the Gordon Taylor equation.[7, 8]

$$T_g = \frac{X_a T_{ga} + kX_w T_{gw}}{X_a + kX_w}$$

**The Gordon Taylor Equation or, Equation 1**

Using the onset temperature for pure amorphous salbutamol sulfate obtained by Craig of 121.7 °C for $T_{ga}$ with experimental value of 116.5 °C for $T_g$ taken from Figure 2, the water mass fraction $X_w$ was calculated to be 0.18 %(w/w), given (K=0.088 and $T_{gw}$ for amorphous water of 135 °K). The weight loss before the glass transition was 0.08% and 0.19% after. Considering the Gordon Taylor equation, the value shown in Figure 2 appears a reasonable match to Craig's reported values.[7]

### 7.2.3 Powder X-ray Diffraction

The amorphous and crystalline standards were run on the Bruker D8 in Perspex sample holders, with a Mylar cover slip, to reduce alteration of the sample by moisture. The measurement rate was 1 second per 0.007°. The crystalline standard showed clear well defined sharp Bragg peaks (see Figure 3). These were consistent with the 2θ reflections predicted using Mercury[9] from the single crystal structure determination for salbutamol sulfate determined by Leger (produced from an aqueous racemic mixture).[10]

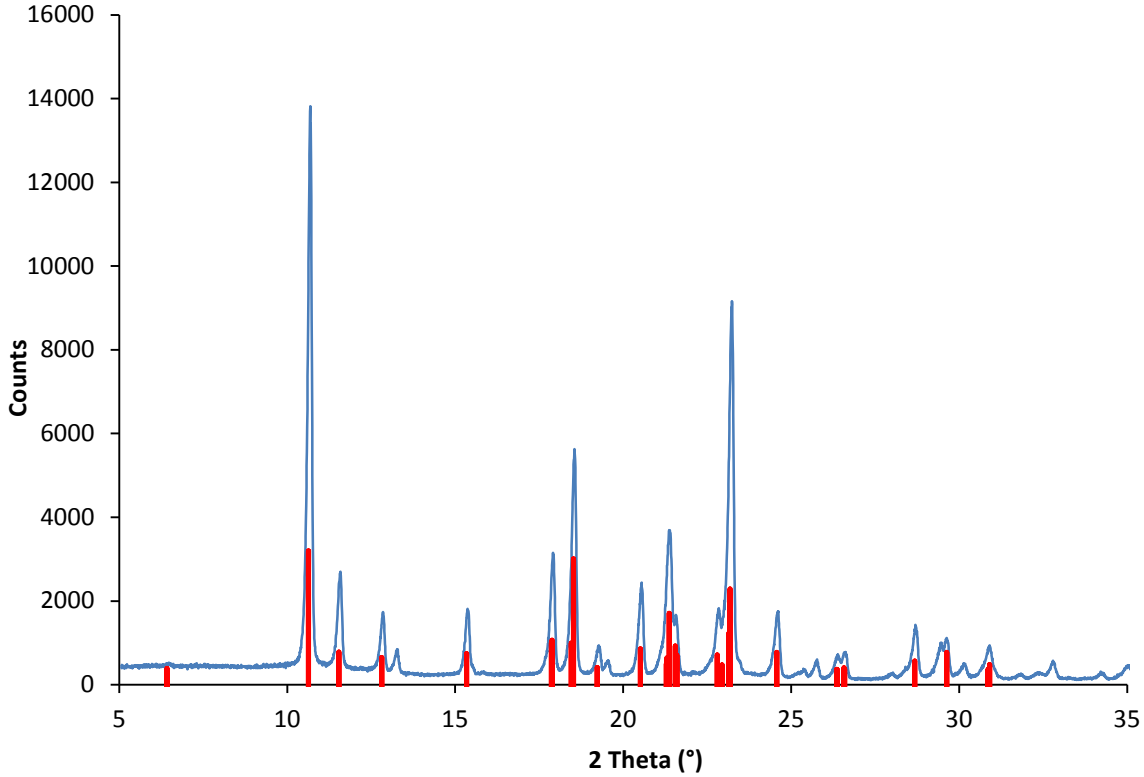


**Figure 3 Powder X-ray diffraction pattern of the crystalline salbutamol sulfate standard – blue calculated diffraction peaks from Leger et al are shown in red**

The reduced pair distribution function G(r) was calculated using the GETpdfX2 software.[11] This process uses all the data in the powder X-ray diffraction pattern to produce the G(r) plot shown in Figure 4. The reduced pair distribution function shows no reduction in oscillation over the range 0 to 100 Å, suggesting that order in the crystalline standard extends beyond the 100 Å range.[12]

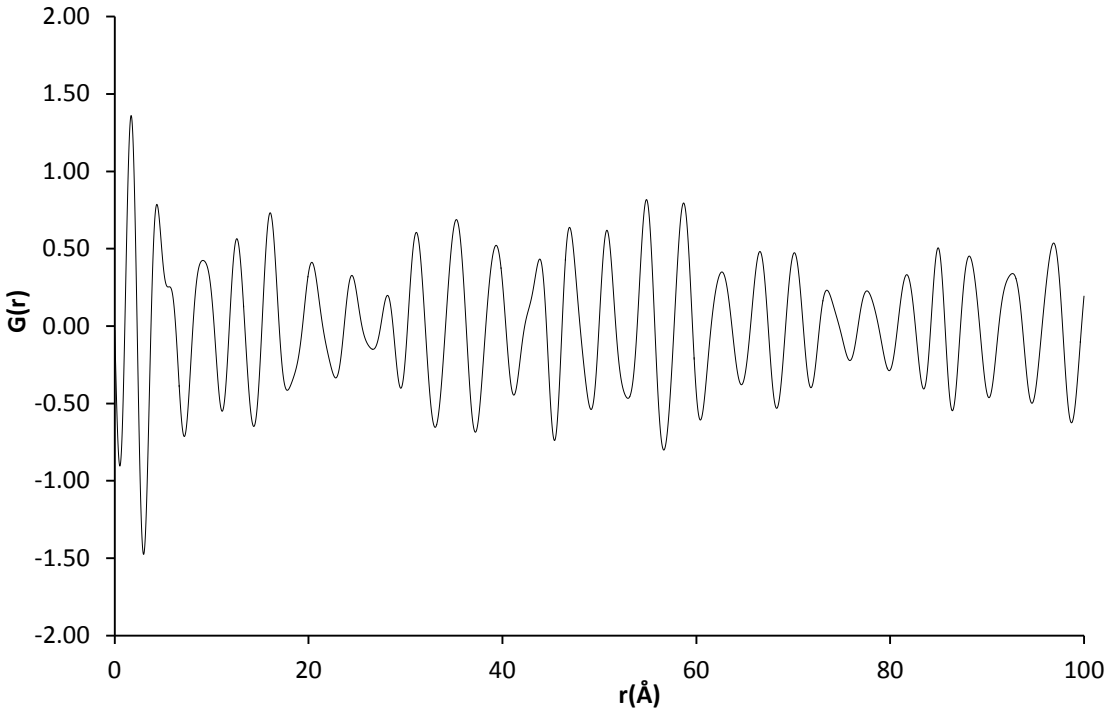


**Figure 4 Reduced pair distribution function calculated from the crystalline salbutamol sulfate powder diffraction data**

The powder X-ray diffraction pattern of the spray dried amorphous standard as shown in Figure 5 shows no clear Bragg reflections but a characteristic amorphous halo.

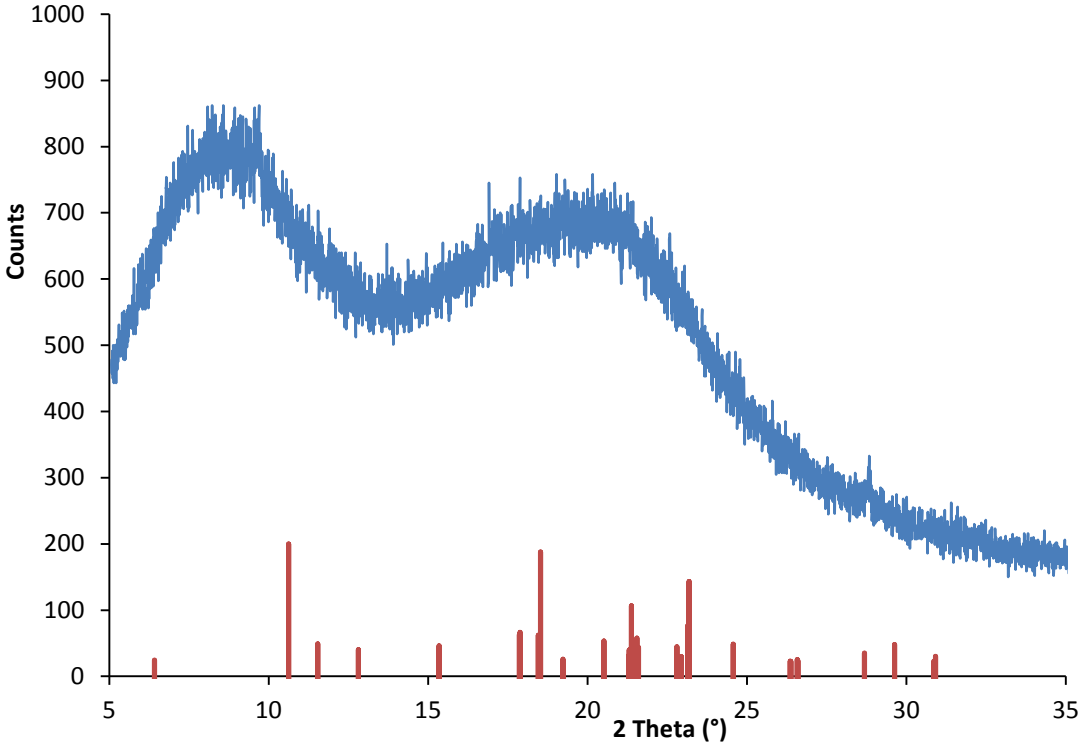


**Figure 5 Powder X-ray diffraction pattern for spray dried amorphous standard – blue calculated diffraction peaks from Leger et al are shown in red**

The absence of Bragg peaks suggests that the standard does not contain crystals of significant size or quantity, (significant in this case means below the detection limit of the diffractometer). The reduced pair distribution function shown in Figure 6, demonstrates the long range property of random order where G(r)= 0 for the spray dried amorphous standard. The small continuous oscillation about the G(r)= 0 line is due to the long wavelength of copper $K_{\alpha 1}$ X-rays used to calculate G(r). The use of shorter wavelength radiation usually reduces the size of these oscillations.[12] The extent of order can be found by fitting straight lines to the plot of the maximum and minima calculated using Equation 1.

$$\mathbf{y = \ Ln|1 - G(r)|} \qquad \textbf{Equation 2}$$

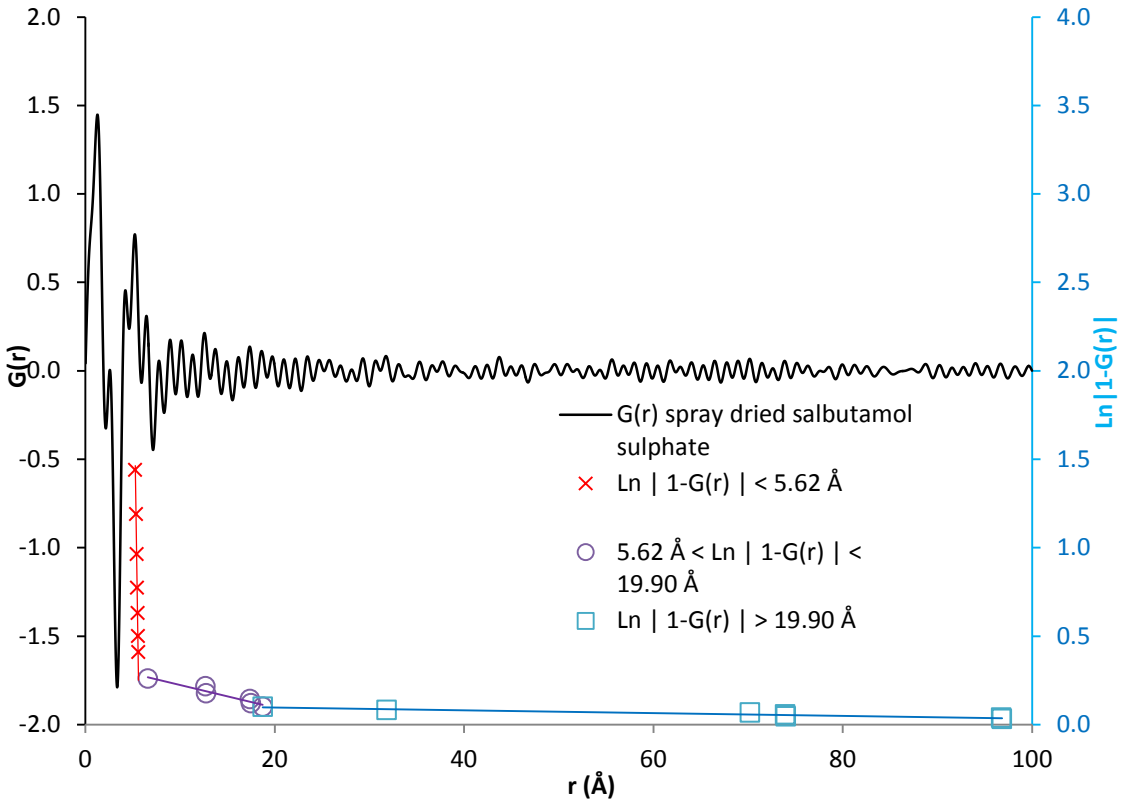


**Figure 6 Reduced pair distribution function calculated from the spray dried salbutamol sulfate powder diffraction data**

The maximum at 1.13 Å represents the average bond length between atoms in the structure. The two intersections of the $\mathbf{y = \ Ln|1 - G(r)|}$ line shown in Figure 6 suggests two instances at 5.6 and 19.9 Å implying step changes in the loss of order. This can be accounted for by examining the distance between atoms within the salbutamol sulfate molecule. The distance between all atoms in the salbutamol molecule was calculated from the Leger crystal structure determination and formed

into the histogram shown in Figure 7.[10] This was based on atoms bonded to adjacent atoms, but inclusive of atoms at either end of the molecule.

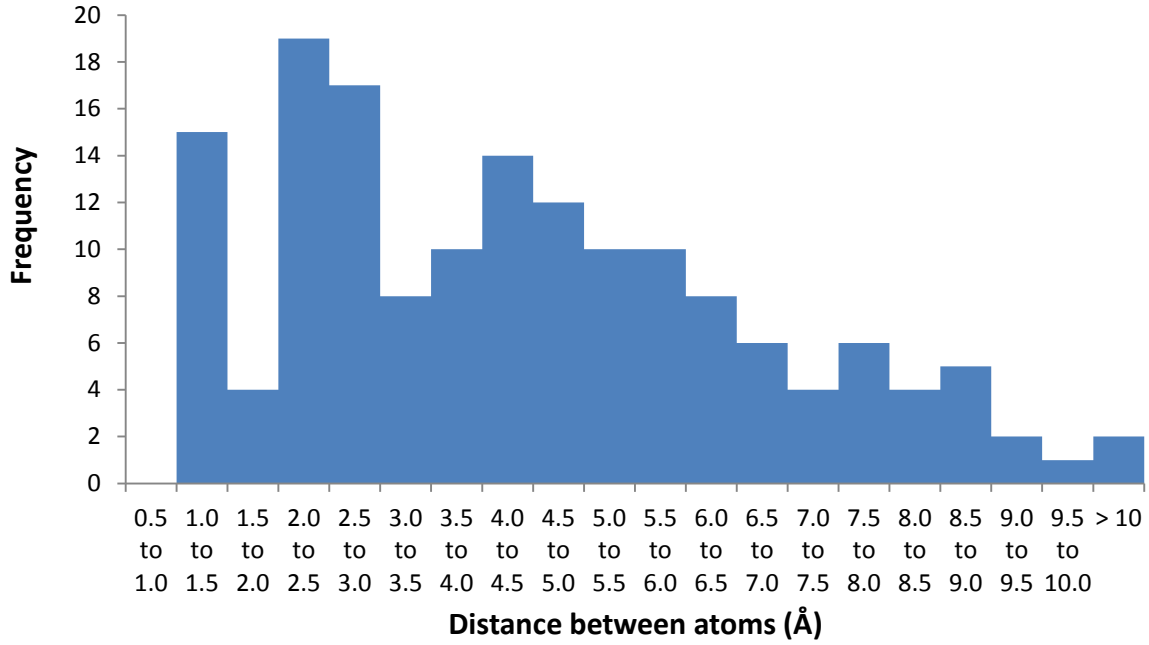


**Figure 7 Distances between atoms in a molecule of salbutamol sulfate as determined from the crystal structure determination of Ledger[10]**

The maxima and minima in the histogram of Figure 9 correspond well to the maxima and minima shown in the reduced pair distribution function. The maxima in Figure 7 for the bins "1.0 to 1.5" and "4 to 5" corresponds to the maxima seen at 1.3 Å and between 4 to 7 Å seen in Figure 8. The minimum in Figure 8 at 3.29 Å also corresponds to the minima seen in Figure 7 between 3.0 to 3.5 Å. This correspondence between Figure 8 and Figure 9 at short distances (less than 10 Å) suggests that local order within the salbutamol molecule has largely been retained during the spray drying process. In chapter 1 the random packing of spheres was discussed, chapter 1 figure 19 showed that up to 5 sphere diameters a small degree of order was retained, whereas Figure 6 of this chapter suggests that within the length of two salbutamol molecules (20 Å) the structure becomes random.

This is consistent with observations of Zografi.[13] The random close packing of spheres provides an incomplete model for amorphous structures of small molecules such as salbutamol sulfate. The random close packing of spheres only provides the opportunity for the random positioning of one sphere relative to another, and does not demand an orientation requirement; the salbutamol ion is not spherical, making

orientation a variable that cannot be randomised.[13] Furthermore, the salbutamol cation contains 5 bonds that are free to rotate (see Figure 8) which creates the opportunity for the ion to exist in a large number of different confirmations.[13] The additional variables of orientation and confirmation provide a greater opportunity for random positioning for each atom. The reduced pair distribution function reflects the greater opportunity for randomly placing atoms, and so G(r) decays much more rapidly than would be expected for a spherical model.

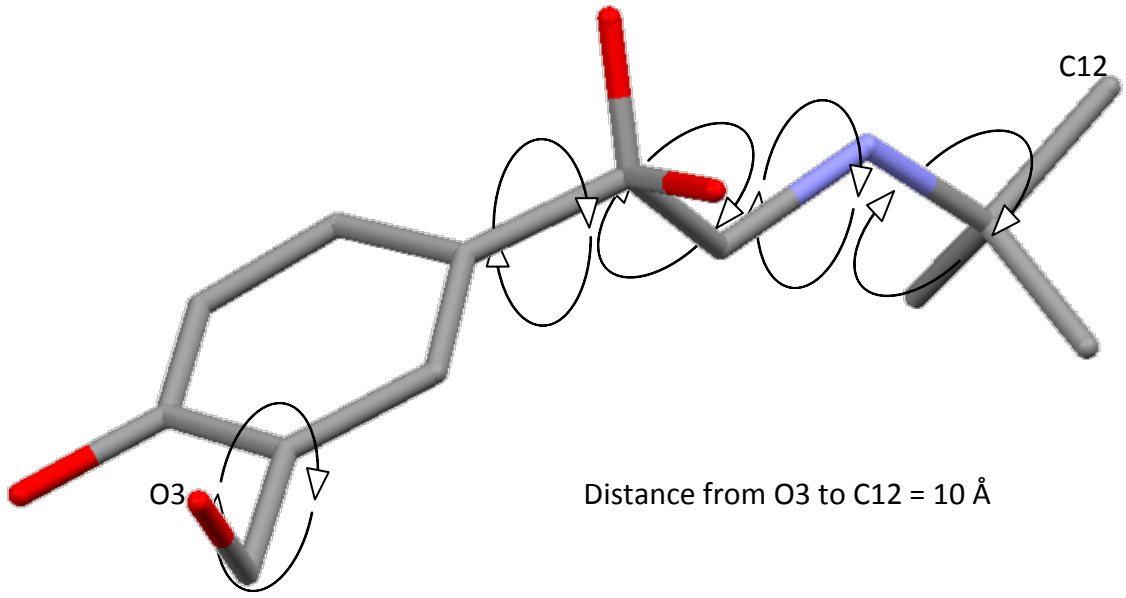


**Figure 8 Bond rotations within the salbutamol molecule[10]**

The random structure of amorphous salbutamol sulfate is enabled by the hydrogen bonding network that operates between salbutamol molecules and the sulfate group. In an amorphous structure, the hydrogen bonds can be expected to form a three dimensional continuous random network, with average hydrogen bond distances similar to those seen in the crystalline material, but with a much broader distribution of lengths.[14]

### 7.2.4 Infrared

The infrared spectrum of the crystalline standard was taken on the Perkin Elmer spectrum 100 instrument using the attenuated total internal reflectance accessory. The spectrum is shown in Figure 1. The crystalline standard shows identical features to

the sample prepared by Palacios by re-crystallisation of salbutamol sulfate racemate from water.[15, 16, 16]

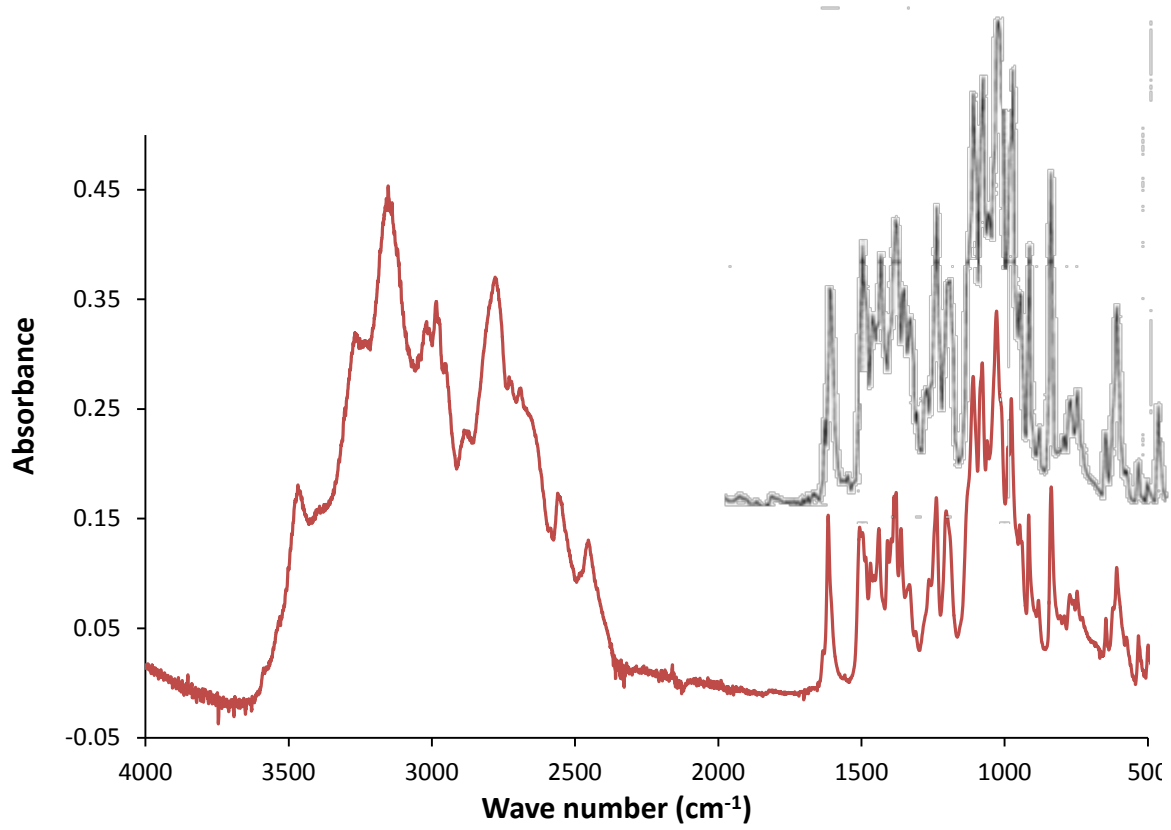


**Figure 9 Infrared spectra of crystalline salbutamol sulfate racemate black [16], red crystalline salbutamol sulfate 11082801**

The FT-IR spectra of the amorphous standard and that reported by Craig,[7] in Figure 10 shows many matching peaks and displays the broad features expected of an amorphous material, especially in the regions expected for hydrogen bonds. Salbutamol sulfate possesses OH and NH bonds that show broad peaks in the region 3000 to 3600 $cm^{-1}$ (consistent with the continuous random network model discussed in chapter 1 section 1.6.2.)

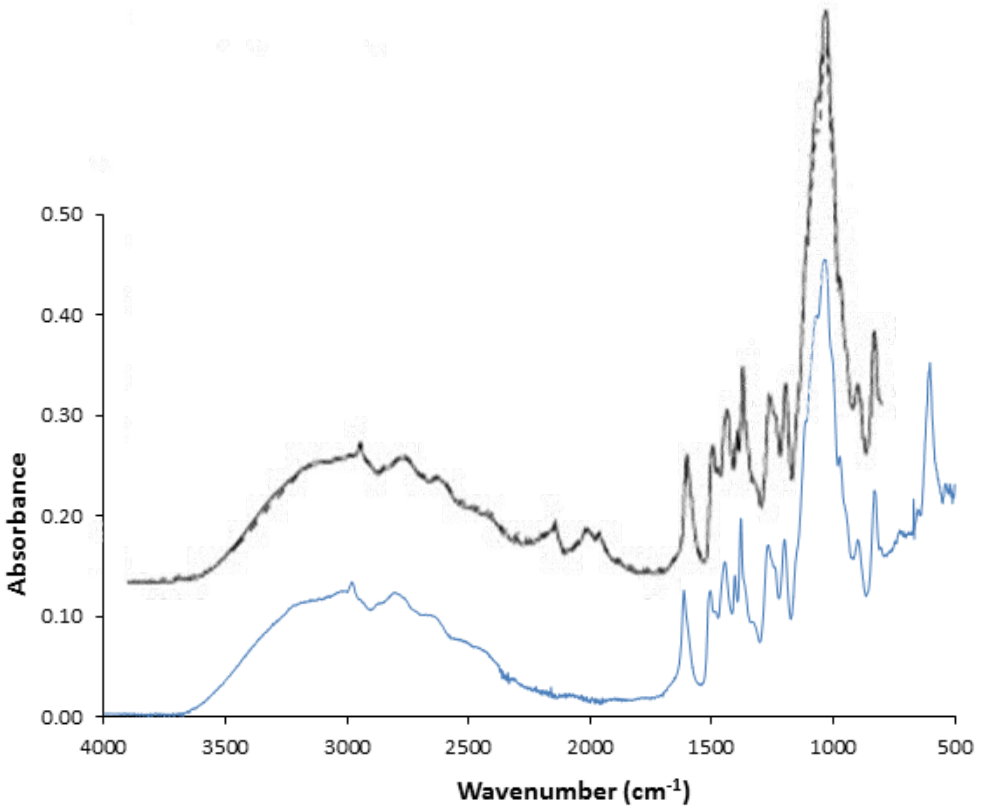


**Figure 10 FT-IR Spray dried amorphous standard spectra blue line from 3M supplied standard, black line from Craig et al[7]**

### 7.2.5 Scanning Electron Microscope

Figure 12, the SEM picture of the amorphous standard shows, dimpled spheres in the size range 0.5 to 3.0 µm. This type of morphology is similar to the amorphous spray dried salbutamol sulfate reported by Craig.[7] Figure 13 shows the SEM of the crystalline standard which was originally generated from micronised material. The crystalline standard shows rounded edges to the fractured angular shapes. Although their particle size is similar, the morphology of the amorphous and crystalline standards is distinctive.

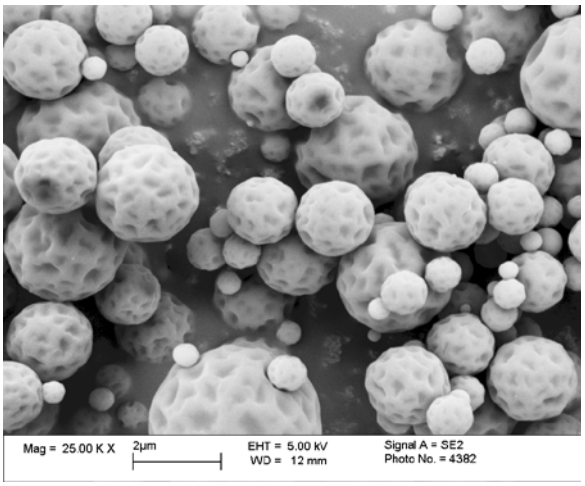


Figure 11 SEM of spray dried salbutamol sulfate amorphous standard

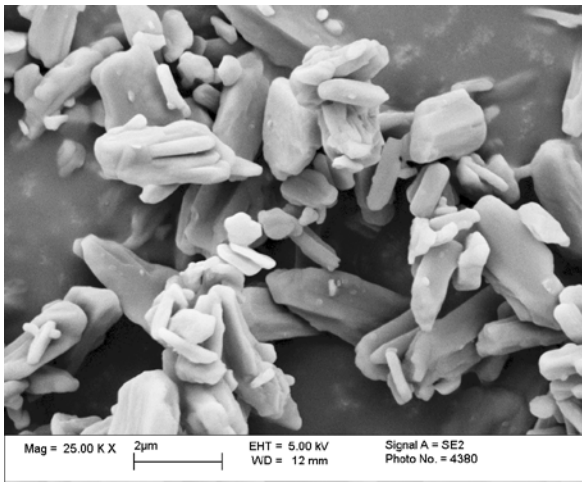


Figure 12 SEM of the salbutamol sulfate crystalline standard

### 7.2.6 Dynamic Vapour Sorption

#### – determination of Critical humidity glass transition point

Determination of the critical relative humidity glass transition point for spray dried salbutamol sulfate was carried out using DVS equipment in a ramped mode rather than discrete. Figure 14 shows the DVS plot in ramped mode (6% per hour), the point of inflection on the mass curve is said to mark the change from surface adsorption to bulk absorption and is known as the relative humidity glass transition point.[17]

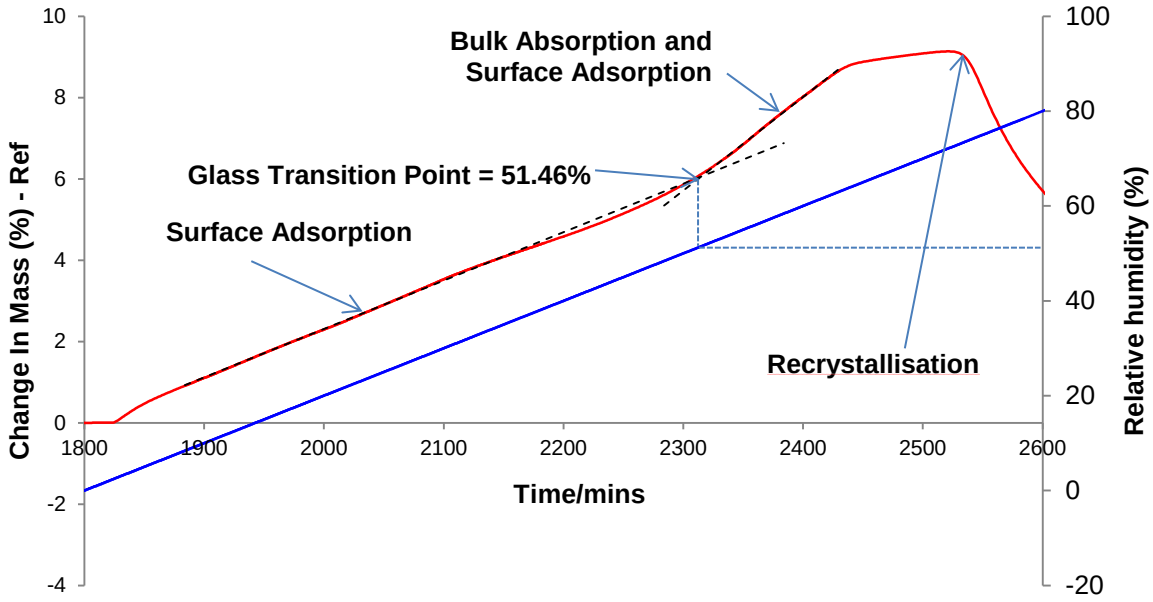


Figure 13 DVS plot with a ramp rate of 6% relative humidity per hour for spray dried salbutamol sulfate batch PJ190210. Red line represents mass change and blue line relative humidity.

The critical relative humidity glass transition point is determined from a number of such plots using different humidity ramp rates. Finally a plot of relative humidity glass transition points against ramp rate gives the critical relative humidity glass transition by extrapolation to a zero ramp rate, see Figure 15.[17] The critical relative humidity glass transition is useful to determine, since it predicts the maximum relative humidity at which amorphous salbutamol sulfate can be expected to remain stable and not undergo change to the crystalline form.[17] In addition, it also suggests the maximum humidity value to which DVS equilibrium relative humidity measurements can be expected to be linear.

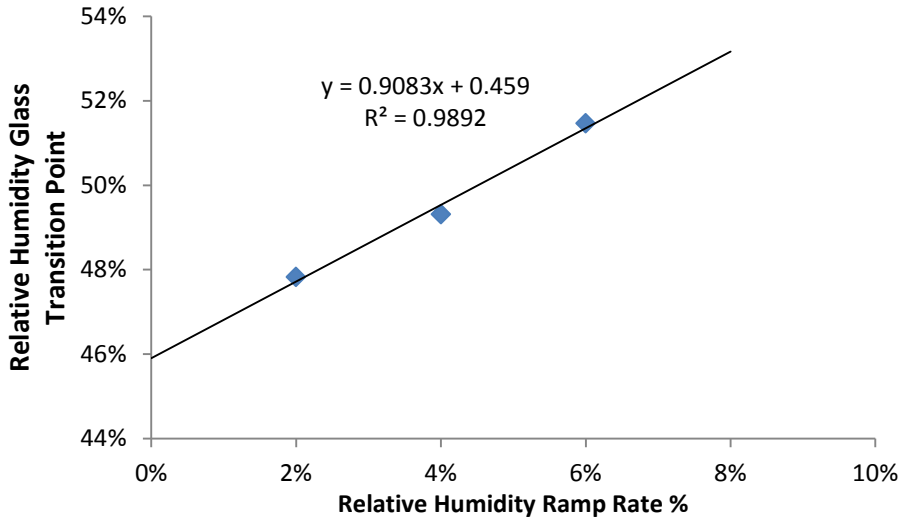


**Figure 14 Plot of relative humidity glass transition points against relative humidity ramp rate**

The critical relative humidity glass transition point determined for the amorphous standard of 45.9% was not consistent with Thielmann's work on a similar sample of salbutamol sulfate prepared by spray drying, which produced a value of 66.4% at 25°C [17] This implies materials considered amorphous by X-ray diffraction produced via spray drying may be variable in their behaviour towards moisture, or DVS instrument conditions may influence the results for this particular test.

### 7.2.7 Dynamic Vapour Sorption - changing humidity in discrete steps

The amorphous and crystalline salbutamol standards were subjected to DVS runs using discrete steps in relative humidity. The results from these runs are shown in Figure 16 and Figure 17. The standards were subjected to humidity cycles that increased from

0% to 90% in 10 % steps and then back down to 0% again, with the cycle repeated to ensure no further mass changes were possible. The step changes in humidity only proceeded when the time limit of 360 minutes was reached for each step, or the mass change per minute was less than 0.0005%.

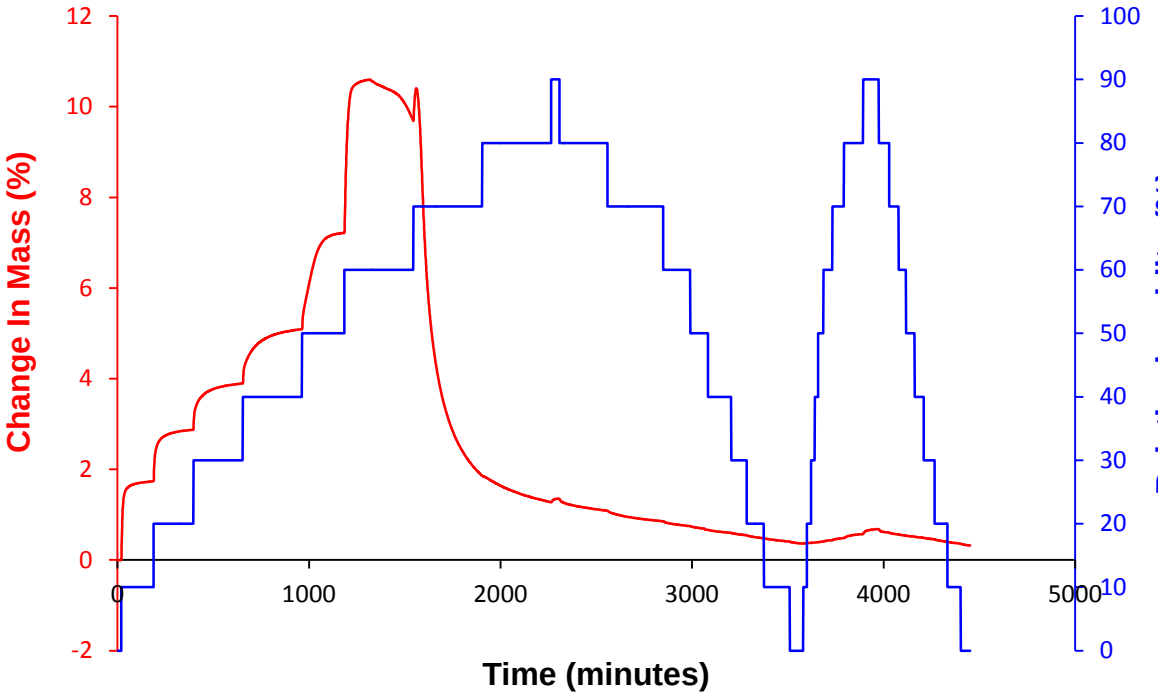


**Figure 15 Spray dried amorphous standard DVS, run using discrete steps in relative humidity. Red line represents mass change and blue line relative humidity.**

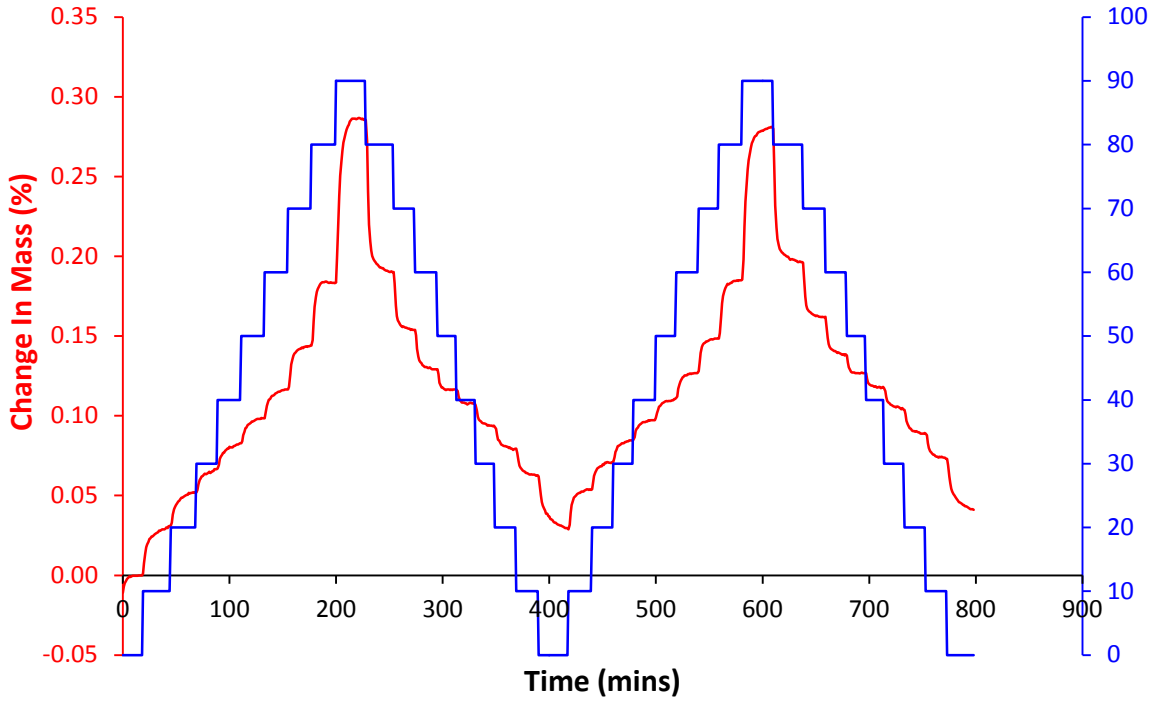


**Figure 16 Crystalline standard DVS, run using discrete steps in relative humidity. Red line represents mass change and blue line relative humidity.**

DVS presents a means of demonstrating a crystalline sample is free from amorphous content, (provided the amorphous material absorbs the solvent vapour), since the DVS response will be identical for both cycles.

The major difference between Figure 16 and Figure 17 is the scale of the mass change axis. The amorphous standard showed a maximum mass change of about 10.3%, whereas the crystal standard showed a maximum mass change of about 0.24%. The crystalline standard in Figure 17 showed the two cycles to have very similar mass changes. In contrast, the amorphous standard showed a second cycle to have a very different mass change profile to the first. The mass changes for the second cycle corrected to a zero value for the final measurement are shown in Table 3. These results show both materials behave in a similar manner, once the second cycle has been reached and demonstrates that the DVS run conditions are capable of converting an entirely amorphous sample to an entirely crystalline sample.

| Relative Humidity | Crystalline | Spray Dried |
|---|---|---|
| 90% | 0.24% | 0.20% |
| 80% | 0.16% | 0.16% |
| 70% | 0.12% | 0.13% |
| 60% | 0.10% | 0.12% |
| 50% | 0.09% | 0.10% |
| 40% | 0.08% | 0.08% |
| 30% | 0.06% | 0.07% |
| 20% | 0.05% | 0.05% |
| 10% | 0.03% | 0.03% |
| 0% | 0.00% | 0.00% |

**Table 1 Comparison of mass change for both crystalline and spray dried samples for the DVS second cycle corrected by the final mass change**

### 7.2.8 Characterisation of DVS residues

The powder X-ray diffraction pattern was taken of the amorphous spray dried sample after its DVS run, this showed a near identical pattern to that calculated using Mercury from Leger's data, (see Figure 18).[9, 10]

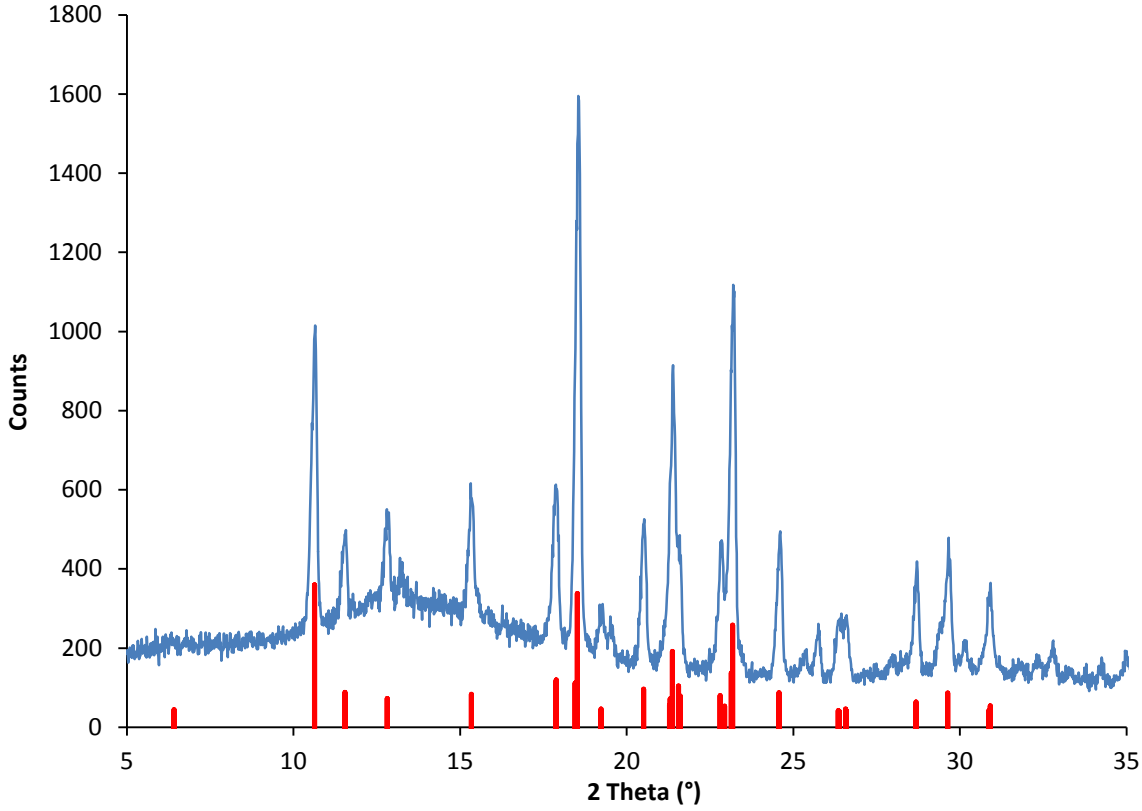


**Figure 17 powder X-ray diffraction pattern of spray dried (amorphous standard) after DVS[9, 10]**

## 7.3 Discussion for the Amorphous and Crystalline standards

The properties of the amorphous standard were consistent with its status; it showed a glass transition point,[8] the powder X-ray diffraction pattern showed only a diffuse halo,[18] its reduced paired distribution function showed evidence of long range random structure.[12] The infra-red spectrum showed broad peaks, between 2250 and 3600 $cm^{-1}$ consistent with the continuous random network of hydrogen bonds.[7, 14] The properties of the crystalline standard were also consistent with its status; the powder X-ray diffraction pattern matched that of Leger et al,[10] the melting point onset at 189.9 °C was consistent with York's work[6] and the infrared spectrum matched Palacios[15]. The DVS results for the crystalline sample in Figure 17 shows identical results for both cycles, which suggests of significant amorphous content is absent from the crystalline standard.

## 7.4 Preparation of mixtures

To achieve good intimate mixing of the two standards, it was critical to ensure the two powders flowed freely. Water is able to act as a plasticiser to hydrogen bonded small organic molecules in the amorphous state. Water enters their structures and their glass transition point drops below ambient conditions, and so they take on plastic properties, (becoming sticky).[19] Ensuring atmospheric moisture did not contaminate the amorphous standard was critical to ensuring the two powders flowed freely for intimate mixing.[19]

A five place Ohaus discovery balance was used for this work, unfortunately it was not possible to transfer this balance in to the argon glove box. The weighing of sample mixes was carried out by first tarring the labelled glass vials with paired polythene seals and then placing them in the argon glove box. The spray dried amorphous standard was roughly weighed into the vials. The vials were then sealed and removed from the glove box, and re-weighed on the balance after 3 hours equilibrating in the laboratory atmosphere. The sealed vials were then placed back in the glove box and the crystalline standard roughly weighed into the vials. The vials were once again sealed, removed from the glove box, allowed to equilibrate with the lab atmosphere and weighed on the Ohaus discovery balance. The recorded weights for both amorphous spray dried and the crystalline standards are shown in Table 4. The sealed glass vials were placed on a roller bed mixer, set at 60 revolutions per minute and left for 24 h.

| Sample ID | Tare (mg) | Spray Dried + Tare (mg) | Spray Dried Content (mg) | Spray Dried + Crystalline + Tare (mg) | Crystalline Content (mg) | Amorphous content (%w/w) |
|---|---|---|---|---|---|---|
| 11092001 | 4638.87 | 4644.24 | 5.37 | 5085.14 | 440.90 | 1.20 |
| 11092004 | 4615.61 | 4641.64 | 26.03 | 4838.87 | 197.23 | 11.66 |
| 11092002 | 4597.48 | 4629.67 | 32.18 | 5078.83 | 449.17 | 6.69 |
| 11092006 | 4656.61 | 4699.19 | 42.58 | 4793.20 | 94.01 | 31.17 |
| 11092005 | 4583.43 | 4606.69 | 23.25 | 4735.83 | 129.14 | 15.26 |
| 11092003 | 4616.44 | 4639.36 | 22.93 | 4907.37 | 268.01 | 7.88 |
| 11092007 | 4559.28 | 4604.88 | 45.60 | 4636.90 | 32.02 | 58.75 |

**Table 2 Weights of amorphous and crystalline standards in calibration mixes**

## 7.5 Methods for amorphous content measurement

Two different methods for measuring amorphous content were described by Gorny.[5] The first used a correlation between equilibrium mass change from cycle to cycle at humidity values of 10%, 20%, 30% and 40%, which had previously been described by Mackin.[20] The second method employed by Gorny measured the difference in areas under the mass curves for the two cycles, and had first be described by Van Oort. [5]

The idea of measuring the difference between the first and second DVS cycles assumes that an amorphous material absorbs a plasticising solvate into its structure, which brings about crystallisation. All DVS methods use the fact that the amorphous phase absorbs a solvent reversibly until crystallisation occurs, at this point the excess water is expelled. The crystallisation process may produce a solvated polymorph, if one exists for the material under test but in this case none are reported for salbutamol sulfate.

### 7.5.1 Equilibrium mass change in sorbate vapour - Zografi

The percentage mass change at equilibrium was proportional to the amorphous content at a fixed sorbent vapour pressure. [1] The percentage mass change at equilibrium is calculated using Equation 2. The dry mass is measured by exposing the sample to a flow of dry nitrogen for a set period, or until the mass change is less than 0.0005%. The equilibrium mass change is then measured by exposing the sample to a fixed humidity (or sorbent vapour pressure) and allowing the sample to equilibrate until the mass changes by less than 0.0005%. Figure 18 shows the point at which the "*dry mass*" was recorded (in green) and the points at which the equilibrium mass is measured at 10, 20, 30 and 40% relative humidity are recorded.[1]

$$Mass\ change\ \% = \frac{equilibrium\ mass - dry\ mass}{dry\ mass} \times 100$$ Equation 3

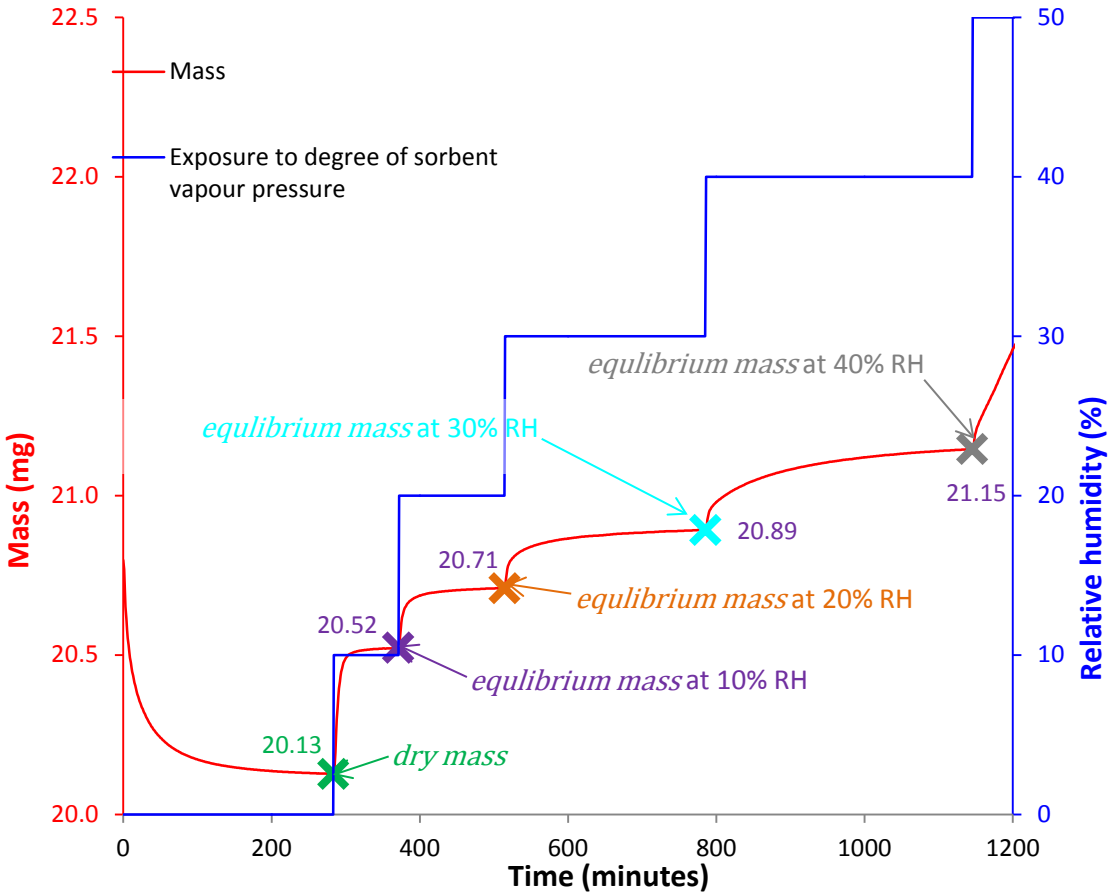


**Figure 18 DVS run showing mass against time with step changes in relative humidity (RH) using a sample of spray dried salbutamol sulfate**

Zografi's method[1] requires that further DVS runs are carried out on mixtures containing known amorphous content. The results from the mixtures reported in Table 4 are plotted in Figure 19.

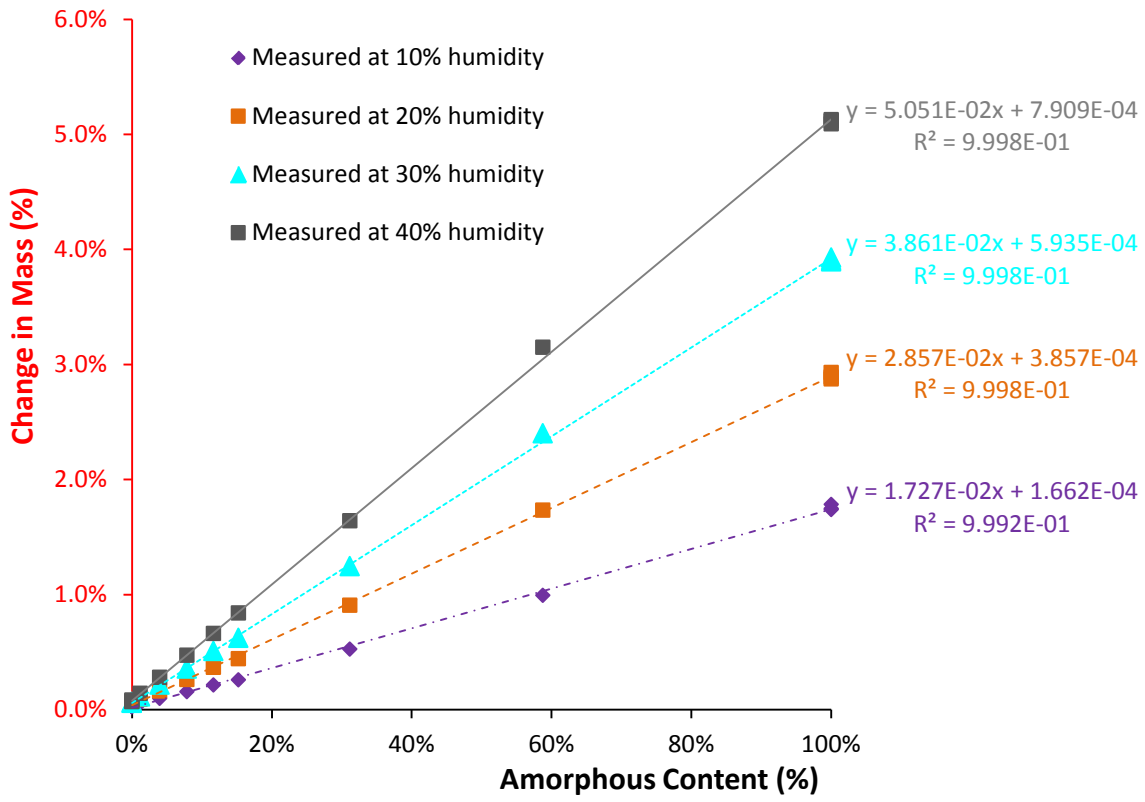


**Figure 19 Amorphous content calibrations using the Zografi method with 10%, 20%, 30% and 40% fixed humidity levels, using salbutamol sulfate spray dried content as the amorphous material**

### 7.5.2 Stoichiometric re-crystallisation - Buckton

The methodology developed by Buckton uses sorbent vapour to chemically change the amorphous content into a solvated polymorph. The DVS program to carry this out requires three steps, a step to remove any solvent that has adsorbed or absorbed by the sample and to record this "initial mass". The second step subjects the sample to a high level of sorbent vapour where the sorbate is absorbed by the amorphous phase and eventually crystallises to a form a sorbate polymorph, or hydrate. After crystallisation, the excess sorbate is expelled from the sample. The third step of the DVS program is a drying step to remove any physi-sorbed sorbate and record a "final mass" once a constant mass is achieved. The amorphous content is calculated with Equation 1 using the molecular weight of the solvate polymorph and non solvate polymorph. [3]

$$\frac{(Final\ mass/Initial\ mass)}{((M_r + solvate\_M_r)/M_r)} \times 100 = amorphous\ content \qquad \textbf{Equation 4}$$

Since salbutamol sulfate does not produce a solvated polymorph, this technique is not suitable for measuring the amorphous content.

### 7.5.3 Corrected Equilibrium mass change in sorbate vapour - Mackin

The method described by Macking involves drying the sample and then completing two cycles that raise the sorbate level to 90% of its maximum level in 10% steps and back to 0%. The first cycle of increasing sorbate vapour pressure allows the amorphous content to be calculated from the equilibrium mass change as shown by Zografi.[1] Amorphous samples have small particle sizes (see Figure 14) and therefore high surface areas and the process of absorption is rapid. The physi-sorption of sorbate vapour on to the surface can also increase the mass. The Mackin method attempts to correct for the physisorbed species by subtracting the percentage mass change for each sorbate step of the second cycle from the first. [20]

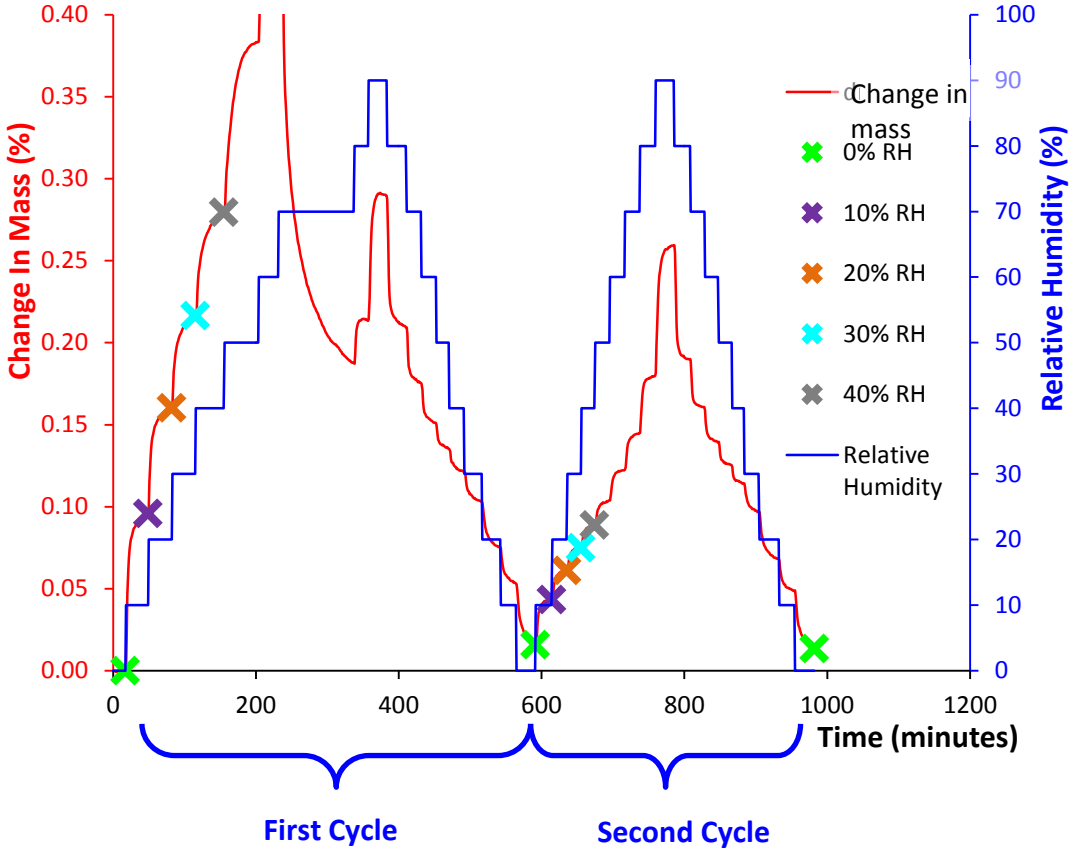


Figure 20 DVS run on salbutamol sulfate mix of 3.97% spray dried and 97.03% crystalline

Figure 3 shows the points used to carry out an amorphous content calibration using the Mackin method, the first and second relative humidity cycles are shown along with the coloured pairs of points.[20] Each coloured point pair were used to calculate the difference in mass change for first and second cycle, this was then used to construct the calibration line for the amorphous content, (see Figure 4).[20]

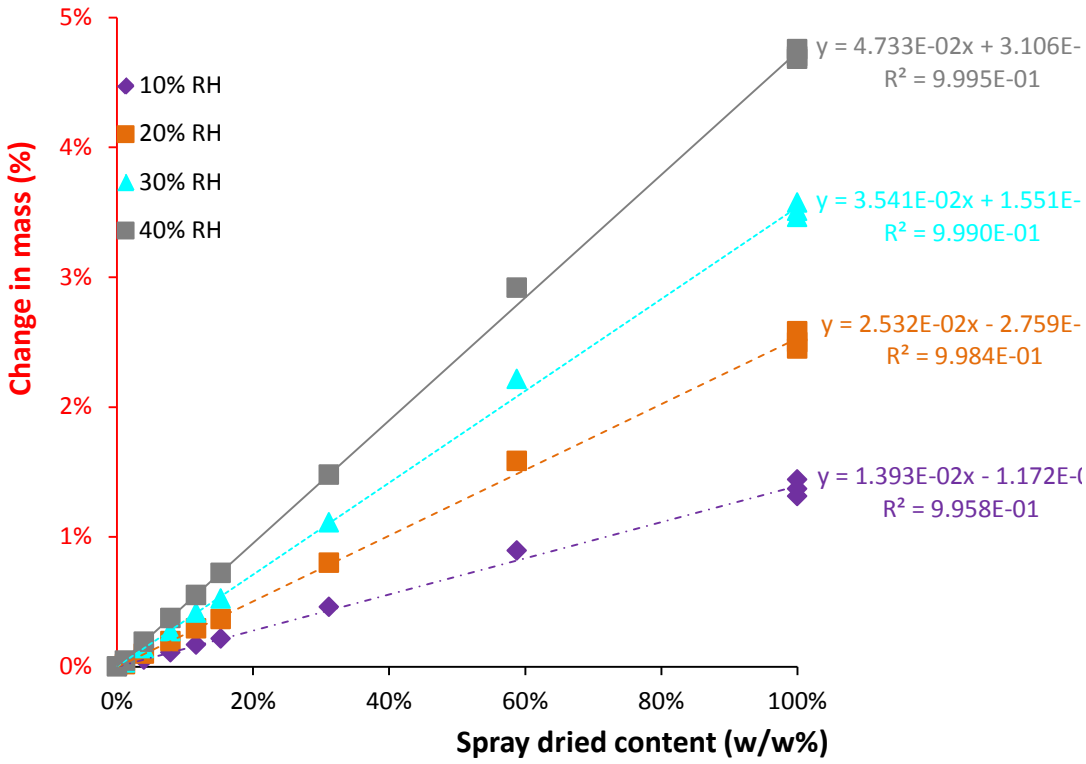


**Figure 21 Amorphous content calibrations using the Mackin method using 10%,20%, 30% and 40% fixed humidity levels, using salbutamol sulfate spray dried content as the amorphous material**

### 7.5.4 Area difference under mass change curve for the two cycles - Van Oort

Calibration using the difference between the areas of mass change for the two cycles was put forward by Van Oort.[4] This was carried out using the data from the same runs shown in Figure 22 and Figure 19.

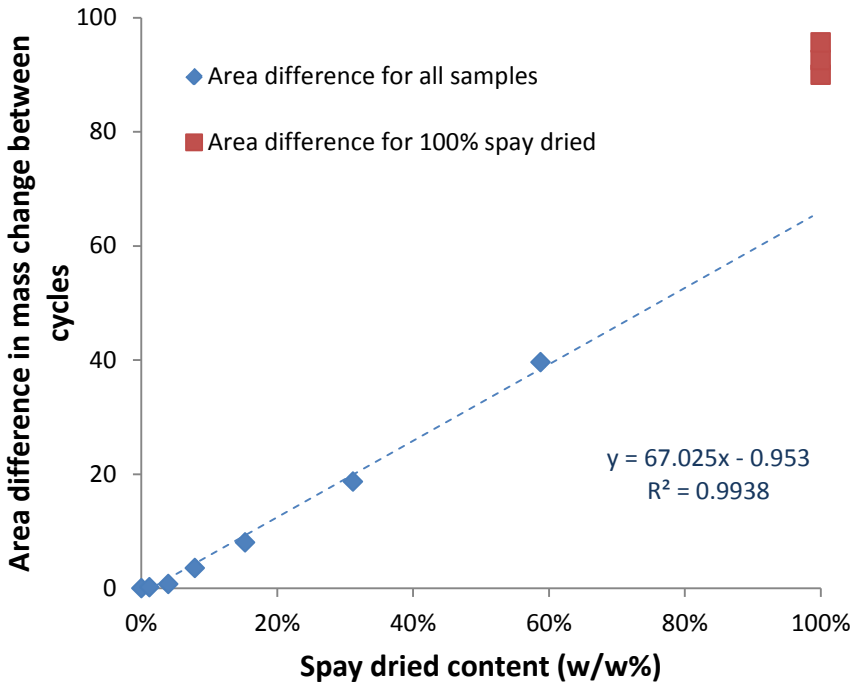


**Figure 22 Amorphous content calibrations using the Van Oort method, subtracting the second cycle area from the first, plotted against spray dried content**

In this case the 100% spray dried samples do not appear to match the calibration line produced by the mixtures. The sample size used for all the mix samples was between 40 and 45 mg, whereas a mass of 20 to 25 mg was used for the 100% spray dried samples, (to reduce time spent per run). To produce a calibration using this particular method it may be necessary to use an identical sample mass that is repeated for all runs.

## 7.6 Assessment of Calibration Statistics

The data points used in the three calibrations are set out in Table 4, this shows the mass change at equilibrium with atmospheres containing 10, 20, 30 and 40% humidity at 25°C on both the first and second humidity cycles. The straight line statistics for the Zografi and Mackin methods are set out in Table 5, The statistics allow the random errors in measuring a sample's amorphous content to be predicted, allowing the limits of detection and analysis to be proposed. The Zografi and Mackin methods both provide better linear calibrations than the Van Oort method (comparing $r^2$ values), following these results the Van Oort or area method was not considered further in this study.

| Content | | | | | | | | | | | | | |
|---|---|---|---|---|---|---|---|---|---|---|---|---|---|
| % spray dried | 0% | 0% | 0% | 1.20% | 3.97% | 7.88% | 11.66% | 15.26% | 31.17% | 58.75% | 100.00% | 100.00% | 100.00% |
| % crystalline | 100% | 100% | 100% | 98.80% | 96.03% | 92.12% | 88.34% | 84.74% | 68.83% | 41.25% | 0.00% | 0.00% | 0.00% |
| 1st cycle | | | | | | | | | | | | | |
| 10% | 0.03% | 0.03% | 0.02% | 0.05% | 0.10% | 0.15% | 0.21% | 0.26% | 0.53% | 0.99% | 1.75% | 1.74% | 1.78% |
| 20% | 0.05% | 0.04% | 0.04% | 0.09% | 0.16% | 0.26% | 0.37% | 0.44% | 0.91% | 1.73% | 2.89% | 2.87% | 2.93% |
| 30% | 0.07% | 0.06% | 0.06% | 0.11% | 0.22% | 0.36% | 0.51% | 0.62% | 1.24% | 2.40% | 3.91% | 3.89% | 3.93% |
| 40% | 0.08% | 0.07% | 0.07% | 0.14% | 0.28% | 0.47% | 0.66% | 0.84% | 1.64% | 3.15% | 5.13% | 5.09% | 5.12% |
| 2nd cycle | | | | | | | | | | | | | |
| 10% | 0.05% | 0.04% | 0.04% | 0.05% | 0.04% | 0.04% | 0.05% | 0.04% | 0.07% | 0.10% | 0.44% | 0.37% | 0.34% |
| 20% | 0.07% | 0.05% | 0.05% | 0.07% | 0.06% | 0.07% | 0.07% | 0.07% | 0.11% | 0.15% | 0.44% | 0.38% | 0.35% |
| 30% | 0.08% | 0.06% | 0.06% | 0.08% | 0.08% | 0.08% | 0.09% | 0.10% | 0.14% | 0.19% | 0.44% | 0.38% | 0.35% |
| 40% | 0.10% | 0.07% | 0.07% | 0.10% | 0.09% | 0.10% | 0.11% | 0.12% | 0.16% | 0.23% | 0.45% | 0.39% | 0.36% |
| Difference between first and 2nd cycle | | | | | | | | | | | | | |
| 10% | -0.02% | -0.01% | -0.01% | 0.00% | 0.05% | 0.11% | 0.17% | 0.21% | 0.46% | 0.89% | 1.31% | 1.37% | 1.44% |
| 20% | -0.02% | -0.01% | -0.01% | 0.02% | 0.10% | 0.19% | 0.29% | 0.37% | 0.80% | 1.58% | 2.45% | 2.50% | 2.58% |
| 30% | -0.02% | 0.00% | 0.00% | 0.03% | 0.14% | 0.27% | 0.41% | 0.52% | 1.11% | 2.21% | 3.46% | 3.51% | 3.57% |
| 40% | -0.01% | 0.00% | 0.00% | 0.04% | 0.19% | 0.37% | 0.55% | 0.72% | 1.48% | 2.92% | 4.68% | 4.70% | 4.75% |
| Mass (mg) | 20.13 | 44.16 | 26.33 | 40.22 | 41.39 | 41.39 | 41.39 | 40.44 | 40.38 | 39.84 | 26.72 | 21.58 | 23.15 |
| 1st cycle area | 0.29 | 0.27 | 0.29 | 0.56 | 1.13 | 3.97 | 2.74 | 8.74 | 19.67 | 41.59 | 90.30 | 93.86 | 96.65 |
| 2nd cycle area | 0.29 | 0.27 | 0.32 | 0.39 | 0.39 | 0.46 | 0.63 | 0.72 | 1.00 | 2.00 | 0.34 | 1.28 | 1.02 |
| $1^{st}$ - $2^{nd}$ Cycle area | 0.01 | 0.00 | -0.03 | 0.17 | 0.74 | 3.51 | 2.11 | 8.02 | 18.67 | 39.59 | 89.97 | 92.58 | 95.63 |

**Table 3 Data from DVS runs for the salbutamol sulfate amorphous content calibration using the Zografi, Mackin and Van Oort methods.**

| % spray dried | 0.00% | 0.00% | 0.00% | 1.20% | 3.97% | 7.88% | 11.66% | 15.26% | 31.17% | 58.75% | 100.00% | 100.00% | 100.00% |
|---|---|---|---|---|---|---|---|---|---|---|---|---|---|
| **Zografi method** | **intercept** | **slope** | **$r^2$** | **$s_{y/x}$** | $\bar{y}$ | $\bar{x}$ | **n** | $\sum(x_i-\bar{x})^2$ | $\sum x_i^2$ | **$s_{y/x}$/b** | **1+(1/n)** | **$s_b$** | **$s_a$** |
| 10% | 0.017% | 1.727% | 0.9992 | 0.022% | 0.59% | 33.07% | 13 | 206.55% | 313% | 1.254% | 1.09 | 0.0151% | 0.0074% |
| 20% | 0.039% | 2.857% | 0.9998 | 0.019% | 0.98% | 33.07% | 13 | 206.55% | 313% | 0.676% | 1.09 | 0.0134% | 0.0066% |
| 30% | 0.059% | 3.861% | 0.9998 | 0.026% | 1.34% | 33.07% | 13 | 206.55% | 313% | 0.678% | 1.09 | 0.0182% | 0.0089% |
| 40% | 0.079% | 5.051% | 0.9998 | 0.034% | 1.75% | 33.07% | 13 | 206.55% | 313% | 0.676% | 1.09 | 0.0238% | 0.0117% |

| % spray dried | 0.00% | 0.00% | 0.00% | 1.20% | 3.97% | 7.88% | 11.66% | 15.26% | 31.17% | 58.75% | 100.00% | 100.00% | 100.00% |
|---|---|---|---|---|---|---|---|---|---|---|---|---|---|
| **Mackin method** | **intercept** | **slope** | **$r^2$** | **$s_{y/x}$** | $\bar{y}$ | $\bar{x}$ | **n** | $\sum(x_i-\bar{x})^2$ | $\sum x_i^2$ | **$s_{y/x}$/b** | **1+(1/n)** | **$s_b$** | **$s_a$** |
| 10% | -0.001% | 1.393% | 0.9958 | 0.039% | 0.46% | 33.07% | 13 | 206.55% | 313% | 2.798% | 1.09 | 0.0271% | 0.0133% |
| 20% | -0.003% | 2.532% | 0.9984 | 0.043% | 0.83% | 33.07% | 13 | 206.55% | 313% | 1.712% | 1.09 | 0.0302% | 0.0148% |
| 30% | 0.000% | 3.541% | 0.9990 | 0.050% | 1.17% | 33.07% | 13 | 206.55% | 313% | 1.400% | 1.09 | 0.0345% | 0.0169% |
| 40% | 0.003% | 4.733% | 0.9995 | 0.046% | 1.57% | 33.07% | 13 | 206.55% | 313% | 0.969% | 1.09 | 0.0319% | 0.0157% |

**Table 4 Straight line statistics for amorphous salbutamol sulfate content for the Zografi and Mackin methods**

| | Gorny | | | This study | | | |
|---|---|---|---|---|---|---|---|
| | Slope | Intercept | @100% | @100% | 95% cfl | Slope | Intercept |
| 10% RH | 1.46 | 0.0430 | 1.50% | 1.39% | 0.089% | 1.39 | -0.0012 |
| 20% RH | 2.32 | 0.0406 | 2.36% | 2.53% | 0.099% | 2.53 | -0.0028 |
| 30% RH | 3.37 | 0.0309 | 3.40% | 3.54% | 0.113% | 3.54 | 0.0002 |
| 40% RH | 4.82 | 0.0059 | 4.83% | 4.74% | 0.105% | 4.73 | 0.0031 |
| 50% RH | 6.86 | -0.0279 | 6.83% | | | | |

| Uncertainty to 95% cfl | |
|---|---|
| slope | Intercept |
| ±0.060 | ±0.00029 |
| ±0.066 | ±0.00033 |
| ±0.076 | ±0.00037 |
| ±0.070 | ±0.00034 |
| | |

Table 5 Comparison of the previous Gorny et al[5] work against this study

## 7.7 Comparison between this study's findings and the Gorny paper

The Gorny study does not show a data table of values, but does give the slope and intercept of the calibration lines using the Makin method. All comparisons have therefore been restricted to the Makin method. Table 7 shows the slope and intercept data obtained from the Gorny study, along with the results from this study and their random errors for slope and intercept.

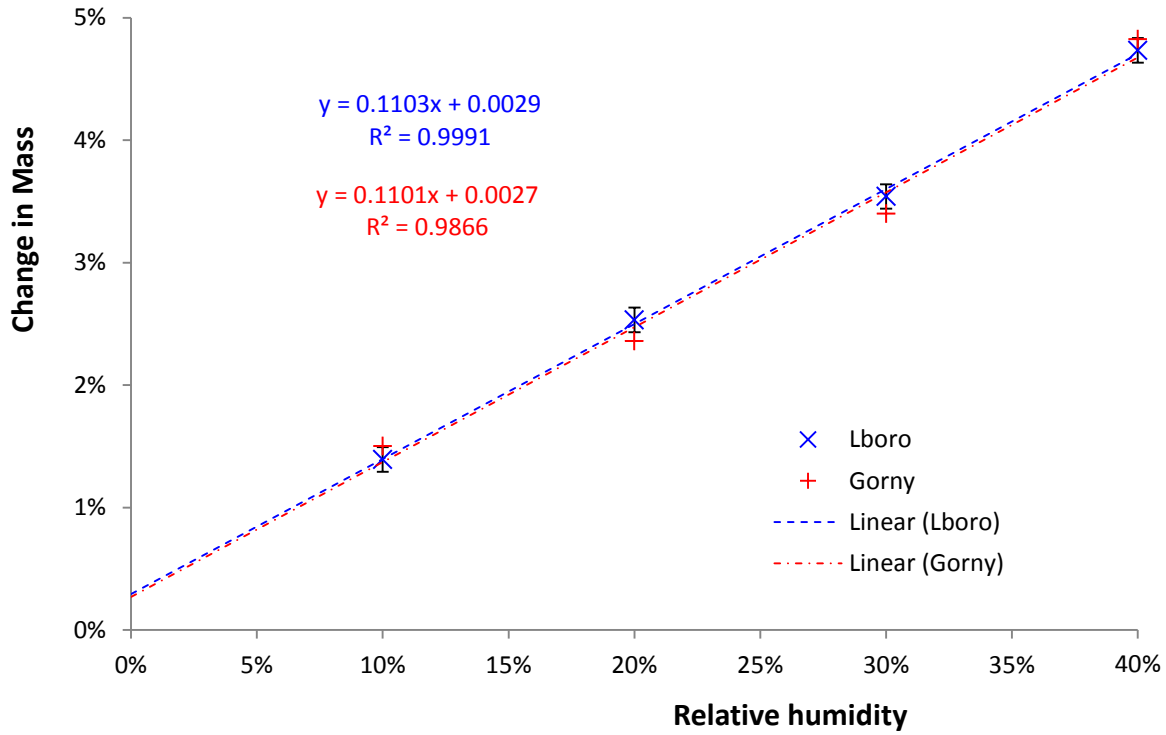


**Figure 23 Comparison between this study's results and Gorny's[5] for the mass change in a 100% amorphous (spray dried sample)**

The columns in Table 7 headed "@100%" are the slope and intercept values used to estimate the change in mass for a 100% amorphous sample. These values are plotted in Figure 23 along with the 95% confidence limits for this study shown as error bars. The Gorny estimates of mass change all fall outside the error bars (except for the 40% RH point), however the straight line fit for both estimates produce slope and intercept values that are nearly identical. One explanation for Figure 23 is that both sets of results have similar means, but differences in variation. This hypothesis can be tested using a paired t-test, the result of which can be seen in Table 7.[21]

**Null proposed hypothesis:**

Estimates of the 100% amorphous responses from both this and the Gorny study are not significantly different at the 95% confidence level.

| | Gorny | This study |
|---|---|---|
| 10% RH | 1.50% | 1.39% |
| 20% RH | 2.36% | 2.53% |
| 30% RH | 3.40% | 3.54% |
| 40% RH | 4.83% | 4.74% |

| Difference |
|---|
| -0.11% |
| 0.17% |
| 0.14% |
| -0.09% |

| Values calculated on difference | |
|---|---|
| Mean | 0.03% |
| Standard deviation | 0.15% |
| n | 4 |
| Calculated t value | 0.37 |
| t critical (two tailed) | 3.18 |

**Table 6 paired test on estimated 100% amorphous results from this and the Gorny study**

Table 7 shows the critical t value for a two tailed test, (since there is no preconceived idea as to whether the results will be different by a positive or negative amount). The calculated t value is less than the critical t value, so the null hypotheses is not rejected. Although this does not prove that the two sets of results are the same, it can be said that the results from this study and Gorny's are not significantly different.[21]

## 7.8 Conclusions

The crystalline and amorphous standards used to produce the calibration mixes are consistent with been pure phases. The calibration data appears to be repeatable given the low standard deviation for the pure standards and the linearity of response for the mixes. The results also appear to be reproducible, since the 100% amorphous estimates are not significantly different to Gorny's study. Should DVS instrument responses at equilibrium prove to be universal for an amorphous material, the work required to quantify amorphous materials by each instrument owner could be reduced to looking up a literature value (for the Makin method). The caveat to this calibration is that amorphous materials generated by different techniques (i.e. milling or freeze drying or rapid quenching from the melt) may not produce similar DVS results.

***References***

1 A. Saleki-Gerhard, C. Ahlneck and G. Zografi, *International Journal of Pharmaceutics,* 1994, 101, 237 (DOI:10.1016/0378-5173(94)90219-4).

2 K. Lochmann, L. Oger and D. Stoyan, *Solid State Sciences,* 2006, 8, 1397-1413 (DOI:10.1016/j.solidstatesciences.2006.07.011).

3 G. Buckton and P. Darcy, *International Journal of Pharmaceutics,* 1995, 123, 265-271.

4 M. Van Oort, *1st International Workshop on Physical Characterization of Pharmaceutical<br />Solids, Lancaster, PA September*, 2000.

5 M. Gorny, M. Jakobs, V. Mykhaylova and N. A. Urbanetz, *Drug Developement and Industrial Pharmacy,* 2007, 33, 235-243 (DOI:10.1080/03639040601128647).

6 M. H. Shariare, M. de Matas and P. York, *Int. J. Pharm.,* 2011, 415, 62-72 (DOI:10.1016/j.ijpharm.2011.05.043).

7 L. C. Grisedale, P. S. Belton, M. J. Jamieson, S. A. Barker and D. Q. M. Craig, *Int. J. Pharm.,* 2012, 422, 220-228 (DOI:10.1016/j.ijpharm.2011.10.055).

8 D. Q. M. Craig and M. Reading, *Thermal analysis of pharmaceuticals*, CRC distributor; Taylor & Francis, New York; London, 2006.

9 C. F. Macrae, I. J. Bruno, J. A. Chisholm, P. R. Edgington, P. McCabe, E. Pidcock, L. Rodriguez-Monge, R. Taylor, J. van de Streek and P. A. Wood, *J. Appl. Cryst.,* 2008, 41, 466 (DOI:10.1107/S002188980600731X).

10 J. M. Leger, M. Goursolle, M. Gadret and A. Carpy, *Acta Crystallogr. ,Sect. B:Struct. Crystallogr. Cryst. Chem.,* 1978, 34, 1203 (DOI:10.1107/S056774087800521X).

11 X. Qiu, J. W. Thompson and S. J. L. Billinge, *J. Appl. Crystal.,* 2004, 37, 678.

12 T. Egami, S. J. L. Billinge, T. Egami and B, *Underneath the Bragg Peaks: Structural Analysis of Complex Materials*, Pergamon, Amsterdam, 2003.

13 S. Bates, G. Zografi, D. Engers, K. Morris, K. Crowley and A. Newman, *Pharmaceut. Res,* 2006, 23, 2333 (DOI:10.1007/s11095-006-9086-2).

14 R. Hilfiker, *Polymorphism : in the pharmaceutical industry / Weinheim : Wiley-VCH, 2006*, Wiley-VCH, Weinheim, 2006.

15 M. A. Palacio, S. Cuffini, R. Badini, A. Karlsson and S. M. Palacios, *J. Pharm. Biomed. Anal.,* 2007, 43, 1531-1534 (DOI:10.1016/j.jpba.2006.11.009).

16 S. M. Palacios and M. A. Palacio, *Tetrahedron: Asymmetry,* 2007, 18, 1170-1175 (DOI:10.1016/j.tetasy.2007.05.010).

17 D. J. Burnett, F. Thielmann and J. Booth, *International Journal of Pharmaceutics,* 2004, 287, 123-133.

18 S. E. Dann, *Reactions and characterization of solids*, Royal Society of Chemistry, Cambridge, 2000.

19 Y. H. Roos, in *Encyclopedia of Food Sciences and Nutrition (Second Edition)*, ed. Editor-in-Chief: Benjamin Caballero, Academic Press, Oxford, 2003, p. 6094-6101.

20 L. Mackin, R. Zanon, J. M. Park, K. Foster, H. Opalenik and M. Demonte, *International Journal of Pharmaceutics,* 2002, 231, 227-236.

21 J. N. M. Miller J.C., *Statistics and Chemometrics for Analytical Chemistry*, Pearson Education, Edinburgh, 2000.

# CHAPTER 8

# Micronised salbutamol sulfate properties with age

## 8.1 Introduction – stability study

Salbutamol sulfate is a $\beta_2$ antagonist used to treat asthma. For optimum efficacy, the drug must be delivered to the respiratory regions of the lungs with a particle size of between 0.5 and 5 microns.[1] The manufacture of salbutamol sulfate for inhalers takes crystals with a range of particle sizes and micronises them into the respirable size range (see chapter 1 section 1.1.4). The process of reducing salbutamol sulfate particle size via micronisation has been shown to produce amorphous content by Pfeiffer.[2]

All amorphous materials are thermodynamically unstable,[3] so there is a risk of changes to efficacy over time. Stability testing is essential to pharmaceutical quality control, ensuring that manufactured drugs will perform identically to their clinical trials, even after storage on the pharmacy shelf.[4] The amorphous content of micronised salbutamol sulfate has been shown to change to crystalline on exposure to water vapour,[5] hence the interest in removing amorphous material from formulated salbutamol sulfate to improve shelf-life. This work seeks to investigate the stability of salbutamol sulfate micronised by 3M standard production methods and compare it to a development material described as 3M PET stabilised.

A stability protocol was prepared for two storage conditions; one ideal and the other non-ideal. For the ideal conditions, the samples were stored in sealed screw top glass vials in a desiccator over silica desiccant. The non-ideal conditions were a compromise between practical considerations of constructing an experiment using a saturated salt solution to generate a known relative humidity, and the expected conditions in the home. A study of temperature and humidity levels in Edinburgh children's bed rooms was made by Strachan,[6] who showed significant reporting of wheezing for children living in rooms with patches of fungus. The World Health Organisation suggests that the lowest relative humidity for germination of some species of fungi is 62–65%.[7] A relative humidity of 65% was therefore chosen for reasonably poor storage conditions.

## 8.2 Experimental – stability study

### 8.2.1 Sample source –stability study

All the samples were sourced from the 3M site Derby Road Loughborough. Three micronised batches were used, two fresh from manufacturing and one that had aged in a screw top bottle stored in the pilot plant at 20° C with 50% humidity. A fourth sample was a development sample of respirable particle size and low amorphous content. The age and source of the samples are shown in Table 1.

| Batch Number | GLA089 | GLB092 | GJC012 | 3M PET |
|---|---|---|---|---|
| **Source** | Factory | Factory | Factory | Development |
| **Micronised** | Yes | Yes | Yes | No |
| **Age (days)** | 0 | 2 | 182 | 1 |
| **Date of initial DVS run** | 05-Feb-2010 | 01-Mar-2010 | 10-Feb-2010 | 17-Feb-2010 |
| **Date of manufacture** | 5-Feb-2010 | 27-Feb-2010 | 12-Aug-2009 | 16-Feb-2010 |

**Table 1 Salbutamol sulfate stability study samples, the samples were stored in the pilot plant at 20 °C in a desiccator**

### 8.2.2 Stability study protocol

The two storage stations were held at 20 °C, with relative humidity of 0% and 65%. The storage periods used in this study were one and six weeks. These were scheduled to test materials as quickly as possible at their time point and to keep the instrument available for other workers.

The schedule involved staggering the start date by one week for each sample. The samples stored in ideal conditions were placed in individually labelled glass vials and kept sealed with screw top lids, which were in turn placed in a desiccator (over silica desiccant). At the time points, the appropriate vial was removed from the desiccator and placed in a sealed polythene bag.

The samples stored at 65% relative humidity were placed in a desiccator over a saturated solution of potassium nitrite made with deionised water.[8] Each sample required was placed in an individual labelled screw top glass vial, with their screw tops removed. At their various time points the vials were removed from the desiccators with their screw caps replaced tightened, and placed in sealed polythene bags.

### 8.2.3 Instrumental Techniques

The FT-IR measurements were carried out using the Shimadzu 8400 with Golden Gate ATI accessory. Powder X-ray diffraction patterns were recorded used the Bruker D8 measuring from 5 to 100° 2θ using a step size of 0.014767° per 0.5 seconds. The sample holders for the Bruker D8 were covered with mylar slips to reduce exposure to the atmosphere moisture, and prevent alteration of the samples. The SEM micrographs were produced on a Carl Zeiss 1530 VP field emission gun scanning electron microscope (FEG-SEM). The DSC measurements used the TA instruments SDT Q600 using open alumina sample pans with temperature and heat flow calibrations set out in chapter 3.

DVS was used to quantify the amorphous content as described in chapter 7 using the Zografi method. To reduce the run time on the instrument, the number of steps in the second cycle was reduced from 19 to 7 by using only the 0, 50, 60, 90, 60, 50 and 0% steps. The first DVS cycle remained identical to that used in chapter 7 allowing the quantification using the Zografi method. Sample sizes of between 40 and 50 mg were loaded on to the quartz pans for each run.

## 8.3 Results

### 8.3.1 DVS

The Zografi calibration set out in chapter 7 was calculated from the mass gain % at the different relative humidity levels, which are shown in Table 2.[9] The DVS runs for each of the samples at their initial time point are shown in figures 1 to 4, along with the calculation of amorphous content in tables 3 to 10 for each of the samples time points and stations.

| | Slope | Intercept | $r^2$ | $S_{x/y}$ | LoD |
|---|---|---|---|---|---|
| 10% RH | 1.73% | 0.02% | 0.9992 | 0.02% | 0.06% |
| 20% RH | 2.86% | 0.04% | 0.9998 | 0.02% | 0.08% |
| 30% RH | 3.86% | 0.06% | 0.9998 | 0.03% | 0.11% |
| 40% RH | 5.05% | 0.08% | 0.9998 | 0.03% | 0.13% |

**Table 2 DVS calibration line fit statistics for the different humidity levels for salbutamol sulfate found using the Zografi method.**

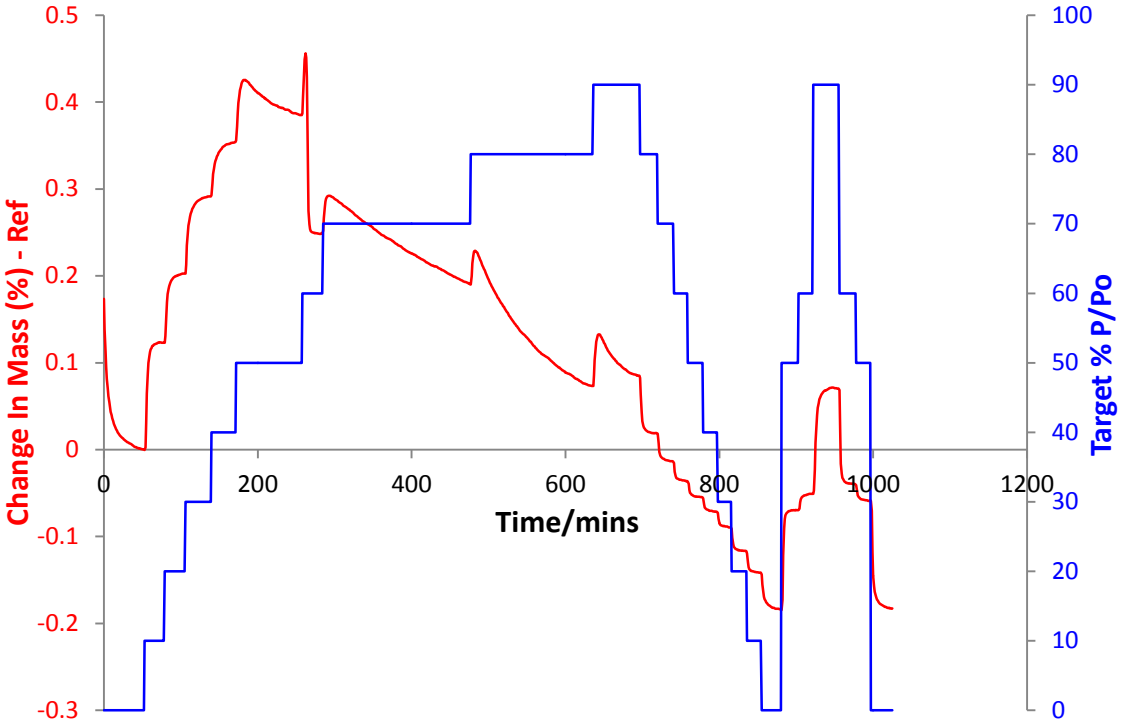


**Figure 1 DVS run for the initial time point for sample GLA089. Sorption by the sample is shown in red as percent change in mass and the relative humidity is shown in blue.**

| | Relative humidity level | | | |
|---|---|---|---|---|
| | **10% RH** | **20% RH** | **30% RH** | **40% RH** |
| **Readings (mass change first cycle)** | 0.12% | 0.20% | 0.29% | 0.36% |
| **Estimating amorphous content** | 6.17% | 5.75% | 6.05% | 5.48% |
| **Estimated uncertainty at the 95% confidence limit** | 2.88% | 1.55% | 1.55% | 1.55% |
| **Result with uncertainty** | 6 ±3% | 6 ±2% | 6 ±2% | 5 ±2% |

**The amorphous content of GLA089 is 6 ±2%**

**Table 3 DVS results for the initial time point of sample GLA089**

**Estimated amorphous content**

| %RH level | One Week 65%RH | One Week 0%RH | Six Weeks 65%RH | Six Weeks 0%RH |
|---|---|---|---|---|
| 10% | < LoD | 6 ±3% | < LoD | 6 ±3% |
| 20% | 2 ±2% | 5 ±2% | < LoD | 5 ±2% |
| 30% | 2 ±2% | 3 ±2% | < LoD | 3 ±2% |
| 40% | 1 ±2% | < LoD | < LoD | 3 ±2% |

**Table 4 Sample GLA089 results from DVS runs at initial and one week time points with exposure to 0 and 65% relative humidity**

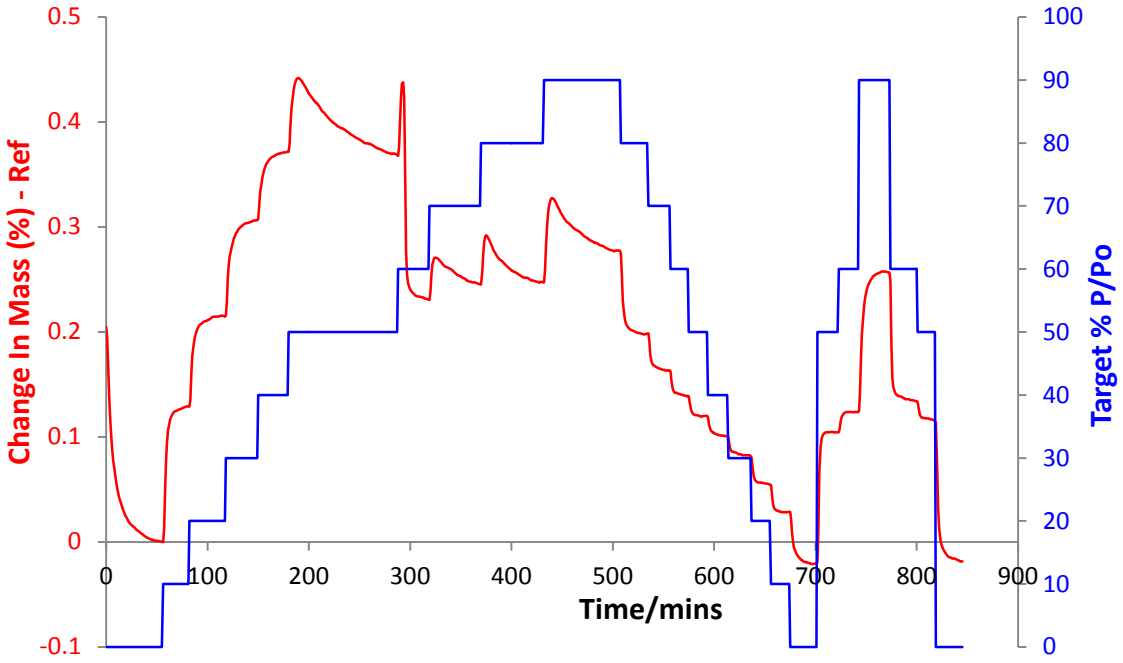


**Figure 2 DVS run for the initial time point for sample GLB092. Sorption by the sample is shown in red as percent change in mass and the relative humidity is shown in blue.**

| | Relative humidity level | | | |
|---|---|---|---|---|
| | **10% RH** | **20% RH** | **30% RH** | **40% RH** |
| **Readings (mass change first cycle)** | 0.13% | 0.22% | 0.31% | 0.37% |
| **Estimating amorphous content** | 6.51% | 6.19% | 6.40% | 5.79% |
| **Estimated uncertainty at the 95% confidence limit** | 2.87% | 1.55% | 1.55% | 1.55% |
| **Result with uncertainty** | 7 ±3% | 6 ±2% | 6 ±2% | 6 ±2% |

**The amorphous content of GLB092 is 6 ±2%**

**Table 5 DVS results for the initial time point of sample GLB092**

**Estimated amorphous content**

| %RH level | One Week 65%RH | One Week 0%RH | Six Weeks 65%RH | Six Weeks 0%RH |
|---|---|---|---|---|
| 10% | < LoD | 6 ±3% | < LoD | 7 ±3% |
| 20% | < LoD | 5 ±2% | < LoD | 6 ±2% |
| 30% | < LoD | 6 ±2% | < LoD | 6 ±2% |
| 40% | < LoD | 5 ±2% | < LoD | 5 ±2% |

**Table 6 Sample GLB092 results from DVS runs, at one and six week time points with exposure to 0 and 65% relative humidity**

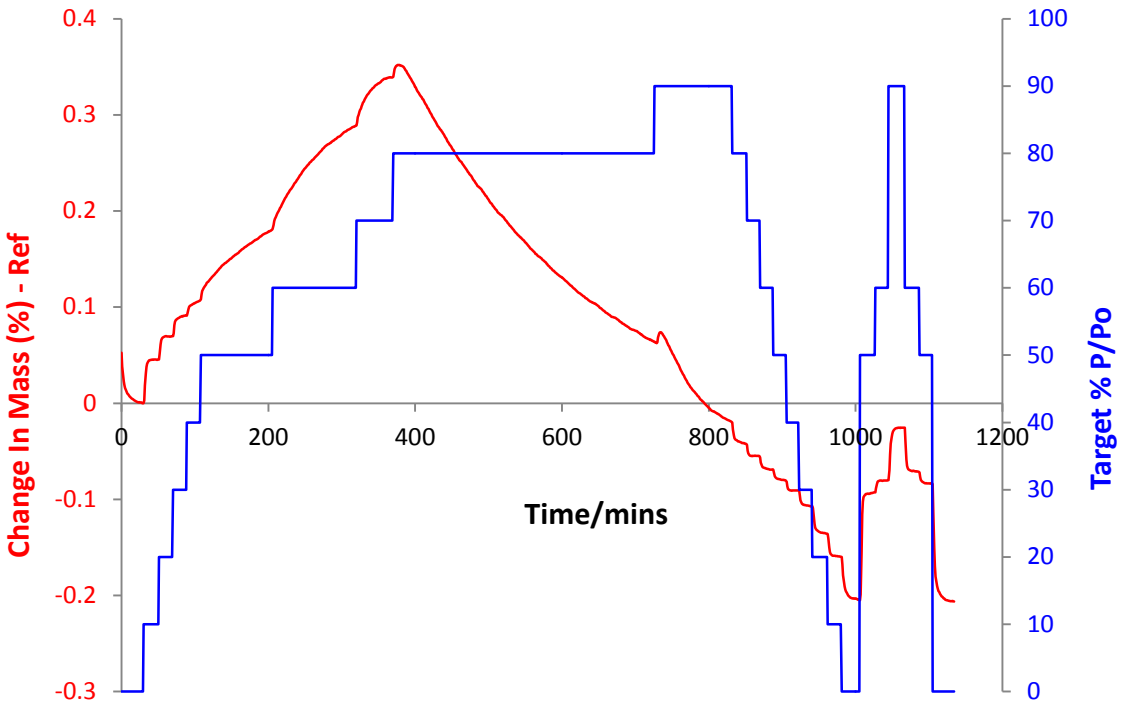


**Figure 3 DVS run for the initial time point for sample GJC012. Sorption by the sample is shown in red as percent change in mass and the relative humidity is shown in blue.**

| | Relative humidity level | | | |
|---|---|---|---|---|
| | **10% RH** | **20% RH** | **30% RH** | **40% RH** |
| **Readings (mass change first cycle)** | 0.00% | 0.05% | 0.07% | 0.09% |
| **Estimating amorphous content** | -0.95% | 0.25% | 0.27% | 0.24% |
| **Estimated uncertainty at the 95% confidence limit** | 2.90% | 1.56% | 1.57% | 1.56% |
| **Result with uncertainty** | < LoD | < LoD | < LoD | < LoD |

**The amorphous content of GJC012 is below the detection limit**

**Table 7 DVS results for the initial time point of sample GJC012**

**Estimated amorphous content**

| %RH level | One Week 65%RH | One Week 0%RH | Six Weeks 65%RH | Six Weeks 0%RH |
|---|---|---|---|---|
| 10% | 2 ±2% | 1 ±2% | 1.73% | 1.73% |
| 20% | 1 ±2% | 1 ±2% | 1.05% | 1.75% |
| 30% | < LoD | 0.52% | 0.78% | 3.89% |
| 40% | < LoD | 0.20% | 0.59% | 3.17% |

**Table 8 Sample GJC012 results from DVS runs at initial, one and six week time points with exposure to 0 and 65% relative humidity**

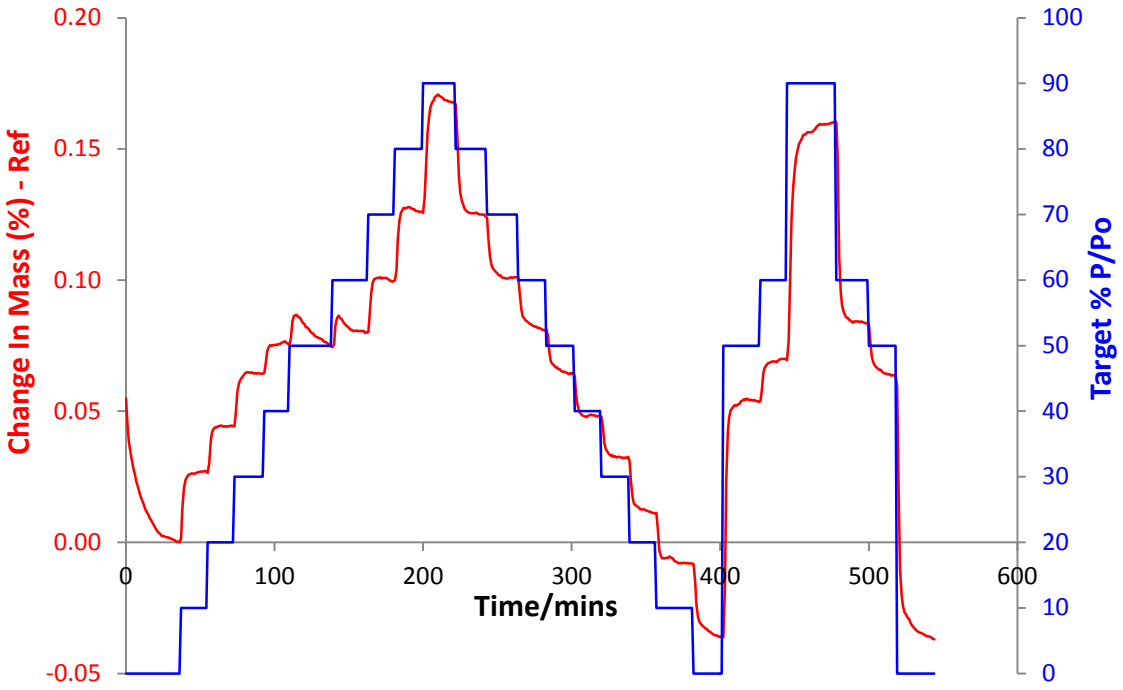


**Figure 4 DVS run for the initial time point for 3M PET sample. Sorption by the sample is shown in red as percent change in mass and the relative humidity is shown in blue.**

| | Relative humidity level | | | |
|---|---|---|---|---|
| | **10% RH** | **20% RH** | **30% RH** | **40% RH** |
| **Readings (mass change first cycle)** | 0.00% | 0.03% | 0.04% | 0.06% |
| **Estimating amorphous content** | -0.88% | -0.42% | -0.39% | -0.29% |
| **Estimated uncertainty at the 95% confidence limit** | 2.90% | 1.56% | 1.57% | 1.56% |
| **Result with uncertainty** | < LoD | < LoD | < LoD | < LoD |

**The amorphous content of GJC012 is below the detection limit**

**Table 9 DVS results for the initial time point of sample 3M PET**

**Estimated amorphous content**

| %RH level | One Week 65%RH | One Week 0%RH | Six Weeks 65%RH | Six Weeks 0%RH |
|---|---|---|---|---|
| 10% | < LoD | < LoD | < LoD | < LoD |
| 20% | < LoD | < LoD | < LoD | < LoD |
| 30% | < LoD | < LoD | < LoD | < LoD |
| 40% | < LoD | < LoD | < LoD | < LoD |

**Table 10 The 3M PET results from DVS runs at initial and one week time points with exposure to 0 and 65% relative humidity**

Table 11 shows the initial results for samples 3M PET and GJC012 (aged micronised) with amorphous content below the limits of detection, making further calculation of their results from subsequent time points and stations pointless.

| | Initial | One Week 65%RH | One Week 0%RH | Six Weeks 65%RH | Six Weeks 0%RH |
|---|---|---|---|---|---|
| **GLA089** | 6 ±2% | 2 ±2% | 5 ±2% | < LoD | 4 ±2% |
| **GLB092** | 6 ±2% | < LoD | 6 ±2% | < LoD | 6 ±2% |

**Table 11 Summary of results for freshly micronised salbutamol sulfate**

### 8.3.2 Results for X-ray powder diffraction

The X-ray powder diffraction patterns are shown in Figure 5, which all appear very similar. Unfortunately the patterns are noisy, which is due to the mylar cover and the low power of the X-ray tube at the time they were taken. The coincidence of the reflections shown in Figure 5 with the Leger values calculated from single crystal work (shown as vertical violet lines), suggests that poorly crystalline salbutamol sulfate is present in the samples.[10]

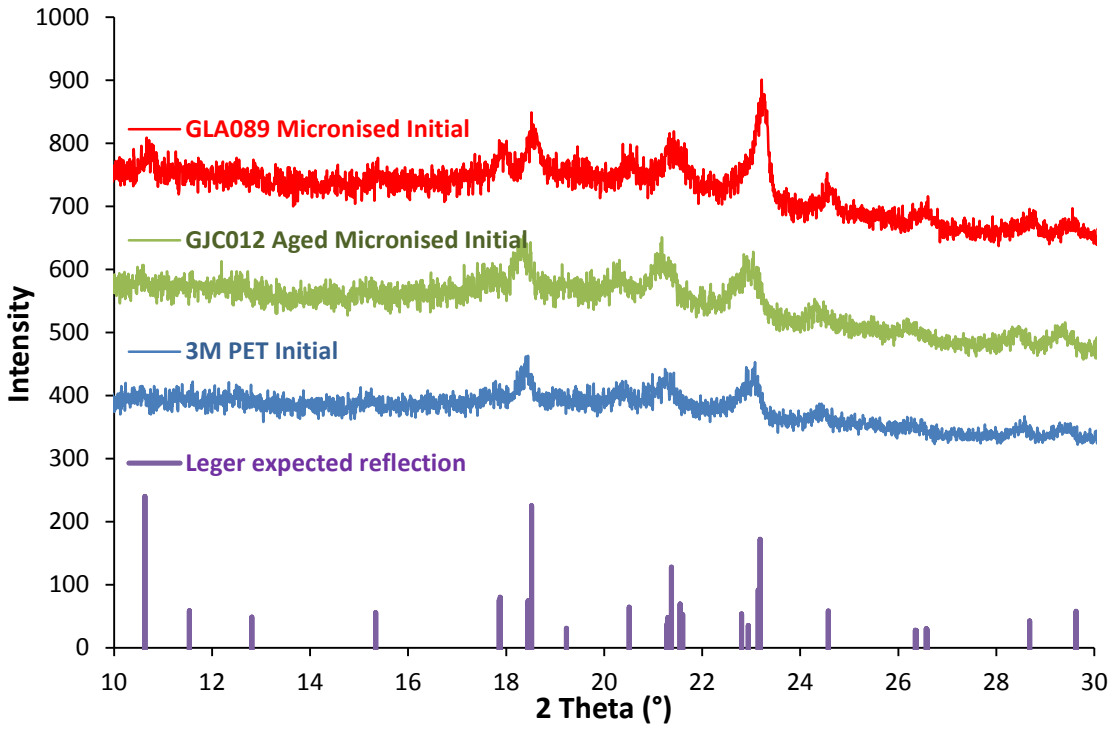


**Figure 5 X-ray powder diffraction patterns for samples at initial time point, with calculated reflections for salbutamol sulfate shown as vertical lines**

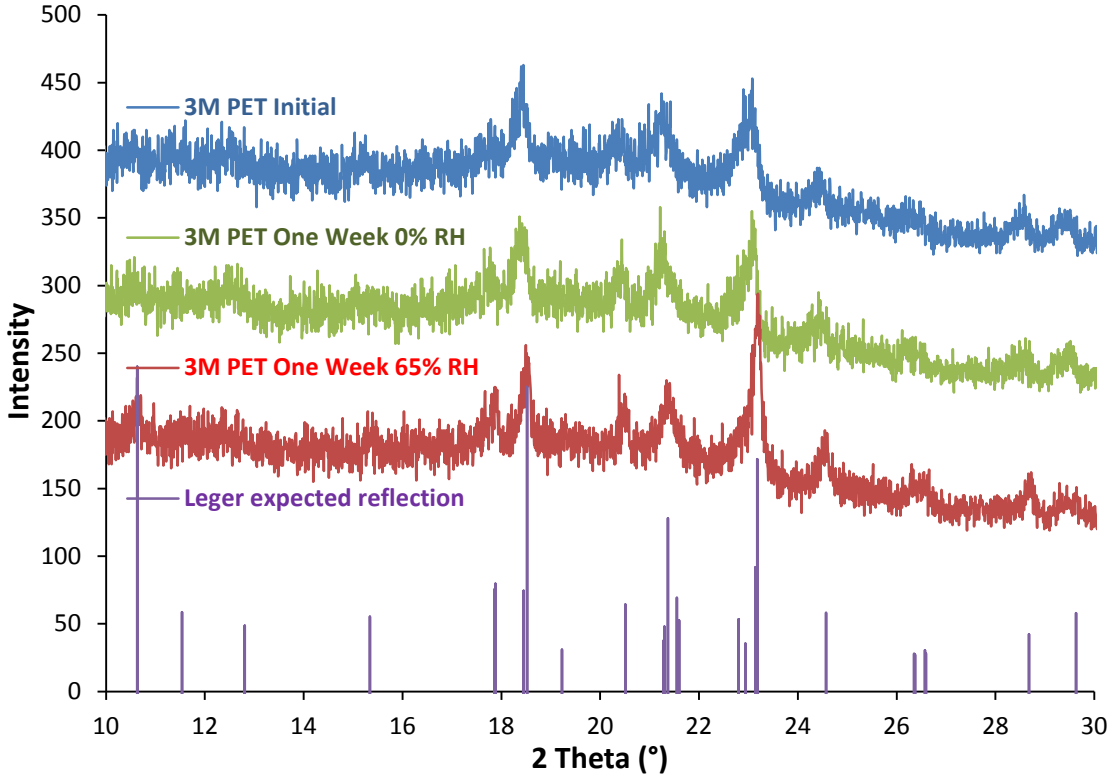


**Figure 6 X-ray powder diffraction patterns for the 3M PET sample from all storage stations and time points of one week and initial.**

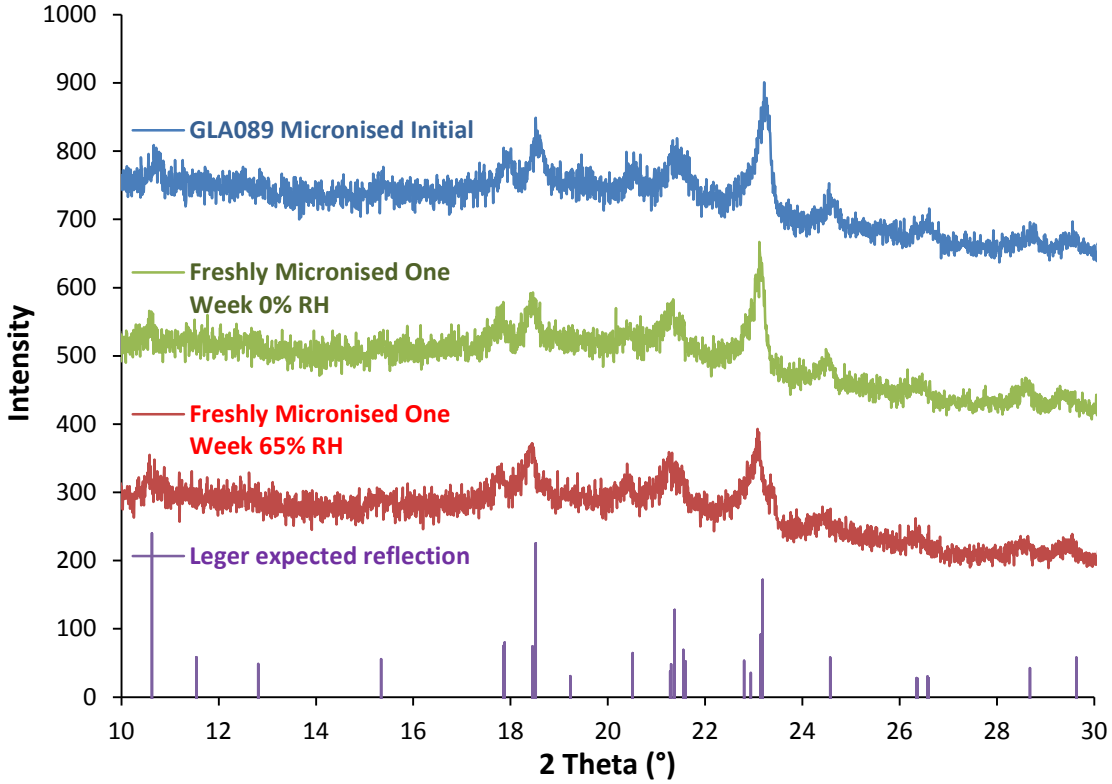


**Figure 7 X-ray powder diffraction patterns for the GLA089 (freshly micronised) sample from all storage stations and time points of one week and initial.**

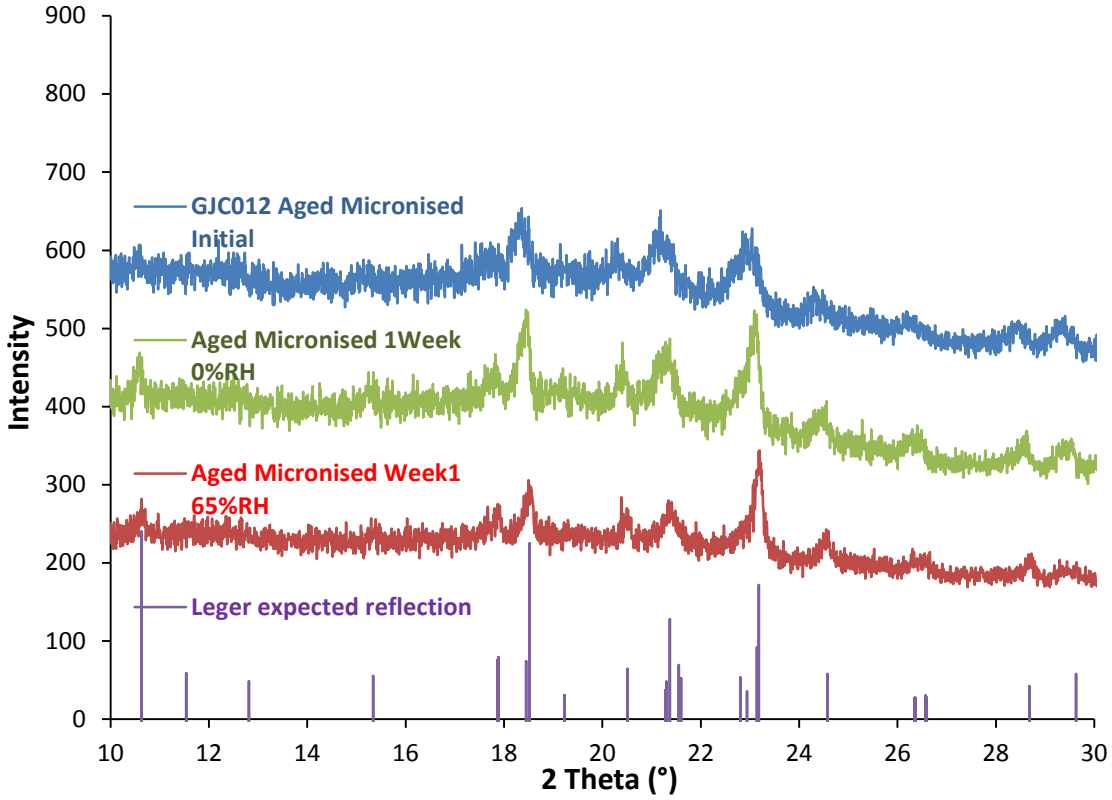


**Figure 8 X-ray powder diffraction patterns for the GJC012 (aged micronised) sample from all storage stations and time points of one week and initial.**

### 8.3.3 Results for FT-IR spectra

The infra-red spectra of all the samples at the different time points and storage stations are shown in Figure 9. The most striking feature of these spectra is their similarity. Palacios crystalline salbutamol sulfate spectrum is shown in black and is consistent with all the samples shown in both figures.[11]

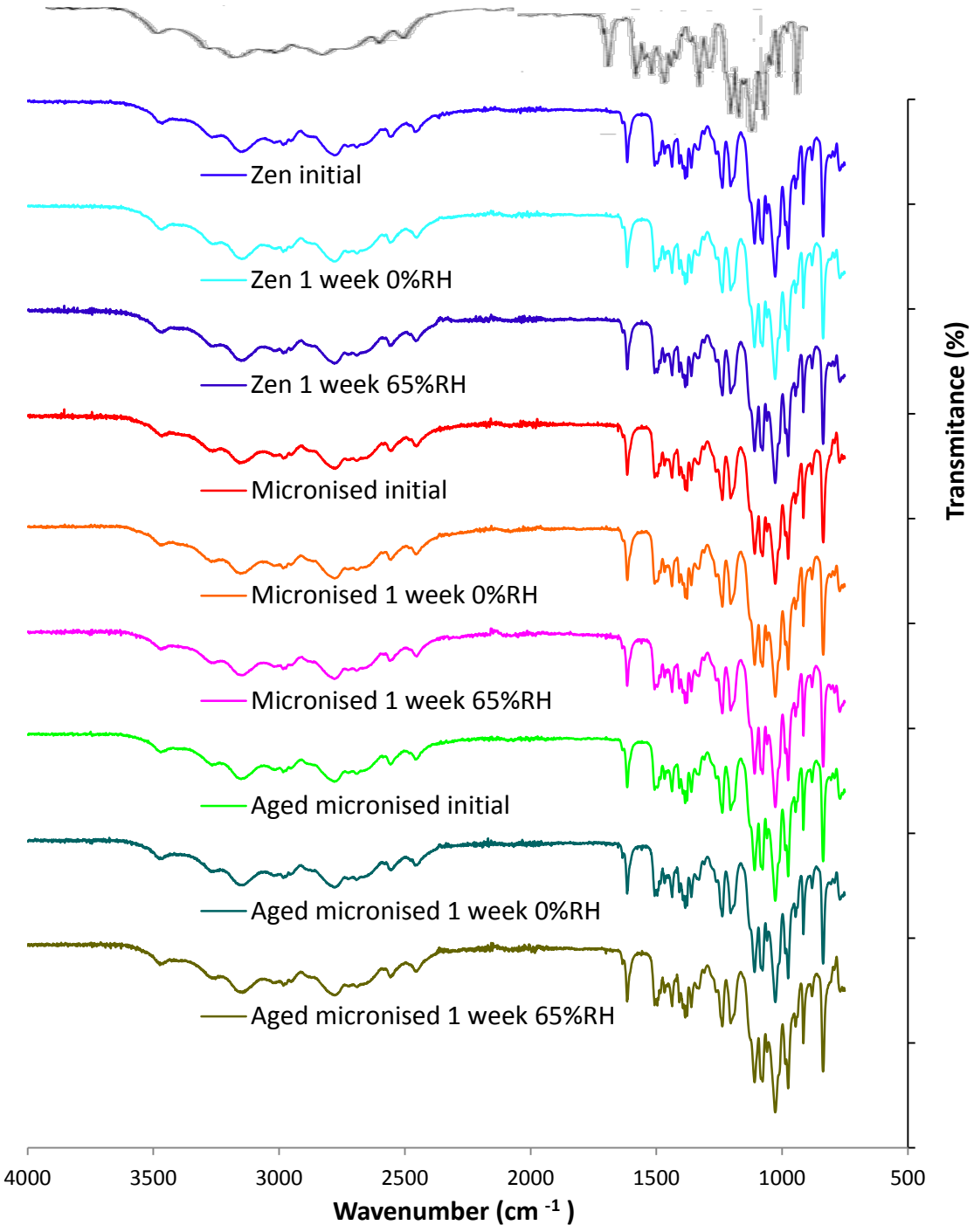


**Figure 9 FT-IR spectra of salbutamol sulfate stability samples, Palacios crystalline FT-IR spectra is shown in black for comparison**

### 8.3.4 Scanning Electron Microscopy

The freshly micronised samples show elongated, highly angular and irregular shapes in contrast the aged micronised sample, which are much more rounded. In contrast to the micronised samples highly regular crystalline shapes are displayed by the 3M PET development sample.

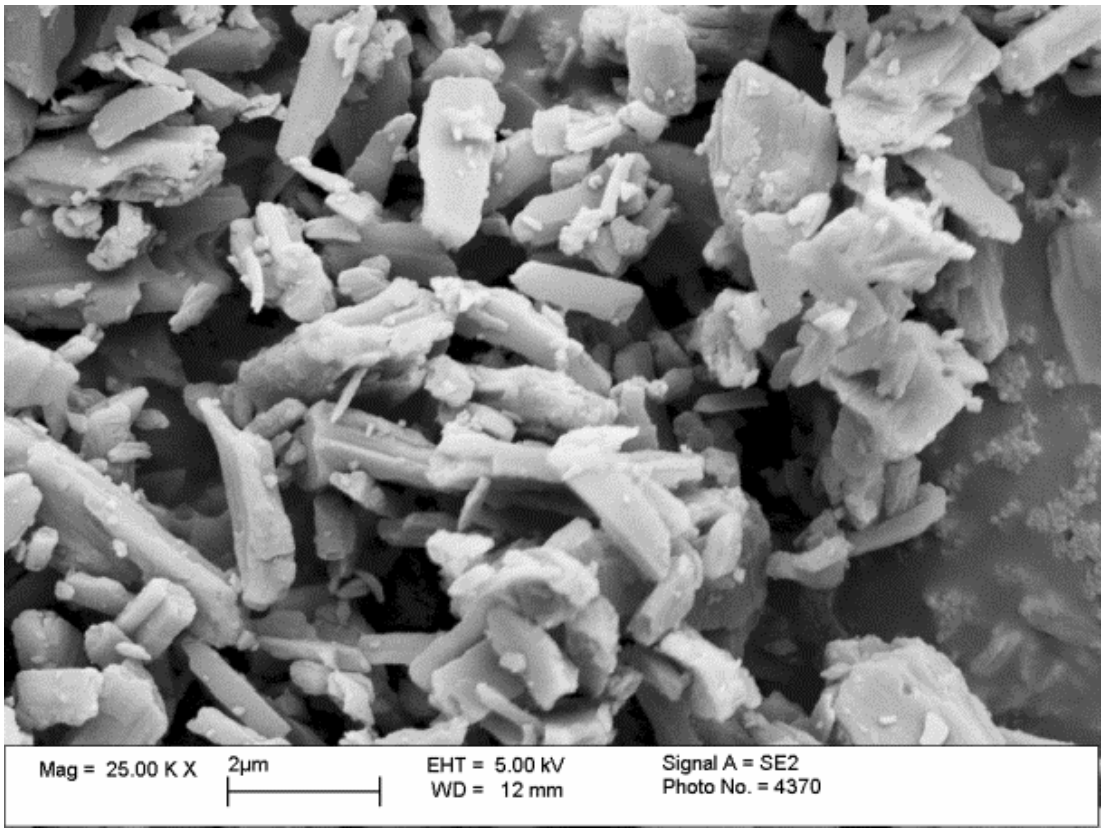


**Figure 10 Scanning Electron Microscope pictures of the samples at the Initial time point for sample GLA089 Freshly micronised**

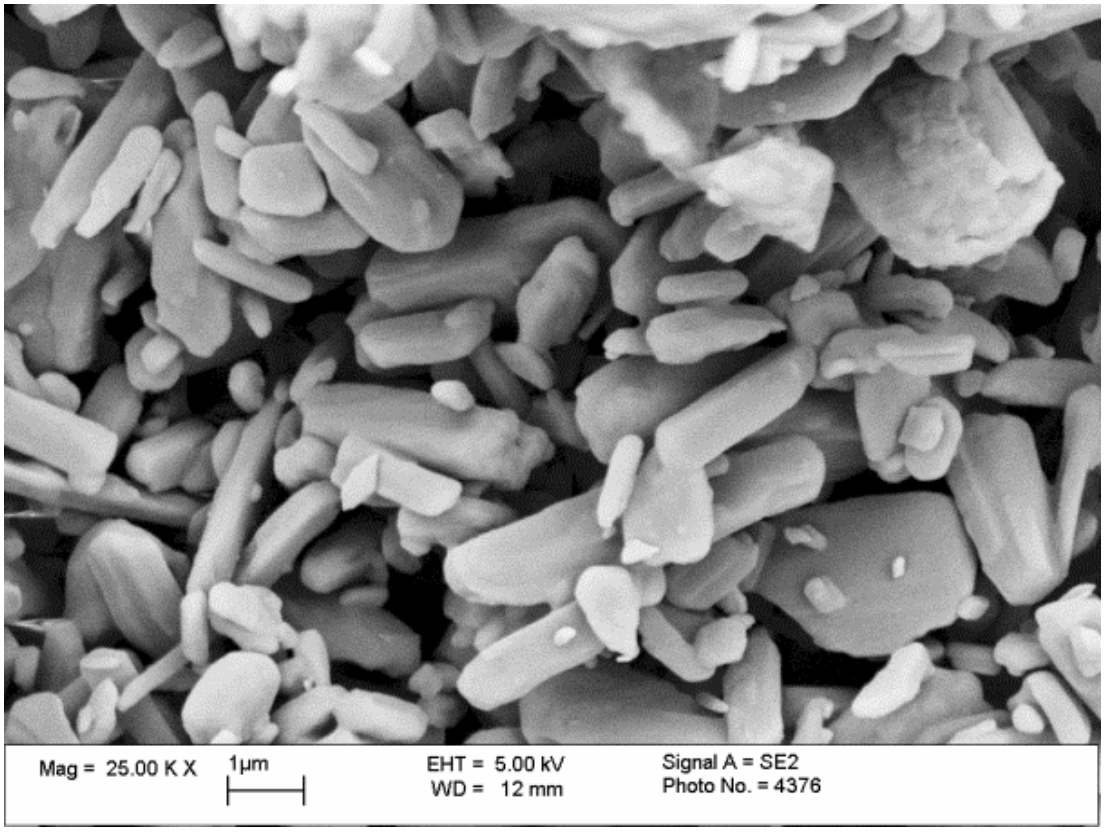


**Figure 11 Scanning Electron Microscope pictures of the samples at the Initial time point of sample GJC012 (aged micronised)**

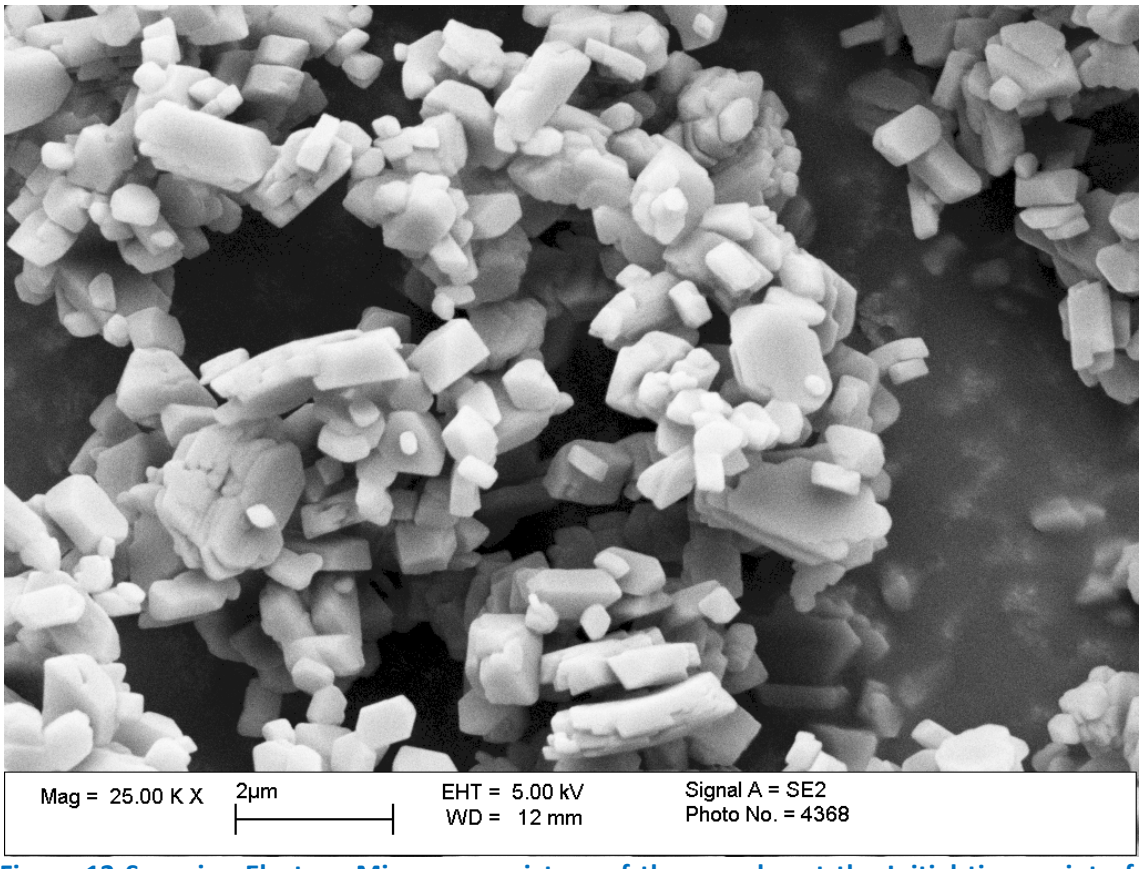


**Figure 12 Scanning Electron Microscope picture of the samples at the Initial time point of sample 3M PET development sample**

The Feret size (defined as the maximum possible distance between two points on the particles perimeter) provides a measure of particle size, which was calculated from the micrographs using ImageJ and displayed in Table 12.[12] To produce these values, 30 particles in each image were measured. Table 12 shows both micronised samples with similar means, both much larger than the 3M PET sample.

| microns | 3M PET | GLA089 Micronised | GJC012 Aged Micronised |
|---|---|---|---|
| **Mean** | 0.5 | 1.6 | 1.4 |
| **SD** | 1.7 | 1.6 | 1.8 |

**Table 12 particle size analysis expressed as feret diameter in microns from micrographs shown in. [12]**

SEM pictures were taken of the samples 3M PET, freshly micronised GLA089 and aged micronised GJC012 samples for both stations at the 1 week time point are shown in figures 13 to 18. The most dramatic change was seen in the freshly micronised GLA089 sample, the sample stored at 65% relative humidity (Figure 14), were the particles appear to have become more rounded after just one week. In contrast the same material (freshly micronised GLA089) store at 0% relative humidity can be seen in Figure 13 to have retained the highly angular and irregular shapes observed at the initial time point in Figure 10.

It is very difficult to observe any difference between the SEM pictures for the aged micronised sample GJC012 at the initial time point (Figure 11), one week at 0% relative humidity and one week at 65% relative humidity. This suggests that the aged micronised sample has undergone very little change during its time on storage at either 0 or 65% relative humidity.

The initial 3M PET sample seen in Figure 12 showed clear crystalline characteristics, with regular angles, sharp vertices and smooth crystal faces. These characteristics remain unchanged in the SEM pictures at one week for the 0 and 65% relative humidity stations (Figure 17 & Figure 18). This suggests that the 3M PET sample has undergone very little change if any during storage.

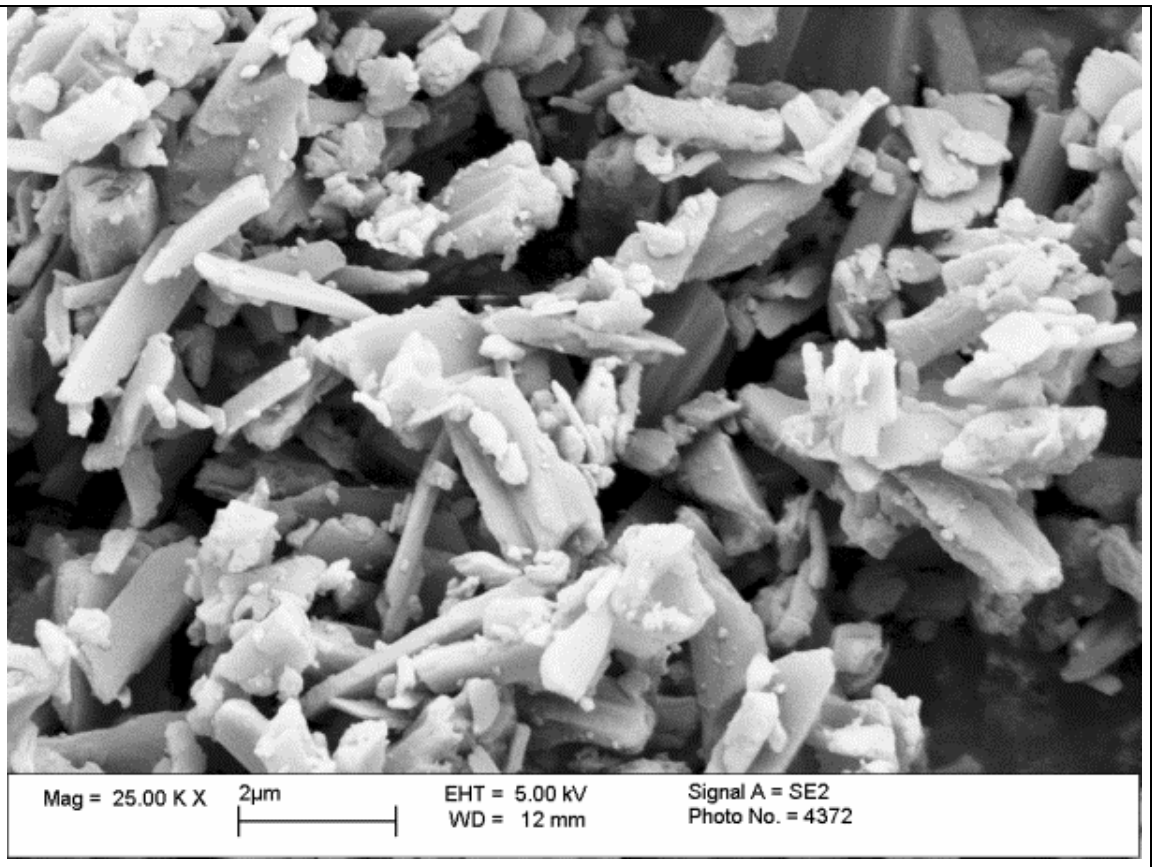


**Figure 13 Freshly micronised sample GLA089 held at 0% Relative Humidity for 1 Week**
Identical to the initial samples, showing fractured irregular shapes

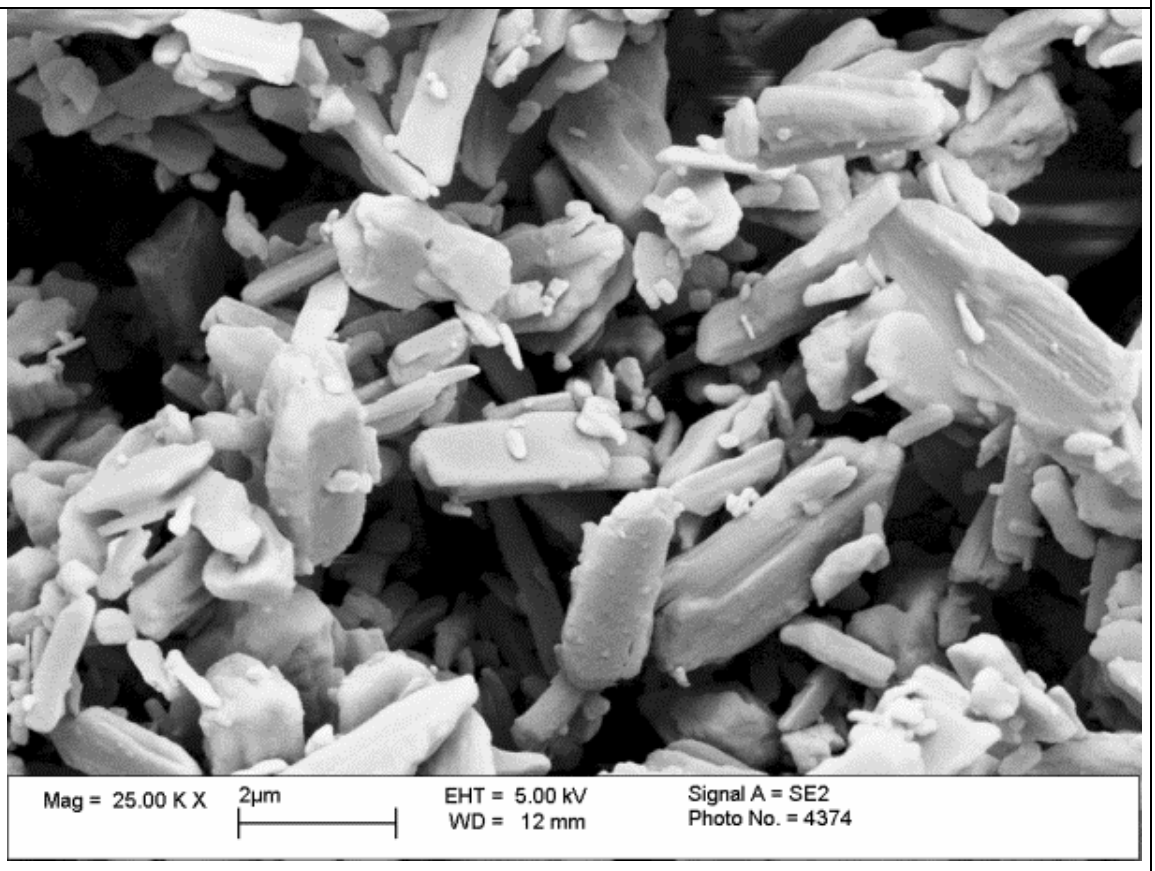


**Figure 14 Freshly micronised sample GLA089 held at 65% relative humidity for 1 Week**
Edges and corners have become more rounded compared to the initial sample

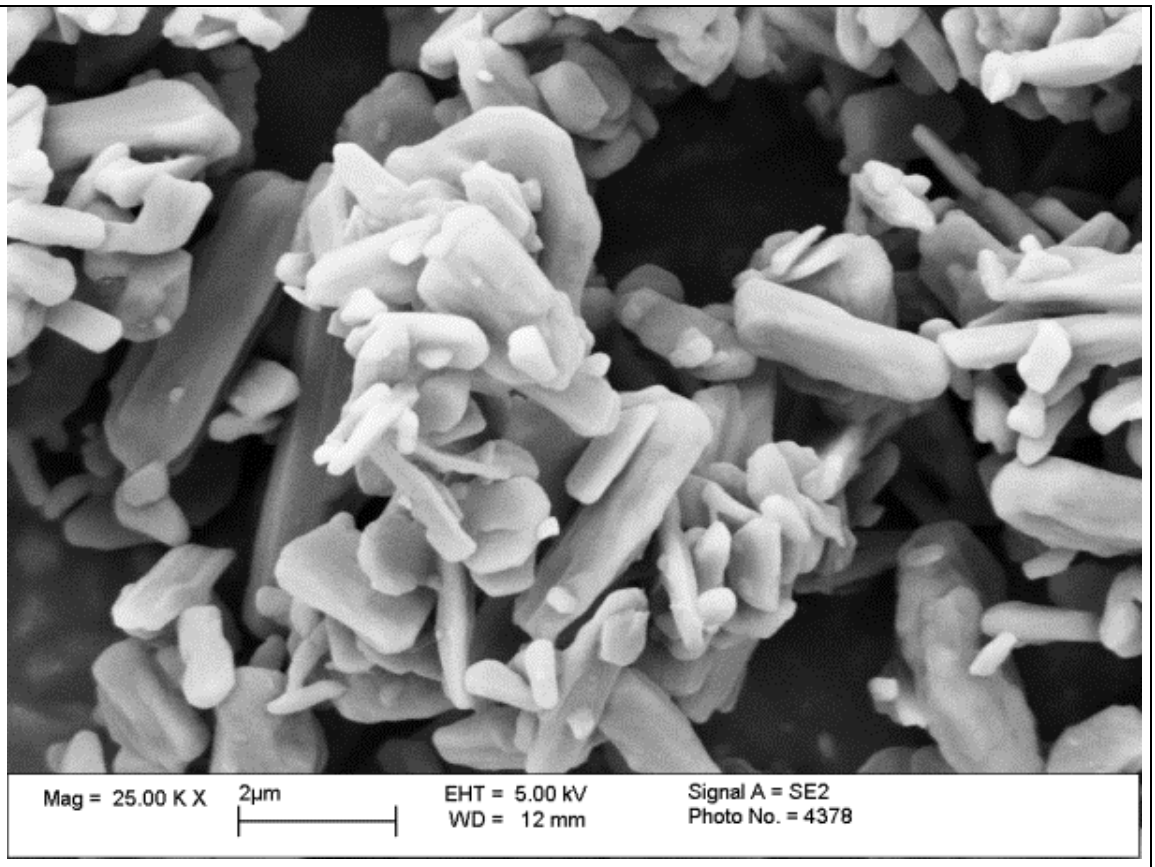


**Figure 15 GJC012 aged micronised sample held at 0% Relative Humidity after 1 Week**
Identical to initial sample with rounded edges and corners compared to the GLA089 initial

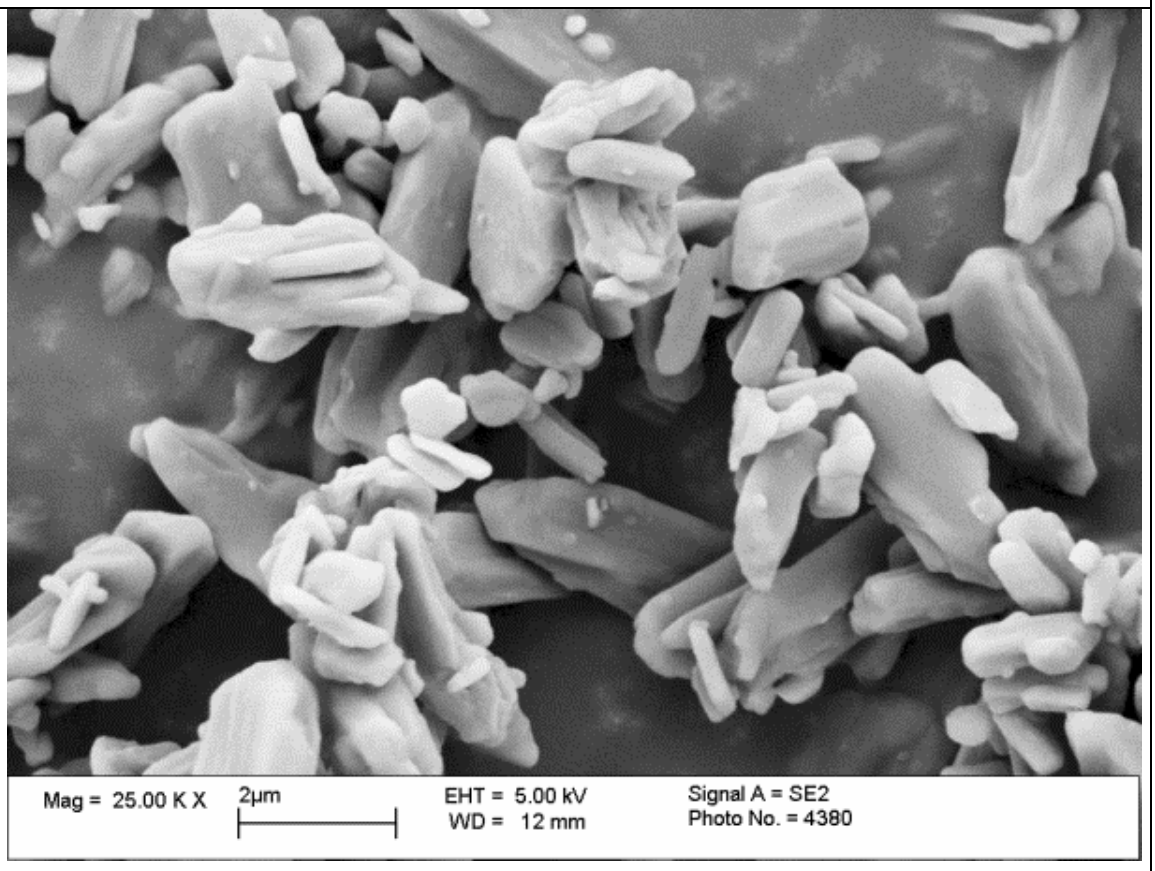


**Figure 16 GJC012 aged micronised stored at 65% Relative Humidity for 1 Week**
Identical to initial sample with rounded edges and corners compared to the GLA089 initial

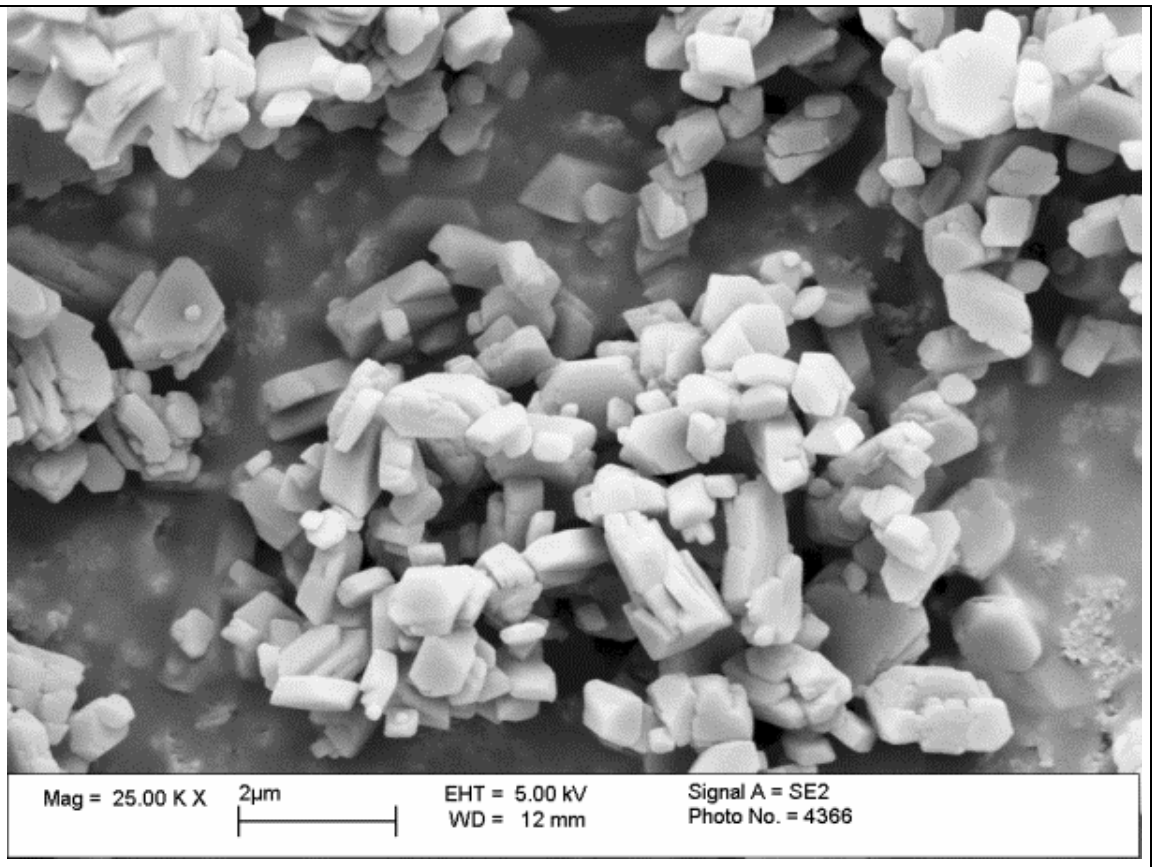


**Figure 17 3M PET development sample held at 0% relative humidity for 1 Week**
Small regularly shaped crystals identical to initial sample

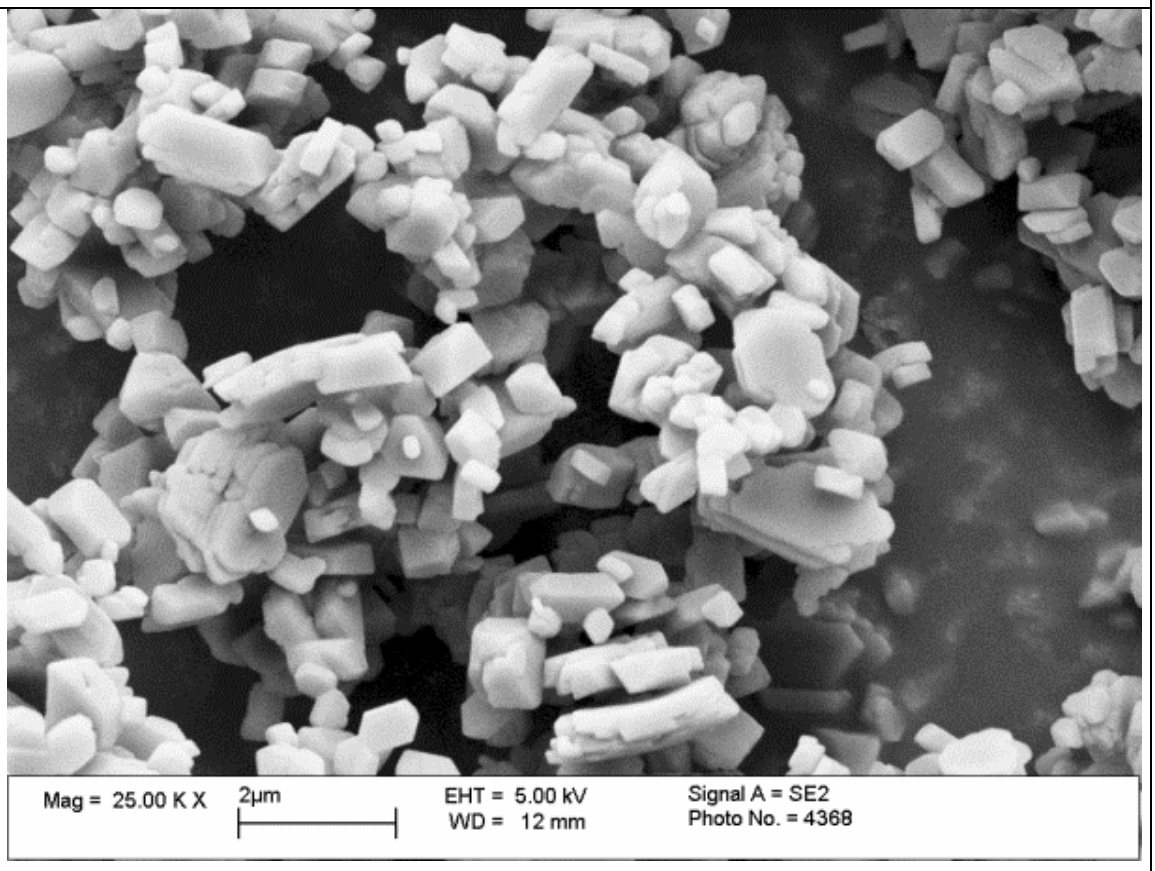


**Figure 18 3M PET development sample held at 65% relative humidity for 1 Week**
Small regularly shaped crystals identical to initial sample

### 8.3.5 Differential Scanning Calorimetry (DSC)

The gravimetric analysis accompanying the DSC results in section 7.2.2 of chapter 7 show salbutamol sulfate decomposes when it melts or when the glass transition point is reached. The decomposition reaction means that the heat of fusion will not be an accurate measure of the crystalline content. The DSC traces for the initial samples are shown in Figure 19 along with the crystalline sample behaviour identified in section 7.2.2 of chapter 7, shown as a dashed black line. Comparison with the crystalline trace shows the 3M PET sample to behave near identically. Neither of the micronised samples showed an obvious glass transition point similar to that seen in the spray dried sample set out in section 7.2.2 of chapter 7, however the heat capacity measurements for both micronised samples are greater than those of the crystalline sample seen in chapter 7. This is entirely consistent with the presence of amorphous content, (the heat capacity of the spray dried sample in section 7.2.2 of chapter 7 was greater than the crystalline). The freshly micronised sample GLA089 shows a heat capacity consistently greater than the crystalline, were as the aged micronised sample GJC012 shows a deviation that appears to increase with temperature.

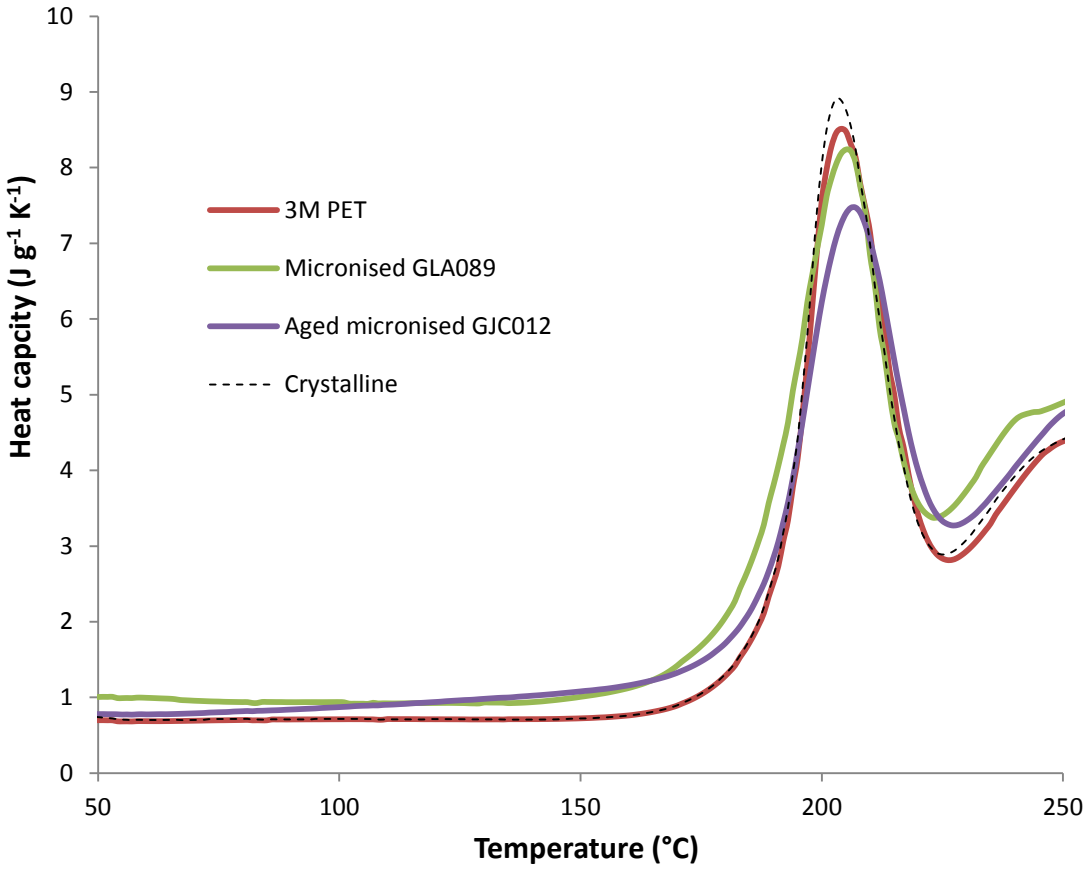


**Figure 19 Differential scanning calorimetry runs on the samples at the initial time point**

All the heat capacity profiles of the 3M PET time points and storage stations are similar to that of the crystalline sample discussed in chapter 7, (see Figure 20). These results suggest that no amorphous content can be seen in the 3M PET prior to the stability study and no amorphous content is seen after. The only difference between the heat capacity profiles is the heat of fusion which is a little larger for the sample held for 1 week at 0% relative humidity.

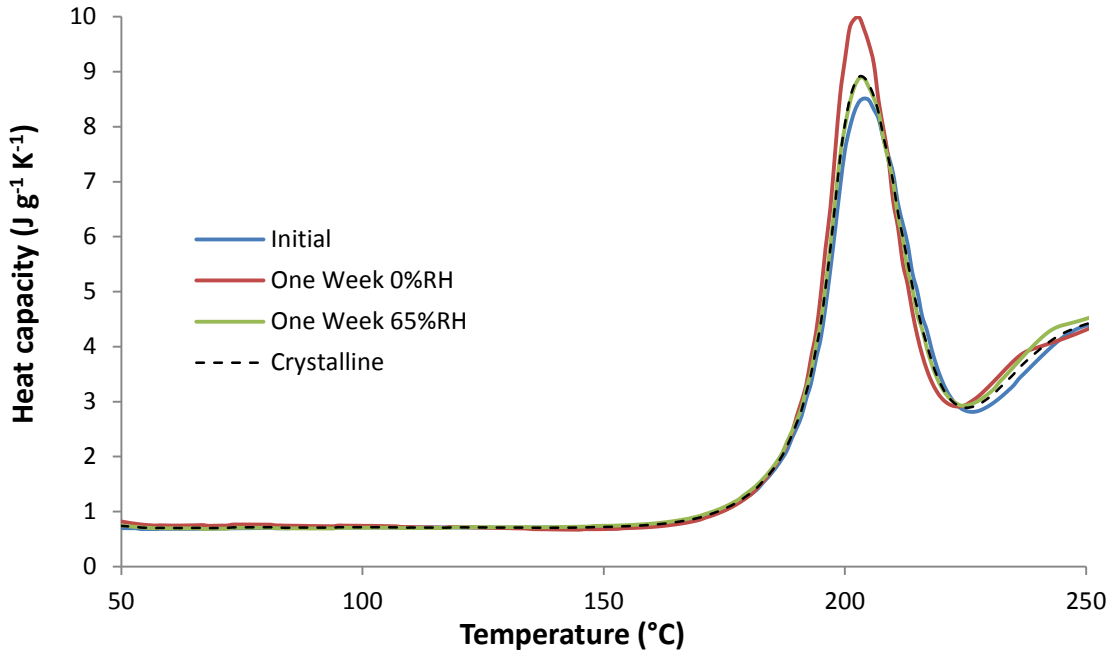


**Figure 20 Differential scanning calorimetry of the 3M PET stability study samples. The crystalline salbutamol sulfate sample is represented by the dashed line**

The freshly micronised sample GLA089 (see Figure 21) shows a heat capacity greater than that of the crystalline standard between 70 and 180 °C for all time points and stations, suggesting it contains an amorphous content even after exposure to 65% humidity for 1 week.

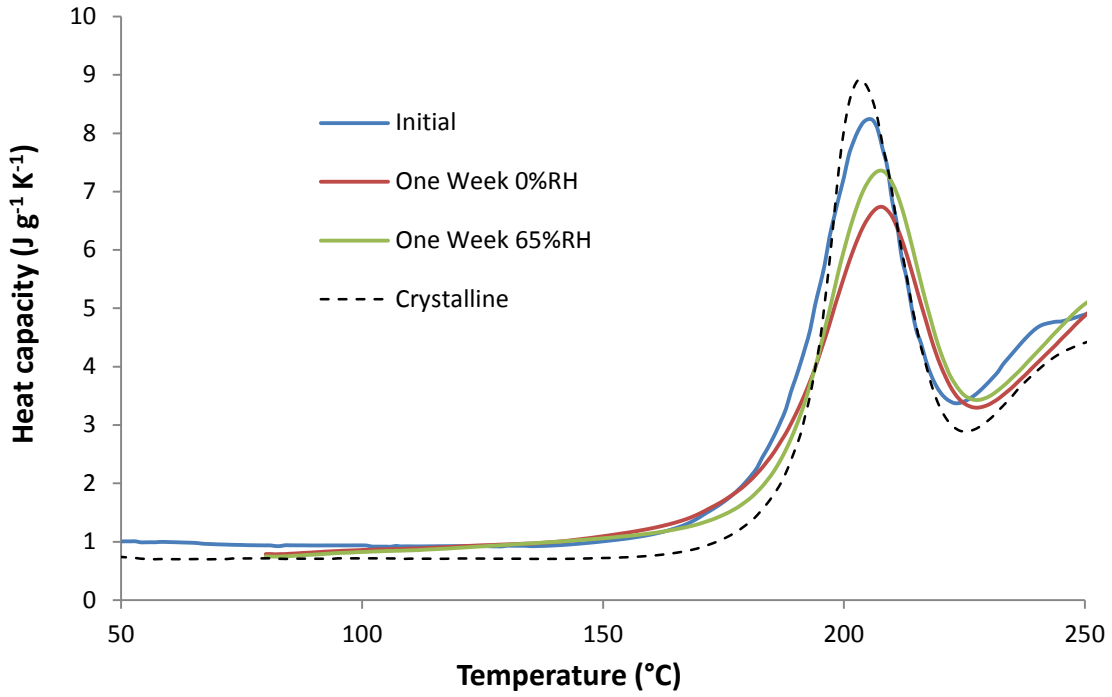


**Figure 21 Differential scanning calorimetry of stability study micronised sample GLA089. The crystalline salbutamol sulfate sample is represented by the dashed line**

The heat capacity profiles of the aged micronised sample GJC012 for each time point and station are shown in Figure 22. Their similarity suggests that no detectable change occurs as a result of this stability study. It should also be noted that the profiles do not follow that of the crystalline particularly well, the heat capacity is greater than crystalline between 70 and 180 °C, suggesting an amorphous content is present.

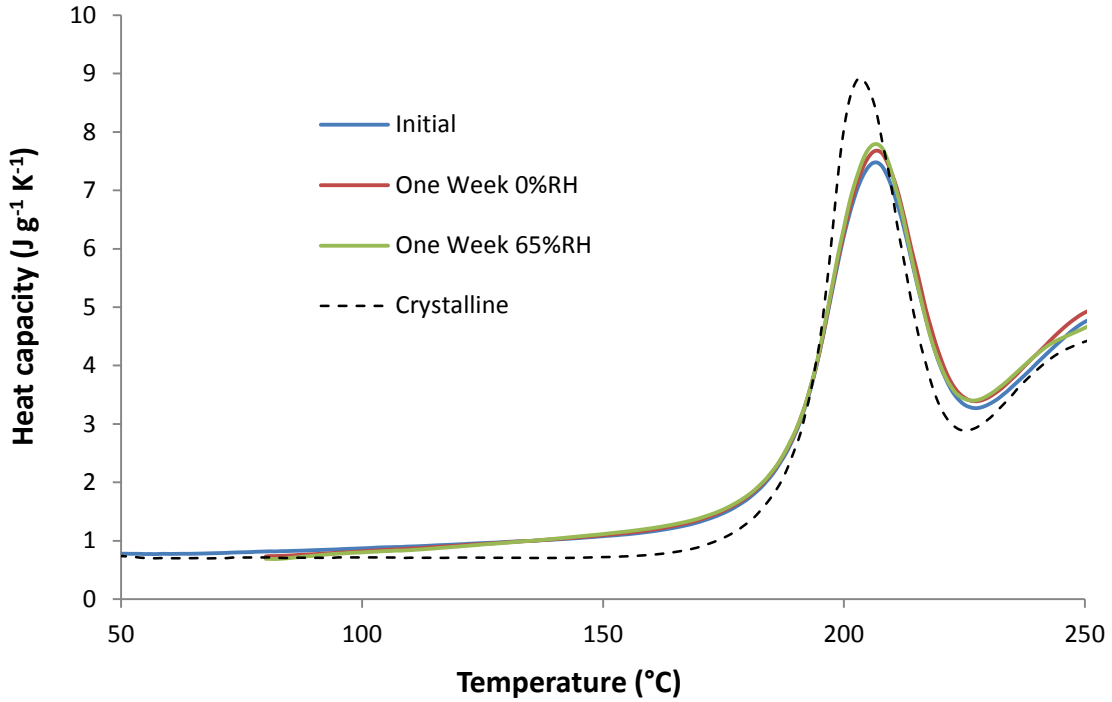


**Figure 22 Differential scanning calorimetry of stability study aged micronised sample GJC012. The crystalline salbutamol sulfate sample is represented by the dashed line.**

## 8.4 Discussion – stability study

The X-ray powder diffraction, DSC and infra-red data confirm the materials as salbutamol sulfate, however both powder X-ray diffraction and infra red failed to differentiate between the different samples at the initial time point and all others.

The DSC trace for the 3M PET sample was almost identical to the crystalline trace, suggesting that the 3M PET sample is crystalline. The heat capacity of the freshly micronised sample GLA089 was consistently greater than the aged micronised sample GJC012, suggesting that the freshly micronised sample possessed a greater amorphous content.

The SEM micrographs for each of the initial samples were different. The micronised samples were made up of broken crystals, with no sign of cleavage planes, making the pieces irregular in shape, elongated and highly angular. The edges and vertices of the freshly micronised sample GLA089 were much sharper than the aged micronised sample GJC012. The freshly micronised sample GLA089 appeared different after storage at 65% relative humidity for just one week, this showed much more rounded particles. The 3M PET sample by contrast, was composed of whole un-broken crystals. The SEM micrographs of the 3M PET sample did not appear to change with storage conditions.

Work in section 7.6 of chapter 7 has shown that DVS response to salbutamol sulfate can be related to amorphous content. A summary of the amorphous content calculated from the DVS responses are given in Table 13.

| Sample | Initial | One Week 65%RH | One Week 0%RH | Six Weeks 65%RH | Six Weeks 0%RH |
|---|---|---|---|---|---|
| GLA089 freshly micronised | 6 ±2% | 2 ±2% | 5 ±2% | < LoD | 4 ±2% |
| GLB092 freshly micronised | 6 ±2% | < LoD | 6 ±2% | < LoD | 6 ±2% |
| GJC012 aged micronised | < LoD | < LoD | < LoD | < LoD | < LoD |
| 3M PET | < LoD | < LoD | < LoD | < LoD | < LoD |

**Table 13 Summary of amorphous content for salbutamol sulfate stability study**

Table 13 results for the amorphous content of freshly micronised samples, show them to crystallise when held at 20 °C in 65% relative humidity. Referring back to the previous section 7.6 of chapter 7, the critical relative humidity glass transition point for spray dried salbutamol sulfate was determined to be 46% relative humidity, predicting that storage in an environment above this humidity would result in crystallisation. The storage of all the samples in an environment of 65% relative humidity would be expected to eliminate any amorphous content, the results show in Table 13 are consistent with this, even for GLA089 (since the result of 2 ±2% could include zero). The results in Table 13 for the freshly micronised sample GLA089 also show a reduction in amorphous content over time even when stored in a desiccator at 20 °C, however in contrast to this the sample GLB092 shows no reduction in amorphous content over time.

The model pharmaceutical material lactose in its amorphous form sorbs water which acts as a plasticiser, to prevent this amorphous pharmaceutical materials are often stored in desiccators to preserve their properties. The aged micronised material GJC012 was stored for 182 days in a glass jar within a desiccator. Table 13 results for the aged micronised sample GJC012 showed amorphous contents below the limit of detection for all storage stations and time points. Provided the aged micronised sample GJC012 was originally micronised in a manner similar to the freshly micronised samples GLA089 and GLB092 the low amorphous content suggest that crystallisation has occurred while the GJC012 was stored in a screw top jar in a desiccator at 20 °C over 182 days.

The amorphous content of the 3M PET sample in Table 13 all fall below the limit of detection for the analysis. The DVS sorption change in mass results, are shown in Table 14 for the crystalline salbutamol sulfate (used as a calibration standard in section 7.6 of chapter 7) and the 3M PET sample at initial time point. The results for the two runs in Table 14 appear very similar, the t-test examines this, via the null hypothesis that; the two sets of results could have been drawn from the same population, or alternatively that the two sets of results were drawn from separate populations. The percentage probability returned in Table 14 of 92% suggests the null hypothesis is accepted, that these results could have been drawn from the same population. The behaviour of the 3M PET is consistent with that of an entirely crystalline material.

| Relative humidity step | Sorption change in mass (% w/w) | |
|---|---|---|
| | 3M PET | Crystalline salbutamol sulfate |
| 10% | 0.02703 | 0.0249 |
| 20% | 0.04433 | 0.0435 |
| 30% | 0.06430 | 0.0579 |
| 40% | 0.07574 | 0.0713 |
| 50% | 0.07477 | 0.0868 |
| Paired t-test | 92.0% | |

**Table 14 Comparison of 3M PET to crystalline salbutamol sulfate t-test**

## 8.5 Conclusions

The storage of freshly micronised salbutamol sulfate at 20 °C in an environment containing 65% relative humidity will decrease in amorphous content over time periods as little as one week. Provided the manufacturing process remains consistent, storage of micronised salbutamol sulfate at 20 °C in a screw top bottle placed in a desiccator over a period of 6 months shows a reduction in amorphous content. The 3M PET sample shows properties are consistent with entirely crystalline salbutamol sulfate, as demonstrated by the SEM pictures, powder diffraction patterns, heat capacity profiles and Dynamic Vapour Sorption. In addition the 3M PET samples do not appear to change with time and storage conditions during this study. This work suggests that freshly micronised salbutamol sulfate changes when stored at ambient conditions in contrast to the 3M PET material.

## 8.6 Introduction

A key aspect of pharmaceutical manufacture is “correct dosing”, too much drug may be harmful and equally too little will fail to control the symptoms of the patient.[4] A typical Ventolin pressurised Metered Dose Inhaler (pMDI) supplies 200 metered doses of 100 µg. This equals 20 mg of salbutamol sulfate per canister.[13] The loss of just a few milligrams of salbutamol sulfate in the canister could result in under dosing. Some of the salbutamol sulfate dose may be lost by adhesion to the canister walls, therefore understanding the surfaces and properties of salbutamol sulfate that affect adhesion is important for correct dosing in MDI inhalers. To reduce salbutamol sulfate to a respirable particle size, requires micronisation, which converts some of the crystalline material to amorphous. The surface energy of an amorphous material is usually greater than its equivalent crystalline form, so the adhesive properties of micronised salbutamol sulfate is greater than its crystalline form.[3]

The conclusion of the previous stability study was that the amorphous content of salbutamol sulfate can change with storage conditions and duration. For salbutamol sulfate, this means that the adhesive properties may also change with time. Although a repeatable micronisation process may be used during manufacturing, the length of time a material has to wait before it is placed in a pMDI canister may vary, due to demand, breakdowns and manufacturing programmes. These production issues make it very difficult for a manufacturer to place salbutamol sulfate with a consistent amorphous content into pMDI canisters.

The manufacturer of salbutamol sulfate pMDI, 3M has developed a rapid screening technique for measuring adhesion to canister walls. This technique allows comparison of different canister coatings. In addition 3M have developed an alternative method of preparing salbutamol sulfate particles of respirable size which is referred to here as 3M PET. Chapter 7 identified how amorphous content could be quantified by Dynamic Vapour Sorption, the technique utilises the sorption of water vapour by amorphous salbutamol sulfate and its conversion to the crystalline form.

## 8.7 Experimental

### 8.7.1 Adhesion to internal can surface (developed by Chris Blatchford of 3M)

The adhesion to internal can surface test was carried out in three steps; first 1.25 mg of the salbutamol sulfate sample was deposited evenly on the internal canister surface, the second shaking and re-dispersion of the deposits during simulated inhaler use, and third assay by dissolving the remaining deposits in water with assay by UV/vis spectroscopy.

The salbutamol sulfate sample (1.0 g) was dispersed in decafluoropentane (400 g) by placing it in a sonic bath for 1 minute. An Eppendorf pipette was used to transfer 0.5 g of the suspension into the canisters, which were immediately placed on a horizontal rolling mixer set to 35 RPM for 10 minutes. During this time, most of the decafluoropentane evaporated, to remove any remaining the canisters were placed in an oven at 50 °C for 5 minutes. Each 5ml canister was filled with decafluoropentane and then sealed. The canisters were then inverted 10 times with a rolling shake and the fluid immediately discarded. This process was repeated to make a total of 2 identical removal cycles in total.

The canisters were then rinsed three times with acidified water (sulfuric acid 0.1% w/w), into a 15 ml volumetric flask and made up to volume. The solution absorbance was measured at 276 nm and the absorbance results normalised to the entire salbutamol sulfate sample (1.25 mg per canister). The results were then expressed as a percentage of salbutamol sulfate deposited.

### 8.7.2 Sample source - adhesion to internal can surface

Five samples of factory prepared batches of micronised salbutamol sulfate of different ages and the 3M PET development sample were measured by Chris Blatchford for canister adhesion properties, these are summarised in Table 15.

| Batch Number | GNB013 | GMJ098 | GLB092 | GJI070 | 3M PET |
|---|---|---|---|---|---|
| Source | Factory | Factory | Factory | Factory | Development |
| Micronised | Yes | Yes | Yes | Yes | No |
| Age (days) | 3 | 82 | 688 | 1600 | 581 |

Table 15 Sample codes, sources and age

### 8.7.3 Instrumentation

The dynamic vapour sorption (DVS) method used was identical to that detailed in section 7.6 of chapter 7 for the determination of amorphous content. DSC, FT-IR and X-ray diffraction were not carried out, since the work on the stability study had shown that these techniques could not differentiate between micronised samples of different age.

### 8.7.4 Results

### 8.7.5 Adhesion to internal can surface (developed by Dr C.G. Blatchford of 3M)

The results for the different materials and can surfaces are shown in Table 16, which shows the percentage of salbutamol sulfate retained on the internal can surface after the decafluoropentane had been discarded. These results show anodised and epoxy coatings to have strong adhesive properties. The 3M plasma and PTFE coated cans showed adhesive properties that appear to vary with their salbutamol sulfate test material.

| | | Anodised | Epoxy | 3M plasma coated can | PTFE |
|---|---|---|---|---|---|
| GNB013 0 months | 1 | 100 | 101 | 90 | 79 |
| | 2 | 101 | 101 | 86 | 84 |
| | 3 | 101 | 102 | 86 | 88 |
| GMJ098 4 months | 1 | 99 | 102 | 84 | 72 |
| | 2 | 100 | 99 | 79 | 66 |
| | 3 | 101 | 102 | 78 | 69 |
| GLB092 24 months | 1 | 99 | 101 | 80 | 84 |
| | 2 | 99 | 100 | 78 | 82 |
| | 3 | 101 | 100 | 77 | 85 |
| 3M PET | 1 | 100 | 102 | 18 | 17 |

| | | | | | |
|---|---|---|---|---|---|
| **stabilised** | 2 | 97 | 101 | 9 | 8 |
| | 3 | 99 | 101 | 4 | 11 |
| **GJI070** | 1 | 98 | 98 | 2 | 2 |
| **41** | 2 | 95 | 93 | 4 | 2 |
| **months** | 3 | 95 | 91 | 8 | 3 |

**Table 16 Normalised percentage results of deposition test applied to different can coatings**

### 8.7.6 Dynamic Vapour Sorption (DVS)

The raw data for five samples used in the adhesion to internal can surface test are shown in Table 17. These raw results show the samples GNI070 and 3M PET to have near identical first and second DVS cycles suggesting that these are nearly entirely crystalline materials.

| | **Batch Number** | **GLB092** | **GMJ098** | **GJI070** | **GNB013** | **3M PET stabilised** |
|---|---|---|---|---|---|---|
| | **Micronised** | **Yes** | **Yes** | **Yes** | **Yes** | **No** |
| **DVS Readings** | **Age (days)** | **688** | **82** | **>1200** | **3** | **581** |
| Mass change first cycle | 10% RH | 0.06% | 0.05% | 0.05% | 0.13% | 0.03% |
| | 20% RH | 0.10% | 0.09% | 0.07% | 0.23% | 0.05% |
| | 30% RH | 0.13% | 0.14% | 0.09% | 0.32% | 0.07% |
| | 40% RH | 0.15% | 0.19% | 0.11% | 0.40% | 0.09% |
| Mass change second cycle | 10% RH | 0.06% | 0.00% | 0.06% | 0.05% | 0.04% |
| | 20% RH | 0.09% | 0.00% | 0.08% | 0.07% | 0.06% |
| | 30% RH | 0.11% | 0.00% | 0.10% | 0.10% | 0.08% |
| | 40% RH | 0.13% | 0.00% | 0.12% | 0.11% | 0.10% |
| Difference in mass change between cycles | 10% RH | 0.00% | 0.05% | -0.01% | 0.08% | -0.01% |
| | 20% RH | 0.01% | 0.09% | -0.01% | 0.16% | -0.01% |
| | 30% RH | 0.02% | 0.14% | -0.01% | 0.23% | -0.01% |
| | 40% RH | 0.02% | 0.19% | -0.01% | 0.29% | -0.01% |

**Table 17 DVS results for salbutamol sulfate samples used to test adhesion to internal can surfaces**

## 8.8 Discussion

From the DVS results observed in Table 17, the estimated amorphous content was calculated using the Mackin calibration described in section 7.6.2 of chapter 7, and set out in Table 18 along with calculated errors and limits of detection.[14]

| Batch Number | GLB092 | GMJ098 | GJI070 | GNB013 | 3M PET stabilised |
|---|---|---|---|---|---|
| Micronised | Yes | Yes | Yes | Yes | No |
| Age (days) | 688 | 82 | >1200 | 3 | 581 |
| **Estimating amorphous content** | | | | | |
| 10% RH | 0.38% | 3.68% | -0.64% | 5.64% | -0.51% |
| 20% RH | 0.63% | 3.84% | -0.23% | 6.37% | -0.19% |
| 30% RH | 0.54% | 3.91% | -0.23% | 6.42% | -0.24% |
| 40% RH | 0.42% | 3.99% | -0.25% | 6.07% | -0.26% |
| **Estimated uncertainty at the 95% confidence limit** | | | | | |
| 10% RH | 6.46% | 6.43% | 6.47% | 6.42% | 6.47% |
| 20% RH | 3.95% | 3.94% | 3.96% | 3.92% | 3.96% |
| 30% RH | 3.23% | 3.22% | 3.23% | 3.21% | 3.24% |
| 40% RH | 2.24% | 2.23% | 2.24% | 2.22% | 2.24% |
| **Result with uncertainty** | | | | | |
| 10% RH | < LoD | 4 ±6% | < LoD | 6 ±6% | < LoD |
| 20% RH | < LoD | 4 ±4% | < LoD | 6 ±4% | < LoD |
| 30% RH | < LoD | 4 ±3% | < LoD | 6 ±3% | < LoD |
| 40% RH | < LoD | 4 ±2% | < LoD | 6 ±2% | < LoD |
| Average | < LoD | 4 ±4% | < LoD | 6 ±4% | < LoD |

**Table 18 Amorphous content from DVS analysis calculated by Mackin method[14]**

The calculation of amorphous content from DVS readings via the Mackin method subtracts the second cycle mass reading from the first cycle mass reading, and unfortunately doubles the error in the result calculated.[14] The Zografi method uses only the mass gain on the first cycle to calculate amorphous content and so carries forward much less error than the Mackin method.[9, 14] The DVS reading set out in Table 17 were used to calculate the amorphous content using the Zografi method and are set out in Table 19 as results with errors.[9]

| | Slope | Intercept | $r^2$ | $S_{x/y}$ | LoD |
|---|---|---|---|---|---|
| 10% RH | 1.73% | 0.02% | 0.9992 | 0.02% | 0.08% |
| 20% RH | 2.86% | 0.04% | 0.9998 | 0.02% | 0.10% |
| 30% RH | 3.86% | 0.06% | 0.9998 | 0.03% | 0.14% |
| 40% RH | 5.05% | 0.08% | 0.9998 | 0.03% | 0.18% |

| **Batch Number** | **GLB092** | **GMJ098** | **GJI070** | **GNB013** | **3M PET stabilised** |
|---|---|---|---|---|---|
| **Micronised** | **Yes** | **Yes** | **Yes** | **Yes** | **No** |
| **Age (days)** | **688** | **82** | **>1200** | **3** | **581** |
| **Esimating amorphous content** | | | | | |
| 10% RH | 2.65% | 1.94% | 1.82% | 6.40% | 0.93% |
| 20% RH | 2.14% | 1.96% | 1.26% | 6.81% | 0.56% |
| 30% RH | 1.79% | 2.06% | 0.90% | 6.82% | 0.34% |
| 40% RH | 1.43% | 2.23% | 0.61% | 6.45% | 0.20% |
| **Estimated uncertainty at the 95% confidence limit** | | | | | |
| 10% RH | 2.89% | 2.89% | 2.89% | 2.87% | 2.89% |
| 20% RH | 1.56% | 1.56% | 1.56% | 1.55% | 1.56% |
| 30% RH | 1.56% | 1.56% | 1.56% | 1.55% | 1.57% |
| 40% RH | 1.56% | 1.56% | 1.56% | 1.55% | 1.56% |
| **Result with uncertainty** | | | | | |
| 10% RH | < LoD | < LoD | < LoD | 6 ±3% | < LoD |
| 20% RH | 2 ±2% | < LoD | < LoD | 7 ±2% | < LoD |
| 30% RH | < LoD | 2 ±2% | < LoD | 7 ±2% | < LoD |
| 40% RH | < LoD | 2 ±2% | < LoD | 6 ±2% | < LoD |
| Average | 2 ±2% | 2 ±2% | < LoD | 7 ±2% | < LoD |

**Table 19 Amorphous content from DVS analysis calculated by Zografi method.[9]**

The micronised sample GJI070 (aged for 1200 days) along with the 3M PET stabilised development sample shows very low adhesion to the can coatings 3M plasma and PTFE. These materials have amorphous contents below the limit of detection for the analysis. In contrast the samples GLB092 and GMJ098 both show amorphous contents of 2±2%, with adhesion values of between 66 to 85%. The adhesive properties set out in Table 16 for the 3M plasma and PTFE coated cans are plotted against amorphous content in Figure 23. This shows that small changes in amorphous content produce a large change in properties. Given that micronisation is thought to modify the surface,

a small amorphous content could make the entire sample surface amorphous and radically alter properties such as adhesiveness.[15]

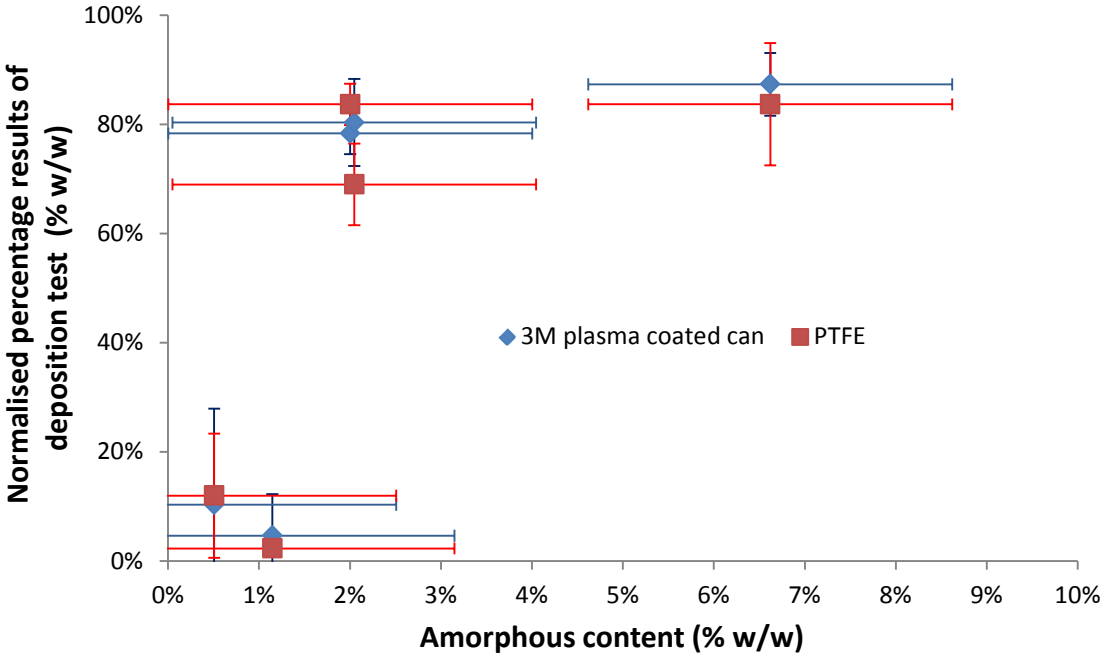


**Figure 23 Salbutamol sulfate deposited on can surface of the 3M plasma and PTFE coated cans plotted cans against the salbutamol sulfate amorphous content calculate using the Zografi method[9]**

If the assumption is made that the 3M micronization process is consistent, then a plot of amorphous content against sample age can be made, where the slope follows a negative exponential decay curve (see Figure 24).

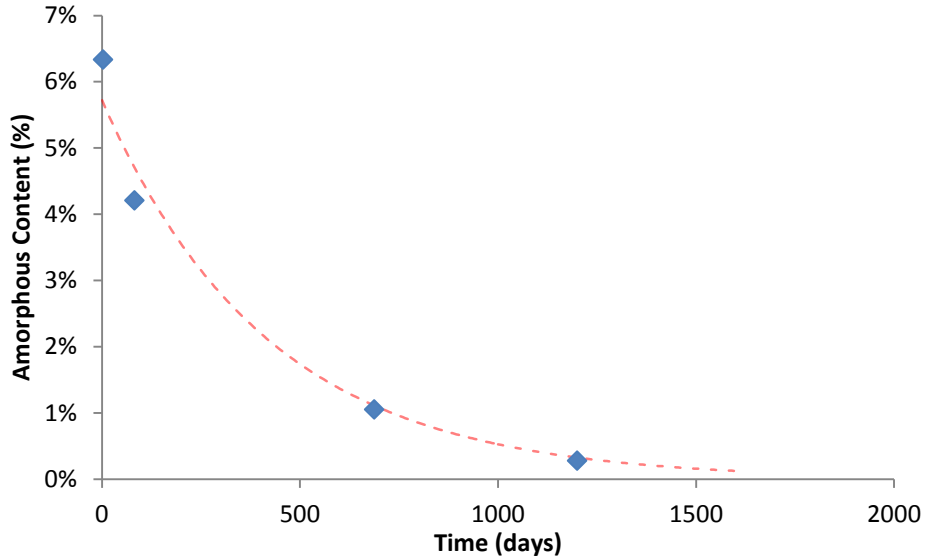


**Figure 24 Amorphous content (calculated by the Mackin method) against sample age in days[14]**

## 8.9 Conclusions

For salbutamol sulfate, low levels of amorphous contents (i.e. 2±2%) have a profound effect on its adhesive properties; this is shown especially with the cans coated with 3M plasma and PTFE. The amorphous content of micronised salbutamol sulfate appears to diminish with age even when stored in sealed glass bottles. The development sample 3M PET stabilised and the micronised sample GJI070 (aged for more than 1200 days) show no detectable amorphous content. These two samples also showed the lowest levels of adhesion to the cans coated with 3M plasma and PTFE.

***Reference***

1 S. S. Park and A. S. Wexler, *Journal of Aerosol Science,* 2008, 39, 266-276.

2 K. Brodka-Pfeiffer, P. Langguth, P. Graβ and H. Häusler, *European Journal of Pharmaceutics and Biopharmaceutics,* 2003, 56, 393-400.

3 S. R. Elliott, *Physics of amorphous materials (Second Edition)*, Longman Scientific & Technical, Harlow, 1990.

4 M. E. Aulton, *Pharmaceutics the Science of Dosage form Design, Second Edition. Churchill Livingstone 2002.*, Livingstone, Churchill, 2002.

5 M. Gorny, M. Jakobs, V. Mykhaylova and N. A. Urbanetz, *Drug Developement and Industrial Pharmacy,* 2007, 33, 235-243.

6 D. P. Strachan and C. H. Sanders, *J. Epidemiol. Community Health,* 1989, 43, 7.

7 'World Health Organization', *WHO guidelines for indoor air quality: dampness and mould*, World Health Organization, 2009., 2009.

8 D. R. Lide, *CRC handbook of chemistry and physics : a ready-reference book of chemical and physical data*, Boca Raton, London, 2009.

9 A. Saleki-Gerhard, C. Ahlneck and G. Zografi, *International Journal of Pharmaceutics,* 1994, 101, 237.

10 J. M. Leger, M. Goursolle, M. Gadret and A. Carpy, *Acta Crystallogr. ,Sect. B:Struct. Crystallogr. Cryst. Chem.,* 1978, 34, 1203.

11 M. A. Palacio, S. Cuffini, R. Badini, A. Karlsson and S. M. Palacios, *J. Pharm. Biomed. Anal.,* 2007, 43, 1531-1534 (DOI:10.1016/j.jpba.2006.11.009).

12 C. A. Schneider, W. S. Rasband and K. W. Eliceiri, *Nature Methods,* 2012, 9, 671.

13 British Medical Association, *Nurse prescribers formula*, British Medical Association/Royal Pharmaceutical Society of Great Britain, London, 2002.

14 L. Mackin, R. Zanon, J. M. Park, K. Foster, H. Opalenik and M. Demonte, *International Journal of Pharmaceutics,* 2002, 231, 227-236.

15 M. D. Jones, P. Young and D. Traini, *Adv. Drug Deliv. Rev.,* 2012, 64, 285-293.

# CHAPTER 9

# Further work and Conclusions

# 9 Further Work

During the course of this thesis a number of different analytical techniques have been used to characterise the different lactose crystalline polymorphs and amorphous samples prepared from the crystalline bulk materials. A number of stories have not been completed due to the finite time available in the laboratory. Some suggestions for further work are summarised in the following sections where additional study could be performed.

## 9.1 Accurate determination of heat capacity using heat flux DSC

The calibration of heat flux DSC for heat flow measurement is usually undertaken via a two point calibration of an empty pan and a sapphire. The measurements from this calibration use the differential of temperature measurement of a sample and standard against time as a means of calculating heat flow. This process can produce good data for the determination of the heat of fusion when a material melts, because there is a change in the signal at this point. However, heat flux DSC is not able to provide quantitative measurements of heat flow when a sample is stable. The determination of amorphous content by measuring the change in heat capacity at the glass transition point is not an accurate measurement, since chapter 5 section 5.7 shows that these quantities are variable depending on the mode of preparation. However, these measurements could be potentially useful, since accurate determination of the heat capacity of an amorphous crystalline mix above the glass transition point could allow accurate determination of amorphous content if the origin of the sample was known.

Accurate heat capacity can be found from calibration experiments that use different weights of a standard with known heat capacity. These measurements show some fluctuation from run to run due to factors such as pan position, contact and sample weight. However, since these fluctuations are consistent throughout the entire experiment, compensatory factors can be determined by carrying out multiple experiments with different weights of the standard. For any temperature within the calibration range, the instrument response against standard weight used should form a straight line. The slope of this line dr/dw is critical for calculating sample heat capacities. At any given temperature the heat capacity of the sample can be found by

multiplying the standard materials known heat capacity with the samples dr/dw and dividing by the standards dr/dw

While the preliminary work has already been carried out during the course of these studies, the writing of a programme to automate this work and output data in a readily usable format is highly desirable.

## 9.2 Use of DSC to investigate amorphous lactose

Identifying stable conditions for storage is of vital importance to the pharmaceutical industry since changes during the storage process can lead to issues with dosing. The Kauzamann temperature is the lowest glass transition point that could theoretically be obtained. It marks a stability point above which the amorphous material is able to crystallise.

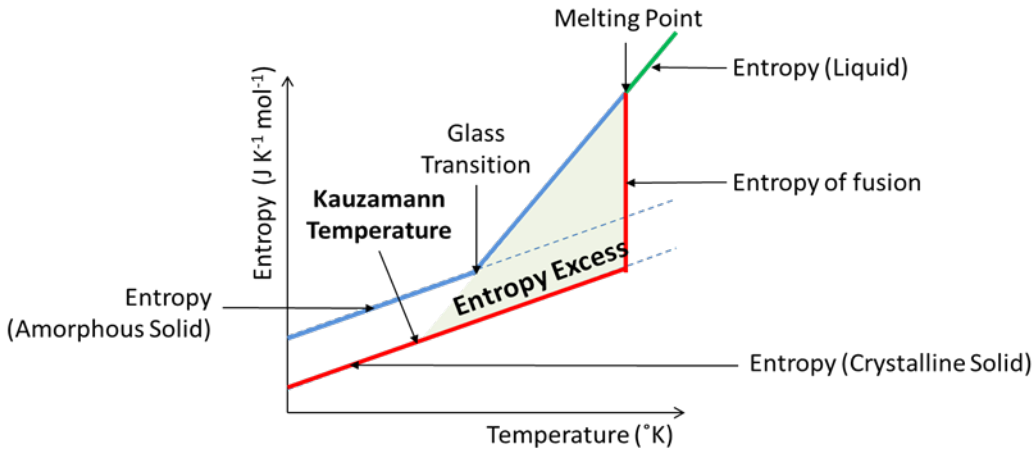


**Figure 1 Determination of the Kauzamann temperature using Entropy of Glass and Crystalline Materials** [1]

The Kauzamann temperature is the point where the entropy of the crystalline form and amorphous form are equal, and is thought to be the temperature below which translational and rotational motions cease to be significant to the stability of pharmaceutical glasses (see Figure 1). The Kauzamann temperature also allows calculation of the maximum amount of energy that can be stored in a glass relative to the crystalline form, which is critical to understanding the energy balance of solubility.[2]

The Kauzamann temperature is obtained from the intercept between the entropy of the crystalline state and the extrapolated line for the entropy of the liquid state. The

entropy excess is obtained by subtracting the entropy of the crystalline form from the amorphous form.

To identify the Kauzamann temperature, spray dried samples were prepared where the temperature of the spray dryer was varied in order to plot heat capacity against temperature of preparation. The heat capacities of these glasses must be found over a range of temperatures from below the Kauzamann temperature up to the crystalline melting point to allow the Kauzamann temperature to be calculated. In addition, a plot of the heat capacity of the crystalline forms must be determined. Heat capacity is easily obtained using Differential Scanning Calorimetry. Once this heat capacity data is obtained the Gibbs function can be calculated for all the polymorphs, allowing prediction of their thermodynamic and kinetic stability, relative to one another.[1] To produce a Gibbs free energy plot, the energy difference between the different polymorphs has to be determined at a particular temperature. This can be once all the forms become liquid, or can be determined by solubility at lower temperatures.

Prior to this work the isomer ratio within amorphous lactose was unknown and so the comparison between crystalline and amorphous would not have been correctly calculated. At present a number of different amorphous spray dried samples have been collected and characterised using DSC. The data necessary for this calculation have been collected with the exception of the energy difference between the amorphous materials prepared via different routes and the crystalline polymorphs.

## 9.3 Determining crystal structure of α-lactose stable and β-lactose

The structures of the anhydrous anomers of lactose are relatively poorly defined, particularly in the case of the α anomer where the limited solubility in any solvent other than water has made preparation of single crystals impossible. Only one structure determination using Rietveld methods has been published and the data was mixed phase with significant quantities of the hydrated phase. The GSAS (General Structural Analysis System) program can manipulate small molecules as rigid bodies; a rigid body being a framework group of atoms and bonds that are isolated within the unit cell.[3] The rigid body can be subjected to translations and rotations within the unit cell and subgroups within the rigid body can undergo internal rotations relative to one

another. Less than 5% of the 'Rietveld'-community make active use of rigid bodies, suggesting such an approach taking into account isomer purity could be unique.[4] The latest editions of GSAS have made the input of rigid bodies much easier from existing CIF files. Refining the α-lactose stable using rigid body frameworks should allow the two dihedral angles Φ (phi) and Ψ (psi) of the glycosidic link to be identified for the first time.[5]

## 9.4 Conclusions

The main objective of this thesis was to find suitable techniques to identify and quantify amorphous lactose and to investigate whether amorphous lactose standards prepared using one method such as spray-drying are suitable standards for materials prepared by other routes. Similar techniques were then applied to other active pharmaceutical ingredients, salbutamol sulphate.

Initial work in this thesis concentrated on preparing the three crystalline polymorphs of lactose, α lactose monohydrate and the two anhydrous anomers α and β. After characterisation using SSNMR, IR spectroscopy, X-ray Diffraction and thermal methods (DSC and DVS), it was apparent that no single technique would be suitable for identifying and characterising these materials due to their complex nature and similar spectroscopic fingerprints.

Amorphous is a term which is used in a curious way throughout the literature. In its most literal sense it should mean that a material has a glaseous composition where there is literally no order at all. The way in which a glass is generally produced means that long range order is not possible as the random viscous melt cools too rapidly to allow the molecules to order (crystalline). The random melt structure is therefore frozen in time leading to a range of environments. However, misunderstanding of the term amorphous has led to the assumption that materials with very small particles (which do not give an X-ray pattern) are glaseous in their nature. This leads to the use of some unfortunate terminology such as the 'amorphous form' or 'amorphous polymorph' implying a material with a single state of disorder. Spray-dried and freeze-dried amorphous materials are prepared from solutions, and so there is logical reasons why they should have a similar properties to a material prepared from a melt. The act of adding water to lactose for example causing mutarotation generating anhydrous β anomer at the same time as maintaining some of the hydrated α form. This contrasts

markedly with the melting process, where the high melting point of lactose means no water is available to the sugar once it has reached the molten state. This thesis has demonstrated that the route of preparation alters the composition of the amorphous product significantly suggesting that many of the literature methods for quantifying amorphous lactose are fundamentally flawed, as no account of the method of preparation is taken into account. DVS measurements clearly show different levels of water uptake depending on the route of preparation and that true glassy samples prepared via the melt method are very poor standards

The composition of amorphous samples were examined by a number of techniques before showing that a modified derivatisation method was the most reliable way to determine α:β ratios. Significant and quantifiable differences were revealed between amorphous materials prepared using different standards which was possible due to the significantly different elution times from the different polymorphs.

The use of relaxation times in SSNMR has been shown to allow good discrimination between amorphous and crystalline lactose and salbutamol sulphate. In addition, some preliminary experiments have shown that the presence of oxygen as well as water may affect $T_1$

**References**

1 S. R. Elliott, *Physics of amorphous materials (Second Edition)*, Longman Scientific & Technical, Harlow, 1990.

2 D. Q. M. Craig and M. Reading, *Thermal analysis of pharmaceuticals*, CRC distributor; Taylor & Francis, New York; London, 2006.

3 A. C. Larson and R. B. Von Dreele, *General Structure Analysis System (GSAS)*, LAUR 86-748, Los Alamos National Laboratory, Los Alamos, 1994.

4 R. E. Dinnebier, *Powder Diffr.,* 1999, **14**, 84-92.

5 T. K. Lindhorst, *Essentials of carbohydrate chemistry and biochemistry*, Wiley, Chichester, 2000.